

INSTITUTE FOR SPACE STUDIES

DRA

Research Review

1972

(NASA-TM-X-70290) RESEARCH REVIEW, 1
JANUARY - 31 DECEMBER 1972 (NASA) 229 p
HC \$14.50 CSCL 03A

N74-32251

Unclass

G3/30 17056

GODDARD SPACE FLIGHT CENTER
NATIONAL AERONAUTICS AND SPACE ADMINISTRATION

GODDARD INSTITUTE FOR SPACE STUDIES

Research Review

January 1, 1972 to December 31, 1972

I. SPACE SCIENCES

January 1, 1972 to June 30, 1972

Balloon-borne Infrared Astronomy.....	1
Far Infrared Spectroscopy.....	6
Molecule Formation and Grain Destruction in Interstellar Shock Waves.....	7
Far IR Observations of H II Regions.....	10
Radio Observations.....	11
Laboratory Astrophysics.....	14
Theoretical Investigations.....	17
Planetary Atmospheres.....	18
Basic Theory of Scattering in Planetary Atmospheres.....	22
Climate Studies with Numerical Models.....	25
Origin of Mare Lavas.....	28
The Nature of Sinuous Rilles.....	30
Crystallization of Matter at High Densities.....	33
Neutrino Astronomy.....	34
Evolution of Massive Stars.....	35
Beta Lyrae and Magnetic Fields in Stars.....	36

July 1, 1972 to December 31, 1972

Radio Observations of Interstellar Molecules.....	39
Laboratory Astrophysics.....	41
<u>Ab Initio</u> Calculation of Molecular Properties, and Processes.....	43
Far Infrared Astronomy.....	45
Neutrino Astronomy.....	48
Evolution of Massive Stars.....	48
Rotation of Massive Stars in Binary Systems.....	50
Neutron Stars: Interiors.....	51
Neutron Stars: Glitches.....	53
Stellar Opacity and Equation of State.....	55
Interpretation of Optical and Radio Interstellar Lines.....	56
Observations of Peculiar A-Type Stars.....	56
Search for Black Holes.....	57
Fundamental Data for Contact Binaries.....	57
Gas Clouds in Dense Star Clusters.....	58
Cooling of Neutron Stars.....	58
Jupiter Occultation Experiment.....	60
The Formation of Planets and Stars.....	62

II. APPLICATIONS

January 1, 1972 to June 30, 1972

Program on Stratospheric Chemistry and Global Pollution.....	67
Carrier Balloon Systems Studies: NOAA Request.....	75

Investigation of Need for Reference Level	
Measurements in GARP.....	77
Use of Simulated VTPR Radiance Measurements in a	
General Circulation Model.....	79
Preparation for Use of Real VTPR Radiance Data	
in a General Circulation Model.....	81
Tests of a Procedure for Deriving Atmospheric	
Temperature Profiles from Satellite Radiance	
Measurements.....	83
Acquisition of the 370/165.....	88
Facilitating the Use of Fortran Programs with	
Parallel Processing Computers.....	90
Preparation of the Data Utilization Plan in DST.....	92
Cloud Scattering and Absorption Effects in the	
GISS Model.....	94
Diagnostic Studies of the GISS Five-Level Model.....	96
Effects of Cloud Distribution in Numerical Modeling...	104
Alternative Parameterization of Moist Convection.....	109
Preliminary Studies on Long-Range Forecasts.....	114
Numerical Simulation of Small-Scale Convection.....	117
Flight Measurements of Cloud Polarization.....	119
Earth Resources Study.....	122

July 1, 1972 to December 31, 1972

Parameterizations of Moist Convection in the GISS	
Model of the Global Atmosphere.....	127
A Parameterization for the Absorption of Solar Radia-	
tion in the GISS Model of the Global Atmosphere..	132
Treatment of Long-Wave Radiative Transfer in the GISS	
Model of the Global Atmosphere.....	135
Diagnostic Studies of the GISS Model of the	
Global Atmosphere.....	137
Spectral Studies of GISS Model of the Global	
Atmosphere.....	140
Objective Sea-Level Pressure Analysis for Sparse	
Data Areas.....	141
Flight Measurements of Cloud Polarization.....	144
Theoretical Studies of Baroclinic Waves.....	147
Numerical Simulation of Small-Scale Convection.....	150
Atmospheric Chemistry and Global Pollution Studies....	154
Remote Sensing of Earth Resources: Multispectral	
Photographic Discrimination of Different	
Lithologies, Bagdad, Arizona.....	188
Mariner 9: Preliminary Photographic Examination	
of the Martian "Canyonlands" and "Chaotic	
Terrain".....	189
Evaluation of the Geological Usefulness of Gemini,	
Apollo and ERTS-A Satellite Photographs of	
the Southwest.....	193
Improving the Efficiency of Computer Programs.....	197
Implementation of the 370/165.....	199
Receipt of VTPR Sounding Data.....	200
Pre-processing of VTPR Data.....	201
Retrieval Program.....	203

Elimination of Clouds in VTPR Data.....	206
Tuning the Retrievals.....	210
Accuracy of VTPR Temperature Retrievals.....	213

III. PUBLICATIONS

IV. GISS COLLOQUIA

I. SPACE SCIENCES

January 1, 1972 to June 30, 1972

BALLOON-BORNE INFRARED ASTRONOMY. (W. Hoffmann, R. Emery, P. Aannestad)

This is a continuing program of astronomical surveys and observations in the far infrared (100-micron wavelength) region of the electromagnetic spectrum. Observations are carried out with a stabilized, ground controlled, 12-inch telescope and associated balloon gondola developed and built at GISS and Columbia University. The analysis program for detecting sources, and determining their position, intensity, and significance is carried out on the GISS Institute IBM 360-95 computer. Concurrently, a laboratory program of Fourier transform spectroscopy has been initiated for development of better filters in the far infrared. A new cryogenically cooled telescope is being developed in collaboration with Cornell University.

During the past year, Hoffmann, Emery and Aannestad have (1) published a catalog of 72 far infrared sources detected during a survey of the galactic plane (Ap. J. (Letters) 170 L89(1971)), (2) carried out two balloon flights from Parana Argentina to survey the Southern galactic plane and the Magellanic clouds, (3) carried out two balloon flights from Palestine, Texas to observe extragalactic sources and infrared stars, and (4) made a number of improvements and additions to the balloon gondola.

The 100-micron catalog is the first such far infrared catalog published. Most of the sources are newly discovered. They appear to represent a variety of astronomical objects. About two-thirds of the sources are associated with H II regions as determined by radio recombination line observations, optical observations, and radio continuum measurements. Twenty-two of the objects have been observed to have molecules OH and formaldehyde. Six have been identified with dark nebula and 12 were unidentified.

Workers in other fields of astronomy have begun to use this catalog to make new discoveries. D. Dickinson of the Smithsonian Astrophysical Observatory has observed OH line emission in two of the dark nebula and two of the unidentified objects. There is now a growing body of evidence that the far infrared emission is thermal radiation from dust clouds heated to above normal interstellar temperatures by one or more hot stars. The dust in these regions plays an important role in the formation of molecules from the dissociating radiation from the nearby stars. Additional evidence for this comes from recent observations (by P. Solomon of the University of Minnesota) of a ridge of CO line emission connecting the sources Sgr A and Sgr B 2 in the galactic center. This is the first independent support for this feature of the GISS 100 μ map published in 1971 (Ap. J. (Letters) 164 L23).

The balloon flights carried out from Argentina have yielded approximately 40 new 100-micron sources in the very southern sky. Most of these sources appear along the galactic plane which was covered from $l_{II} = 260^\circ$ to $l_{II} = 310^\circ$. Figure 1 shows some of the regions of the sky surveyed. The new sources include two faint objects and a bright very extended ($3/4^\circ$) object at the edges of the Coal Sack nebula, the Carina nebula, which is over $3/4^\circ$ in extent, and might show some structure at 100 microns, and a source near 30 Doradus, which is perhaps the nucleus of the Large Magellanic cloud, the nearest galaxy to the Milky Way. Over two-thirds of the new sources coincide with radio sources. Several of the sightings on these flights confirm previous observations of faint sources in Orion which have not been otherwise identified. Table 1 gives a preliminary listing of the new sources.

The Coal Sack is a dark nebula in the southern Milky Way extending 4° in size and containing a number of small bright nebulae and continuum radio sources. It has a distance of 170 parsecs, diameter of 8 pc and mass of dust grains about $14 M_\odot$. The entire cloud could not be mapped in the far infrared. The three sources observed are probably associated with H II regions in the nebula. If so, the brightest of them, object No. 38 has a 80 - 135 micron luminosity of $2.8 \times 10^3 L_\odot$.

The Carina nebula, NGC 3372, is a large bright nebula extending $2^\circ \times 3^\circ$; it is at a distance of 1700 parsecs making its linear extent about 80×52 parsecs. It is dominated by the unusual star, Eta Carinae, located near its center. Eta Carinae underwent a nova-like explosion in the 1840's. At present, it is faint visually, but at 10 and 20 microns it is the brightest object outside the solar system. It is variously described as a pulsating super massive star or as a "slow" super nova where visual properties are sharply effected by the dust it is inbedded in.

The 100-micron measurements of the Carina nebula show an object extended at least $3/4^\circ$ with a 80 - 135 μ luminosity of approximately $4 \times 10^5 L_\odot$. The analysis is continuing, in an attempt to distinguish the Eta Carinae object from the extended nebula.

The Large Magellanic cloud is of particular interest because it is the closest galaxy to the Milky Way (50 kiloparsecs). It is also very different in structure from the Milky Way. It is irregular rather than spiral, and has less interstellar dust. Its nucleus is believed to be in the direction of 30 Doradus in the Tarantula nebula. The radio properties of this region are very similar to those of the galactic center.

If the central part of the Large Magellanic cloud has the same far infrared size, luminosity and spectrum as the center of our galaxy, we should expect to observe a flux of $10^{-21} \text{ Wm}^{-2} \text{ Hz}^{-1}$. Such a flux is clearly not observed. The object (No. 4) that appears to be in the direction of 30 Doradus is $1 \times 10^{-22} \text{ Wm}^{-2} \text{ Hz}^{-1}$ or 10 times fainter, indicating a clear difference in the dust content or the stellar luminosity of the central part of the Large Magellanic cloud from that of the center of the Milky Way.

The flights carried out in Texas in June are now being analyzed. The inclusion of a photograph camera for star fields will aid in obtaining more accurate positions.

The program for the coming year includes:

1. A series of tests of the telescope, secondary chopper, and detector in an environmental test chamber to locate and eliminate the source of excess system noise
2. Additional survey and extragalactic observing flights from Texas
3. Collaboration with Cornell University on a cryogenically cooled telescope to be flown on our gondola. This should substantially improve the sensitivity over the present system and help to pave the way for cryogenically cooled infrared space telescopes
4. Preparation of instruments for studying the galactic center region in the far infrared with the NASA 91-cm airborne telescope

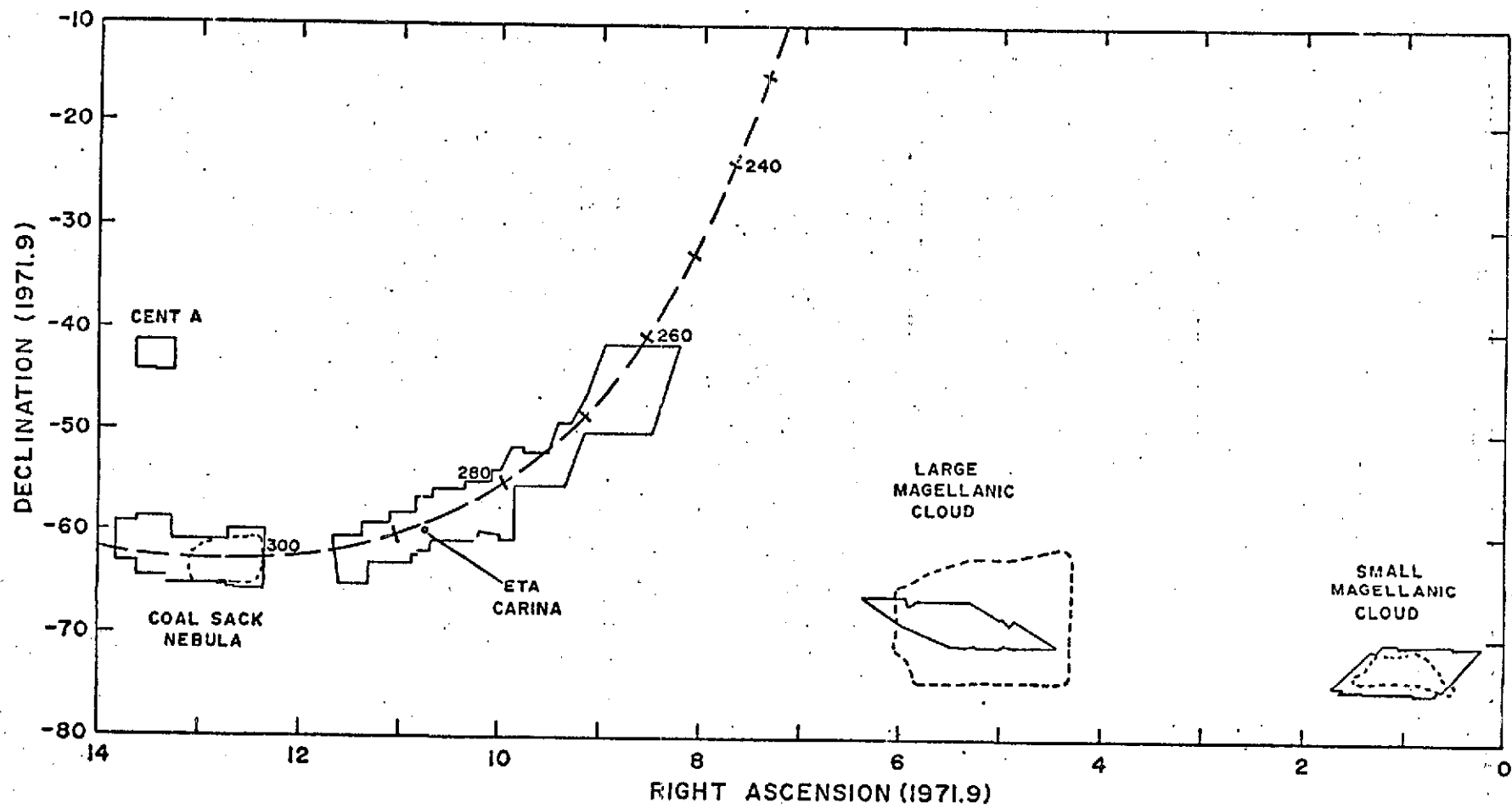


Figure 1. Regions of sky covered flights B-7, B-8 Nov., Dec., 1971.

Table 1

100 MICRON SOUTHERN HEMISPHERE SOURCE LIST

No.	$\alpha(1950)$			$\delta(1950)$	Flux	Signifi- cance σ 's	Identification
	h	m	s		$10^{-22} \text{ W m}^{-2} \text{ Hz}^{-1}$		
1	5	14	51	-44 39	.6	3.5	
2	5	17	38	-45 08	.7	4.1	
3	5	31	44	-5 00	.3	3.8	LHE 151
4	5	36	16	-69 22	1.0	5.4	OSRO 29 00172 (30 Doradus, Large Magellanic cloud)
5	5	37	55	-70 00	.5	2.7	(Large Magellanic cloud)
6	5	39	07	-1 53	10	22	ORION B
7	8	55	44	-47 04	8.0	39	KES 05
8	8	57	19	-43 34	2.6	18	KES 04
9	8	59	49	-48 15	1.6	8	KES 06
10	8	59	42	-47 22	1.3	6.5	SG 268.0 - 01.0
11	9	01	29	-48 00	.7	3.7	KES 07
12	9	04	26	-42 56	.6	2.9	
13	9	09	41	-48 24	.5	2.6	
14	9	10	26	-49 35	.5	2.7	
15	9	15	03	-49 31	.6	3.2	
16	9	18	07	-50 08	.6	3.2	
17	9	20	52	-50 10	.6	2.9	
18	9	20	31	-51 07	.5	4.1	
19	9	22	22	-51 48	1.8	14	KES 08
20	9	56	36	-56 28	.6	3.7	
21	9	57	30	-54 41	.4	2.6	
22	9	59	30	-56 21	.5	2.8	MP 0959-56
23	10	03	21	-56 53	1.0	10	KES 09
24	10	10	47	-57 24	.6	5	SG 283.2 - 01.1
25	10	11	00	-60 00	.4	2.7	
26	10	17	21	-57 45	1.0	6.2	SG 284.0 - 01.0
27	10	21	02	-57 25	5.6	37	KES 10
28	10	40	18	-59 17	6	40	ETA CAR Nebula
29	10	42	45	-58 36	.9	6	RCW 53
30	10	44	29	-58 45	.4	2.7	MSH 00404
31	10	46	46	-59 40	.6	2.6	SG 288.0 - 00.8
32	10	58	37	-60 38	.7	2.6	KES 13
33	11	09	25	-61 00	6.3	22	KES 14
34	11	12	29	-60 59	6.6	23	SG 291.6 - 00.5
35	11	18	35	-59 54	.9	3.1	
36	12	28	52	-62 22	.5	2.6	BA 300.6 + 0.1 (Coal Sack Nebula)
37	12	34	41	-63 34	.7	3.8	(Coal Sack Nebula)
38	13	07	29	-62 19	5.0	27	KES 18 (Coal Sack)
39	13	09	40	-61 00	.8	4.1	BA 305.6 + 1.6
40	13	10	08	-62 28	1.6	8	SG 305.6 + 00.0
41	13	45	28	-61 21	1.1	5	DTG 309.9 + 0.4

FAR INFRARED SPECTROSCOPY. (R. J. Emery)

A laboratory for far infrared Fourier transformer spectroscopy has been established (1) to permit direct measurement of the filter band pass characteristics for the far infrared systems used in the GISS balloon borne observing program; (2) to provide measurements for the development of new filter systems using combinations of "capacitive" and "inductive" electroformed metal mesh patterns on mylar and polyethylene substrates, and (3) to provide experience for future far infrared astronomical line spectroscopic measurements.

The system consists of a Fourier spectrometer, liquid helium, cooled germanium bolometer, controller, digitizer and tape recorder. The instrumentation and computer programs are complete and have been fully tested. Present work includes refinement of the technique for producing accurately registered mesh patterns and measuring the transmission properties of various meshes. This is in preparation for designing a series of accurately controlled far infrared band pass filters.

MOLECULE FORMATION AND GRAIN DESTRUCTION IN INTERSTELLAR SHOCK WAVES. (P. Aannestad).

Since high temperatures can overcome the activation energies involved in many chemical reactions, shock waves may be a way of forming interstellar molecules. Such waves are set up when interstellar gas clouds collide or when they encounter expanding H II regions. The OH molecule is often found to be associated with H II regions, and it was suggested by Dieter and Goss in 1966 that OH may be derived from H₂O as the H₂O is sputtered off interstellar grains in hot shock fronts. Aannestad has investigated in detail both hot gas phase reactions and the destruction of grains as a source for simple molecules in interstellar space.

Figure 1 depicts the variation of various molecular abundances (relative to the H-abundance) as a function of time after passage of the gas through the shock front. It can be seen that OH and H₂O can attain an abundance of $\sim 10^{-5}$ relative to H, but only over a narrow region, $\sim 10^{-3}$ pc, immediately behind the shock front. The column density of OH is about 10^{13} cm⁻², which for hot OH fails by a factor of 10^3 to account for the absorption observations. It is concluded that the sputtering process is inherently inefficient in the formation of OH, since the high temperatures also destroy OH rapidly via the reaction $\text{OH} + \text{H} \rightarrow \text{H}_2 + \text{O}$.

Figure 1 indicates that the molecules CO, CN, and CH are very abundant far behind the shock front. This is of importance since recent observations indicate that CO is very abundant near interstellar H II regions. Similarly, CN is known to be anomalously abundant in the immediate neighbourhood of the H II region near the cluster NGC 7822, and in front of the star 20 Aql.

The sputtering process is a way of destroying interstellar grain mantles, and Figure 2 indicates how the final grain radius depends upon the shock velocity for various abundances of molecular hydrogen. It appears that the critical shock velocity for complete removal of the grain mantle (radius = 0.05 μ) is 13-15 kms⁻¹. This leads to a destruction probability of $(4.3-1.4) \times 10^{-8}$ yr⁻¹, and to a steady state distribution of grain radii given by $n(a)/n(a_0) = e^{-20(a-a_0)}$ where a is the grain radius in microns and a_0 is the core radius (0.05 μ). The average grain radius for core-mantle grains is then found to be $\bar{a} = 0.1 - 0.07 \mu$. The smaller value is roughly consistent with the observational limit on the mantle size, if the mantle has ice in it.

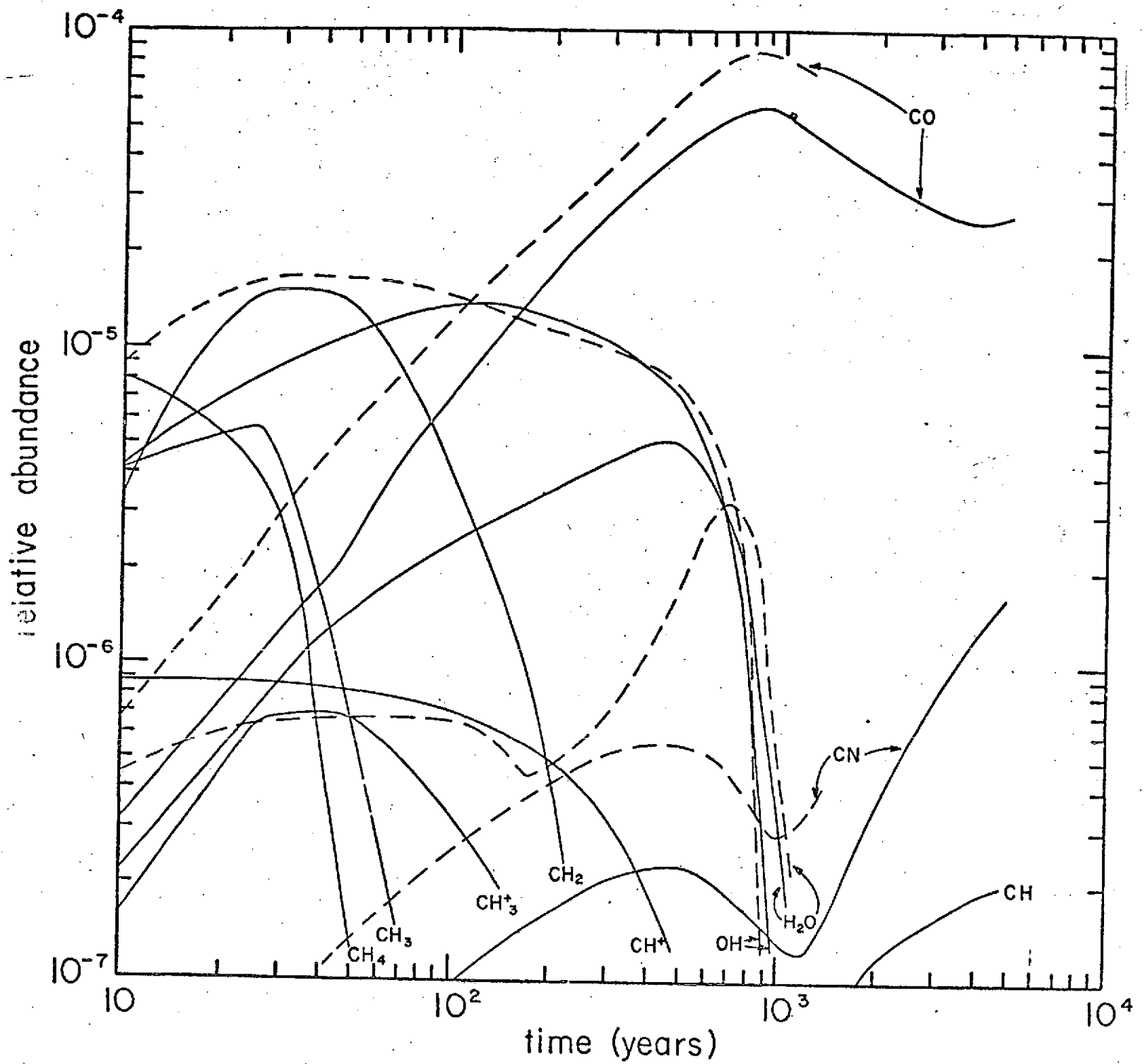


Figure 1. Molecular abundances relative to atomic hydrogen as functions of time. The solid curves are for $H_2/H = 2 \times 10^{-2}$ and a shock velocity $v_1 = 10 \text{ hours}^{-1}$. The dashed curves are for the same H_2 abundance, but with $v_1 = 15 \text{ hours}^{-1}$.

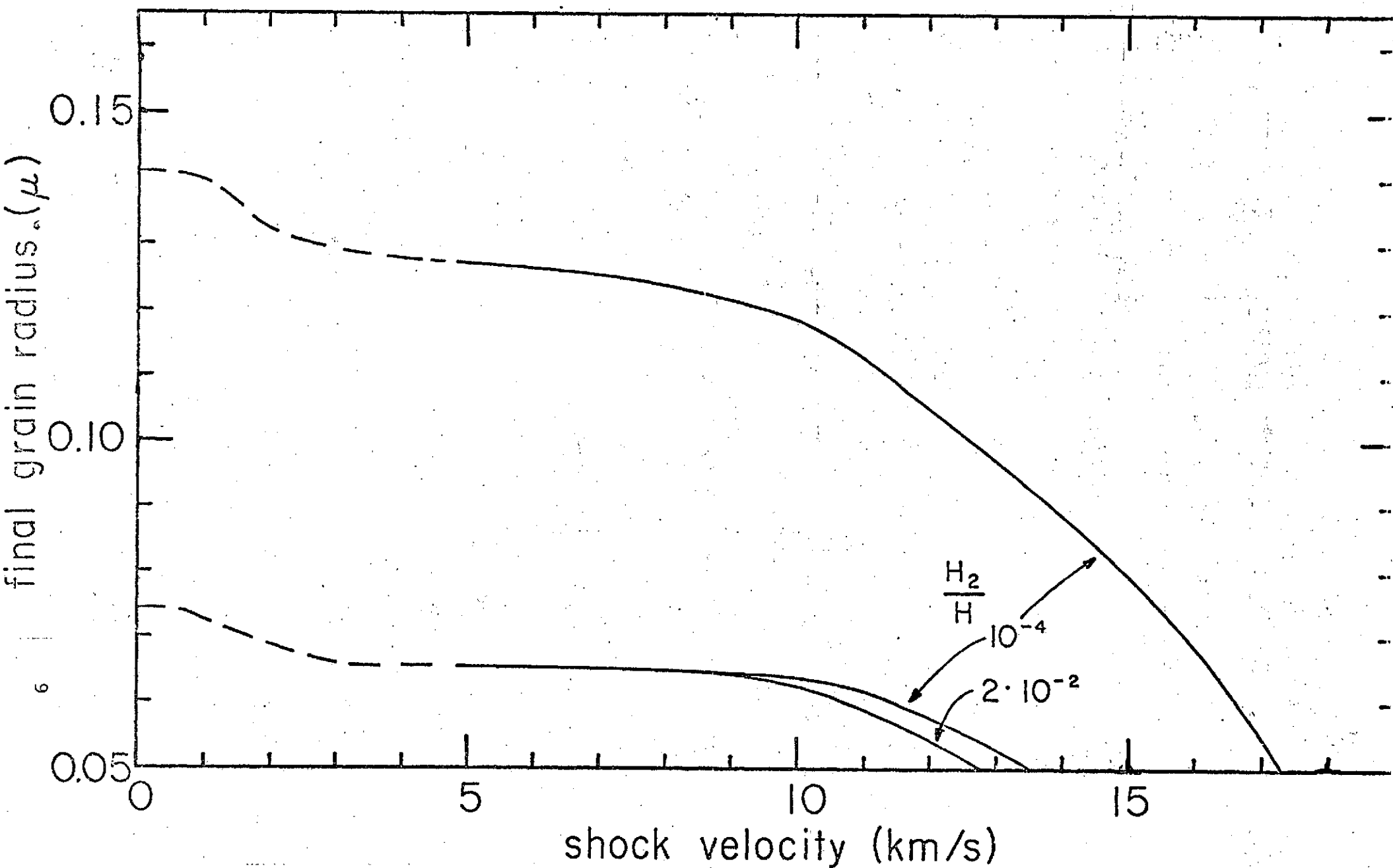


Figure 2. Final grain radii as functions of the shock velocity. The upper and lower curves correspond to two different pre-shock conditions for the dust and gas. The molecular hydrogen abundance is as indicated.

FAR IR OBSERVATIONS OF H II REGIONS. (P. Aannestad).

Far infrared observations of H II regions by Hoffmann, Frederick and Emery yielded objects for which the ratio of the 100μ flux density to the radio continuum flux density varied over three orders of magnitude. However, if sources with radio sizes much larger than the IR sizes are excluded (Figure 1), the linear relationship found by Harper and Low is roughly confirmed. In the figure, the lines attached to a given source refer to uncertainties in the radio measurement, and the source numbers refer to Hoffmann et al.'s 100μ survey. It seems that thermal reradiation from dust grains of short wavelength radiation is a universal mechanism in H II regions. However, as is shown by the dashed line in Figure 1, the 100μ flux exceeds the Lyman- α flux for many sources. This means that, unless there are other sources of energy input to the dust, the dust must compete effectively with the gas for Lyman continuum radiation. This is difficult to understand unless the dust to gas ratio is anomalously high in these sources, suggesting an as yet unknown mechanism for the separation of gas and dust.

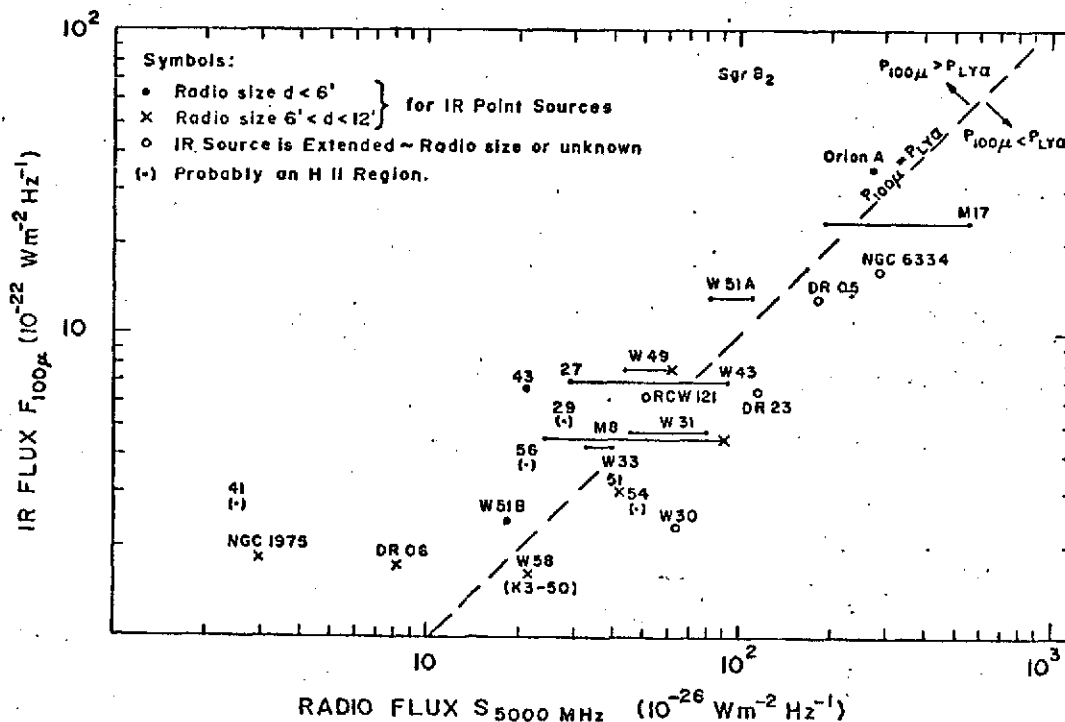


Figure 1. 100μ flux densities plotted vs. radio flux densities at 5000 MHz . The dashed line denotes where the total 100μ power equals the power in the Lyman - α line.

RADIO OBSERVATIONS. (P. Thaddeus, M. L. Kutner).

As part of the continuing collaboration with Bell Telephone Laboratories (A.A. Penzias, R.W. Wilson, K.B. Jefferts), observing capability has been extended to wavelengths as short as 1.7 mm. Using the 36-foot telescope of the National Radio Astronomy Observatory, Thaddeus and Kutner have detected, for the first time, interstellar hydrogen sulfide (H_2S). This molecule appears to be moderately abundant in a number of sources (see Figure 1).

The 172 GHz line of $HC^{15}N$ was also detected. This is the first observation of ^{15}N in any non-terrestrial source. The observations yield an isotopic abundance ratio $b/a = (^{14}N/^{15}N)/(^{12}C/^{13}C)$ of 2.6 ± 0.8 in Orion, in agreement with the terrestrial value 3.11, indicating that the carbon and nitrogen isotopic ratios a and b have separately their terrestrial values. (Figure 2).

At this wavelength, an as yet unidentified line, U169.3, has also been found.

Several lines of methanol have been detected at a frequency of 145 GHz in the Orion Nebula, Sgr B2, Sgr A and DR 21 (OH). An analysis of these lines indicated that in Orion they are described by a unique excitation temperature ($\sim 25^{\circ}K$) which in turn yields information on the excitation of this molecule. (Figure 3).

Using the NRAO 140-foot telescope, Thaddeus and Kutner have made a study of 6-cm formaldehyde (H_2CO) anomalous absorption in dark clouds. The strength of the 6-cm line at a number of locations was compared with the optical extinction, and a rather tight correlation was found, indicating either a density dependence of the pumping mechanism responsible for the anomalous absorption or an association between molecules and interstellar dust.

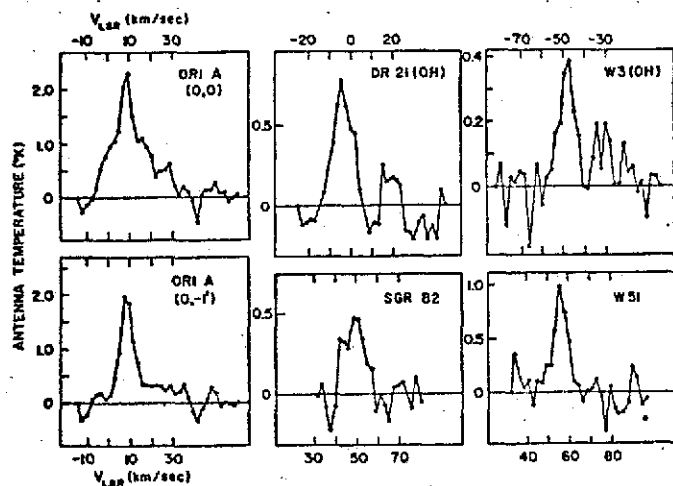


Figure 1. The stronger H_2S , $1_{10} \rightarrow 1_{01}$, 168.7 GHz, emission lines, observed at a resolution of 2.1 km/sec. The rather broad wings on the line observed in the center of the Orion infrared nebula (upper left) are probably real, and do not have a counter -- part in other molecular lines.

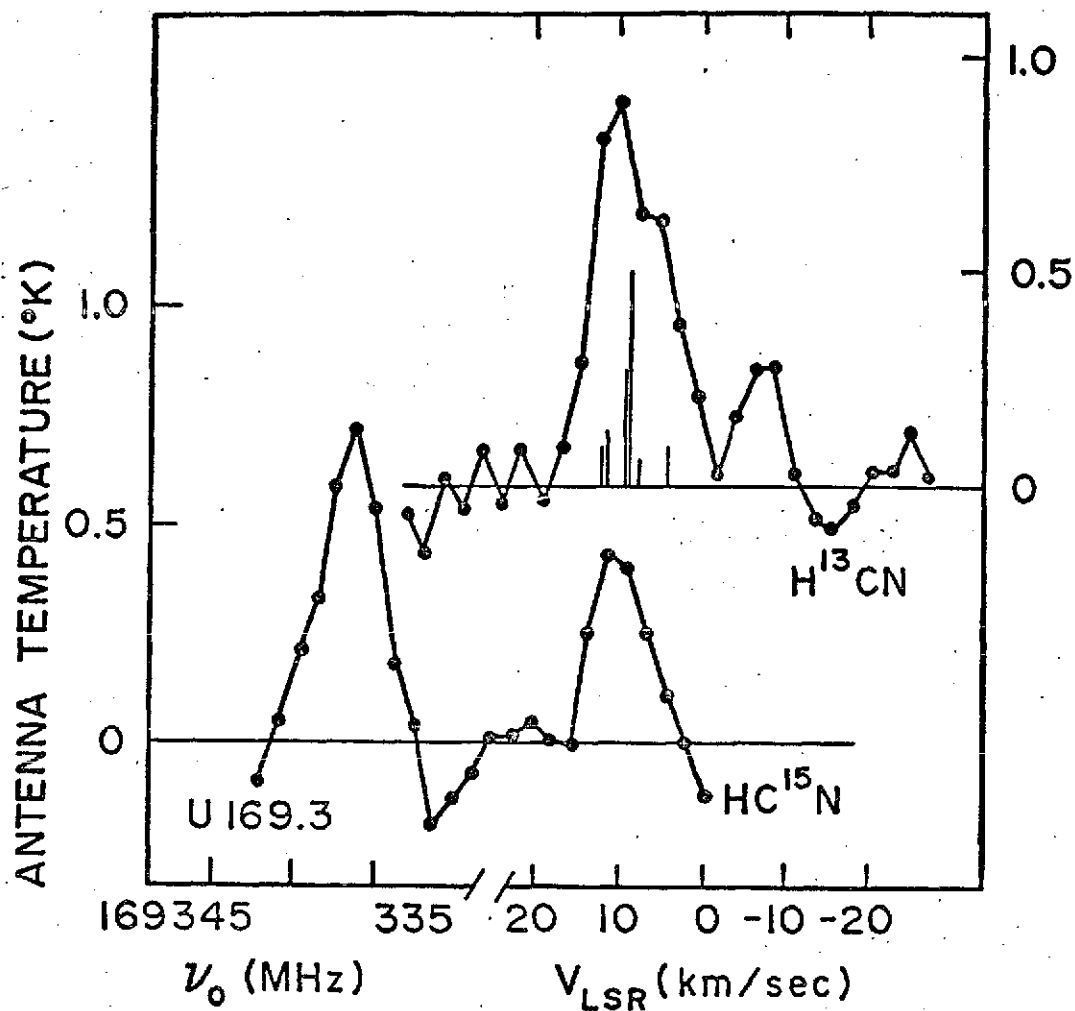


Figure 2. The $J = 2 \rightarrow 1$ lines of $H^{13}CN$ and $HC^{15}N$, and U169.3, in the infrared nebula in Ori A. The $H^{13}CN$ line is somewhat wider than that of $HC^{15}N$ - probably because of the indicated quadrupole hyperfine structure of the nitrogen-14.

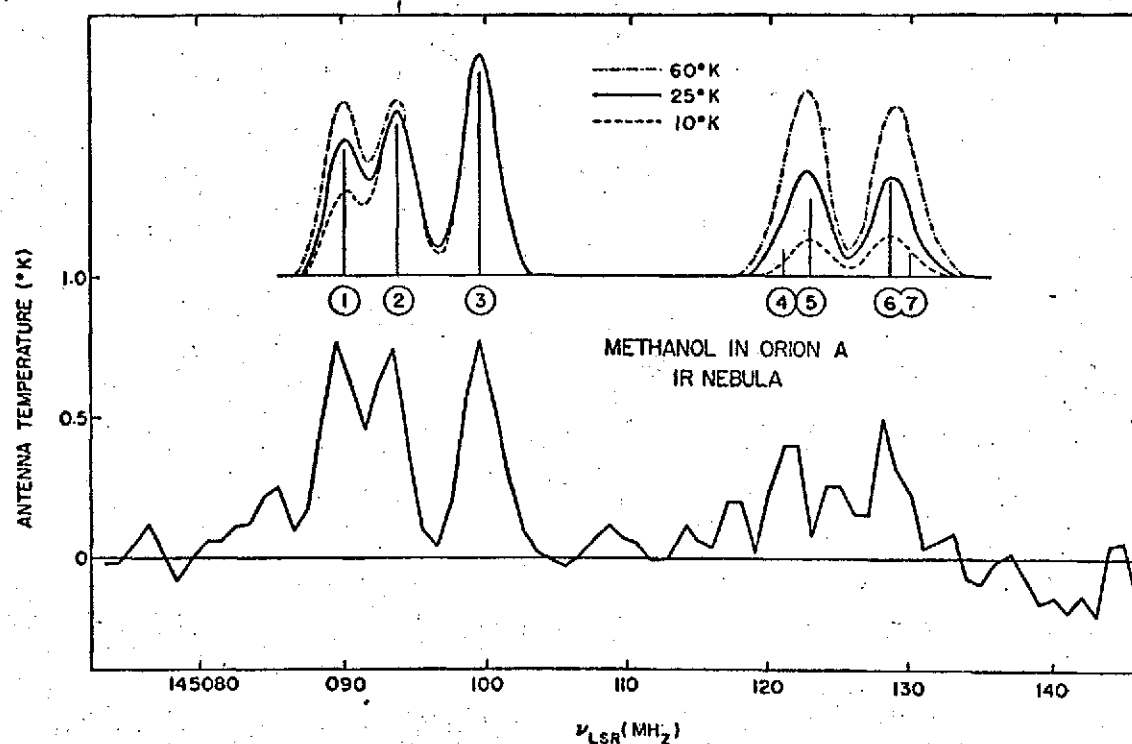


Figure 3. The lower section is the observed spectrum of the $J = 3 \rightarrow 2$, $K = 0$ lines of methanol in the Orion infrared nebula. Above are the predicted spectra for the indicated excitation temperatures. The sticks indicate the positions of the seven lines.

LABORATORY ASTROPHYSICS. (P. Thaddeus, G.R. Tomasevich, K.D. Tucker, L. Gaines, R.B. Nerf, M.A. Sonnenberg).

Beam maser studies of formaldehyde and its isotopic species have been completed. For the normal species and for the ^{13}C and ^{18}O species, the hyperfine structure (hfs) for all rotational transitions of foreseeable astronomical interest has now been determined. A number of methanol transitions in the neighborhood of 1 cm have been detected in a maser for the first time, and hfs has been observed. These transitions are currently being investigated with improved resolution in order to determine the hyperfine coupling constants.

A new maser, with a fourfold increase in resolution over existing ones, has been constructed for the continuing study of the magnetic hfs of simple organic rings (Figure 1). Five transitions of furan at $\lambda \sim 6$ cm have been observed with a linewidth of only 500 Hz, allowing the small magnetic coupling constants to be determined. The fully deuterated species is being studied to obtain information about the molecular field gradients. Hyperfine structure in formic acid and pyrrole, observed previously with lower resolution, is also being studied in the new maser.

Frequencies of millimeter-wavelength transitions of H_2^{12}CO and H_2^{13}CO of astronomical interest have been measured to a precision generally exceeding one part in 10^6 . Using this data in cooperation with Kirchoff, Lovas and Johnson of the National Bureau of Standards, we have improved the accuracy of the values of the rotational constants of the two species by an order of magnitude (Table 1).

During the past year, the study of the pressure broadening of the low-lying rotational absorption lines of formaldehyde (H_2CO) has continued. Self- and foreign-gas-broadening parameters for a number of 2 mm transitions have been obtained, and are being compared with widths calculated using the Anderson (1949) and Tsao and Curnutte (1962) theory of pressure broadening. The $\text{H}_2\text{CO}-\text{H}_2$ excitation cross sections, which will be compared with those obtained by Thaddeus (1972) are of particular astrophysical interest in connection with the absorption of the 3° K cosmic blackbody radiation by interstellar formaldehyde clouds.

A survey was made in the laboratory for a simple organic molecule with an absorption line at 169337.3 MHz, for identification of the radio line U169.3 (see above). Over twenty simple organic molecules were studied. The most likely candidate is methanol, with $10_0 \rightarrow 10_1$ absorption at 169335.34 MHz.

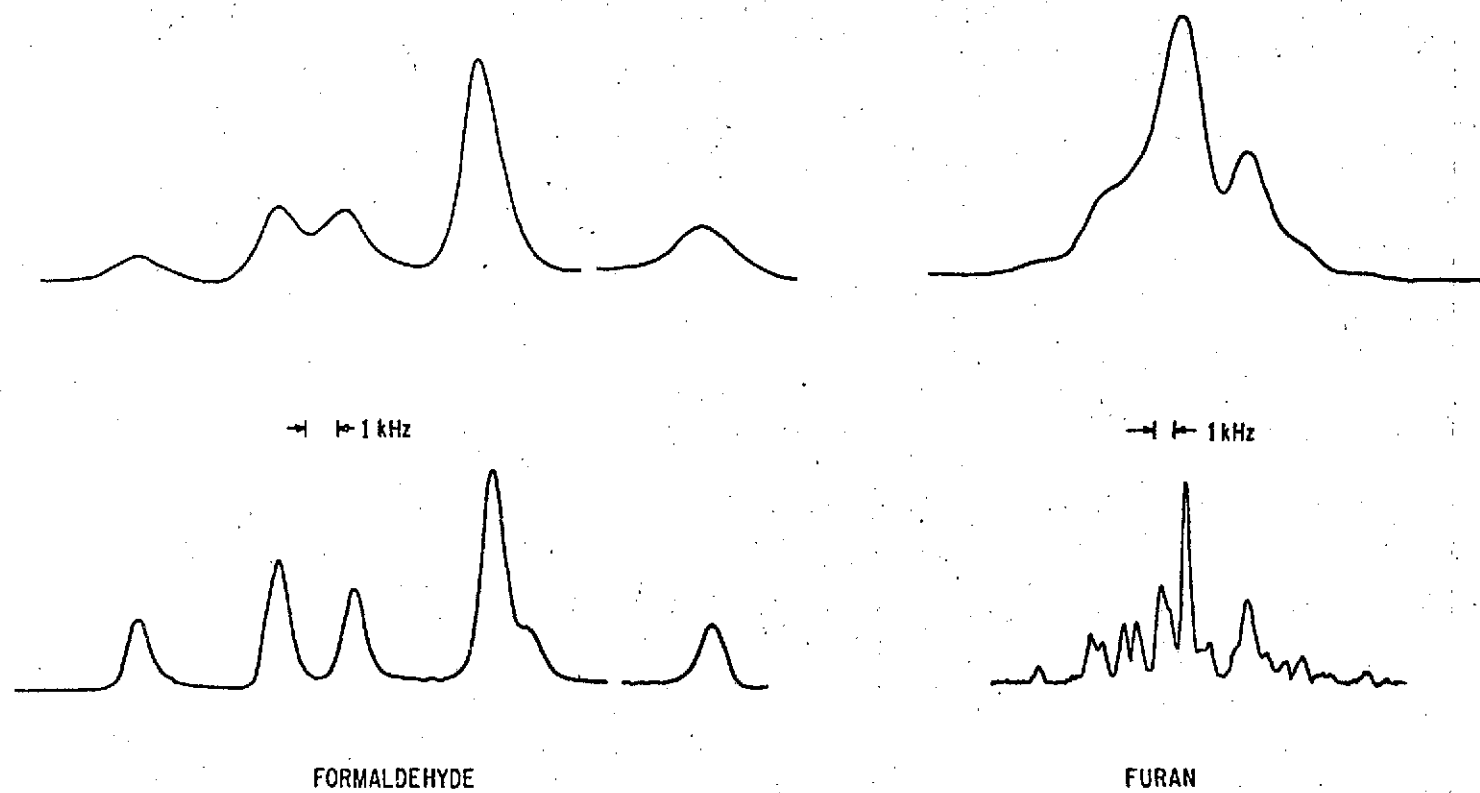


Figure 1. *Magnetic hfs of two simple organic rings.*

Table 1

FORMALDEHYDE FREQUENCIES

Transition	H_2^{12}CO				H_2^{13}CO			
	Observed (kHz)		Calculated (kHz)		Observed (kHz)		Calculated (kHz)	
$4_{13}^{-4}14$	48 284 521 \pm 11		48 284 518 \pm 7		45 920.064 \pm 10		45 920 059 \pm 13	
$5_{14}^{-5}15$	72 409 099 \pm 32		72 409 096 \pm 15		68 864 551 \pm 28		68 864 566 \pm 31	
$0_{00}^{-1}01$	72 837 974 \pm 24		72 837 964 \pm 24		71 024 797 \pm 20		71 024 791 \pm 19	
$6_{15}^{-6}16$	101 332 991 \pm 44		101 333.000 \pm 31		---		96 375 752 \pm 62	
$7_{16}^{-7}17$	135 030 466 \pm 32		135 030 476 \pm 56		128 431.390 \pm 220		128 431 421 \pm 112	
$1_{11}^{-2}12$	140 839 526 \pm 32		140 839 536 \pm 32		137 449.969 \pm 30		137 449 971 \pm 28	
$1_{01}^{-2}02$	145 602 966 \pm 33		145 602.976 \pm 35		141 983.749 \pm 32		141 983.764 \pm 31	
$1_{10}^{-2}11$	150 498.355 \pm 34		150 498.355 \pm 32		146 635.690 \pm 33		146 635.686 \pm 28	
$2_{12}^{-3}13$	211 211.468 \pm 48		211 211.464 \pm 45		206 131 629 \pm 46		206 131.641 \pm 33	
$2_{02}^{-3}03$	218 222 186 \pm 49		218 222.212 \pm 59		212 811.221 \pm 47		212 811 208 \pm 48	
$2_{21}^{-3}22$	218 475.620 \pm 64		218 475 621 \pm 86		213 037.360 \pm 120		213 037 291 \pm 129	
$2_{20}^{-3}21$	218 760.077 \pm 49		218 760.049 \pm 86		213 293.500 \pm 120		213 293 579 \pm 129	
$2_{11}^{-3}12$	225 697.787 \pm 78		225 697.788 \pm 45		219 908.526 \pm 56		219 908.503 \pm 33	
$3_{13}^{-4}14$	281 526.950 \pm 120		281 526.913 \pm 143		274 762.120 \pm 190		274 762.126 \pm 92	
$3_{12}^{-4}13$	300 836.610 \pm 130		300 836.627 \pm 143		293 126 514 \pm 65		293 126.519 \pm 92	

THEORETICAL INVESTIGATIONS, (P. Thaddeus, S. Green).

Use of the Hartree-Fock method has been examined for calculating properties (dipole and quadrupole moments, hyperfine constants) of diatomic molecules. Techniques have been developed for improving upon the Hartree-Fock results by means of selective configuration interaction. Calculations have been done on NO $X^2\Pi$ and $A^2\Sigma^+$, CO $a^3\Pi$, CN $X^2\Sigma^+$ and $B^2\Sigma^+$, OH $A^2\Sigma^+$, and ClF $X^1\Sigma^+$. Results for ClF indicate that a determination of the dipole polarity by Flygare et al. is incorrect.

Using accurately calculated potential energy curves of Green et al., Franck-Condon factors for the A to X transition in CH^+ were computed. Because of a large discrepancy with the RKR results of Liszt and Smith, the latter were re-examined and found to be in error; there is now excellent agreement of Franck-Condon factors determined from Morse, ab initio, and RKR potentials.

In order to perform accurate calculations on rotationally inelastic scattering of H_2CO and H_2O , the close-coupling formalism has been modified to handle symmetric rotors. Current diatomic scattering programs are being modified to incorporate these changes.

PLANETARY ATMOSPHERES, (R. W. Stewart).

Analysis of the radio occultation data returned by the Mariner Mars 6 and 7 spacecraft has been completed (with J. S. Hogan and S. I. Rasool). The published results derived from this program have been lower atmospheric temperature profiles and ionospheric electron density profiles over four points on the Martian globe. A complete error analysis was also performed on the occultation data and the results are in the process of publication.

A theoretical study of the Mars and Venus ionospheres has also been completed. The principal result of this study was the inadequacy of known ionization sources to provide the correct magnitude of the observed electron densities. A companion investigation of the ion composition of these planetary ionospheres indicated that O_2^+ is probably the major ion throughout the altitude range over which electron densities have been observed.

Figures 1, 2, and 3 compare the observed electron density profiles in the Mars and Venus atmospheres with theoretical calculations. The error bars on the observed profiles are from the error analysis of the radio occultation data for the Mariner 6 and 7 cases and are the confidence limits given by the experimenters for the Mariner 4 and 5 cases. The error bars on

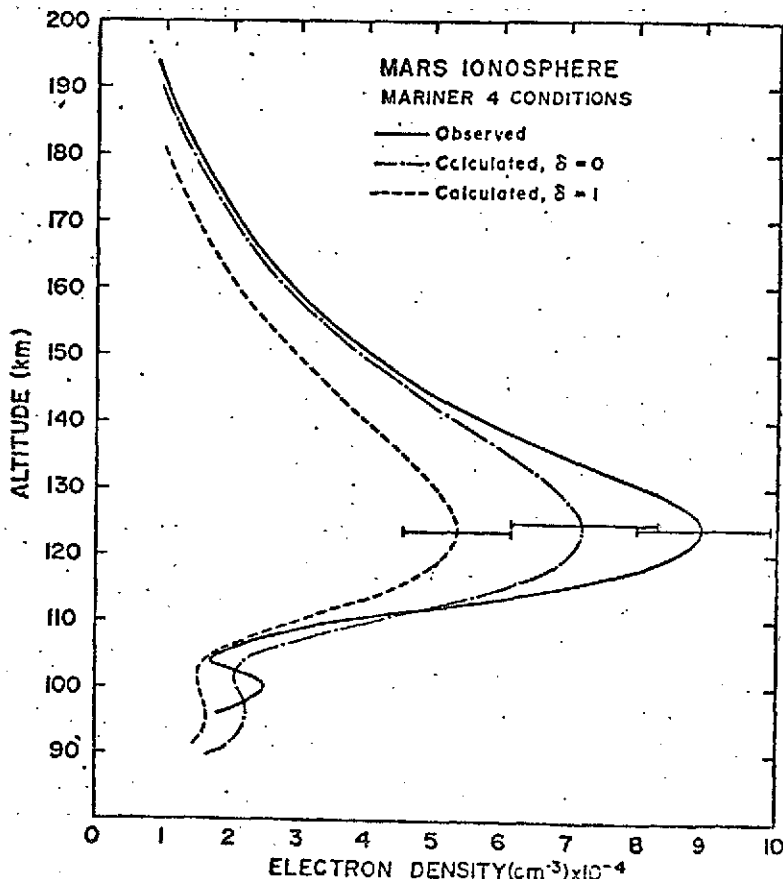


Figure 1. Observed and calculated electron densities for Mariner 4 conditions. The two calculated profiles are obtained by scaling the solar flux data for intermediate solar activity to solar minimum conditions assuming a zero-to-one and one-to-one variation in EUV to 10.7 cm flux. See text for a discussion of the error bars.

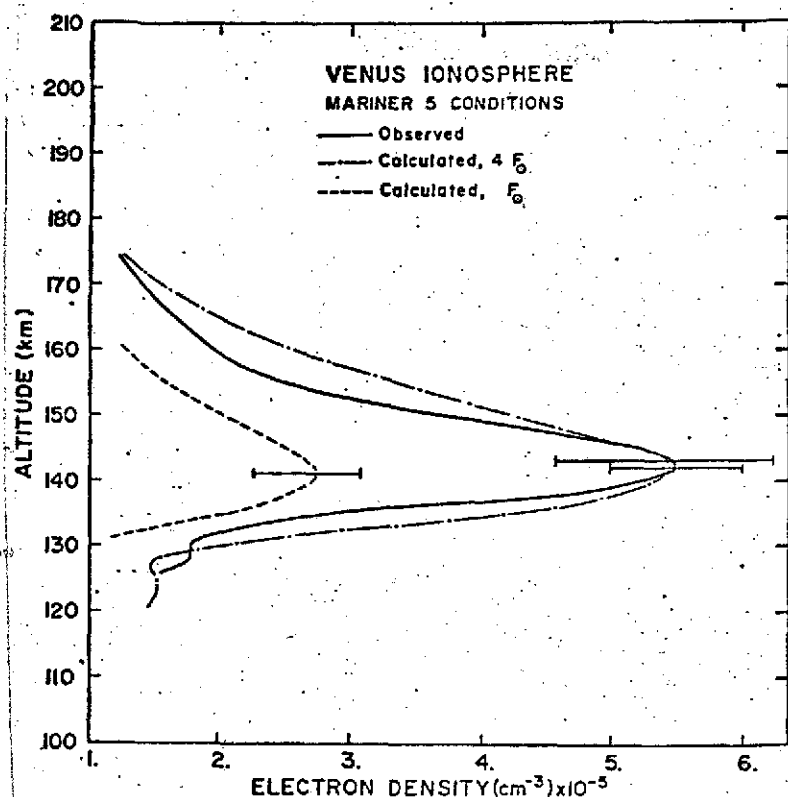


Figure 2. Observed and calculated electron densities for the Venus ionosphere under Mariner 5 conditions. The two calculated profiles are obtained by using measured solar fluxes directly (F_0) and by arbitrarily multiplying these fluxes by four ($4F_0$). See text for a discussion of the error bars.

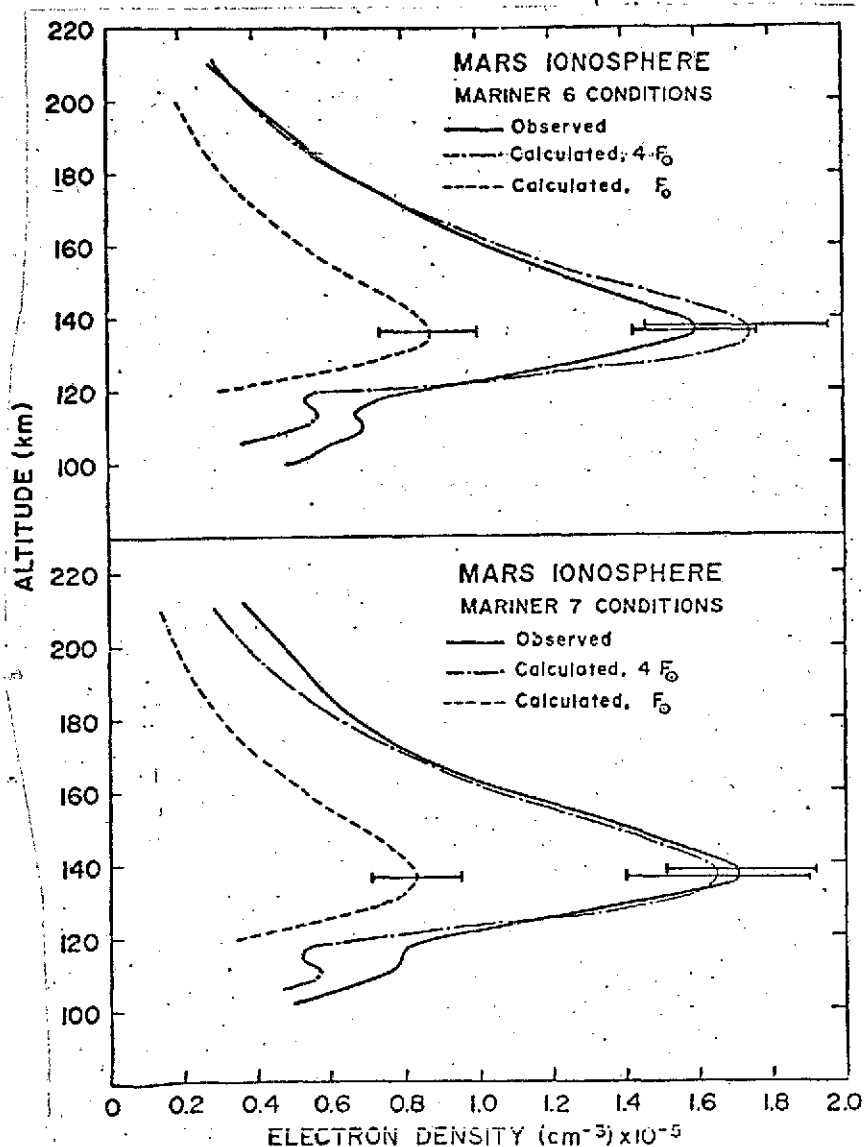


Figure 3. Observed and calculated electron densities for the Martian ionosphere under Mariner 6 and 7 conditions. The two calculated profiles in each case are obtained by using measured solar fluxes by four ($4F_0$). See text for a discussion of the error bars.

the theoretical profiles are derived by combining the uncertainties in the various quantities included in the calculation. The discrepancy between observed and calculated values has not yet been explained, but it was suggested in the paper from which these figures are taken that the solar wind might provide the missing ionization. The magnitude of the required ionization source is shown in Table 1.

Figures 4 and 5 show the theoretically calculated ion compositions of the Mars and Venus ionospheres and indicate the importance of the O_2^+ ion.

A theoretical investigation of atmospheric ozone on the primitive earth has recently been started (with J. C. G. Walker of Yale University). Initial results of this study indicate that dissociation of O_2 by radiation in the Schumann-Runge continuum (1350-1750Å) may have provided a significant source of O_3 in the primitive terrestrial atmosphere in sharp contrast to its minor importance at present. The possibility of large surface O_3 concentrations at past periods in the Earth's history is also indicated by preliminary results.

Table 1

Calculated and observationally required ionization sources at the F_1 peaks in the Mars and Venus ionospheres

Flight	Calculated Source (F_0) (ions/cm ³ sec)	Required Source (ions/cm ³ sec)	Source Deficit (ions/cm ³ sec)	Required Proton Flux at 1 A.U. (cm ⁻² sec ⁻¹)	Required EUV ($\times F_0$)
Mariner 4	1.2×10^3	2.4×10^3	1.2×10^3	1.6×10^8	2.0
Mariner 5	2.8×10^4	11.5×10^4	8.7×10^4	9.6×10^8	4.1
Mariner 6	2.9×10^3	9.9×10^3	7.0×10^3	6.8×10^8	3.4
Mariner 7	2.6×10^3	11.2×10^3	8.6×10^3	9.4×10^8	4.3

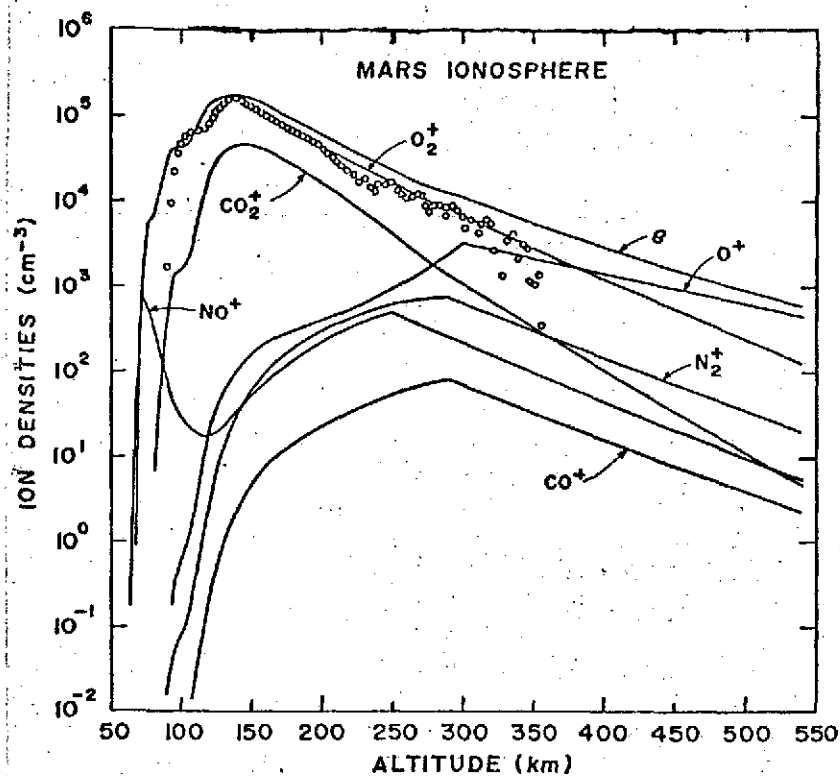


Figure 4. Calculated electron and ion distributions (solid lines) and observed Mariner 6 electron distribution (circles) in the Mars ionosphere.

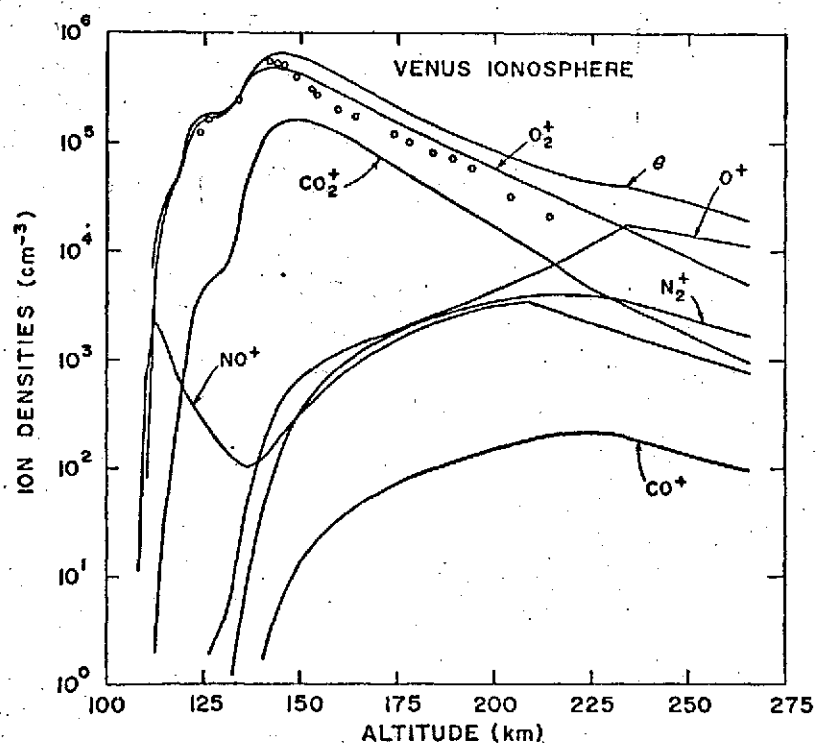


Figure 5. Calculated electron and ion distributions (solid lines) and observed Mariner 5 electron distribution (circles) in the Venus atmosphere.

BASIC THEORY OF SCATTERING IN PLANETARY ATMOSPHERES

(J. Hansen, A. Lacis)

Recent theoretical work in radiative transfer at GISS has been aimed at problems in which basic advances in our modeling capabilities are required for practical applications. The areas of present interest fall into two categories: (1) the interpretation of remote measurements of the intensity and polarization of scattered sunlight, and (2) the computation of the absorption of solar radiation for general circulation models. Although many specific computations have previously been made for single and multiple scattering, an adequate understanding of the relationship of the nature of the scattering particles (refractive index, shape, size distribution) to the characteristics of the scattered light is still lacking. This situation must be improved by basic theoretical work on scattering if remote sensing of cloud and aerosol properties is to be effective. Furthermore the atmospheric models employed, which have generally been idealized as being homogeneous, must be generalized to allow for the major inhomogeneities which occur in the real atmosphere.

The application of remote sensing to the monitoring of particulate air pollution and to cloud studies requires a knowledge of how the intensity and polarization of scattered radiation depend on the properties of the scattering material. Previous theoretical investigations have shown that the linear polarization is the most sensitive of the radiation characteristics to the nature of the scatterers. However, to extract the potential information it is necessary to know the dependence of the polarization on the size distribution and refractive index of the scatterers. A significant contribution to this problem is provided by work being done at GISS, and especially by contour diagrams of the type shown in Figure 1. This diagram shows the percent polarization as a function of the scattering angle and size parameter for scattering by spheres of a given refractive index. The results change from simple Rayleigh scattering for the smallest size parameters to essentially geometrical optics at the largest size parameters, with the primary rainbow at a scattering angle 110° , the second rainbow at 120° and the negatively polarized twice refracted rays at smaller scattering angles. The results for any size distribution follow as weighted averages along vertical lines. The added dimension provided by these plots allows the first clear illustration of the effects of the particle size distribution and refractive index.

Basic theoretical work is also being done for the improvement of parameterization of radiation in general circulation models. Accurate computations of the flux of solar radiation in the atmosphere require solutions of the transfer equation for an inhomogeneous partially absorbing medium. A method for rigorous monochromatic calculations for an inhomogeneous atmosphere has been developed, based on previously published theoretical work of Hansen for the homogeneous case. Currently, methods for efficiently integrating the results over broad spectral intervals are being developed. This is required both for applications to

general circulation models and for calculations of the ultraviolet transmission through a realistic atmosphere to obtain the net radiative effect at ground level of possible changes in the ozone distribution (see R. Stewart's section on stratospheric chemistry and global pollution.

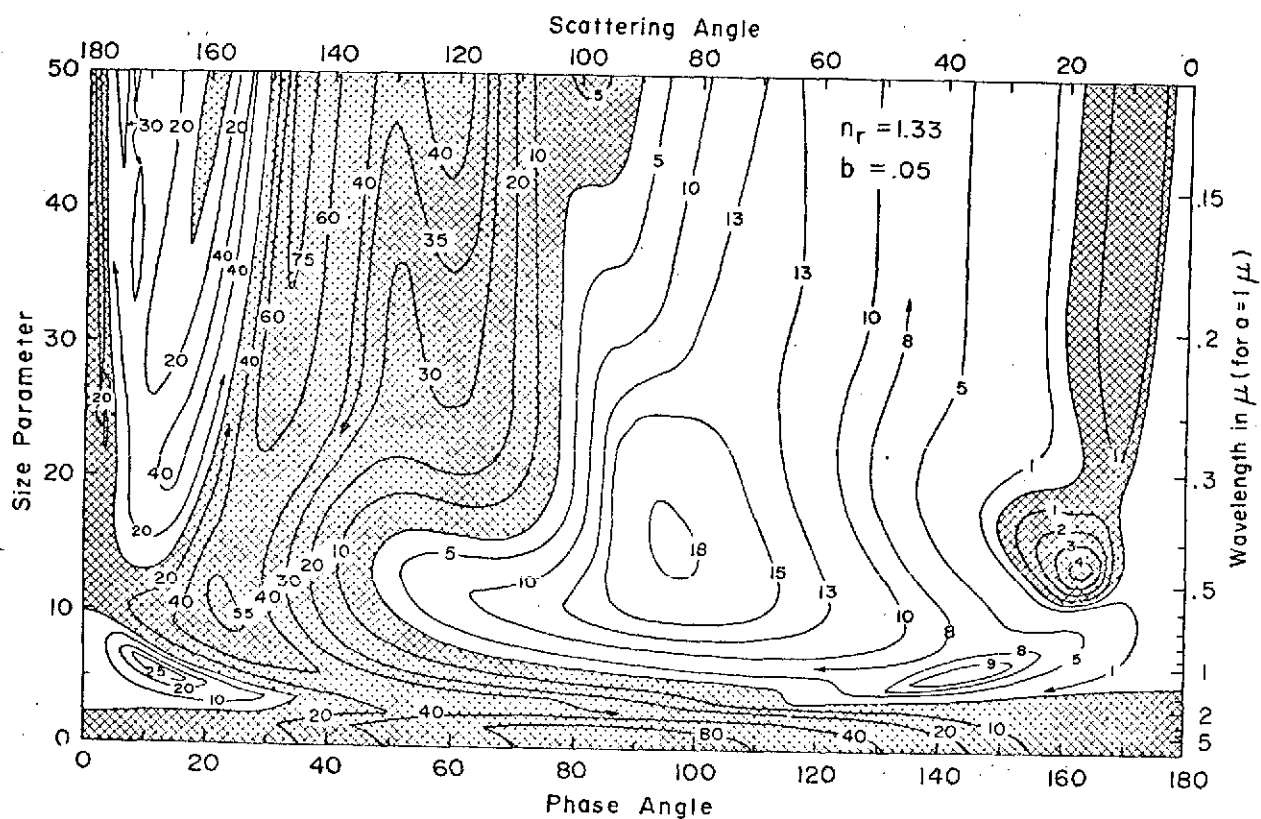


Figure 1. Contour diagram of the percent polarization for single scattering of unpolarized light by a size distribution of spheres with refractive index 1.33. The shaded areas indicate positive polarization and the unshaded indicate negative values. The size parameter is $2\pi a/\lambda$. a is the effective mean radius and b the effective variance for the size distribution.

CLIMATE STUDIES WITH NUMERICAL MODELS. (S.H. Schneider).

(1) *Effects of Aerosol Optical Properties on the Earth's Albedo.* The effect on the earth's albedo from variations in the imaginary part of the index of refraction of atmospheric aerosols has been studied using a two-stream approximation to the multiple scattering problem. For the calculation, the model developed by Rasool and Schneider (1971) is used. It is found that atmospheric aerosols whose imaginary index of refraction (n_i) have values less than about 0.1 tend to raise the earth's albedo, whereas aerosols that have n_i greater than 0.1 tend to lower the planetary albedo. It is concluded, therefore, that better observational data on the values of the imaginary index of refraction of atmospheric aerosols should be obtained before the magnitude of the possible effect on the global climate from increases in aerosols can be computed.

(2) *Numerical Experiments in Climate Stability.* A time-independent zonally-averaged model of the energy balance of the earth-atmosphere system was constructed to test the sensitivity of the earth's climate to small variations in the solar constant. Using this simple model (which included the coupling between the earth's surface temperature and the earth's albedo) it was found that the present interglacial climate could not survive a decrease in the solar constant by even a few percent. This result was obtained because of the strong "positive feedback" coupling between surface temperature and albedo assumed in this model. Similar results have been obtained by Budyko (1969) and Sellers (1969), who also used steady state zonally-averaged models of the heat balance of the earth.

But in order to study the stability of the earth's climate to changes in the earth's *internal* condition, the model was made time-dependent. Therefore, a time-dependent zonally-averaged climatological model, in which the atmospheric fluid dynamical processes have been parameterized from empirical data, has been constructed to perform numerical experiments in climatic stability. By perturbing the initial temperature distribution of the earth, while leaving all external parameters (such as the solar constant) fixed, the model was used to study the uniqueness (or "transitivity" in the sense of E. Lorenz, 1970) of the final equilibrium climate. It was found that the transitivity of this type of climate model depends critically on the functional form of the mathematical expression that describes the temperature dependence of the earth's albedo. For example, if the earth's albedo is calculated such that *at every latitude* a decrease in surface temperature causes an increase in albedo, then even a slight negative perturbation

in the initial surface temperature distribution results in a global glaciation. However, for the more realistic case where this strong temperature-albedo positive feedback coupling is excluded from latitudes that have mean temperatures greater than about 10°C (and thus have very little snow and ice cover), then even a 10°C negative perturbation in the initial temperature distribution is insufficient to cause an expansion of glaciation, and the final steady state climate is transitive (unique and not dependent on the initial conditions).

(3) *Cloudiness as a Global Climatic Feedback Mechanism.*

The possible role of cloudiness as a global climatic feedback mechanism has been studied by computation of the effect of variations in the amount and height of global cloud cover on the radiation balance of the earth-atmosphere. The simple radiation model described in Rasool and Schneider (1971) was used for the computations. Global-average radiation balance calculations show that an increase in the *amount* of cloud cover (with cloud top height and cloud albedo fixed) decreases the surface temperature. However, an increase in effective cloud top *height* (with cloud cover and cloud albedo fixed) increases the surface temperature.

Therefore, to determine the effect of a change in cloudiness on the global climate, it first must be determined whether "change" means one of cloud top height or cloud cover amount. This can be illustrated on Figure 1, which shows that a change in the surface temperature, T_s , need not occur if both the cloud top height and the amount of cloud cover vary so as to follow one of the curves on Figure 1. Furthermore, this result for the effect of an increase in the *amount* of cloud cover on the surface temperature for the global average case does not hold near polar regions of the earth, where the albedo of the cloudy areas is comparable to (or even smaller than) the albedo of the snow-covered cloudless areas, and where, especially in the winter season, the amount of incoming solar energy at high latitudes is relatively small. The exact latitude at which the surface cooling effect crosses over to be a surface warming (from a given increase in global cloud cover amount) depends critically upon the local values of the cloud albedo and the albedo of the cloudless areas used in the calculation. Thus, to determine the possible feedback effects of cloudiness on the climate, accurate data on the relative albedos of cloudy and cloudless areas must be available, and a model with spatial resolution significantly finer than a global average must be used to make the calculations.

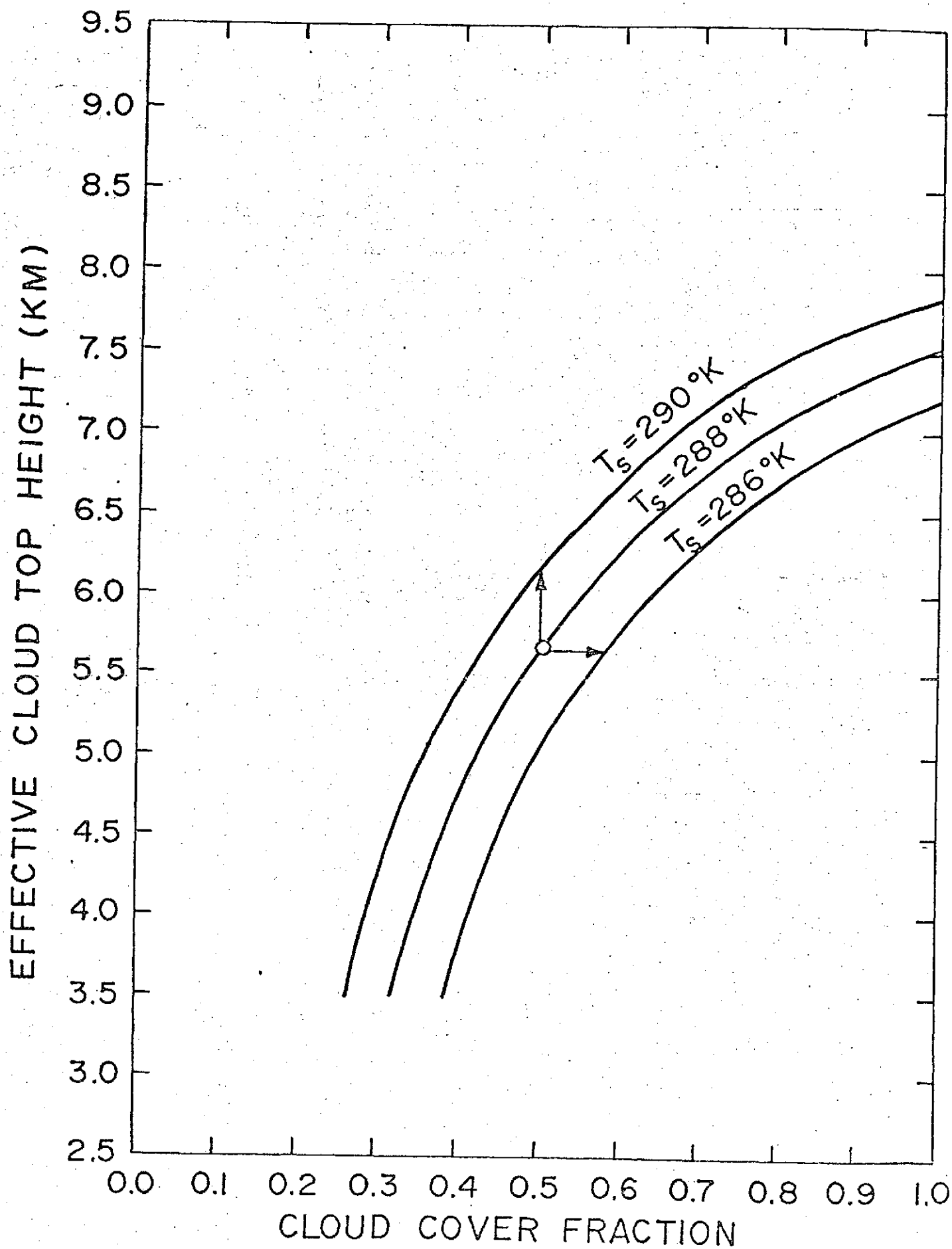


Figure 1. Each curve represents a locus of the possible equilibrium values of cloud top heights and cloud cover amounts that are consistent with a constant value of surface temperature.

ORIGIN OF THE MARE LAVAS. (V. Gornitz)

In spite of petrological and chemical data obtained on lunar material from the Apollo missions, disagreement still persisted, until quite recently, as to the origin of the mare lavas--were they true igneous magmas or impact melts?

A study of Lunar Orbiter and Apollo photographs of Tsiolkovsky and Mare Orientale, as examples of mare-filled impact structures, has revealed that the mare lavas must stem from internal melting because a considerable time interval has elapsed between the time of basin excavation and basaltic extrusions. This is most effectively shown by the significantly higher crater density (2x), hence greater age, on the ejecta blanket and Rook Formation impact breccia as compared with the darker mare filling of the Orientale basin (Figure 1).

Not only is the central mare filling distinctly younger than the ejecta cover, but furthermore, many craters on the ejecta blanket of Orientale were also flooded by lava long after the impact had occurred. Thus, the Mare Orientale basin provides persuasive evidence that the lava filling is derived from internal, igneous sources.

The dating of Apollo 14 and 15 rocks has verified this conclusion for another circular mare. The 3.8-3.9 billion year age of the Fra Mauro Formation (the ejecta blanket of Mare Imbrium) and the 3.3 billion year old basalt flow at Hadley Rille (the latest filling of Mare Imbrium) show that a half billion years separated basin excavation and filling. Chemical analyses on Apollo samples indicate that the Moon's surface is not homogeneous and has experienced igneous differentiation. Evidence for widespread melting of the moon is strengthened by the fact that mare and highland have distinct chemical compositions (orbital X-ray fluorescence spectrometer and chemical analyses on individual rocks) and that the moon's interior is layered (Passive seismometer).

Mare-type lavas are not only confined to large, circular, impact basins, but also fill irregular depressions, like Mare Australe, where evidence for different flooding episodes has been observed. Clearly, volcanism has played as important a role as meteoritic impacts in shaping the lunar surface.

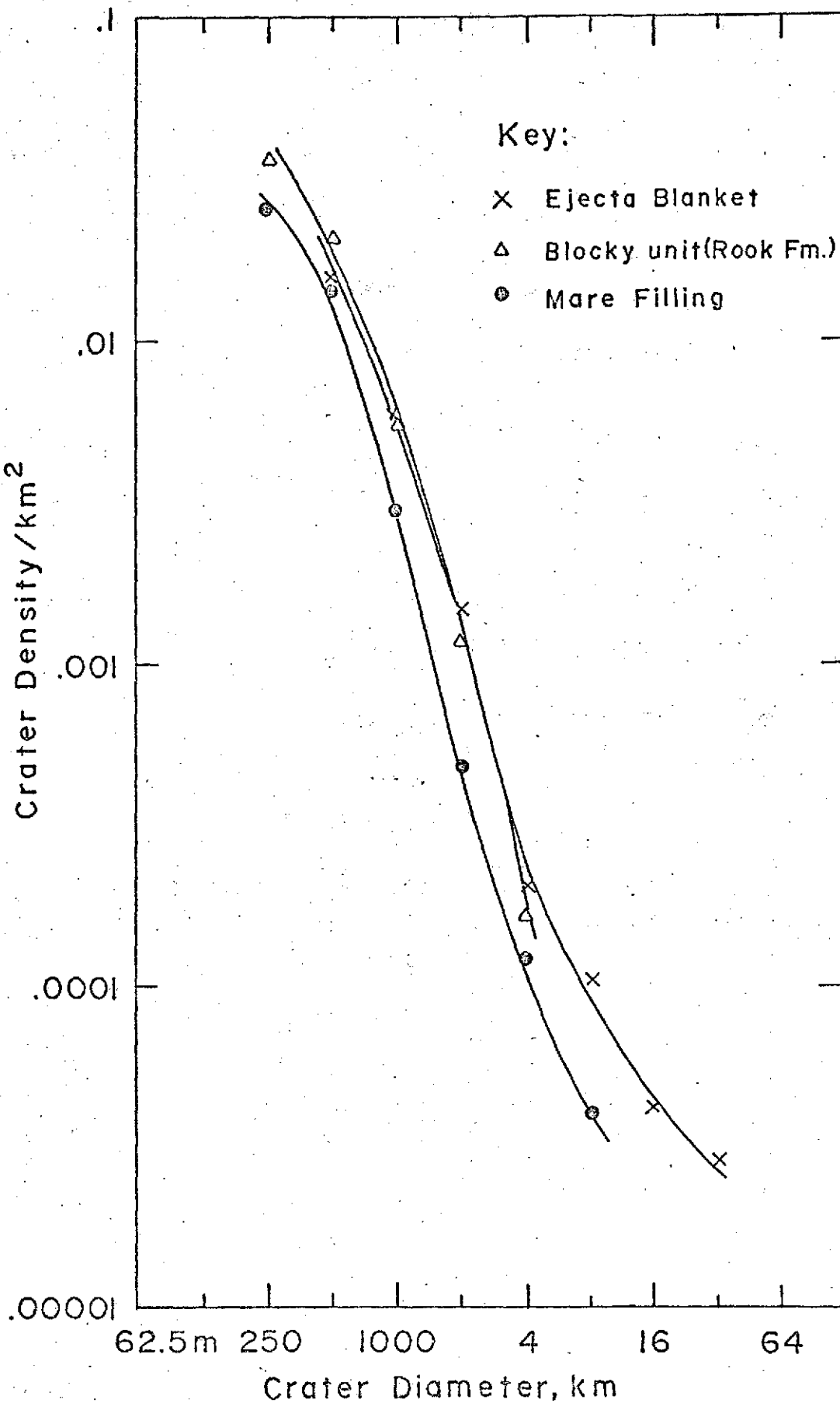


Figure 1. Crater counts in Mare Orientale, showing a significant age difference between ejecta blanket and mare filling.

THE NATURE OF SINUOUS RILLES, (V. Gornitz)

Sinuuous rilles are enigmatic lunar features, whose origin has been widely debated. One popular theory holds that the rilles represent water-eroded streams or valleys carved by ice-melted water under a rubble-covered permafrost layer. The basic argument in favor of water erosion lies in the alleged morphological similarity between the rilles and rivers on earth.

The present study shows that sinuous rilles differ significantly from terrestrial streams in their geometry. The channel of sinuous rilles is wider relative to the meander length, and the radius of curvature is much smaller for the width as compared with rivers (Figures 1 and 2). For instance, the ratio of radius of curvature to channel width lies between 2 and 3 for most rivers, but is about 0.7 for sinuous rilles. Unlike rivers, sinuous rilles are deepest where they are widest, usually close to their presumed source (Figure 3). Some rilles show a slight downhill gradient, although others, such as the Marius Hills Rilles, traverse topographic obstacles--in this case--a wrinkle ridge. The depth of Hadley Rille varies irregularly along its length. The course of several sinuous rilles, including Hadley Rille, appears to be controlled by the prevailing structural trends.

It appears from this investigation that sinuous rilles are not dry "moon-rivers", but may be best explained by a combination of

- i) volcanism: open lava channels or collapsed lava tubes may account for the origin of many of the smaller sinuous rilles that begin in craters, show a downhill gradient and have tight meanders.
- ii) Faulting: other rilles may form by irregular faulting, which could also include gas venting along fractures to produce crater chains.

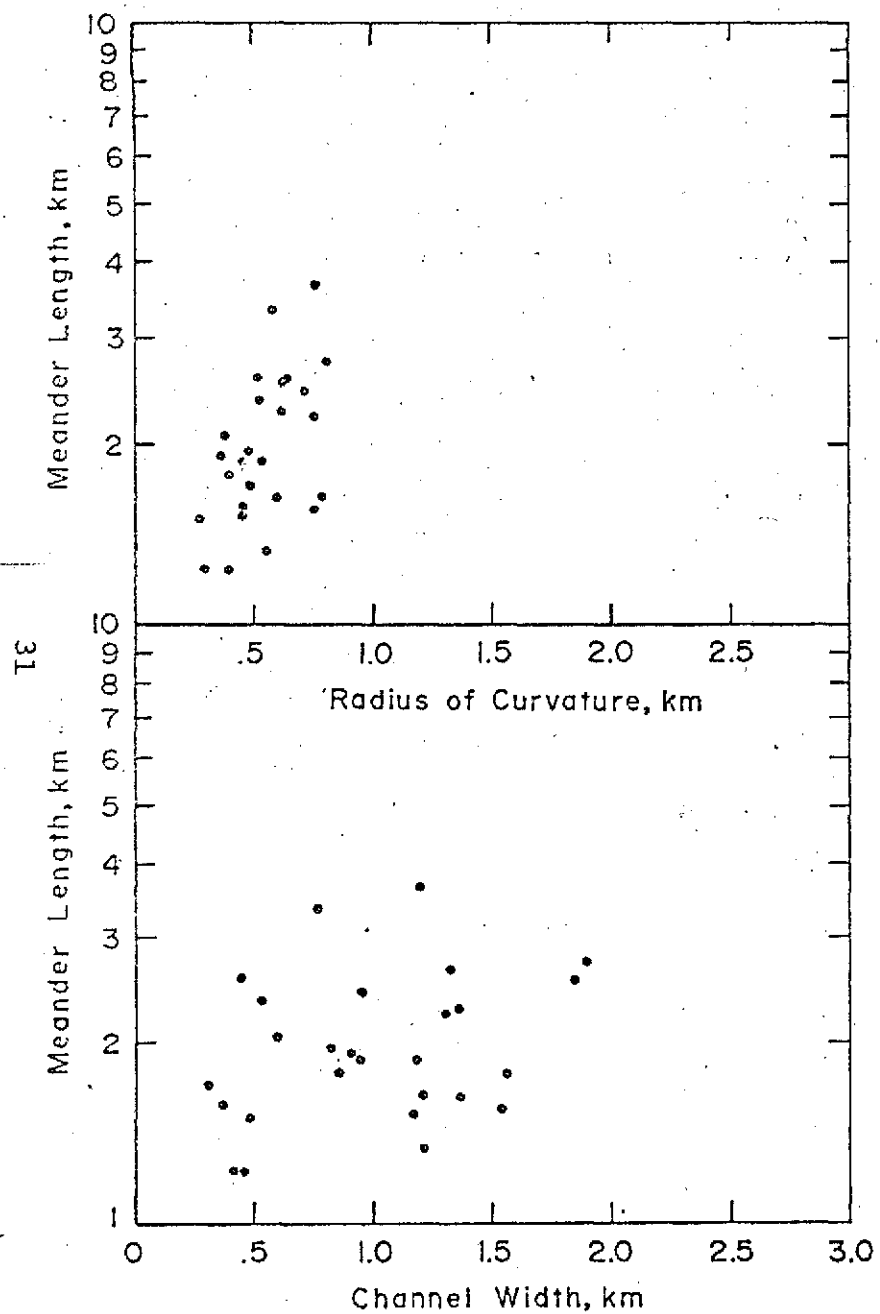


Figure 1. Geometry of lunar rilles.

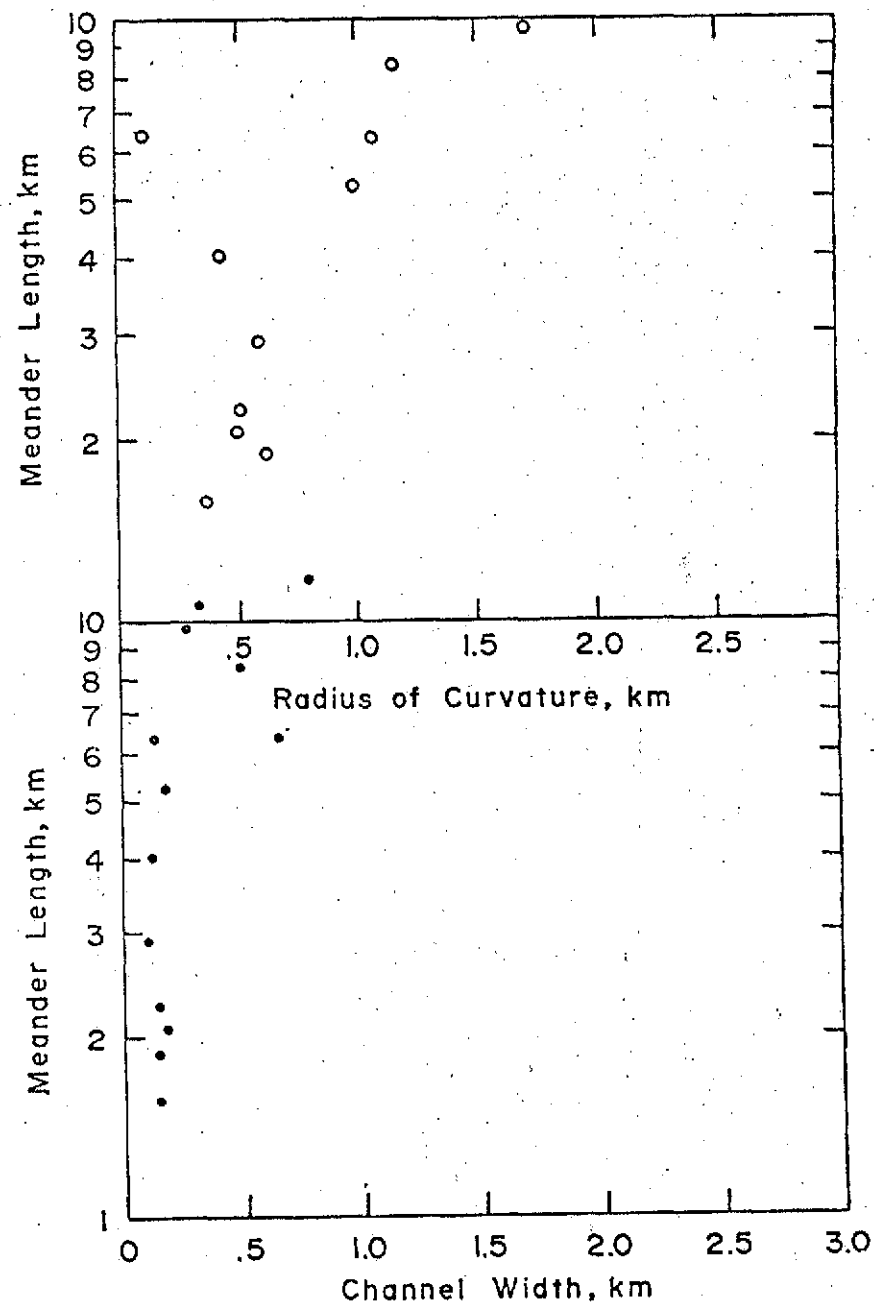


Figure 2. Geometry of terrestrial rivers.

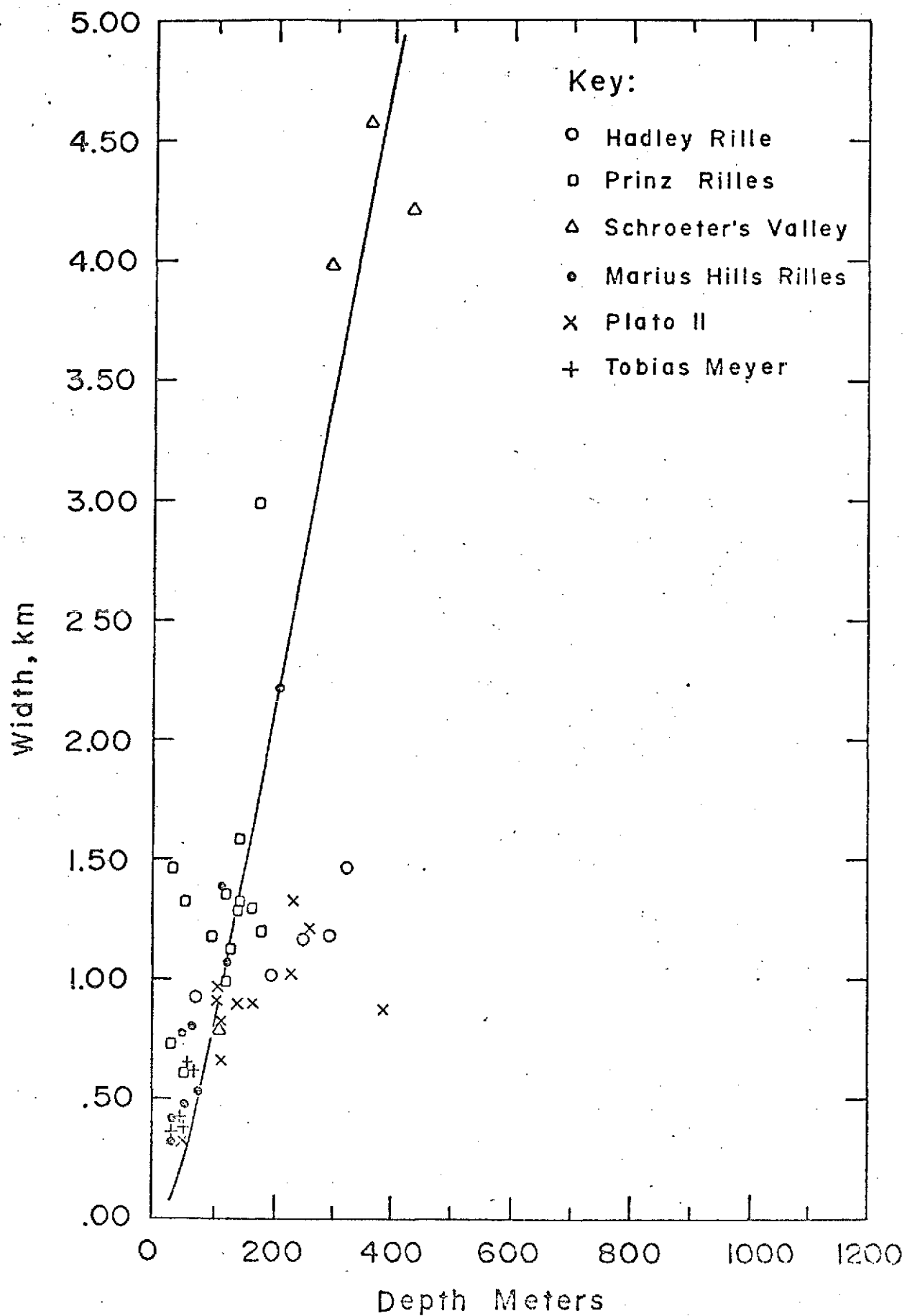


Figure 3. Dimensions of lunar sinuous rilles.

CRYSTALLIZATION OF MATTER AT HIGH DENSITIES. (S.M. Chitre, V. Canuto)

There has been a considerable astrophysical interest of late in the possibility of the crystallization of matter at very high densities ($\rho \gtrsim 10^{15}$ gm/cm³), in connection with ideas on neutron stars. Over the past year, a solid-body model has been developed for dense neutron matter with a view to settling the question of whether a solid-lattice made up of neutrons is energetically the most favorable arrangement in the deep interior of a neutron star. It has been shown recently that in the vicinity of a density of the order of 1.5×10^{15} gm/cm³ neutrons should indeed arrange themselves in a lattice which cannot exist at a lower density because of mechanical instabilities arising from shearing stresses. Such a model of the neutron star, composed of a solid core, a superfluid layer and an overlying solid crust has an important bearing on some of the observed properties of pulsars.

A solid-body model is under development which includes hyperons as well as neutrons and protons. For this purpose, hyperon-hyperon and hyperon-nucleon potentials had to be built up. The problem now is to determine whether a minimum energy configuration is yielded by such a baryonic lattice.

The formulation was also used to determine whether nuclear matter can be a quantum crystal. Results show that it cannot exist in a crystalline structure. The formalism was further applied to derive the physical properties of solid He³. A remarkable agreement was obtained between the theoretical results and the corresponding experimental values.

NEUTRINO ASTRONOMY. (R. Stothers, D. Ezer)

Since a photon generated by thermonuclear reactions requires millions of years to diffuse out of the Sun and, on its way, suffers $\sim 10^{22}$ Compton scatterings, the observed radiance of the Sun can scarcely be regarded as a direct measure of its central temperature. An emitted neutrino, on the other hand, which has little cross-section for interaction with matter, is a direct probe both of the central temperature and of the occurrence (and nature) of thermonuclear reactions as the source of solar energy. For this reason, R. Davis has spent almost a decade in devising and improving a very sensitive experiment to detect the elusive solar neutrinos.

Following the null result of Davis's ^{37}Cl experiment to detect high-energy solar neutrinos expected from beta decays in the central hydrogen-burning reactions in the Sun, new models for the present Sun have been considered to test sensitivity to four important astrophysical quantities. Adoption of the "best" available opacities (with allowance for large possible errors), of hypothetical additional low-energy neutrino sources (presumed to be due to some large $(\text{ev})(\text{ev})$ interaction cross-section), or of a central black hole (supposed to have been the original solar condensation center) only *increase* the predicted solar neutrino flux; moreover, no thermal instabilities in any of the solar models have yet been found which might reduce the central temperature and hence neutrino flux. See Table 1.

Therefore it is concluded that possibly even more drastic remedies for what is "wrong" with current solar models are required, since all other familiar parameters that can be varied have already been checked, by Bahcall, Iben, and others.

Table 1

SOLAR NEUTRINO FLUXES FROM
THE ^8B BRANCH OF THE pp CHAIN,
AT THE EARTH*

Core	Standard Model	Large Opacity	Small Opacity	Black Hole
Mass of black hole (M_\odot)	0	0	0	0.004
Central temp. (10^6 °K)	15.2	16.9	14.2	15.8
Central density (g cm^{-3})	147	149	129	323
ϕ (^8B) ($10^6 \text{ cm}^{-2} \text{ sec}^{-1}$)	4	31	1	7

*Observed flux is $\phi = (0.2 \pm 0.4) \times 10^6 \text{ cm}^{-2} \text{ sec}^{-1}$.

EVOLUTION OF MASSIVE STARS, (R. Stothers, C.W. Chin)

An intensive effort has been devoted to testing the effects of small changes in physical input quantities on the evolutionary "loops" that appear on the H-R diagram during core helium burning in massive stars built with the Ledoux criterion for convective instability. With the old triple-alpha reaction rate, it turns out that the occurrence of the loops is very sensitive to initial helium-to-hydrogen ratio, initial metals-to-hydrogen ratio, and carbon-alpha reaction rate. This explains the scatter in results obtained by many previous investigators. With the new triple-alpha rate, the loop always develops at $15 M_{\odot}$, but never at $30 M_{\odot}$ (see Figure 1). Nevertheless, further theoretical work is necessary before one can use the available observational data for supergiants to infer which criterion for convection, Ledoux or Schwarzschild, is correct for stars. (Laboratory experiments and numerical convection "experiments" have not yet been able to answer this question.)

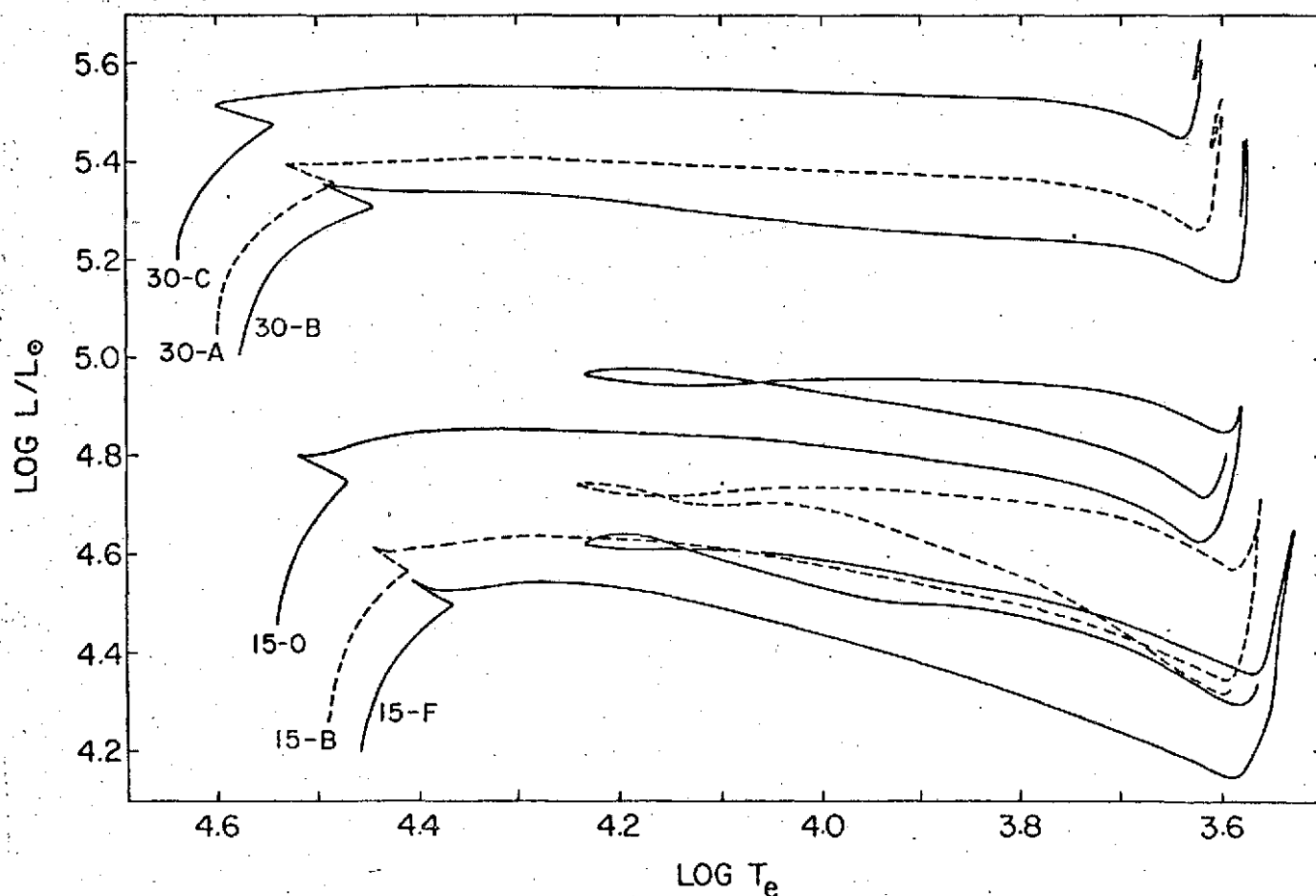


Figure 1. Theoretical H-R diagram showing evolutionary tracks for stars of 15 and 30 solar masses from the initial main sequence to the end of helium burning in the core. The three sequences for each mass reflect changes in the initial chemical composition, but all sequences were calculated with the new triple-alpha rate.

BETA LYRAE AND MAGNETIC FIELDS IN STARS. (R. Stothers, C.W. Chin)

The eminent late astronomer Otto Struve was fond of pointing out that, with the exception of the Sun, Beta Lyrae is the most observed, most published about, and least understood bright star in the sky.

Continuing work on the problem of the peculiar eclipsing-binary system Beta Lyrae has shown that the underluminosity of the massive secondary component with respect to normal main-sequence stars is probably only 1 to 4 astronomical magnitudes (depending on the choice of observed radial-velocity curve, and hence on the mass, of the secondary). Thus a black-hole secondary need not be postulated. It has been further demonstrated that the magnetic field at the surface of the primary, which is the exposed core of an originally more massive star, is very weak, which implies the presence of weak magnetic fields generally in the interior of upper main-sequence stars. Further evidence against strong interior magnetic fields in massive stars comes from the peculiar evolutionary tracks on the H-R diagram expected if the fields suppress core convection, as calculated by Stothers and Chin.

Page intentionally left blank

July 1, 1972 to December 31, 1972

RADIO OBSERVATIONS OF INTERSTELLAR MOLECULES, (P. Thaddeus, M. L. Kutner, P. Encrenaz)

Much of the information obtained about the interstellar medium has come from radio observations of the spectra of interstellar molecules. Apart from the chemical questions of which molecules are most abundant, the molecules also serve as probes of the physical conditions in interstellar clouds. In addition, since isotopic shifts of molecular rotational transitions are of the order of a few per cent of the frequency, molecules are well suited for the study of isotopic abundances, a study directly related to problems in cosmology and stellar nucleosynthesis. For a number of reasons, observations at millimeter wavelengths are of particular importance. At the excitation temperatures prevalent in molecular clouds (10°K to 100°K) many molecules with two or three heavy atoms have their strongest transitions in this spectral region. In particular, the strongest millimeter emission emanates from very dense ($>10^5$ neutrals cm^{-3}) HI regions and the high angular resolution available with radio telescopes in the millimeter region allows detailed study of such regions.

Owing to more favorable weather conditions in the past six months, improved observations of the 2 mm methanol (CH_3OH) lines have been obtained, as previously reported. These observations provide information about the Kleinman-Low nebula, a dense HI region in Orion. It was found that the peak source of methanol emission has an extent less than 0.1 pc. From the relative line intensities the methanol excitation temperature was found to be 90°K (Figure 1); this is very close to the presumed kinetic temperature in this region, indicating a density of $\sim 10^8$ neutrals cm^{-3} , considerably higher than had previously been thought. These observations provide evidence for the existence of dense, hot condensations, possibly protostars, in the region.

The first stage of the study of diffuse dark clouds has been completed with the analysis of the previously reported correlation, found between 6 cm formaldehyde (H_2CO) absorption and optical extinction. This data indicates that the mechanism responsible for the formaldehyde production is dependent upon the presence of radiation. This is contrary to some of the earlier ideas on molecular abundance, but helps explain the fact that the formaldehyde-to-hydrogen ratio does not appear to be appreciably higher in regions of high density and extinction than in regions of moderate density and extinction. These are uncertainties in this work related to problems of cloud geometry and testing these conclusions by observation of a number of other clouds is planned.

In addition, a project to learn more about the physical conditions in these diffuse dark clouds by observation of the millimeter transitions of a number of molecules has been begun. So far observations have been made of $^{12}\text{C}^{16}\text{O}$ and $^{13}\text{C}^{16}\text{O}$ and observations of HCN and H_2CO are planned shortly. This work is being done on the 16 foot radio telescope at McDonald Observatory, Texas, as part of the GISS collaboration with the Bell Telephone Laboratories, Harvard, and the University of Texas to develop this instrument for spectral line observation, and greatly increase the available observing time in the millimeter region of the spectrum.

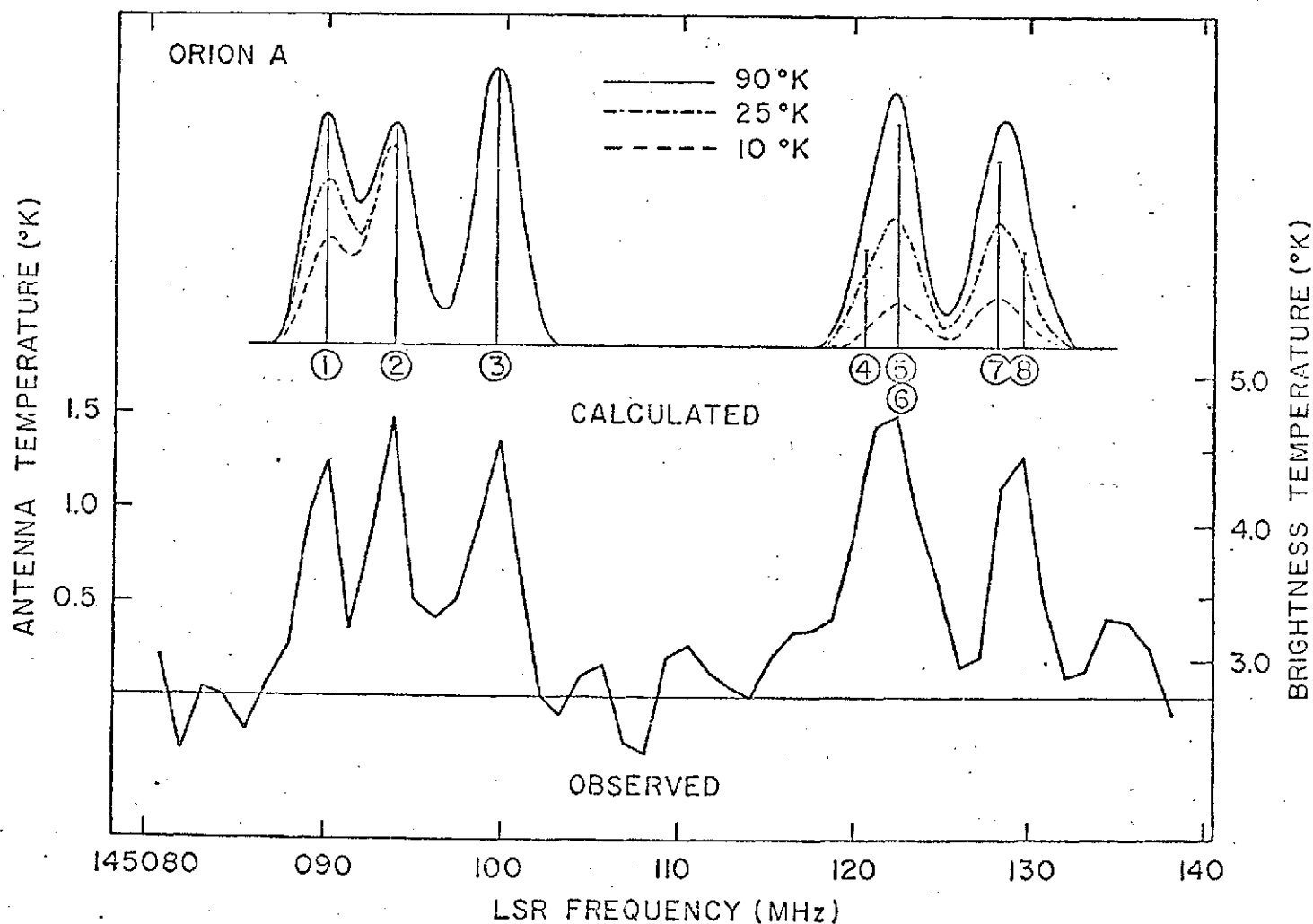


Figure 1. Calculated and observed methanol excitation temperature curves for Orion A.

LABORATORY ASTROPHYSICS. (K. Tucker, (Columbia University);
G. Tomasevich, P. Thaddeus)

Laboratory studies of the hyperfine structure (hfs) in the microwave spectra of some simple organic molecules, which are candidates for detection in interstellar space, are being continued using a beam maser with a line-width of only 500 Hz. The high resolution and sensitivity of the maser allows absolute transition frequencies to be measured to an accuracy of about one part in 10^8 which, for astronomical purposes, removes any possible uncertainty in the rest frequency of the molecules' transition. Furthermore, it is now possible to resolve the very compact hfs produced by the weak magnetic interactions (spin-rotation and spin-spin) of nuclear magnetic moments in rather complex molecules. For closed-shell molecules, these interactions have magnitudes of only a few kHz and cannot be resolved by conventional absorption spectroscopy.

Measurements of the hfs of four rotational transitions of the normal isotopic species of the five-membered ring furan (C_4H_4O) have been completed. The observed and best fit theoretical spectra are shown in Figure 1. Analysis of the hfs has yielded very precise values for the spin-rotation and spin-spin coupling constants. In particular, the three diagonal elements of the spin-rotation tensor for both pairs of equivalent protons have been determined to an accuracy of about 10Hz, and the interproton distances to an accuracy of 0.008 or better.

The principal result of this work is the demonstration that beam maser spectroscopy is no longer restricted to very light molecules, which have few energy levels populated at room temperature, but can be successfully applied to molecules with molecular weights of up to 100. The experimental spectra of Figure 1, which receive time constants of at most 3 seconds, were obtained, implying that at low microwave frequencies (2 - 5 kHz) this maser has a sensitivity comparable to a Stark-modulated absorption spectrometer. Computer signal averaging is currently being implemented

Other molecules presently being studied include pyrrole (C_4H_5N) and cyclopentadiene (C_5H_6). For each molecule, observing the deuterized species in order to obtain information about molecular field gradients is planned.

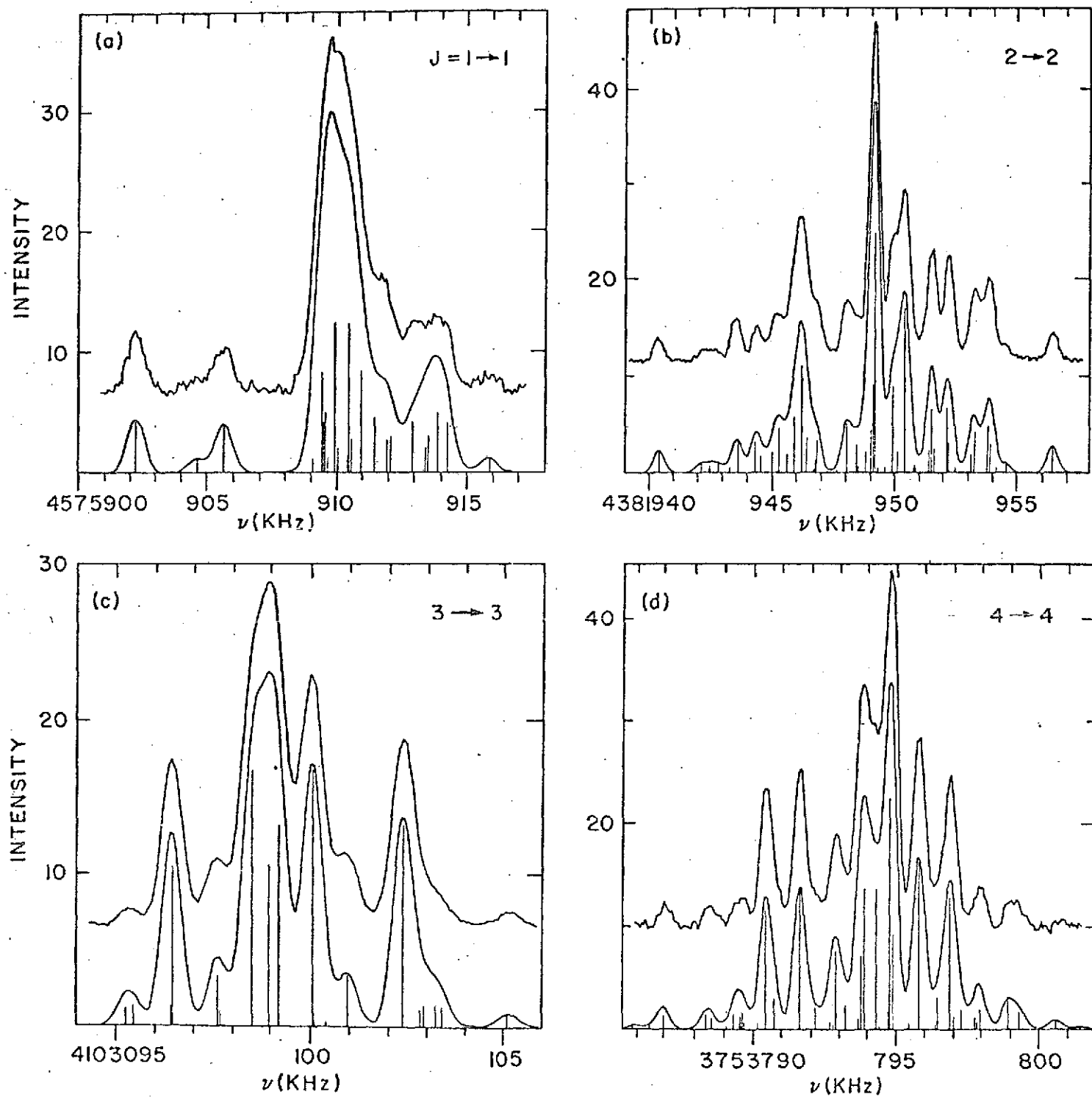


Figure 1. Spectra of four rotational transitions of furan (C_4H_4O).

AB INITIO CALCULATION OF MOLECULAR PROPERTIES AND PROCESSES. (S. Green)

A large number of molecular species have been observed in interstellar space. In order to analyze the observations and also to understand the interactions among these species, knowledge of certain molecular properties, such as energy levels, oscillator strengths, Franck-Condon factors, dipole moments, etc., are necessary. In several cases, the interstellar species have been difficult to prepare and measure under laboratory conditions. However, in these same cases, the molecules often contain only a few nuclei and electrons and, hence, with current computing capabilities one can deduce their properties from a direct solution of the equations of quantum mechanics.

One aspect of our current work is the development of techniques for the accurate calculation of properties, such as the electric dipole moment, which depend only on the charge distribution in the molecule. (See, for example, S. Green, J. Chem. Phys. 57, 2830, 4694 (1972).) This work has been essentially completed within the last year. A related project which is also near completion is a study of various properties of the CH^+ molecular ion. Potential energy curves have been obtained (S. Green, P. S. Bagus, B. Liu, A. D. McLean, and M. Yoshimine, Phys. Rev. A 5, 1614) which have been useful in understanding the spin-change scattering that is important in cooling the interstellar medium. Franck-Condon factors have also been obtained (S. Green, S. Horenstein, and C. F. Bender, Ap. J., in press) and, very recently, absolute oscillator strengths for the astrophysically important transitions. These latter calculations showed that earlier, estimated values were in error, and should be quite important in a proper understanding of the abundance of CH^+ and also of certain proposed mechanisms for the interstellar creation of this species. Some other species for which calculations have been performed at ClF , NO ground and first Rydberg state, OH excited state, and the valence states of SO .

A second area of study has been the calculation of energy transfer in collision processes. In particular we are obtaining cross sections for rotational excitation of molecules at the very low kinetic temperatures believed to be found in interstellar clouds (10 to 150°K). We are using the quantum-mechanically accurate close-coupling method for which rapid numerical techniques have recently become available, and have somewhat modified existing formalism and computer programs in order to handle the astrophysically interesting cases. Calculations are in progress for excitation of CO by H_2 molecules, and calculations on H_2CO will be initiated very soon. For formaldehyde, ab initio calculations will also be used to

obtain the interaction potential; these are being done in collaboration with H. F. Schaefer at Berkeley and W. A. Lester at IBM, San Jose. The formaldehyde results should be useful in understanding the anomalous absorption found in this species by Thaddeus. Similar calculations are contemplated on H_2O and OH in an attempt to understand the maser action observed in these molecules.

FAR INFRARED ASTRONOMY. (W. Hoffman and P. Aannestad)

Observations in the infrared region of the spectrum (1μ to 1000μ) are of importance for our understanding of how stars form and evolve, how interstellar dust and molecules are formed, and how these processes are related to each other and to the high infrared luminosity of galactic nuclei. The current program includes:

- 1) A balloon-borne survey at 100 microns of the galactic plane and detailed observations of a number of infrared stars, galactic H II regions and extragalactic sources.
- 2) Identification and analysis of these observations.
- 3) Studies of the mechanism of interstellar molecule formation in the presence of dust and ionizing radiation.

100 μ Balloon-Borne Observations. Two 100 micron far-infrared balloon flights were carried out from Palestine, Texas in June 1972. Several programs were carried out during those flights.

- 1) Parts of the northern Milky Way not previously covered were surveyed.
- 2) The very interesting region of the galactic plane in Cygnus was covered again to refine positions of previously discovered sources.
- 3) A number of galactic and extragalactic sources were repeatedly scanned to provide a lower threshold for detection by superposing the scans during analysis. These objects include the Seyfert galaxy NGC 1068, the Andromeda Galaxy M31, and a number of infrared stars.
- 4) The galactic center region was rescanned to improve on a previously published map.
- 5) A photographer camera was operated photographing background star fields in order to improve position determination.

While the analysis of these flights is not complete, it appears that most of these programs were successful. The photographic camera, operating with 1/8 second exposures while the telescope was scanning, has provided clearly measurable star images. Approximately 1000 photographs were taken. These are now being digitized in preparation for computer analysis.

A number of new sources along the galactic plane have been discovered. These are in the process of tabulation and identification.

Current and future work include the following:

- 1) The gondola is being refurbished for a set of flights planned for February 1973. A change in the landing impact absorbing structure should reduce landing damage. Efforts are being made to reduce system noise.
- 2) Flights for June are planned for mapping the galactic center region at six wavelengths. This will provide considerable information about the different temperatures and characteristics of the various parts of this region.
- 3) Design has begun for the Goddard-Cornell cryogenically cooled balloon-borne infrared telescope.

Analysis of Far Infrared Observations of the W3 Region. The 100 μ infrared data obtained during the recent balloon observations in June 1972, are currently being reduced. One of the objects searched for, and found to be a strong far infrared source, was the galactic H II region W3. The preliminary data indicate that both W3A and W3B were seen at 100 μ , and that a previously unknown source may exist near to these sources. The detection limit is such that the emission from W3 cannot originate from free-free and free-bound transitions in the ionized hydrogen plasma, and the radiation is probably due to circumstellar dust heated to a temperature of $T \approx 50$ °K. The dust particles in this source would typically be at distances $R \approx 10^4/T^2$ pc, or at $R = 4$ pc for $T = 50$ °K. This is somewhat larger than the observed size of the strongest radio component (A) in W3, which is about 1 pc in diameter. This indicates that the particles responsible for the 100 μ emission are situated outside or in the outskirts of the H II region. A model for the

radiation, taking into account the distribution of dust throughout the H II region, including realistic optical and thermal properties of the dust, is currently being developed.

A Mechanism of Interstellar Molecular Formation. Also under investigation is the idea that the formation as well as the destruction of complex molecules in interstellar space depends upon the radiation field. In particular, this may explain the surprising tendency of formaldehyde to be equal or more abundant in regions of less shielding of the radiation field. The assumption is that formaldehyde is catalyzed from H_2O and CO by UV photons ($\sim 2000 \text{ \AA}$) on interstellar grain surfaces² (an assumption supported by laboratory experiments) and destroyed in the gas phase by far UV photons ($\sim 1500 \text{ \AA}$). For reasonable assumptions about the properties of interstellar grains and for a yield of 2×10^{-5} formaldehyde molecules per incident near UV photon of 10^{-9} in unshielded clouds (extinction $\leq 1 \text{ mag}$). For shielded clouds (extinction $\geq 8 \text{ mag}$) the ratio is about an order of magnitudes smaller, 10^{-10} . This is to be compared with the observed ratios of 2×10^{-9} and 3×10^{-10} , respectively. A more detailed investigation of these processes is currently in progress.

NEUTRINO ASTRONOMY. (R. Stothers, D. Ezer, S. M. Chitre)

The problem of why Davis has not detected the large expected flux of solar neutrinos in his ^{37}Cl experiment is still unsolved. Definite detection would give astrophysicists assurance that nuclear reactions are the source of solar energy (or at least that the branch of the pp chain which contains the detectable ^8B -decay neutrinos occurs in the sun). Detection would also fix the central temperature, since the ^8B neutrino flux goes like T^{13} .

Chitre, Ezer, and Stothers have suggested that, if a large primordial magnetic field is concentrated near the center of the sun, its pressure would assist gas pressure in supporting the weight of the overlying layers and therefore cause a lowering of the central temperature and density. However, the rest of the sun's core would be largely unaffected, and so the sun's luminosity, which goes like the rate of the pp chain or a moderate T^4 , would also be unaffected. It is found that a magnetic field strength of about 10^9 gauss in the inner 10 per cent of the sun's mass can reduce the solar neutrino flux to a value compatible with Davis's observed upper limit. Such a field configuration does not conflict with any known information about the sun's oblateness, hydromagnetic stability, decay time of the field, or cosmogonical processes.

EVOLUTION OF MASSIVE STARS. (R. Stothers, C. W. Chin)

In 1965 Schwarzschild and Harm discovered a hitherto completely unsuspected property of evolved stellar models. The helium-burning shell surrounding the inert carbon core of a $1 M_{\odot}$ star becomes secularly (thermally) unstable. The manifestation of the instability is an enormous localized pulse of nuclear-generated luminosity. Further work corroborated this newly discovered stellar instability, but indicated that it would not be found in massive stars because of the damping effect of high radiation pressure.

Recent work by Stothers and Chin on the evolution of massive stars has shown, however, that this instability continues (on a smaller scale) up to the highest masses tested ($30 M_{\odot}$). A pulse cycle for $15 M_{\odot}$, is shown in Figure 1. More than that, the only situation where the hydrogen-burning shell of a normal star has ever been found to be thermally unstable is in massive stars, shortly after the exhaustion of core hydrogen. This, too, has been

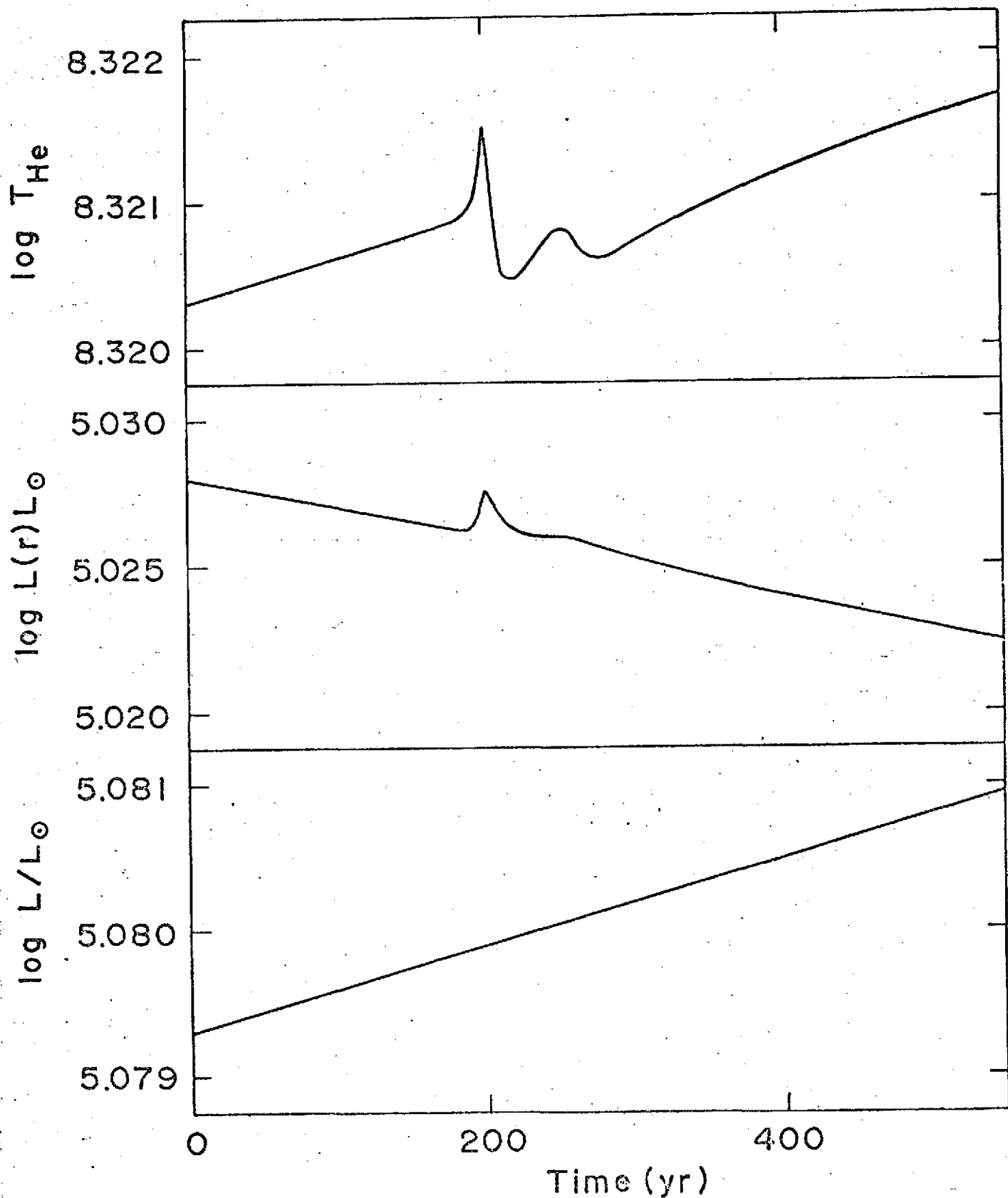


Figure 1. Segment of a pulse cycle in the thermally unstable helium-burning shell of a star of $15 M_{\odot}$. The panels show, from top to bottom, logarithms of the shell temperature, shell luminosity, and surface luminosity.

determined from an extensive survey by Stothers and Chin. Unfortunately, the observational consequences are very slight, and the effects of the instability seem to be equally unimportant in affecting the interior evolution. However, a rosier aspect of all this is that a potential source of uncertainty in understanding and calculating stellar evolution at high mass has been removed.

ROTATION OF MASSIVE STARS IN BINARY SYSTEMS. (R. Stothers)

Binary systems provide much information about stars not readily obtained from the analysis of single stars. For example, masses, radii, and effective temperatures are fundamental data best obtained from such systems. Furthermore, interaction between the binary components yields knowledge of their interior density distributions, chemical compositions, and axial rotation rates. Recently, Stothers has shown that knowledge of their interior magnetic field strengths can also be obtained.

Mostly recently, Stothers has reinvestigated the rotation rates of the most massive members of binary systems. Unexpected deviations from synchronism between the axial rotation period and the orbital revolution period in "normal" close binary systems seem, with the best data at hand, not to be significant, in contrast to many earlier investigations. The notable exceptions are the mass-accreting primaries (but not the mass-losing secondaries) in systems currently exchanging mass between their components. The primaries are apparently spinning up via the capture of angular momentum as well as of mass. It now seems that fast surface rotation, as well as marked underluminosity (caused by fast core rotation which reduces the central pressure and temperature, and therefore the nuclear energy generation rate), are two observational signposts of objects that are accreting, or have recently accreted, extraneous material. On these grounds, Stothers has added Plaskett's star (the most massive star known) to his select list of definite, extreme cases, comprised of Beta Lyrae, μ^1 Scorpii, and V356 Sagittarii.

NEUTRON STARS: INTERIORS. (V. Canuto and S. M. Chitre)

Since the first proposal by Landau in 1936, that a system of neutrons at zero temperature could form a stable configuration, much information has been gathered primarily due to pulsar observations. The present picture of a neutron star is quite different from the original simplified version of Landau and the following structure is now proposed as the most satisfactory:

- 1) $.3M_{\odot} \leq \text{Mass} \leq 2M_{\odot}$
- 2) $R \sim 10 \text{ km.}$
- 3) $I \equiv (\text{moment of inertia}) = 10^{44} \text{ gm cm}^2$
- 4) Surface Temperature, $T \sim 10^7 \text{ }^{\circ} \text{K.}$

Composition: The first few kilometers from the surface are a solid structure made of ordinary nuclei, e.g. Mg, Al, and Cd. The high pressure at the surface has squeezed the atom to such a closely packed entity that the electrons no longer orbit around the atom, but instead move more freely, as in an ordinary solid. Under that circumstance the nuclei do not have their charges screened by the electrons and they repel each other violently. The only way they can avoid each other's repulsion is to freeze into a structural configuration like a solid. By increasing the density (going towards the interior of the star) the electrons acquire more and more energy until they are able to convert protons into neutrons through inverse beta decay. The protons are converted into neutrons and it is calculated that at $\rho \approx 10^{14} \text{ gm/cc}$ the ordinary nuclei have completely disappeared, leaving a system of pure neutrons most probably in the form of gas or liquid.

Before this investigation was started it was generally believed that the gas or liquid structure continued throughout the interior which was supposed to be at a density around 10^{15} gm/cc .

However, it was found by Canuto and Chitre that towards the center of the star a new solid exists, formed of neutrons with a few per cent of hyperons. Crystals of total quantum nature do exist at high pressure in the laboratory. The best known example is solid

He^3 , a substance that becomes a solid only at 30 atm. The formalism developed to treat solid He^3 was adapted and extended to cope with the more complex situation encountered in nuclear forces. Canuto and Chitre show that at densities greater than $2 \cdot 10^{15}$ gm/cc a system of neutrons does indeed crystalize into an FCC (face centered cubic) structure. The core of most pulsars that have masses slightly higher than $1.5M_{\odot}$ can indeed possess a solid core, as indicated in Figure 1.

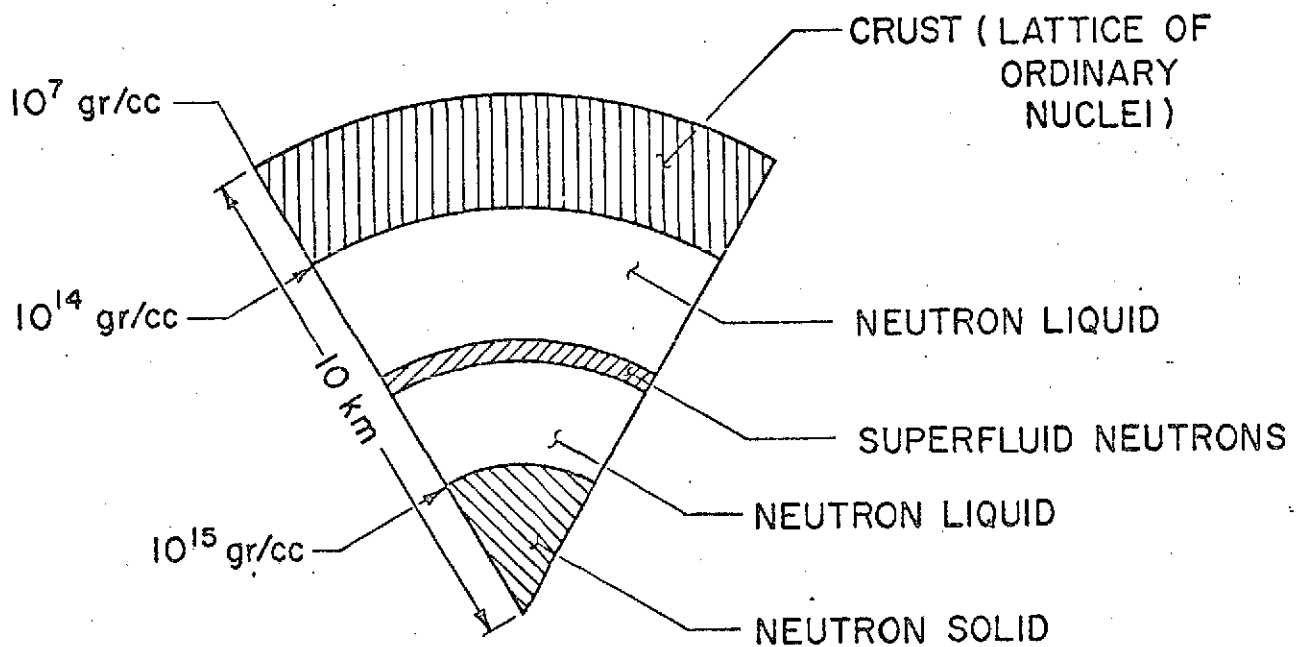


Figure 1. *Proposed structure of a neutron star.*

NEUTRON STARS: GLITCHES, (V. Canuto and S. M. Chitre)

By now 58 pulsars have been identified via their radio emission. Because of their high rotation speed (angular velocity of 200 rad/sec for the Crab Nebula) pulsars must possess an exceedingly high density so as not to be fragmented by the enormous centrifugal forces. Simple estimates give $10^{14} \lesssim \rho < 10^{16}$ gr/cc, a window not yet explored by theoretical physics. Matter at such high densities has no counterpart in any terrestrially known situation and no extrapolation can therefore be made with any degree of reliability. V. Canuto and S. M. Chitre have therefore, tried to deduce from the fine observational data a hint towards understanding high density matter. Pulsars are known to slowly decrease, the rotational energy being converted into electromagnetic radiation. On two different occasions, September 29, 1969, and February, 1969, two of the best studied pulsars, Crab and Vela, were observed to speed up abruptly and then to decrease again. The phenomenon, known as glitch, is illustrated in Figure 1.

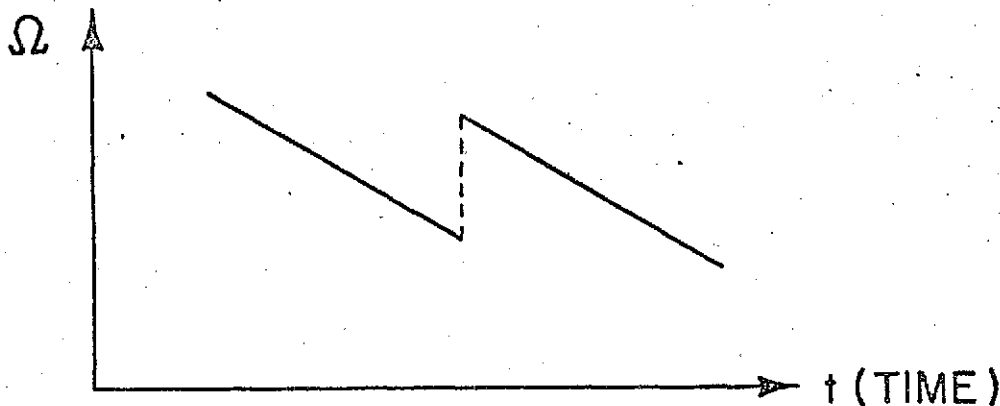


Figure 1. Curve illustrating the glitch phenomenon.

Since the glitch is not accompanied by any other effect of the surrounding plasma, it is safe to conclude that it depends on the interior of the star. The most promising model is the one based on the analogy with earthquakes. The observed slowing down implies a decrease of the original ellipticity $\epsilon(\sim \Omega^2)$ with which the star was formed. Such a decrease of ϵ cannot, however, take place in a continuous manner since the star is a solid. Stresses build up changing the moment of inertia, gives rise to a jump in Ω . Such a model cannot, however, explain why Vela and Crab have jumps different by a factor of 100, i.e., $(\Delta\Omega/\Omega)_{\text{CRAB}} = 10^{-2} (\Delta\Omega/\Omega)_{\text{VELA}}$. Canuto and Chitre have argued that a logical explanation follows if one accepts that one star is slightly denser than the other and its core is solid. If so, in the light star (Crab) the quakes take place at the surface (which can be easily proven to be a solid) whereas in the other, Vela, the quake is internal, i.e., is a corequake. The core, being denser, has more storage of elastic energy and when it quakes, does so more conspicuously. Detailed numerical analysis shows that indeed such a model is capable of explaining the two observed glitches.

STELLAR OPACITY AND EQUATION OF STATE. (T. R. Carson)

Among the important quantities relevant to stellar structure and evolution studies are the equation of state and opacity of the material. Recently new calculations indicate the sensitivity of these quantities upon the physical assumptions made and the various effects included.

Theoretical methods and computer programs for the calculation of equation of state and opacity for stellar material have been developed, based on the Feynman, Metropolis, Teller (FMT) generalized Thomas-Fermi model.

Tables of the parameters corresponding to the solutions of the dimensionless FMT equation have been prepared, from which equation of state and thermodynamic properties can be obtained by simple scaling procedures. These also facilitate the rapid calculations of the atomic properties which determine the opacity.

In the calculation of the radiative opacity, correlation effects on electron scattering of photons and frequency-dependent plasma dispersion effects are fully taken into account. The former can reduce the electron scattering opacity at high densities by a factor of two, while the latter increase the opacity by effectively increasing the absorption coefficient for photons with frequencies near the plasma frequency.

The (electron) conductive opacity is obtained by the methods of Hubbard and Lampe, included as an integral part of the program, so that the total opacity (due to both radiative and conductive sources) can be output. Major efforts have been concentrated on making the program as universally applicable as possible, not only to operate automatically over a very wide range of physical conditions appropriate to stellar problems, but also to permit the input data specifying those conditions to be presented in a variety of forms according to users' requirements.

Final tests are being carried out to ensure that the required accuracy and automatic functioning are preserved at all times.

INTERPRETATION OF OPTICAL AND RADIO INTERSTELLAR LINE. (R. E. White)

Optical interstellar absorption lines provide important data on the physical conditions and chemical composition of the interstellar gas. Using the electron densities derived from his observations of interstellar neutral calcium, CaI, to analyze earlier observations of ionized calcium, CaII, neutral sodium, NaI, and neutral hydrogen HI, White has shown that Ca and probably also Na are usually less abundant in the interstellar gas than in stars. The differences in Ca and Na abundances between "low velocity" and "high velocity" interstellar clouds are consistent with the interpretation that the "low velocity" clouds by depletion of the Ca and Na from the gas onto dust grains.

White has also found that the available CaI observations are inconsistent with the recent interpretation of optical interstellar lines given by Pottasch. Pottasch assumes that the Ca and Na abundances are the same everywhere in the interstellar gas and he derives the physical conditions which are required to explain the observed CaII, NaI and HI line strengths. White has shown that the derived conditions would lead to CaI absorption larger than actually observed.

Millimeter wavelength lines of interstellar molecules arise in dense dust clouds when the earliest phases of star formation occur. To provide a theoretical basis for the interpretation of new millimeter observations, White is studying the radiative transfer of the interstellar CO lines.

OBSERVATIONS OF PECULIAR A-TYPE STARS. (R. E. White)

Many peculiar A-type stars have strong, variable magnetic fields and associated light variations. The light variations differ from color to color and the existing broad- and intermediate-band photometry is insufficient to distinguish among several possible interpretations. During the last part of October and early November, White returned to the Hale Observatories to complete a set of narrow-band scans of the continuous energy distributions of a number of magnetic stars aimed at making possible a consistent interpretation of the light variations and their relationship to the observed magnetic field variations.

SEARCH FOR BLACK HOLES. (R. E. Wilson)

Objects which undergo complete gravitational collapse (black holes) have been predicted theoretically for several decades. It has become apparent during the past two years that it may be possible to identify such objects in certain unusual binary star systems.

It has been pointed out by both Devinney and Wilson that the secondary component of the system β -Lyrae may be a black hole. They argue that the object has the observational characteristics of a stellar black hole: specifically, low optical luminosity, small radius, and a mass much greater (20 times that of the sun) than is permitted for other small, faint objects like neutron stars and white dwarfs. Counter arguments have been made to the effect that the secondary could be a relatively normal star. One of the central issues in this controversy concerns whether or not the secondary is extremely underluminous for its mass. It seems clear that the secondary mass is surrounded by an orbiting disk-like structure, and one would like to know whether the apparent underluminosity of the secondary can result from redistribution by the disk of its radiation in directions away from the observer. Wilson has recently constructed a model to represent the system in terms of a tidally distorted primary star which is eclipsed by a self-luminous secondary disk. This should make it possible to draw accurate conclusions from the excellent photometric observations now available, regarding the detailed nature of the disk and its imbedded mass. It may thus be possible to prove or disprove the black hole hypothesis for this binary. A continuation of this work will consider black holes which may exist in several other binaries such as ϵ -Aurigae.

FUNDAMENTAL DATA FOR CONTACT BINARIES. (R. E. Wilson)

Among the very short period binaries, there exist some which are literally in contact, such that they exchange mass and energy freely and share a common envelope. At present the evolutionary behavior of these binaries is a subject of much interest, but their theoretical study is hampered by a lack of suitably accurate fundamental data (i.e. masses, luminosities, and radii). These data are missing not for lack of observations, but for lack of suitable means

for interpreting the observations. The classical models for analysis of binary stars specify that the components be similar ellipsoids and the models make further simplifying assumptions which are not reasonable for contact binaries. In the present program a computer code computes the correct surface configurations of tidally distorted contact systems and solves by least squares (a differential corrections analysis) for the fundamental data.

GAS CLOUDS IN DENSE STAR CLUSTERS, (S. M. Chitre and A. G. W. Cameron)

Recently it has been realized that stellar collisions in star clusters may play an important role in connection with the tremendous energy emission from quasars and from galactic nuclei. In order to study the properties of such a system more extensively, the structure of a gas cloud maintained in hydrostatic equilibrium in the gravitational potential of a dense star cluster was investigated. The structure equations were integrated numerically to obtain a complete match of the physical variables in the gas cloud and the resulting energy loss rate was found to be in good agreement with the observed rate of energy emission ($\sim 10^{46}$ ergs/sec) from quasars. It has been shown that such a gas cloud which is heated primarily by energetic cosmic ray particles becomes unstable in the presence of rotation and magnetic fields as a result of the hydrodynamical instabilities developing in its central regions. The cloud then collapses to form a differentially rotating disk which wraps the magnetic field lines into a very tight bundle near the axis of the disk. The lateral magnetic pressure is supposed to squeeze the material near the center giving rise to jets being ejected along the axial direction, thus accounting for the observed features associated with quasars and with the nuclei of galaxies.

COOLING OF NEUTRON STARS, (J. Lodenquai; V. Canuto; S. Tsuruta; M. Ruderman, Columbia University)

A neutron star (pulsar) can have a surface magnetic field $B \sim 10^{12}$ gauss. Such huge fields drastically affect the motion of electrons, constraining them to move essentially along the field

lines. As a consequence, atoms in the neutron star surface are cylindrical in shape and have ionization energies of the order of 1 KeV. Furthermore, the cross section for the absorption of scattering of photons traveling along the magnetic field is much smaller than in the corresponding field-free case. Calculations carried out within the past two years have shown that the ratio of the cross sections with and without magnetic field for Thomson scattering, photo-electric effect and inverse bremsstrahlung effect can all be approximated by $(\omega/\omega_H)^2$, where ω is the angular frequency of the radiation and ω_H is the electron cyclotron frequency. In pulsars, the above condition generally holds for temperature $T \approx 10^4$ °K, $T_C \approx 10^6$ °K, and a core temperature $T_C \approx 10^9$ °K. If the core is completely superfluid, the corresponding temperatures are $T_S \approx 10^4$ °K, $T_C \approx 10^5$ °K. These values are considerably lower than the previously quoted values and could therefore explain why the predicted X-ray fluxes from neutron stars were never found.

JUPITER OCCULTATION EXPERIMENT,

(Steven G. Ungar)

The microwave occultation technique has proven useful in measuring certain properties of the atmospheres of planets. The Mariner IV, VI, VII and IX spacecrafts have all successfully sensed the Martian atmosphere using microwave occultation, while the Mariner V spacecraft did the same for the planet Venus.

The Pioneer 10 spacecraft is now on its way to Jupiter, with an expected arrival date of December, 1973. As the spacecraft passes behind the planet, its radio communication signal will pass through the Jovian atmosphere, thus performing the first occultation experiment for one of the giant outer planets.

While occultation has been successfully used to sense the atmosphere of Mars and Venus, Jupiter poses unique problems. Given either an accurate assessment of the composition of an atmosphere, or a detailed picture of its temperature profile (temperature vs. altitude), the occultation technique can provide the other. However, in the case of Jupiter neither the atmospheric composition nor the temperature profile are well known.

The present work is an attempt to model the occultation experiment on the computer, in order to study the ability of the technique to yield useful information on Jupiter's atmosphere. Until now, the work has concerned developing the computer program to "raytrace" through a model of Jupiter's atmosphere, simulating the behavior of a radio wave from Pioneer 10 passing through the Jovian atmosphere. An analysis of the sensitivity of the occultation technique to changes in the atmospheric composition and temperature is about to be started.

A preliminary result of the work accomplished thus far is an apparent ability of the system to detect the top of the convective zone, the portion of the Jovian atmosphere analogous to the Earth's troposphere. Further analysis must be made to confirm this capability.

In order to extract useful information from an occultation system, it is usually necessary to assume that the atmosphere of a planet is "spherically symmetric," i.e., that the atmosphere has a shell-like structure in which there are no variations in temperature or pressure in the horizontal direction. Actually, all planetary atmospheres have some variation horizontally, and

objections have been made to the unquestioned use of the spherical symmetry assumption. Using a program developed at Stanford University by S. Ungar, to raytrace through a non-symmetric atmosphere, studying the effect of horizontal gradients in Jupiter's atmosphere on the results of the occultation experiment is planned.

THE FORMATION OF PLANETS AND STARS.

(W. Quirk)

The problem of the formation of planets and stars is being studied by Dr. William J. Quirk, who has constructed realistic numerical models. The basic idea is that the fragmentation of a rotating cloud of gas into protostars is the most likely process to lead to the formation of stars. In the model, material with an isothermal equation of state is distributed almost uniformly in a disk shape, which is kept in a state of rapid rotation so as to prevent radial collapse. (See Figure 1) Initially the disk is hot so it is stable, but eventually it becomes cold and breaks up into lumps. (See Figure 2) The break-up is caused by the disk's own self-gravitation. One of the most difficult problems in understanding star formation is how the fragments resulting from the breakup of such a rapidly rotating disk can possibly collapse sufficiently to become protostars. One would expect the fragments to have so much angular momentum that they could never become very condensed. The results of this study illustrated in the Figures show that in the final stage, the fragments can indeed become very centrally condensed. This is because most of the angular momentum goes into orbital motion rather than into rotational motion of the protostar.

It is hoped that the development of these protostars can be followed further and the information on the conditions under which planets are formed can be obtained.

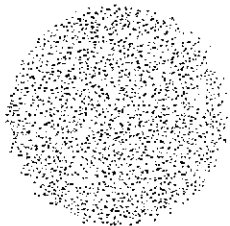


Figure 1. *Initial Stage.*
Rotating gaseous disk.



Figure 2. *Final Stage.*
Fragmentation of disk
into protostars.

Page intentionally left blank

II. APPLICATIONS

Page intentionally left blank

January 1, 1972 to June 30, 1972

PROGRAM ON STRATOSPHERIC CHEMISTRY AND GLOBAL POLLUTION. (R. Stewart)

The objective of this investigation is to determine the global distribution of minor constituents of the troposphere and stratosphere, and the corresponding surface UV levels, produced by addition of specific pollutants, including molecular species and aerosols. The approach to the problem is to develop a stratosphere/troposphere model with coupled photochemistry and dynamics, and to use this model to calculate the distribution of minor constituents and transmission of UV through the atmosphere. The program milestones are:

1. Development of a time-dependent, one-dimensional atmospheric model including complete photochemistry (60 constituents and 160 reactions) and vertical transport by molecular and eddy diffusion. (This development was completed 4/72)
2. Calculation, using the one-dimensional model, of the distribution of minor constituents without contaminants, as a check on the model and to provide starting conditions for injection experiments (to be completed 9/72), and of the effect of specified contaminant injection rates on minor constituents and UV intensity (to be completed 11/72)
3. Development of a limited, three-dimensional model with photochemistry and dynamics partially coupled to include the effect of dynamics on the distribution of stratospheric constituents, but without any feedback from photochemistry to dynamics (to be completed 11/72)
4. Calculation of minor atmospheric constituents with and without contamination, using a three-dimensional model and specified rate of contaminant injection along a given set of aircraft flight paths (to be completed 7/73)
5. Development of a three-dimensional dynamic-interaction model with complete coupling of photochemistry and dynamics (to be completed 1/74)
6. Calculation of minor atmospheric constituents using the three-dimensional dynamic-interaction model, to obtain the global distribution of minor atmospheric constituents in the troposphere and stratosphere resulting from a specified rate of contaminant injection at given locations (to be completed 1/76)

The present emphasis in this study is on solution of the set of coupled non-linear continuity equations for various atmospheric constituents. Table 1 shows the computer modeling studies in progress and projected for the period 7/72 to 1/73.

Table 1

Computer Modeling Studies 7/72 to 1/73					
Model Description	Objective	Status	S/C Ratio ^a	Projected Percent of Total Hours	Total Hours
1. One-dimensional, time-dependent model	Study the effect of specified contaminant injection rates on stratospheric ozone levels and surface UV radiation levels.	Production	150	60%	600
2. Three-dimensional, time-dependent with dynamics	Study the global response of the stratosphere and of surface UV radiation levels to contaminant injection along specified flight paths.	Development	15 (400 pt grid)	30%	300
3. Three-dimensional, time-dependent tropospheric model	Study the distribution of minor atmospheric constituents in the troposphere on local and regional scales.	Development	50 - 100	10%	100

^a The S/C ratio is the ratio of simulation time to computation time.

A one-dimensional, time-dependent model which considers the combined effects of photochemistry and vertical transport by diffusion and advection has been completed. The principal application of this model will be to the problem of contaminant injection into the stratosphere by high-altitude aircraft. Some investigators have indicated that exhaust products from these aircraft could significantly reduce present levels of stratospheric ozone and consequently produce an increase in the level of UV radiation reaching the earth's surface.

Calculations of the natural distribution of minor atmospheric constituents in the altitude range from 0 to 200 km are currently in progress. The photochemistry included in these calculations presently involves about 160 reactions among about 60 constituents and utilizes the latest measurements of the various rate coefficients for these reactions. Table 2 lists some of the important groups of reactions considered in the present model. Table 3 lists the experiments to be carried out in the 7/72 - 1/73 period with this model.

Table 2

OXYGEN PHOTOCHEMISTRY

(CHAPMAN MECHANISM)

REACTION	RATE
$O_2 + h\nu \rightarrow O + O(^1D)$	
$O + O_2 + M \rightarrow O_3 + M$	$1.16 \times 10^{-35} e^{1050/T}$
$O_3 + h\nu \rightarrow O_2 + O$	
$O + O + M \rightarrow O_2 + M$	$3.6 \times 10^{-31} \frac{1}{T} e^{-170/T}$
$O + O_3 \rightarrow O_2 + O_2$	$2.0 \times 10^{-11} e^{-2395/T}$

NO_x PHOTOCHEMISTRY

REACTION	RATE
$NO + O \rightarrow NO_2 + O_2$	$1.33 \times 10^{-12} e^{-2500/RT}$
$O + NO_2 \rightarrow NO + O_2$	$1.67 \times 10^{-11} e^{-600/RT}$
$NO_2 + h\nu \rightarrow NO + O$	
$NO + NO + O_2 \rightarrow NO_2 + NO_2$	$3.33 \times 10^{-39} e^{1046/RT}$
$O + NO + M \rightarrow NO_2 + M$	$2.9 \times 10^{-33} e^{1870/RT}$
$NO_2 + O_3 \rightarrow NO_3 + O_2$	$9.8 \times 10^{-12} e^{-7000/RT}$
$NO_3 + h\nu \rightarrow NO + O_2$	

NO_x PHOTOCHEMISTRY

REACTION	RATE
$O(^1D) + H_2O \rightarrow 2OH$	3.0×10^{-11}
$OH + O_3 \rightarrow HO_2 + O_2$	$1.5 \times 10^{-12} T^{1/2} e^{-1500/T}$
$HO_2 + O_3 \rightarrow OH + 2O_2$	1.0×10^{-14}
$O + HO_2 \rightarrow OH + O_2$	2.0×10^{-11}
$O + OH \rightarrow O_2 + H$	5.0×10^{-11}
$H + O_3 \rightarrow OH + O_2$	2.6×10^{-11}
$OH + OH \rightarrow H_2O + O$	$5.0 \times 10^{-12} T^{1/2} e^{-1500/T}$
$CH + HO_2 \rightarrow H_2O + O_2$	1.0×10^{-11}
$HO_2 + HO_2 \rightarrow H_2O_2 + O_2$	$5.0 \times 10^{-12} T^{1/2} e^{-1000/T}$

METHANE PHOTOCHEMISTRY

REACTION	RATE
$CH_4 + h\nu \rightarrow CH_2 + H_2$	
$CH_4 + O(^1D) \rightarrow CH_3 + OH$	3.0×10^{-11}
$CH_4 + OH \rightarrow CH_3 + H_2O$	$4.7 \times 10^{-11} e^{-2500/T}$
$CH_3 + O_2 + M \rightarrow CH_3O_2 + M$	6.0×10^{-31}
$CH_3O_2 + NO \rightarrow CH_3O + NO_2$	5.0×10^{-13}
$CH_3O_2 + NO_2 \rightarrow CH_2O + HNO_3$	5.0×10^{-12}
$CH_3O + O_2 \rightarrow CH_2O + HO_2$	1.7×10^{-17}
$CH_2O + OH \rightarrow CHO + H_2O$	7.0×10^{-12}
$CHO + O_2 \rightarrow CO + HO_2$	7.0×10^{-12}
$CO + OH \rightarrow CO_2 + H$	$9.0 \times 10^{-13} e^{-500/T}$
$CH_2 + O \rightarrow CO + 2H$	5.0×10^{-11}

H-O-N PHOTOCHEMISTRY

REACTION	RATE
$H_2O_2 + NO \rightarrow HNO_2 + OH$	$< 10^{-20}$
$H_2O_2 + HO_2 \rightarrow HNO_3 + OH$	$< 10^{-20}$
$OH + NO + M \rightarrow HNO_2 + M$	3.3×10^{-33}
$OH + NO_2 + M \rightarrow HNO_3 + M$	3.3×10^{-33}
$HO_2 + NO + M \rightarrow HNO_3 + M$	3.3×10^{-33}
$HNO_3 + h\nu \rightarrow OH + NO_2$	
$HNO_2 + h\nu \rightarrow OH + NO$	
$HNO_3 + O \rightarrow OH + NO_2$	1.7×10^{-11}
$HNO_2 + O \rightarrow OH + NO$	1.7×10^{-11}
$HNO_3 + OH \rightarrow H_2O + NO_2$	$1.7 \times 10^{-11} e^{-1650/T}$
$HNO_2 + OH \rightarrow H_2O + NO$	$1.7 \times 10^{-11} e^{-1650/T}$

Table 3

Program of Computer Simulation Experiments, 7 '72 - 1 '73
One-Dimensional, Time-Dependent Model

Experiment	Runs Required	Simulation Period	Estimated Computer Time
1. Variation of Chapman model reaction rates	2	60 days	20 hrs.
2. Variation of primary NO_x catalytic reduction rates	2	120 days	40 hrs.
3. Variation of primary HO_x catalytic reduction rates	2	120 days	40 hrs.
4. Variation of Nitric & Nitrous acid reaction rates	2	120 days	40 hrs.
5. Effect of CH_4 oxidation and subsequent reactions	2	120 days	40 hrs.
6. Effect of NH_3 oxidation and subsequent reactions	2	120 days	40 hrs.
7. Effect of different NO mesospheric dissociation rates	2	120 days	40 hrs.
8. Effect of variation in lower boundary conditions on stratosphere	1	120 days	20 hrs.
9. Change in K(Z) profile	1	120 days	20 hrs.
10. Max and min injection rates for NO_x	2	120 days	40 hrs.
11. Max and min injection rates for HO_x	2	120 days	40 hrs.
12. Combined effects of HO_x , NO_x injection with and without HC reactions	2	120 days	40 hrs.
13. Study of effect of contaminant injection for "worst" and "best" cases obtained from above experiments	2	1 year	120 hrs.
14. Test and development			60 hrs.

TOTAL 600 hrs.

Some initial results derived from the one-dimensional model are shown in Figures 1 through 5. The agreement between the calculated and observed oxygen components O , $O_2(^1\Delta_g)$, and O_3 is generally good. A secondary, high-altitude maximum in the O_3 profile which has only recently been observed by the OAO-2 satellite is clearly evident in the theoretical model. Evaluation of most other theoretical results is hindered by a lack of observational data. Reasonable results have been obtained for OH (Figure 3) and NO (Figure 4) over the limited altitude range for which observations are available, but the calculated stratospheric density of nitric acid (Figure 5) is one to two orders of magnitude smaller than that indicated by an observation (only one is available). The results presented in Figures 4 and 5 show a substantial conversion of NO and NO_2 to nitric acid in the troposphere and this may indicate the need for a substantial tropospheric source of NO_x which is not contained in the present model.

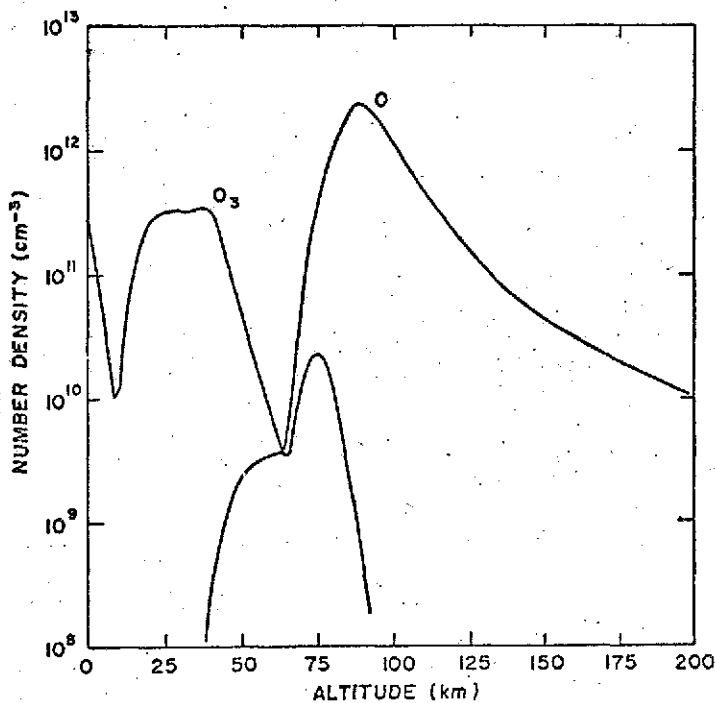


Figure 1. Calculated number densities of O and O_3 vs. altitude.

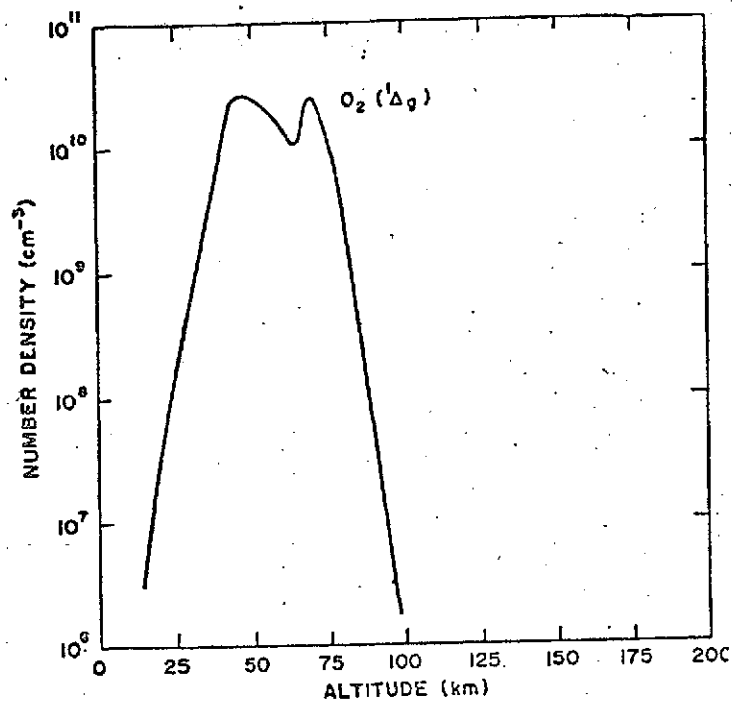


Figure 2. Calculated number density of $O_2(^1\Delta_g)$ vs. altitude.

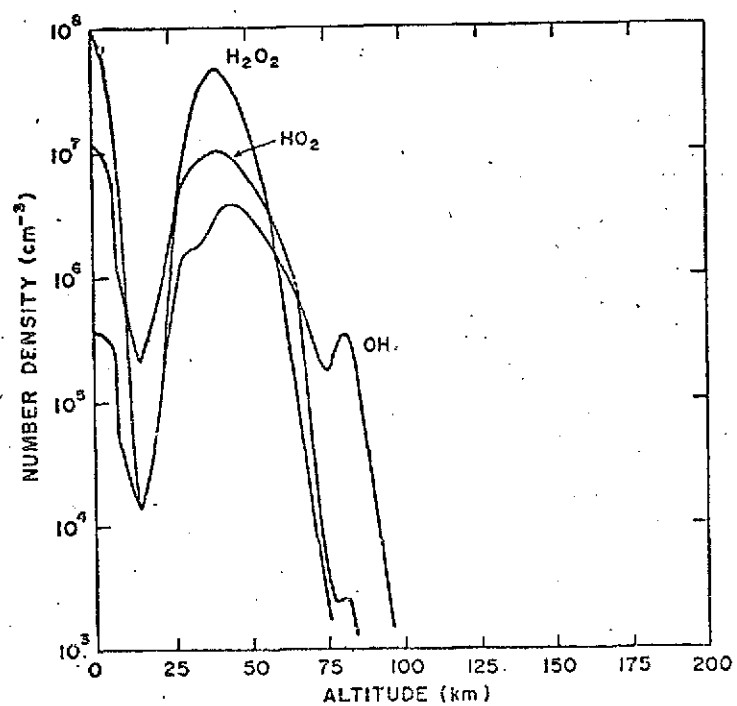


Figure 3. Calculated number densities of H_2O_2 , HO_2 and OH vs. altitude.

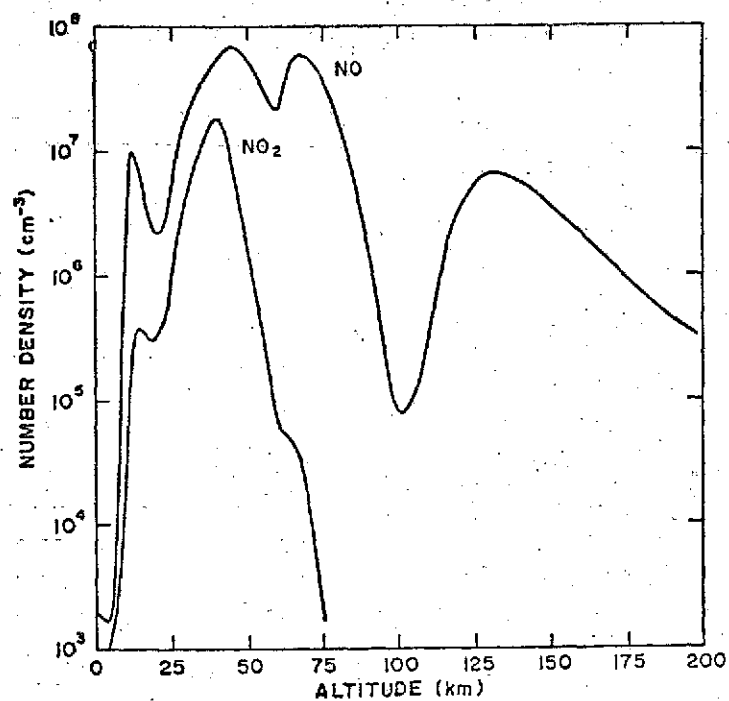


Figure 4. Calculated number densities of NO and NO₂ vs. altitude.

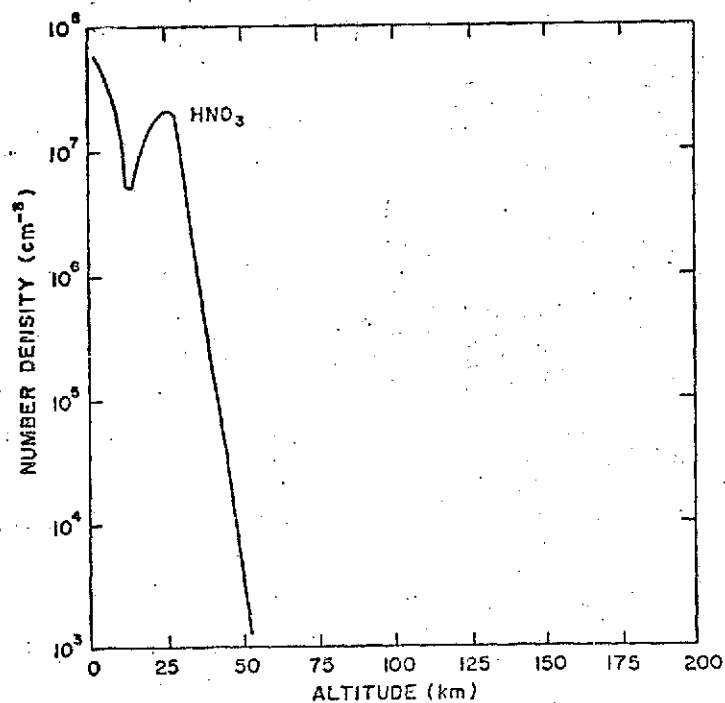


Figure 5. Calculated number density of HNO₃ vs. altitude.

Development of multi-dimensional models are proceeding concurrent with production running of the one-dimensional model described above. Initial applications of these models will be to the study of the O_3 , HO_x , and NO_x distribution in the stratosphere on a global scale and to the study of various contaminant distributions in the troposphere on local and regional scales. Subsequent applications of the three-dimensional stratospheric model will feature the modeling of proposed aircraft flight paths and traffic densities to determine the impact of their engine emissions on surface UV radiation levels over the globe. Table 4 lists the experiments to be carried out with the three-dimensional stratospheric model in the 7/72 - 1/73 period.

Development work on the tropospheric models is presently centered on the mathematical problem of "stiffness" exhibited by the differential equations of chemical kinetics. Stiffness means essentially that the very short time constants encountered in the chemical kinetics equations render their solution by standard numerical techniques impossible if reasonable values of the time step are employed. This problem was encountered in the development of the one-dimensional model and a workable mathematical solution obtained. The inclusion of more efficient methods is desirable, however, in future multi-dimensional models. Dr. C. Weng of CSC has successfully modified an existing numerical technique for integrating stiff equations so that it can be applied to photochemical problems of urban atmospheres and he is now investigating the applicability of other techniques. The extension of these methods from the ordinary differential equations of chemical kinetics to the partial differential equations of atmospheric physics is the most important mathematical problem in the development of the multi-dimensional models.

Table 4

Program of Computer Simulation Experiments, 7 '72 - 1 '73
Three-Dimensional, Time-Dependent Model

Experiment	Runs Required	Simulation Period	Estimated Computer Time
1. Development and testing	-	-	100 hrs.
2. Chapman n. del (pure oxygen) photo- chemistry	1	60 days	50 hrs.
3. Addition of basic HO_x , NO_x catalytic chem- istry to Chapman model	1	60 days	150 hrs.

CARRIER BALLOON SYSTEMS STUDIES: NOAA REQUEST. (R. Jastrow, M. Halem)

At a meeting held at NOAA, in the office of the Associate Administrator for Environmental Monitoring and Prediction, to define the scope of U.S. participation in the First GARP Global Experiment, Dr. R. Hallgren requested a series of simulation studies from GISS. These studies were designed to investigate the trade-off in the accuracy of tropical wind determinations obtained from the carrier balloon system (CBS) with its presently planned coverage (500 km) and an alternative system with a coarser coverage (1000 km).

The implication of these studies might be the implementation of a special, but coarser, observing system with a more limited number of carrier balloons, but supplemented by ships and air support.

The experiments are similar to the simulation studies carried out earlier at the request of the JOC, and reported in the 1971 GISS Research Review. Temperatures are assumed to be known twice daily with a $.5^{\circ}$ rms random error and a 1° sinusoidal systematic error. Winds are assumed to be known in the tropics (-25° to 25°) twice daily at two levels (200 mb and 800 mb) with a 2 m/s RMS wind vector error. The carrier balloon system is simulated by assuming winds are known with a 1 m/s rms wind vector error for all pressure levels and at all grid points in an equatorial region (-10° to 10°) twice daily. This coverage in the GISS model yields a 440 km resolution. The alternative system has the same frequency and accuracy of wind data except that the equatorial winds are known only at every other grid point in the region yielding an 880 km resolution.

The global, nine-level, 4° by 5° grid resolution model was used for these experiments. Previous studies reported by GISS and other groups (GFDL) showed that this vertical resolution is needed to obtain more realistic flows in the tropics.

The simulation studies consist in first integrating the model from an initial state and generating a long history. The experiments starts over again from a randomly correlated initial state which in this case is obtained from a day on the history far removed from the initial day. The model is then integrated forward from this random state, but simulated observational data is continuously inserted at synoptic times. The simulated observational data are generated from the history with JOC specified errors added to the appropriate fields. The experiments were carried out for 14 simulated days and the results are shown in Figure 1.

Regarding the second question -- the need for reference pressures in addition to those provided by the augmented WWW network -- a third experiment inserting exact sea level pressures everywhere was performed. In this case, the global mean wind error is about 1 m/s smaller than in the "land only" case, which is similar to the results obtained by NCAR.

Our interpretation of the NCAR and GISS experiments that have been performed thus far in the reference-level question is the following:

1. Augmentation of the WWW surface stations by a network of buoys with a spacing of 400 to 500 km could improve global mean wind errors by as much as 1 m/s. The gain is significant but the expense would be formidable.
2. Augmentation of the surface stations by a dense network of 200 mb balloons would have little effect.

USE OF SIMULATED VTPR RADIANCE MEASUREMENTS IN A GENERAL CIRCULATION MODEL. (J. Hogan, K. Grossman)

The temperature retrieval method (and technique for smoothing the required initial guess at the temperature profile) developed at GISS by J. Hogan and K. Grossman and described elsewhere in this report has been applied to a simulation of the procedure for using VTPR radiances from the ITOS-D satellite in a general circulation model to generate temperatures, pressures and winds. In this study, the retrieval scheme was used in conjunction with a 5-level circulation model modified from the UCLA 2-level model. The horizontal resolution of the model was 400 km. The model was run out for a number of days from an available initial condition to generate a sequence of states assumed to describe the "real" atmosphere. For these "real" states, outgoing radiances were calculated globally, at 12-hour intervals, to simulate the coverage provided by the VTPR sounder. Jastrow and Halem have verified that the synoptic insertion of temperature data has the same effect as asynoptic insertion, provided the same volume of data per day are inserted in both cases.

The simulated sounder was assumed to have the field of view and scan pattern of the VTPR. However, the radiance measurements were made in channels which differ somewhat from the VTPR channels. Random errors of a magnitude obtainable by the averaging of independent areal measurements made by the VTPR were included for each channel. It was assumed that the basic noise level of the instrument was $0.25 \text{ ergs cm}^{-2} \text{ sec}^{-1} \text{ ster}^{-1} \text{ cm}^1$ for each independent measurement, that 50 soundings would be made every twelve hours within each $400 \text{ km} \times 400 \text{ km}$ grid area of the dynamical model, and that 10 of the 50 soundings would be free of clouds, reducing the noise level after averaging the clear-column radiances to $0.075 \text{ ergs cm}^{-2} \text{ sec}^{-1} \text{ ster}^{-1} \text{ cm}^1$.

Temperatures were retrieved from the simulated radiances at 12-hour intervals, using smoothed temperature profiles generated by the model as initial guesses. These temperatures were inserted into the dynamical model at 12-hour intervals. Also, following a technique developed by Jastrow and Halem, temperature fields linearly interpolated from the observed fields were inserted at 3-hour intervals to obtain better control of error growth in the model. The procedure for carrying out the remainder of the simulation study has been described by Jastrow and Halem.

The wind errors produced by the insertion of retrieved temperatures into the circulation model are shown in Curve A of Figure 1. These wind errors correspond to means of the global RMS zonal and meridional wind errors. The mean wind error for this case, averaged vertically, is 3.1 m/sec. The average error

in pressure resulting from the same retrieved temperature insertion is 2.3 mb. Curve B of Figure 1 shows the result obtained by inserting exact temperatures into the model, with the remainder of the procedure unchanged. The vertically averaged wind error in this case is 2.5 m/sec, with a mean error in pressure of 2.2 mb. The difference between Curves A and B shows the combined effect of the simulated errors in the radiance measurements and the basic inaccuracy of the retrieval method which arises from the half-width and overlap of the weighting functions.

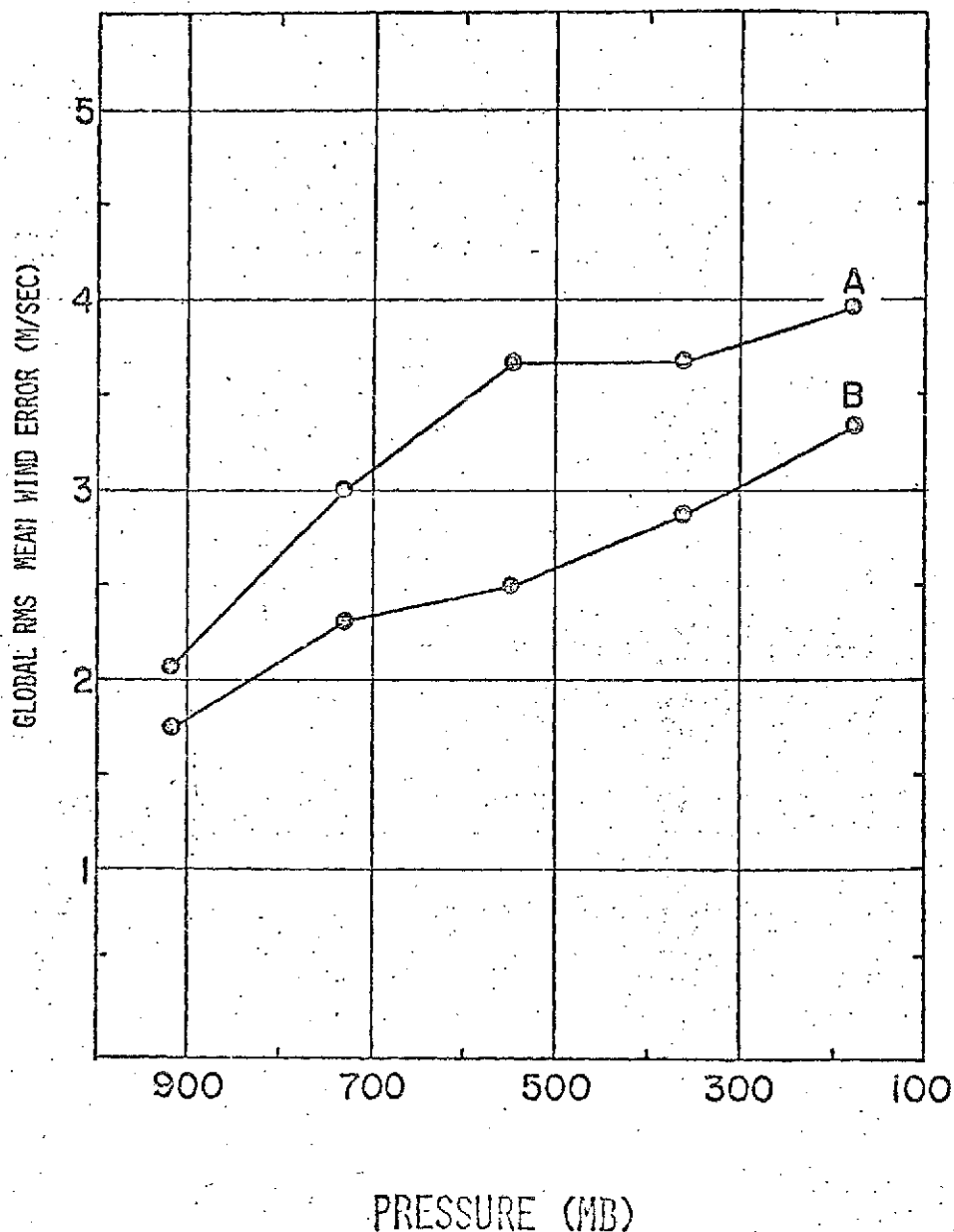


Figure 1. Profiles of global RMS mean wind errors produced by insertion of temperature data. The values shown were obtained by averaging zonal and meridional RMS wind errors. Curve A indicates wind errors obtained by inserting simulated temperature data from the VTPR observations. Curve B indicates wind errors obtained by inserting exact temperature data.

PREPARATION FOR USE OF REAL VTPR RADIANCE DATA IN A GENERAL CIRCULATION MODEL. (J. Hogan)

The method for retrieving atmospheric temperature profiles from satellite radiance measurements (described elsewhere in this report) is being tailored for the processing of actual radiance measurements to be made by the VTPR instrument aboard the ITOS-D satellite. The technique developed at GISS for basic research on the temperature inversion problem and for simulation studies was a simple scheme, applicable only to a clear, dry atmosphere. Although suitable for such experiments and tests, such a scheme cannot be employed in the utilization of real data. Expansion of this scheme to take into account the presence of water vapor and clouds in the retrieval of atmospheric temperature profiles has been undertaken, and the expanded scheme is undergoing testing at the present time. Tailoring of the basic scheme for use with real VTPR radiance data has also required calculating from available data the detailed atmospheric transmission functions in the channels specified for the VTPR instrument.

It is generally acknowledged that the accuracy of retrieved temperature profiles is severely degraded when clouds are present within the field of view of a satellite-borne IR instrument. Thus, a technique for recognition of cloud presence in the radiances themselves has been developed, and refinement and testing of this scheme is underway. This cloud detection method involves checks of observed radiances against climatological "minimum" radiances in the channels which probe the lower troposphere. The cloud detection procedure also involves internal statistical checks made by considering radiances emerging from a field of adjacent areas of observation. The plan is to screen out data from obviously cloudy regions before processing.

Also, a routine has been developed for screening from the body of VTPR data those observations made over high, mountainous terrain. Processing such observations without considering the presence of mountains could lead to erroneous and highly unrealistic temperature profiles. This routine involves positioning the observation on a global topography array available at GISS with a resolution of 0.5° latitude by 0.5° longitude.

Routines for detecting errors in sequence, missing data points and unrealistic data have also been developed. These routines are being combined with the cloud detection and topography check routines in a program designed for preprocessing of the VTPR data before insertion into the dynamical model.

A program is being written to average the radiance data from obviously clear regions over the grid areas of the

dynamical model. The intended procedure is to retrieve average temperature profiles from this averaged radiance data and to insert these profiles into the relationships provided by the model equations to obtain fields of winds and pressures.

TESTS OF A PROCEDURE FOR DERIVING ATMOSPHERIC TEMPERATURE PROFILES FROM SATELLITE RADIANCE MEASUREMENTS. (J. Hogan, K. Grossman)

A program for retrieving temperature profiles from satellite radiance measurements had been developed during 1971 by Hogan and Grossman. This program employs an initial guess at the temperature profile and uses an iterative technique for solving the integral equation of radiative transfer. The program is similar to the method developed by Chahine at JPL, but incorporates a modification suggested by Smith of NESS.

The method of Chahine retrieved temperatures at a number of pressure levels equal to the number of channels in which radiance measurements are made, with temperatures at intermediate levels being obtained by interpolation. Smith modified this approach to allow direct solution for the temperature at any desired number of pressure levels. Also, Smith considered the difference between observed and calculated radiances as an indication of the correction to be applied to the temperature, while Chahine used the ratio of these radiances.

Like Chahine, the GISS method uses the ratios of calculated to observed radiances in each spectral channel to correct the temperature profile from the first guess via iteration. However, like Smith, the GISS method solves directly for the temperature at any desired pressure level by weighting the different temperatures values indicated by the separate channels by the values of the atmospheric weighting functions in these channels at the desired pressure level.

Experiments have been conducted to test the sensitivity of the GISS method to the initial guess at the temperature distribution which all retrieval methods require. Of particular interest were initial guesses of the kind that would be provided by a numerical model of the atmospheric circulation. The objective here was to develop a procedure for direct use of satellite radiation measurements as input to a numerical forecasting scheme.

The tests were performed for a clear, dry atmosphere to avoid the complicating effects of water vapor and clouds. Weighting functions were computed in the 15μ CO_2 band from available line data, adopting a constant line half-width of 0.08 cm^{-1} at STP, and assuming a Lorentz line profile. The weighting functions were calculated for an isothermal atmosphere at 250 K, in seven 5 cm^{-1} -wide spectral channels, within the 15μ CO_2 band. The temperature dependence of the weighting functions was neglected in carrying out these experiments. The procedure was to (a) specify a "correct" temperature profile, (b) compute

the corresponding radiances, and assume these to be the measurements yielded by the satellite-borne instrument, and (c) invert the set of "measured" radiances, starting from a "guessed" temperature profile, different from the "correct" one.

The experiments indicate that, in general, accurate retrievals are obtained for cases in which the initial guess is smooth and its shape bears some resemblance to the shape of the "correct" profile. It was found that the particular case of the isothermal guess, although its shape does not resemble the correct shape, also produces good retrievals, which are insensitive to the isothermal value. Similar results were found by Smith and Chahine with their methods.

However, these types of tests, using a smooth "guess", are not realistic for the case in which the retrieval method is to be combined with the use of a numerical circulation model. In that case, the initial guess is likely to have a "zig-zag" appearance because of the limited vertical resolution of the model. Tests were carried out with a "zig-zag" initial guess, and it was found that the retrieval method does not eliminate the "zig-zag" variations in the profile. For this guess the final result has a substantial error roughly equal to the average scatter of the points in the initial guess.

This effect is illustrated in Figure 1. In the experiment to which this figure corresponds, a "zig-zag" temperature distribution straddling the "correct" profile (Standard Atmosphere), with a maximum departure of about 5°K, was used as the initial guess. Such a guess simulates an operational situation in which a guessed profile generated by the circulation model is similar to the "correct" profile, except for the presence of scatter in the model profile used as the guess. In this case, the retrieved profile is actually less accurate at some levels than the guessed profile.

In general, the guess provided by the general circulation model will have both systematic and random departures from the "correct" profile. To simulate this case, a "zig-zag" profile colder on the average by about 5°K than the "correct" profile (Standard Atmosphere) was used as the guess. Although the systematic error of 5°K in this guess is removed by the retrieval procedure, the random departures persist as in the previous case, so that the retrieved profile has the same "zig-zag" appearance as the guess, and, as a result, had a substantial mean error (Figure 2).

The failure of the retrieval procedure to remove random errors from the guessed profile must be taken into account in the application of satellite radiance measurements to numerical

forecasting. Although the natural source for the first guess in such applications is the numerical model itself, direct use of the model temperature profile as a guess can lead to substantial errors in the retrieved temperatures.

However, a considerable gain in retrieval accuracy can be achieved by smoothing the model-generated guess before it is used in the inversion procedure. In the experiment to which Figure 3 corresponds, a smooth curve of the form $T=ap^b$ was fitted by least-squares to the segment of the "zig-zag" profile below the 300 mb level, that was used as a guess in the case depicted in Figure 2. The smoothed curve was then used as the first guess. For this guess, the retrieved temperatures are found to be close to the "correct" temperatures at all levels.

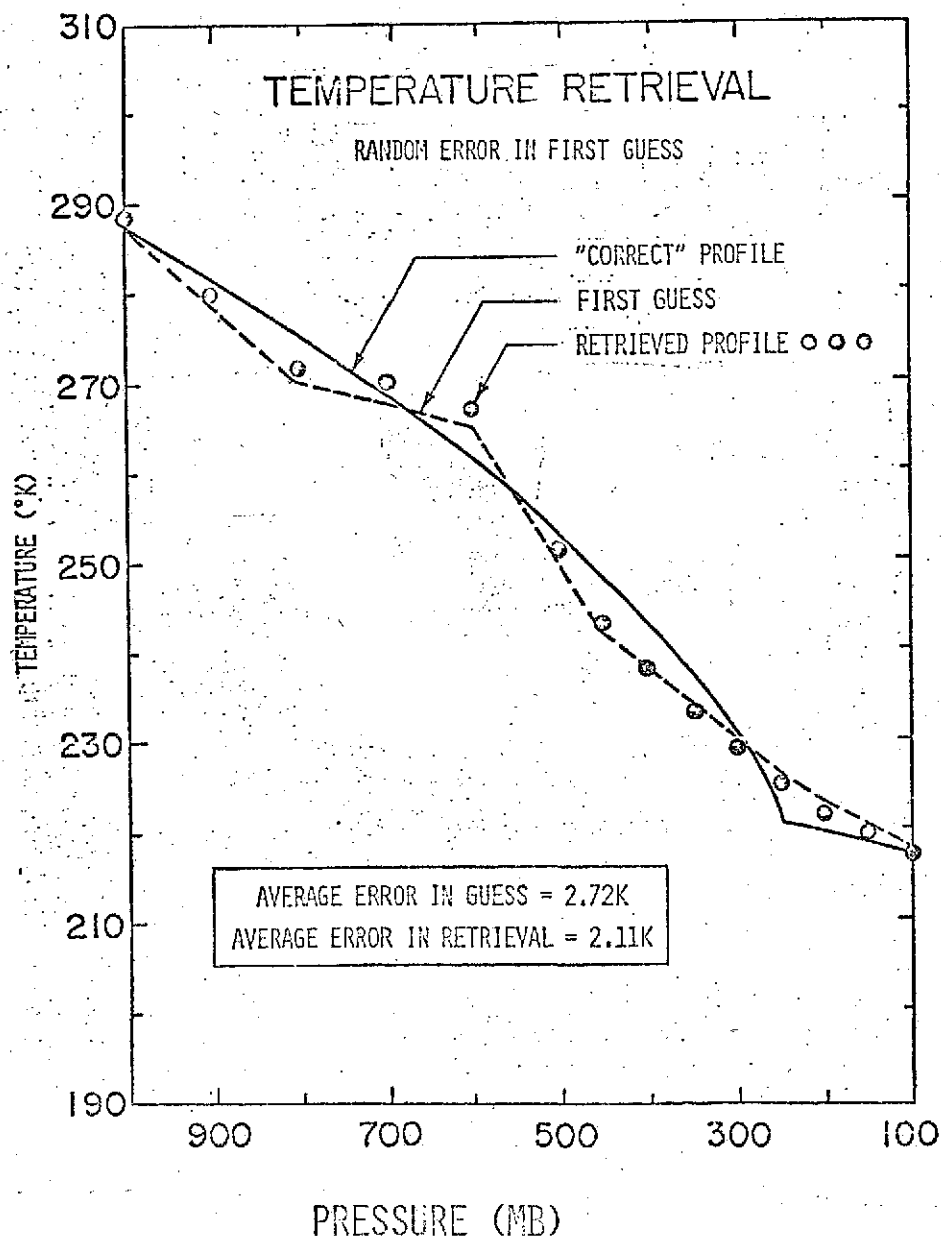


Figure 1. "Correct", first guess, and retrieved profiles, for a case in which the guess contains random errors only.

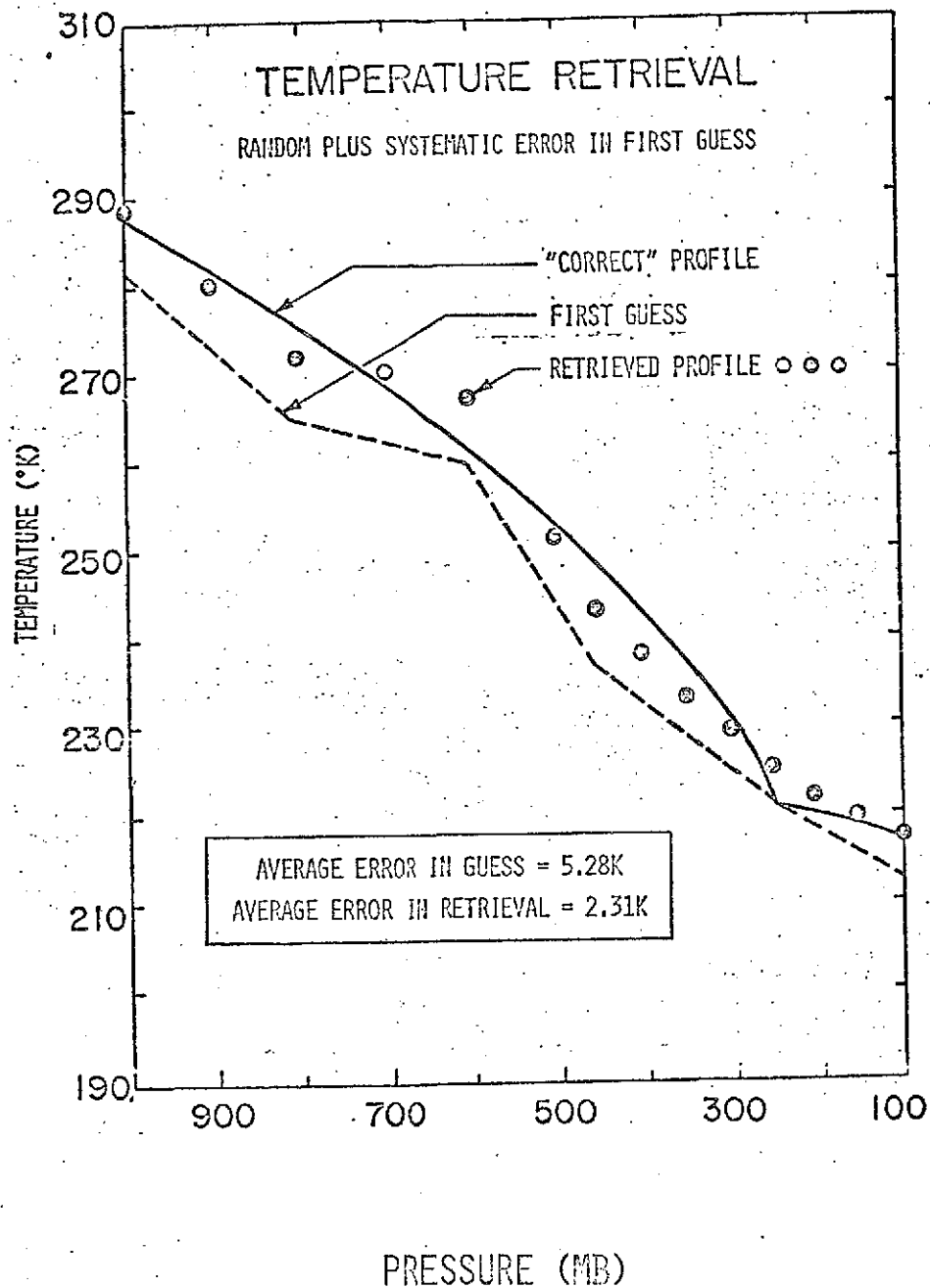


Figure 2. "Correct", first guess, and retrieved profiles, for a case in which the guess contains both random and systematic errors.

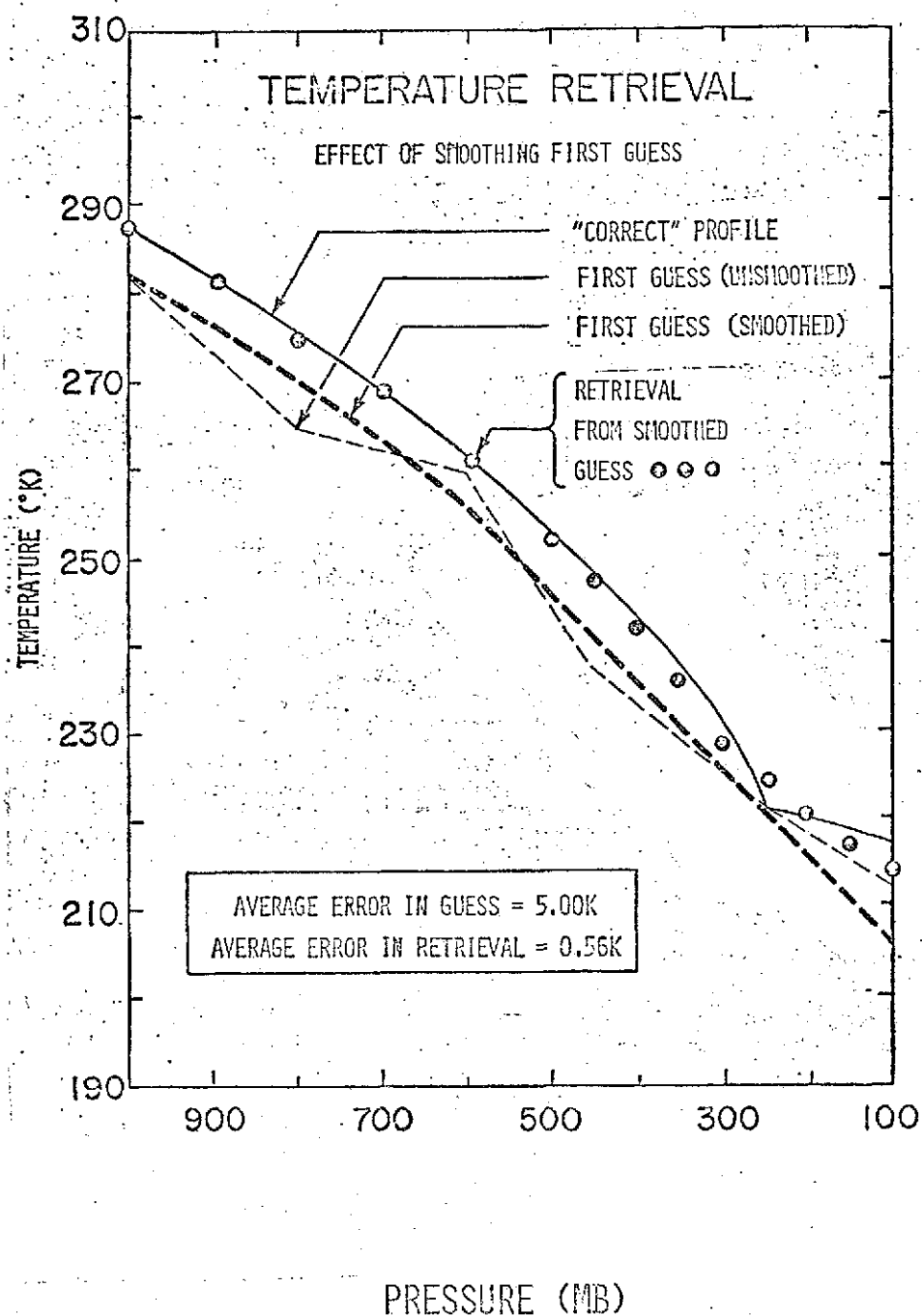
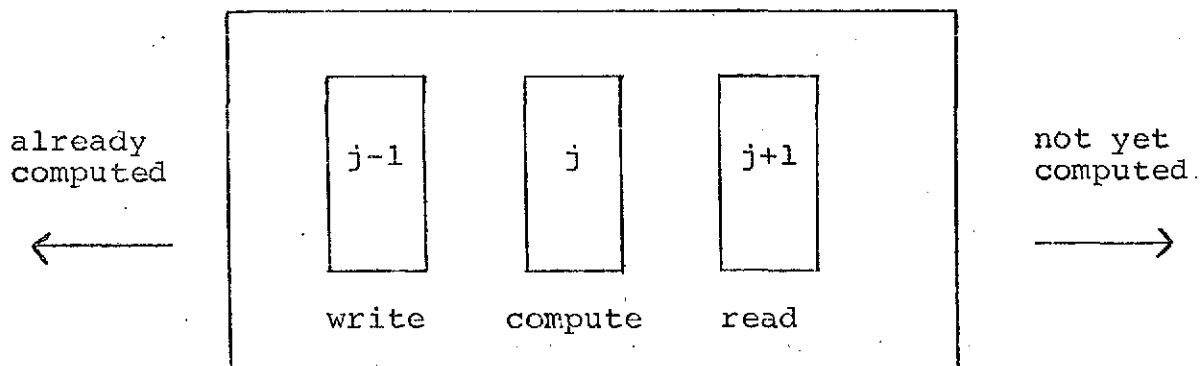


Figure 3. "Correct", first guess, and retrieved profiles, for a case in which random errors are removed by smoothing

ACQUISITION OF THE 370/165. (P. Schneck)

Increased computing power is needed to reach the GISS GARP objectives. A feasibility study was performed examining all available alternatives (pipeline processors, array processors, etc.) that might be used to obtain additional computing capability. The result of this study indicated that only the IBM 370/165, used as a peripheral processor by the 360/95 is a realistic solution.

In order to support the 370/165 two types of software programs are under development. First, the GARP application programs are being modified to work efficiently in the smaller memory of the 370/165. This involves restructuring the numerical difference scheme to permit input, output, and computation to proceed simultaneously on adjacent rows of data elements. Only three rows will be required in storage at one time.



Second, an operating system subset is under development for the 370/165. This will permit use of the 360/95 peripheral devices and memory by the 370/165. This permits use of a minimal 370/165 without renting additional I/O or memory.

The operating system and application programs will permit the 370/165 to work on a different problem than the 360/95 or both machines may work on the same problem. This can be accomplished because of the parallelism inherent in the numerical difference scheme. The two machines will consult a table to find the next work assignment. This approach permits the 360/95 to be responsive to user needs and when time is available it will be used on the GARP program in conjunction with the 370/165.

The figure indicates how the problem is divided into basic units of work which either machine may perform.

1	2	3	4
5	6	7	8
9	10	11	12
13	14	15	16

Whichever machine is ready simply consults the table and begins working on the next unit. When all units are completed the problem is finished.

FACILITATING THE USE OF FORTRAN PROGRAMS WITH PARALLEL PROCESSING COMPUTERS. (P. Schneck)

The next (fourth) generation of computers will be designed to manipulate many operands in parallel in order to achieve increases in speed. The great majority of scientific programs in use today, and virtually all programs at GISS are written in the FORTRAN language. In order to efficiently utilize this new computing power it is necessary to indicate explicitly the parts of a program which can be performed in parallel. Because existing programs have no explicit indications of parallel operations, and programming for parallel machines is significantly different from programming for sequential machines, it is advantageous to have a means for detecting parallel operations in standard FORTRAN programs.

P. Schneck has directed his efforts toward the definition and implementation of methods for recognizing parallel operations implicit in standard FORTRAN programs. One result is a new graph-theoretic construct, the quasi-articulation node, which permits a static analysis of a flow graph to yield information previously only available with a dynamic analysis. By using the quasi-articulation node a static analysis of a program flow graph yields information necessary to determine whether iterative calculations can be performed in parallel. This is equivalent to determining whether the iterations are independent, or feedback can occur. The three cases of program construction are shown below:

A: Feedback:

$$\begin{aligned} &= \dots A(I) \dots \\ A(I+1) &= \dots \end{aligned}$$

B: Potential feedback, but no feedback

$$\begin{aligned} A(I+1) &= \dots \\ &= \dots A(I) \dots \end{aligned}$$

C: No feedback, no potential feedback

$$\begin{aligned} &= \dots A(I+1) \dots \\ &= \dots A(I) \dots \\ A(I-1) &= \dots \\ A(I) &= \dots \end{aligned}$$

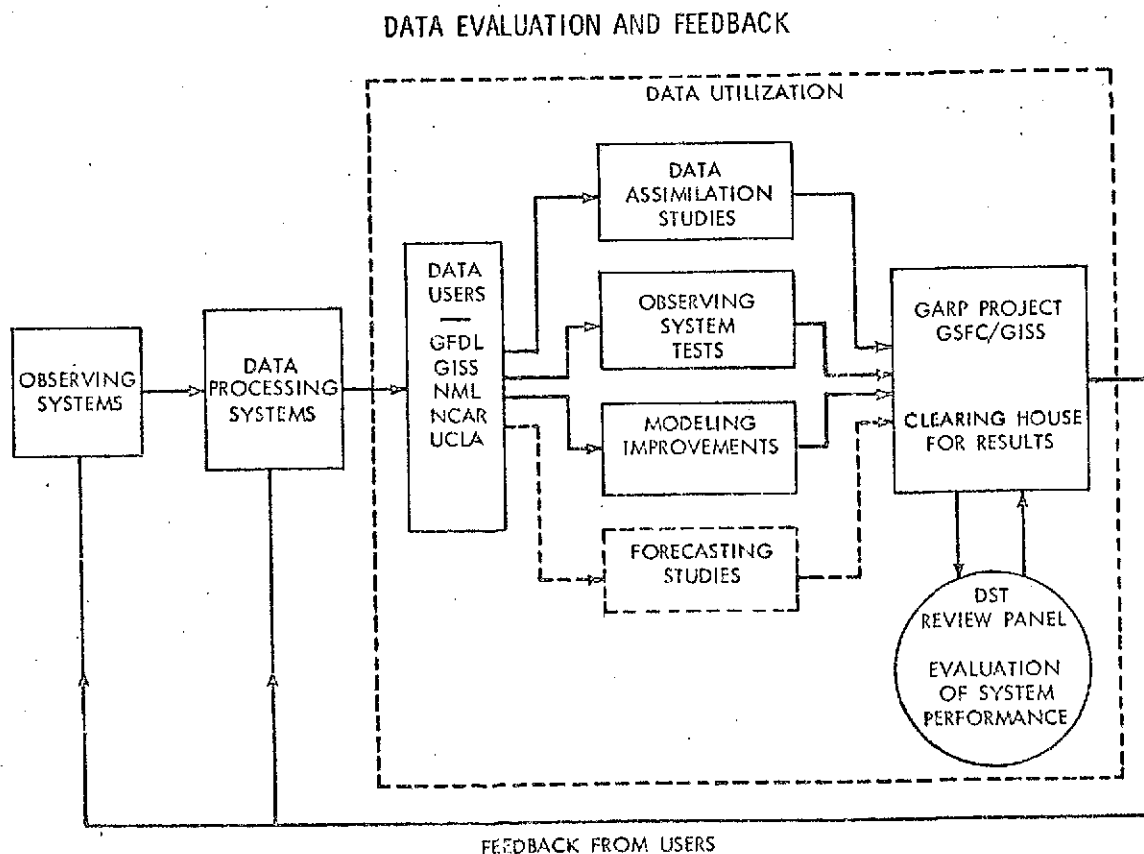
The basic rule concerning detection of feedback may be stated simply. Feedback cannot occur if all subscripts of definitions (left of equal sign) are no greater than any subscript of a use (right of equal sign). If this condition is violated feedback may occur. For each case of potential feedback a second check is made: if the definition back-dominates the use no feedback occurs.

The methods developed at GISS are much simpler to apply than previous methods for detecting parallelism and have already been implemented in a compiler. The compiler accepts a standard FORTRAN program and creates a program in Burroughs extended FORTRAN, detailing parallel operations which may then be used on the ILLIAC-IV computer CDC star or machines with similar parallel processing ability.

PREPARATION OF THE DATA UTILIZATION PLAN IN DST, (R. Jastrow, M. Halem)

The GARP project office at GSFC has assigned to GISS the task of preparing the data utilization plan in DST. During the next two calendar years the implementation of this plan will be the major project at GISS and the greatest part of GISS resources will be dedicated to this program.

The organization of the data utilization plan consists in describing for each of the participating data users (1) provisions for data transfer and data flow, (2) the research activities planned, (3) provisions for data evaluation and feedback, and (4) the schedules and task assignments. Data utilization starts at the point where the data is acquired and converted into meteorological parameters. The chart below shows the role of Data Utilization in the overall DST plan. The enlarged box describes the main elements of the DIU plan. The plan first provides for the establishment of data links for the transfer of the data required by each of the users. Next, the chart shows the specific research activities that are planned by the users. The specific research activities of the users fall into four categories. They are (1) research on data assimilation, (2) observing system tests, (3) model improvements, and (4) testing of forecasting accuracy. Finally, the chart shows the data evaluation functions. The plan provides for the retrieval of the results of the data studies from each of the users and the establishment of a review panel for the evaluation of the systems performance.



The output of the Data Utilization section of the DST is the final step which provides the feedback of the overall system performance to the system designers.

The preparation of the Data Utilization plan will be incorporated into the NASA Data Systems Test Plan. The acceptance of this plan provides the basis for completing the arrangements with the data users, staffing, hardware and software preparations, and establishment of data networks and the initiation of data handling activities.

CLOUD SCATTERING AND ABSORPTION EFFECTS IN THE GISS MODEL,

(J. Hansen, A. Lacis)

An accurate treatment of solar radiation is required for long-range numerical forecasts and for climatological studies. An approximate method has been developed in this project for computing the distribution of absorbed solar radiation throughout the atmosphere as a function of the vertical distributions of water vapor and temperature and cloud amounts. This method is currently used in the multi-level numerical circulation models at GISS. The multiple scattering between different layers of the atmosphere and clouds is fully accounted for by a discrete ordinate method. The integration over frequency is accomplished parametrically by dividing the solar spectrum into two portions: the visible region, in which there is no absorption, and the near-infrared region which is subject to absorption. The optical properties of the clouds in both spectral regions are specified as a function of cloud type based on available atmospheric measurements.

The approximate methods used for the computations of multiple scattering between different layers have been tested against results which are essentially exact (Hansen, 1972). The approximations are accurate to $\sim 10\%$ and the errors can be reduced with an increase in computer time. However, more detailed calculations of the multiple scattering are not warranted until the treatment of related problems in the computations of the heating rates are improved; in particular, the specification of cloud optical properties and the parameterization of the frequency integration have a greater impact on the computed solar heating than do the approximations in the multiple scattering.

The GISS circulation model, like those at NCAR and GFDL, specifies cloud optical properties as a function of cloud type. However, this input data is very poorly known and is a fruitful area for more detailed theoretical work. In particular there is considerable disagreement as to the fraction of solar radiation absorbed within clouds of different types. Lacis and Hansen are working on a method for combining multiple scattering computations with the limited number of available cloud observations to obtain a more reliable specification of optical properties for all cloud types. The basic requirement is a method for rigorously treating gas absorption in the presence of scattering, a problem for which no solution has previously been published. Lacis and Hansen are handling this problem by expressing the variation of the absorption coefficient across absorption bands as a probability distribution, and using this to obtain a distribution function for the single scattering albedo within different cloud types. The absorption

within a cloud then readily follows from standard multiple scattering computations and a summation over all absorption bands. This method is being applied to low level stratus clouds for which measurements of absorption as a function of cloud thickness are available. The computations will be extended to other cloud types for which observations are not available.

DIAGNOSTIC STUDIES OF THE GISS FIVE-LEVEL MODEL. (R. Somerville)

An analysis of the results of the GISS atmospheric circulation models was performed in order to evaluate and improve the models' realism. It is necessary to test proposed changes in the physics subroutines by trial calculations with the entire n-level model. Thus we require sensitive means of determining from such calculations precisely how the model's performance is enhanced or degraded by the changes.

Short- and medium-range forecasts alone, using real atmospheric data for initial conditions and for verification, are insufficient for such purposes, largely because the global atmosphere is observed so poorly that the effects of major model changes may be buried in the observational uncertainty. Also, results from testing model changes by forecasting are invariably clouded by questions of truncation errors, initialization, time-scale, and representativeness. A change may apparently improve one forecast but impair another.

A useful alternative analysis procedure is to compare the model with the atmosphere using averages and other statistical measures rather than instantaneous forecast states. Such comparisons have been made and are given below, using zonal mean data. Both model and observed fields were averaged with respect to longitude over 360 degrees and with respect to time over several weeks and are thus functions of latitude and height only. This procedure is commonly associated with general circulation studies. The goal here is to analyze and improve the model for use in forecasting and in observing system simulation studies.

One run analyzed was a 44-day global 5-level integration with 400 km ("fine") horizontal resolution. The model may be described as following the UCLA 3-level model quite closely in overall design, numerics, and surface physics. However, the Katayama radiation routines of the UCLA model have been replaced by those of J. Hansen and J. Hogan, the moist convection parameterization is the strapping of the 5 levels into 3 and the application of the UCLA Arakawa scheme, and the model top is at 100 mb. The physics of the model is recomputed every half hour.

The initial state, derived from a 2-level run, displays a number of unrealistic features, including large oscillations over Antarctica. These features decay with time, however, and so the analysis was performed for approximately the last half of the run, which should not be markedly affected by the initial state. The run was begun on February 1, with the analysis period taken from February 21 to March 16.

Three fields that are perhaps most fundamental are discussed in this report. These are zonal wind (u), temperature (T), and mixing ratio (q). For each of these model fields a zonal mean (pressure vs. latitude) plot is shown, together with two such plots from observed atmospheric data. In each pair of observed data plots, the upper figure is from Lorenz's monograph, and the lower is from Newell et.al., in The Global Circulation of the Atmosphere, AMS, Boston, pp. 42-90 (1969). All of the observations presented are for northern hemisphere winter.

Two different estimates of the observed atmosphere are shown, so as to give an indication of the observational uncertainty. In comparing the observed figures with each other and with the model figures, it should be kept in mind that in the different plots the tops and bottoms are at various pressure levels, some plots are linear in latitude and some cosinusoidal, some are linear in pressure and some logarithmic, and north is to the right in some figures and to the left in others. The aim is to discern the respects in which the model and real atmospheres differ, to diagnose the causes by pinpointing the relevant weak areas of the model physics, and to device and test alternative physics.

Figures 1 through 3 show model and observed fields of the zonal mean of the zonal component of wind (u) in meters per second. Positive values indicate a wind from west to east.

The simulation is realistic in that both the model and the observed fields are dominated by the prevailing westerlies in middle latitudes. The positions of the jet maxima in the model are quite accurate. However, the magnitudes are about twice the observed value. This is the most serious unrealistic feature. Also, the fact that the model top is at 100 mb may be responsible for the height of the maximum. In the real atmosphere in winter, the eastward component

of zonal wind increases with height at all latitudes from the surface to about 200 mb, and then decreases from 200 mb to above 100 mb except at high latitudes. The GISS model's top is too low, and the model does not show this feature.

The tropical easterlies aloft are present but too strong, and the surface trades are too weak. The polar circulations are poorly defined. The oscillations over Antarctica, which are exaggerated by the linear abscissa, may be partially remnants of the initial state and partially due to imperfections in the conversion from sigma to pressure coordinates over high terrain.

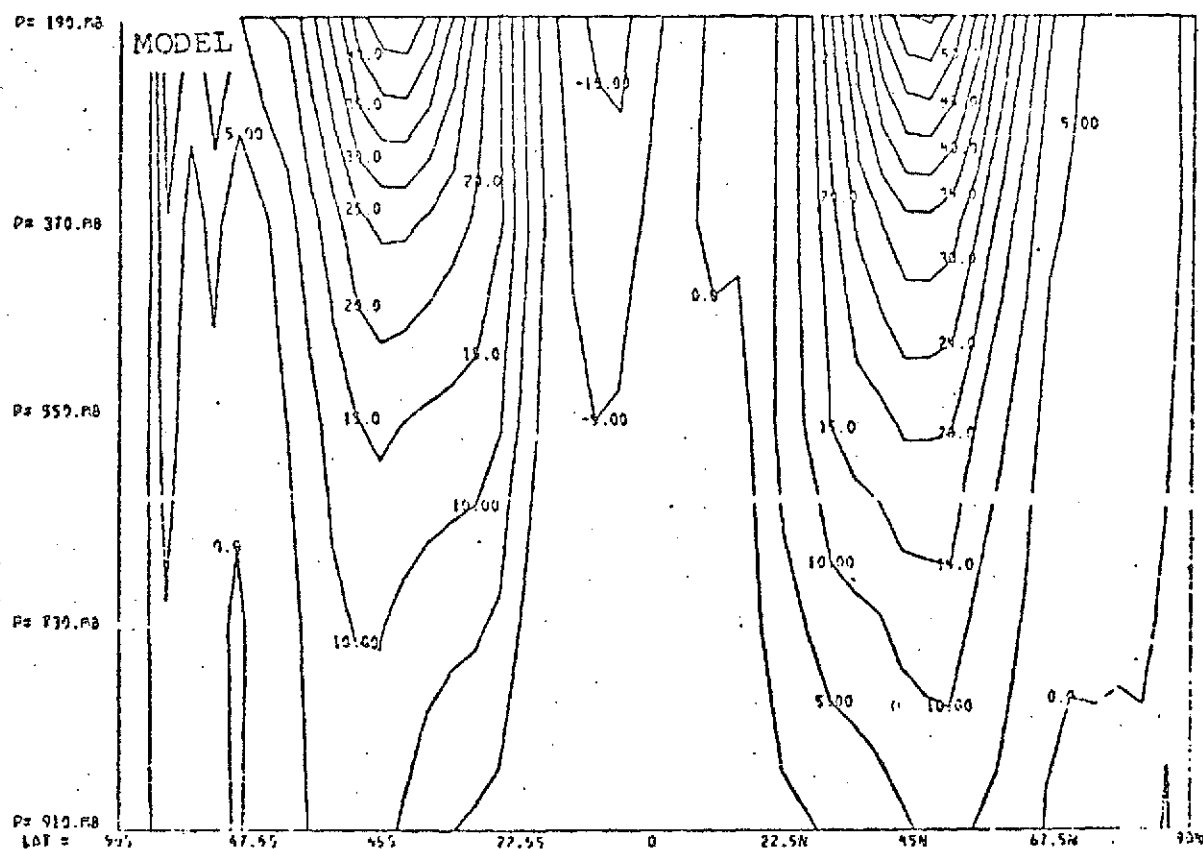


Figure 1. Model field of zonal mean wind component in meters per second.

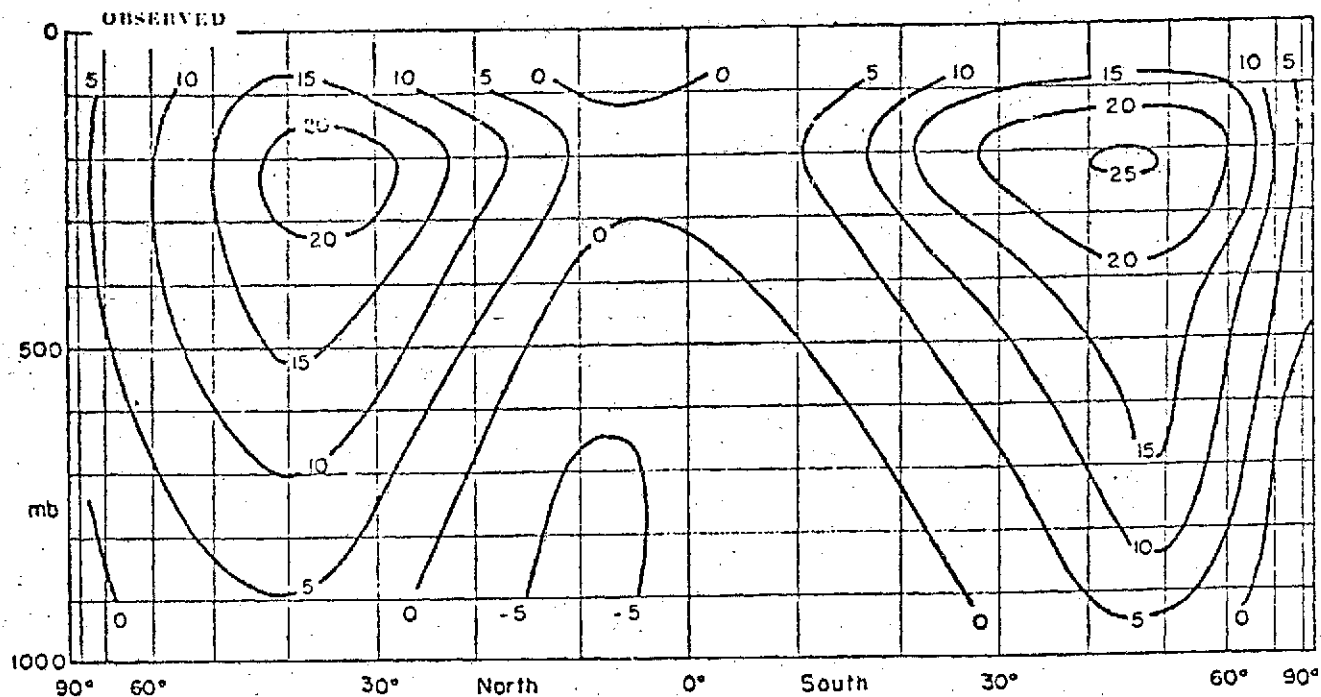


Figure 2. *Observed field of zonal mean wind component in meters per second.*

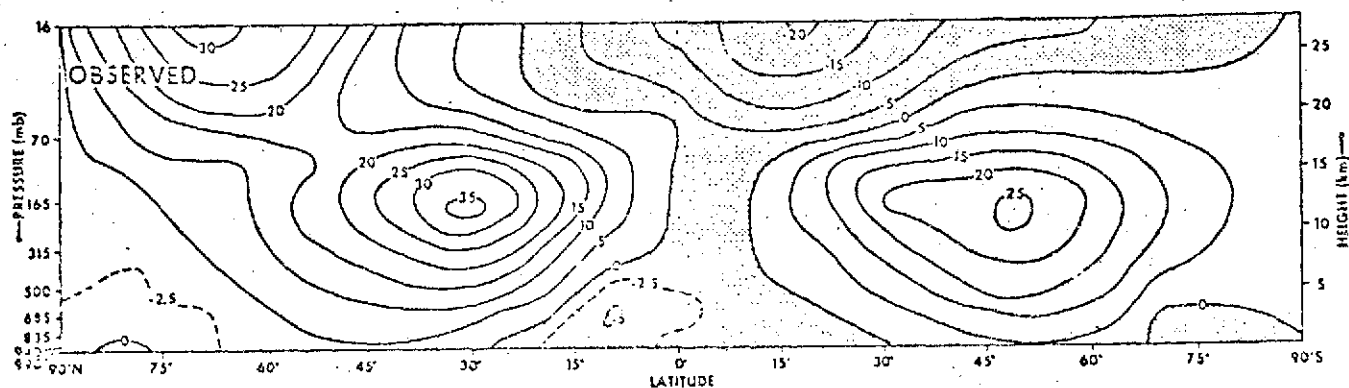


Figure 3. *Observed field of zonal mean wind component.*

As with the zonal wind, the grossest features of the temperature field are well simulated (Figures 4 through 6). Temperature generally decreases upward and poleward. However, there are unrealistic quantitative features. The most obvious is that the high tropical troposphere is about 30 degrees too hot. Thus the static stability is about twice as large as it should be in the upper troposphere.

There is no evidence of a tropopause, which is not surprising on a zonal mean plot. There is also no evidence of a stratosphere, which may be due to the low top and lack of crucial stratospheric physics such as ozone absorption.

Unrealistic features of the zonal wind and the temperature fields are related in obvious ways. The non-tropical free atmosphere is nearly geostrophic, and the tropospheric increase of zonal wind with height is the geostrophic consequence of a decrease in temperature from equator to pole (the thermal wind relationship). Similarly, the failure of the model wind to decrease with altitude above 200 mb is the geostrophic equivalent of the failure of the model temperature to increase poleward at these heights.

Additionally, it may be noted that the surface temperature is well-simulated, which is to be expected, because most of the surface is sea, on which temperature is fixed. The high troposphere over the summer pole is much too cold. Finally, the high-latitude, low-level inversion in the winter hemisphere is absent.

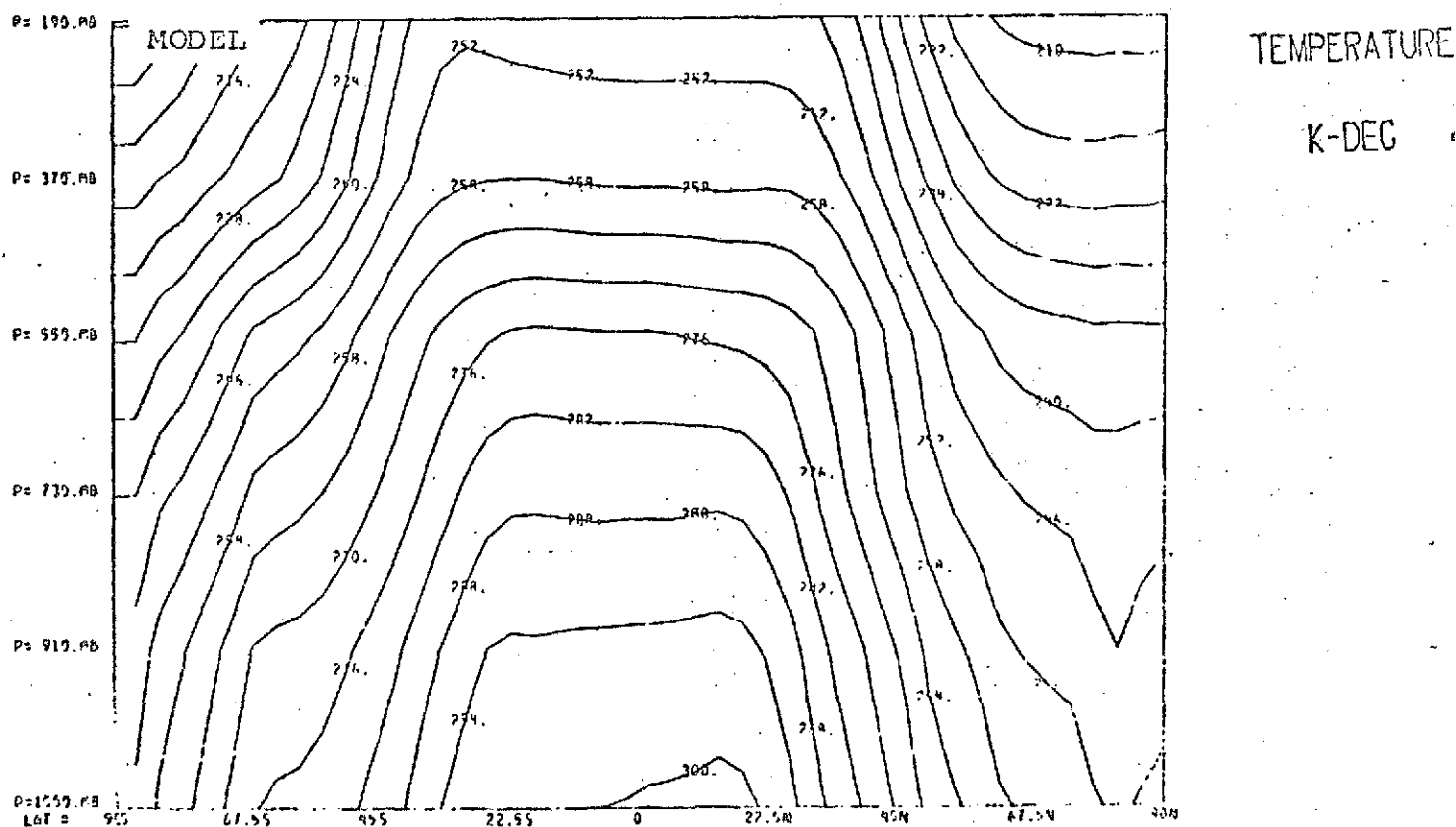


Figure 4. Model temperature field in degrees K.

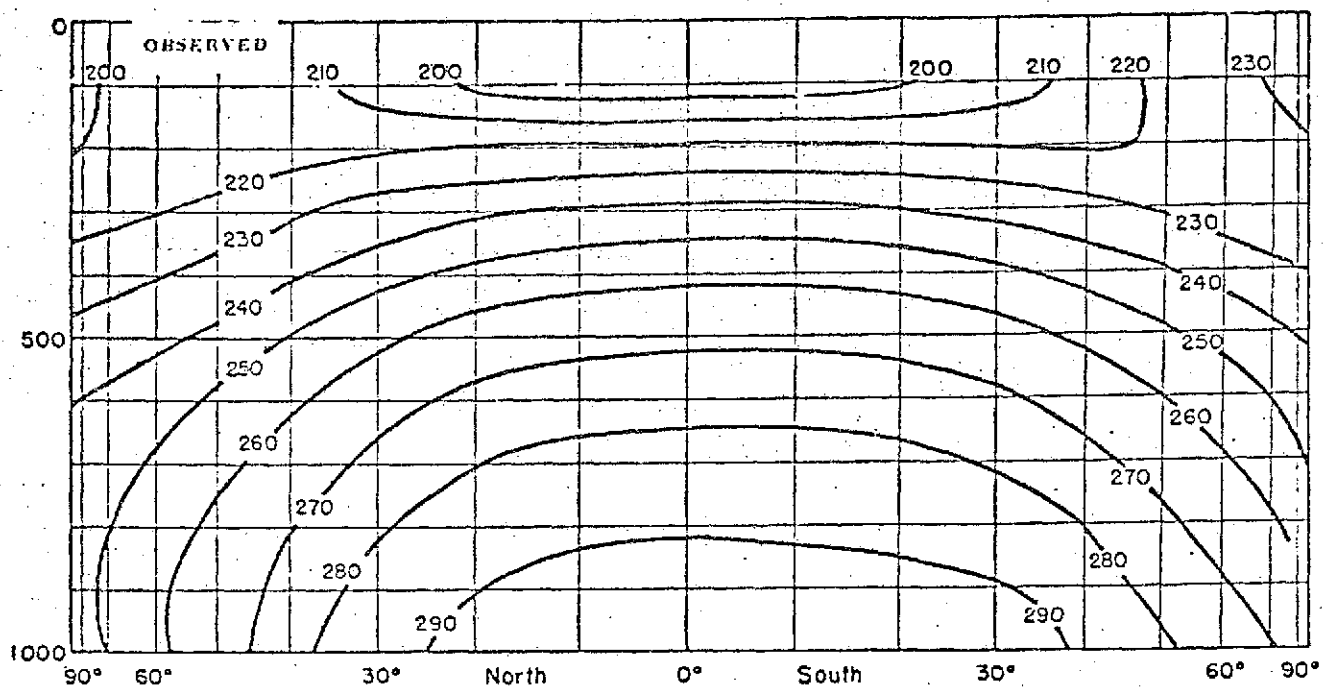


Figure 5. *Observed temperature field in degrees K.*

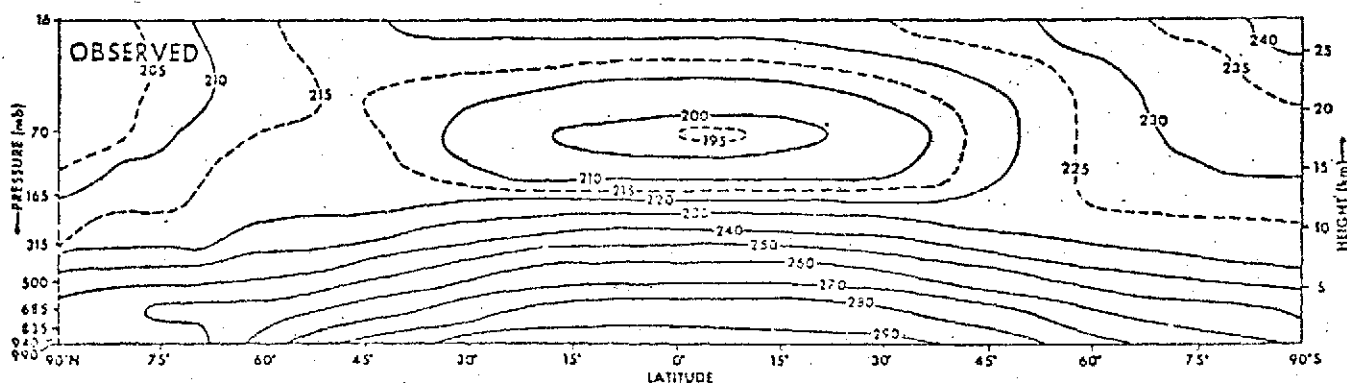


Figure 6. *Observed temperature field.*

In Figures 7 through 9, the moisture field is displayed as mixing ratio, the mass of water vapor per unit mass of dry air, expressed in grams per kilogram. No good observational data exist for the southern hemisphere. For purposes of the present comparisons with real data, mixing ratio and specific humidity are regarded as the same.

Since the saturation specific humidity is a strong function of temperature, the moisture field may be regarded as determined to a good approximation by the temperature field. Thus it is not surprising that the GISS model atmosphere is too wet as well as too hot. The upper tropical troposphere is perhaps four times too moist, and the model is generally too moist at all elevations and latitudes.

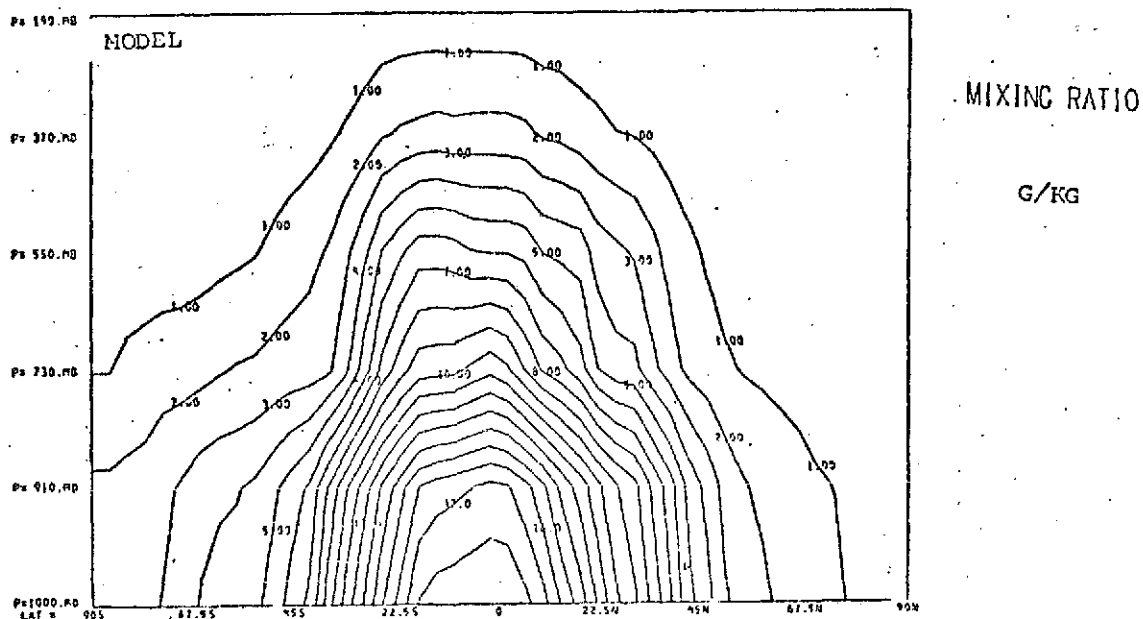


Figure 7. Model moisture field as mixing ratio: grams per kilogram.

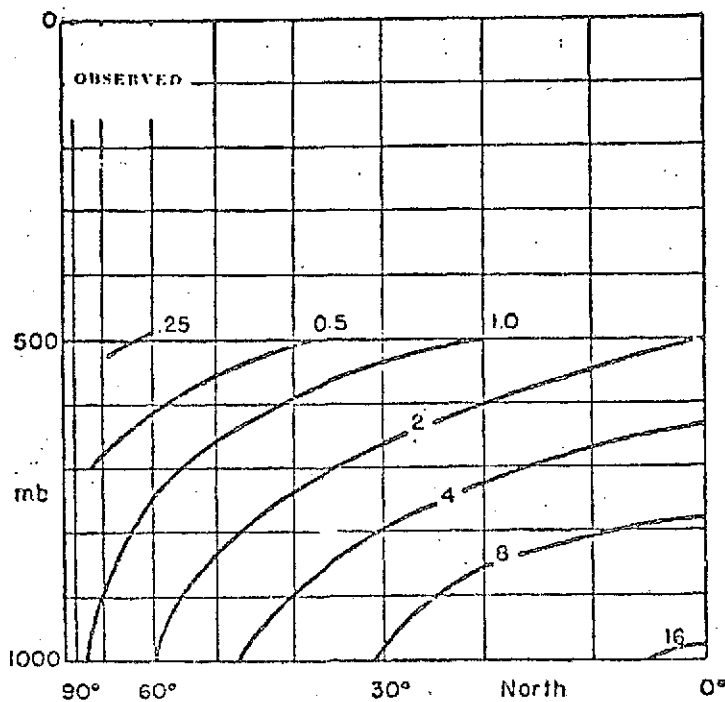


Figure 8. Observed moisture field (grams per kilogram).

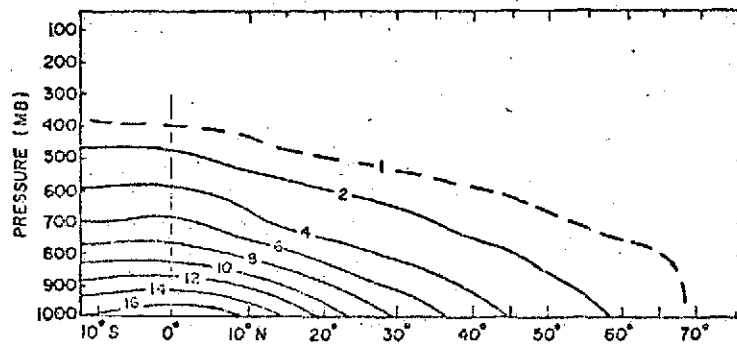


Figure 9. *Observed moisture field (grams per kilogram).*

In summary, the GISS model atmosphere bears a strong qualitative resemblance to the real one, but is too fast, too hot, and too moist. The discrepancies are larger than observational uncertainties.

At present, additional diagnostic studies are being carried out to determine the specific causes of the model's failings, and changes in several areas of the physics are being planned which will bring the calculated and real atmospheric states into better accord. Many of the unrealistic features of this early version of the GISS model have been eliminated in the most recent versions.

EFFECTS OF CLOUD DISTRIBUTION IN NUMERICAL MODELING. (L. Druyan)

A serious deficiency of current circulation models is their inability to accurately forecast cloud distribution. This defect leads to serious errors in the radiative budget calculations, and subsequently affect the computed temperature distribution and circulation patterns. A series of experiments were conducted with the UCLA two-layer model to investigate its sensitivity to the amounts and distribution of cloud cover.

The model presently computes percentage of cloud cover proportional to the relative humidity only when convective instability is present. Otherwise, super-saturation implies total cloud cover and under saturation implies clear skies. The experiments consist of the following alternative specifications of cloudiness:

1. Whenever the UCLA version makes no clouds, use the following empirical formula: $CL = -1.3 + 1.8 RH3$, $0 \leq CL \leq 5$; CL is percent of cloudiness; RH3 is relative humidity in lower level
2. Substitute climatological cloud distribution
3. Allow all radiation calculations to assume no cloud cover anywhere
4. Allow all radiation calculations to assume 100% cloud cover everywhere; refer to this as overcast

The cloud type used for the experiments is half a layer thick with the cloud tops at the interface between the upper and lower layers. (≈ 600 mb)

The discussion below summarizes the results of the experiments in terms of the cloud distribution resulting from the control and experiments (1) and (2), the effects of the different parameterizations on the temperature distribution and the effects on the circulation.

Cloud distribution (based on 15 day averages). The cloudiness generated by the control shows a deficiency when compared to the climatological distribution. This deficiency is about 10% in the zone of maximum cloudiness ($50^\circ - 60^\circ N$) and is 25% too low at $80^\circ N$ and 35% too low just north of the equator.

The cloudiness generated by the empirical formulation of experiment (1) increased the control cloudiness (only north of 40°N) to the climatological values between $40^{\circ} - 60^{\circ}\text{N}$, but it was still 10% too low from $60^{\circ} - 90^{\circ}$.

Examination of the grid by grid distributions of the 15 day average of cloud cover shows that the cloudiness generated in experiment (1) enlarged the areas of high % cloudiness that were computed in the control (the formulation calls for cloudiness based on the relative humidity only where it isn't computed in the control). The climatological distribution covers more grid points yet with high % cloud cover (especially in the equatorial region) but has fewer grid points with as much as 80% cloud cover than does the control. Thus, the control makes a high enough % coverage when it makes clouds, but it makes clouds at too few grid points. In this respect the cloudiness based on the relative humidity formula of experiment (1) goes part of the way toward correcting the cloud deficiency.

It is interesting to note that, in addition to the equatorial zone there are two other large geographic areas in which a high climatological cloud cover is not matched by either the control or that of experiment (1). One area covers the whole of the United States and the other area is over southern Europe and the Mediterranean Sea. The model, however, shows some high values of cloudiness north of Europe (at about $75^{\circ} - 80^{\circ}\text{N}$) where climatology does not.

Reasons for the above may be due only to the particular patterns, cyclone tracks, etc., generated by the model for the particular 14 day experiment that was used, or they may lie in some fundamental shortcoming of the modeling that is suppressing the cloud making mechanisms.

Temperature Distribution. Clouds are used by the model to compute the radiation budget. This in turn determines, in part, the temperature distribution. The forecast state after 13 days of integration was used to compare the results of the different experiments.

UPPER LAYER. A definite trend can be seen by looking at the zonal averages of T_1 in each run. These temperatures decrease at all latitudes when cloudiness is increased. The cloud tops replace the earth's surface as the source of long wave radiation and, because they are cold, they supply less long wave energy to the upper layer.

LOWER LAYER. In the northern latitudes, the effect of the clouds on temperature is the reverse of the upper layer response. The "atmospheres" in which the cloudiness was increased are warmer in this layer and for the control and no cloud runs the lower layer is colder and coldest respectively. Although the extra clouds reflect much of the comparatively small amount of solar energy incident during

the high latitude winter, they also absorb more of the non-reflected solar energy than does clear air; also they reduce the upward flux of long wave radiation by absorbing the ground emitted flux and they reradiate at their lower temperature both upward and downward. (The spread between T3 (zonal average) for the no cloud vs. the overcast runs is about 4.5°C at 58°N .)

The competition between warming due to cloud absorption and greenhouse effect and cooling due to reflection from high albedo clouds depends on latitude. South of 45°N the lower layer of the no cloud atmosphere becomes warmer than the control and overcast atmospheres and in the tropics it is the warmest of all, although only about 0.5°C warmer than the control which is the coldest. The climatological-cloud atmosphere is, surprisingly, the same temperature as the cloudless atmosphere in the lower layer between 20°N - 45°N despite a difference of some 40% cloud cover. The temperature of the lower layer of the overcast atmosphere runs closer to the control temperature for these latitudes.

The temperatures of the lower layer are affected by the advective processes to the largest degree in mid-latitudes and thus there is no trend of cloudiness vs. temperature (T3) south of 45°N . In the tropics, there is only a weak tendency for the cloudless atmosphere to warm more — the overcast tropics were warmer than the partly cloudy, control atmosphere there.

The fact that the effect is greater in the north leads to different meridional temperature gradients which in turn affect the pressure distribution and thus the circulation.

Circulation: The zonal wind. UPPER LEVEL.

The upper layer zonal averages of the zonal wind show that the circulation above the overcast earth attains its peak speed at a lower latitude (34°N) than does the control (40°N) the climate cloud (42°N) or the no cloud (45°N).

LOWER LEVEL. The southward displacement of the peak zonal winds is also apparent for the circulation below the overcast. The smaller north-south temperature gradient in the overcast lower layer leads to lower zonal wind speeds north of 37°N than for the other atmospheres. ($\bar{U}_3 \text{ CONTROL} - \bar{U}_3 \text{OVCAST}$) is 6.5 m/sec at 45°N and -5.0 m/sec at 30°N where the bars refer to zonal averaged values of the lower level zonal wind.

Synoptic Results:

1. Sea - level pressure analysis

AFTER FIVE DAYS INTEGRATION

The charts for the control and the no cloud runs respectively are quite similar. The positions of the major pressure systems are identical in the maps resulting from all of the experiments. Pressure minima are not as low in the overcast forecast as they are in the other experiments and there is evidence of less zonal flow with more closed isobars and deeper troughs in this map. The same tendency appears in the results based on climatological clouds but to a lesser extent.

AFTER 14 DAYS

The only charts that still show some resemblance are those of the control and experiment (1); their differences are surprisingly minor. Strong zonal winds over the Pacific forecast by the no cloud version have been replaced by strong meridional winds in the chart of the overcast atmosphere probably reflecting the diverging values of the north - south gradient resulting from the two runs as discussed above. See the accompanying figures.

The deep Aleutian low on the control is slightly shallowed and displaced southwestward on the climate cloud maps. A well organized low over Labrador on the former has been split into two centers, one of them over Labrador and the other south of Newfoundland on the latter chart. Instead of the massive high pressure system evident off the California coast on the control, the climate cloud forecast indicates a rather compact high center over Vancouver and a weak low center due east of Los Angeles, possibly spawned by a wave from the Aleutian low. A second pressure maximum located over the mid-Atlantic states in the control prognostic has been replaced by a weak ridge extending south-eastward from the northern plain states to the vicinity of Bermuda. A weak low in the control is indicated over North Dakota and is possibly the same disturbance which appears about 1000 km northwest of that position on the map generated by assuming the climatological cloud distribution.

2. 500 mb geopotential analysis

AFTER 5 DAYS

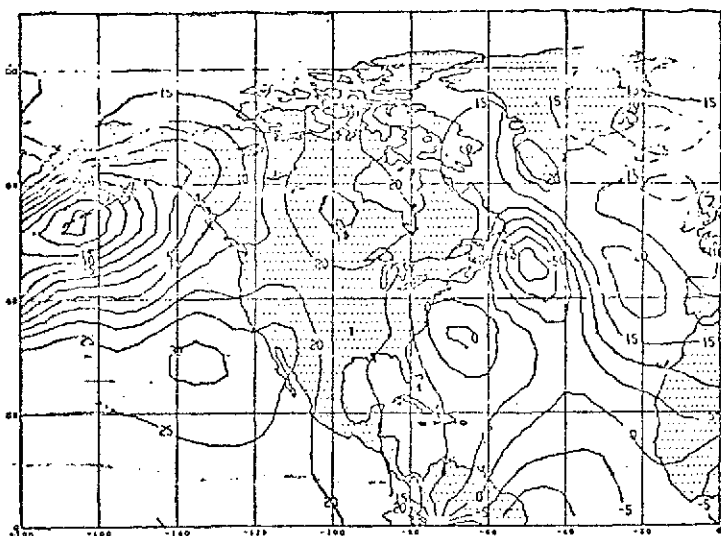
The positions of the three troughs are the same for all of the versions except for a very slight lagging of the Pacific trough in the overcast prognostic. The mid-Atlantic trough is deeper and sharper in the climatology and the overcast than it is in the other results. The trough over the upper Mississippi Valley is similar on the control, RH and climate cloud charts, is deeper on the overcast and shallower on the cloud charts. There are few differences in gradient between any of the charts.

AFTER 14 DAYS

The 500 mb analysis for the integration of experiment (2) was not available. The forecasts for experiment (1) and the control forecast

were quite similar. As was the case at sea level, the overcast atmosphere produces a highly perturbed flow with large amplitude waves and the no cloud situation results in a highly zonal flow as compared with the control forecast. See the accompanying figures.

The results show that the 15 day zonal means of the temperature are quite sensitive to cloudiness distribution. Even the most extreme differences in cloudiness (overcast versus clear skies) affects the circulation only to a minor degree after 5 days, but to a very significant extent after 14 days.

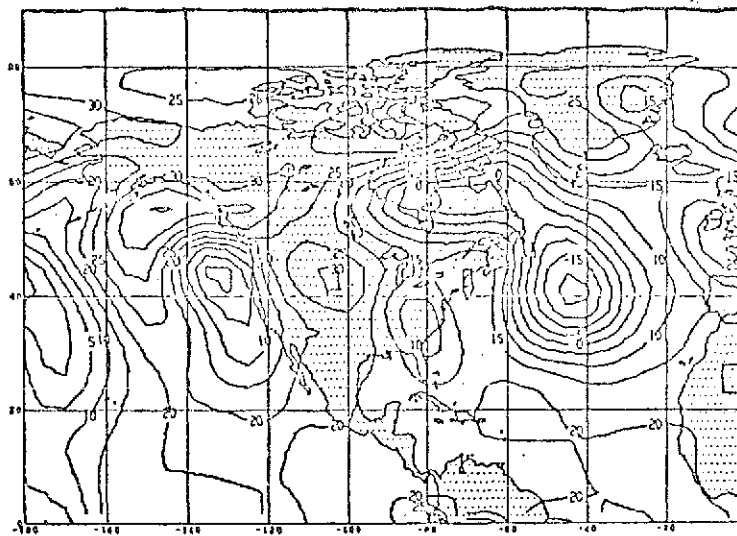


DAY 109

HOUR 0.0

VALUES RANGE BETWEEN -35.00 AND 109.55
FOR CONTOUR INTERVALS OF 5.0

Figure 1a. Smoothed values of sea level pressure, no cloud atmosphere.

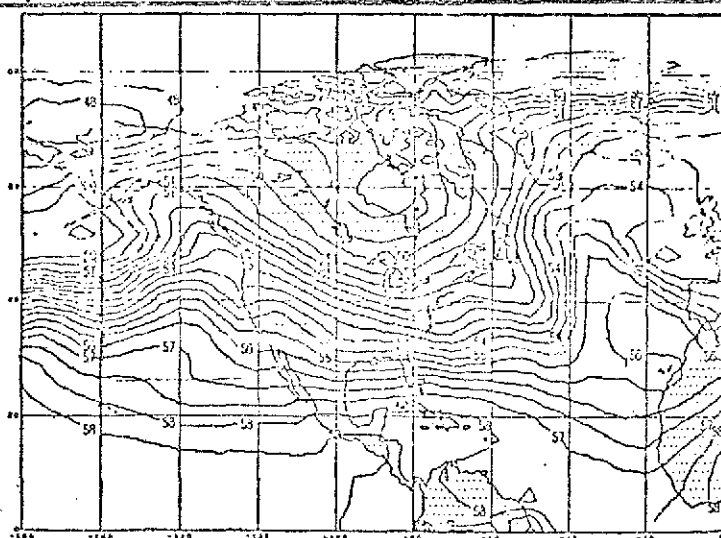


DAY 109

HOUR 0.0

VALUES RANGE BETWEEN -35.00 AND 112.01
FOR CONTOUR INTERVALS OF 5.0

Figure 1b. Smoothed values of sea level pressure, overcast atmosphere.

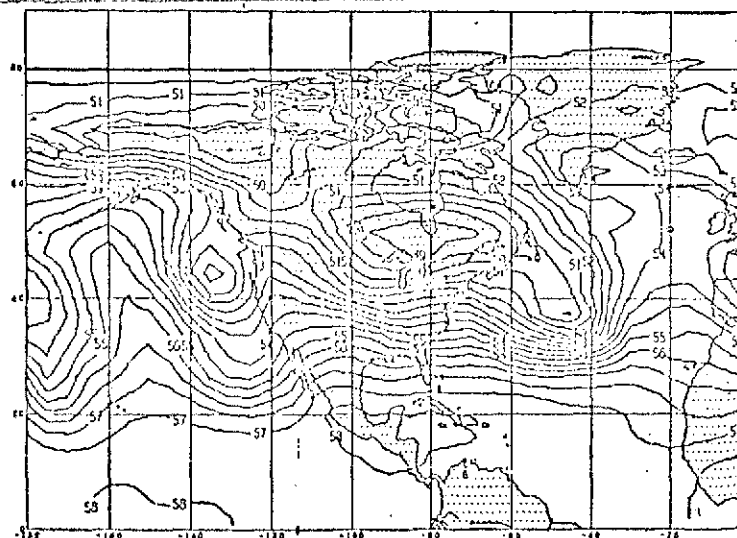


DAY 109

HOUR 0.0

VALUES RANGE BETWEEN -0.50 AND 65.49
FOR CONTOUR INTERVALS OF 0.5

Figure 2a. Unsmoothed 500 mb values of geopotential height surface, no cloud atmosphere.



DAY 109

HOUR 0.0

VALUES RANGE BETWEEN -0.50 AND 66.02
FOR CONTOUR INTERVALS OF 0.5

Figure 2b. Unsmoothed 500 mb values of geopotential height surface, overcast atmosphere.

ALTERNATIVE PARAMETERIZATION OF MOIST CONVECTION, (L. Druyan, R. Somerville)

The UCLA two-level general circulation model computes precipitation by removing the excess moisture from the supersaturated lower layer and also by parameterizing the small-scale convective activity wherever static instability is computed. Since the release of latent heat from condensation is of crucial importance in the atmospheric energy budget, a realistic parameterization of this process is required in circulation models.

In order to determine whether an alternative formulation would substantially modify the evolution of the model atmosphere, a more direct parameterization of the condensation - convection process was devised whereby superadiabatic air columns are immediately stabilized, as are conditionally unstable moist ones. An iteration is performed until the resulting column has at least a neutral lapse rate with respect to the appropriate (moist or dry) adiabatic lapse rate and a relative humidity no greater than a pre-assigned value, tentatively chosen as 80%. Initial tests have been performed using the two-level UCLA model, but the scheme readily generalizes to n-levels.

In the following discussion "M-A" refers to the precipitation-stabilization formulation used in the UCLA two-layer model; "D-S" will refer to the substituted formulation based on a moist convective adjustment.

Circulation patterns (sea-level and 500 mb) were computed and plotted for two ten-day runs initialized with DAY 92 of an M-A history, using both the M-A and D-S formulations.

After the first 24 hours, slight differences are evident on the sea-level chart. Low pressure centers along the latitudes 50° S - 65° S have become deeper in the D-S evolution than in the M-A.

There are differences also within the equatorial belt. A weak low over Brazil is maintained by M-A, but is dissipated by D-S. M-A creates a new weak low over Indonesia whereas D-S does not. In the North Atlantic, a low maintained at the same central pressure by D-S is deepened by M-A. Several highs along the 40° N latitude are maintained at higher central pressures by M-A than by D-S.

The locations of the pressure systems are unchanged. A closed 500 mb high cell over central Africa is weakened by D-S but maintained by M-A. A similar feature is dissipated by D-S over the Southwestern North Pacific Ocean although it is maintained by M-A. Other features of the 500 mb charts are alike.

After four days' integration, the D-S sea-level chart shows more activity in the southern hemisphere than does the M-A. Lows are deeper near 60S latitude on the D-S chart and some appear over South America and Africa that are entirely absent on the M-A chart. The differences in the northern hemisphere are more slight. The positions of major pressure systems are still comparable.

High cells over equatorial regions on the 500 mb chart are still absent from the D-S.

Sea-level pressure charts for the tenth day are shown in Figures 1 and 2. After the tenth day of integration, the greater cyclonic activity produced by D-S in the equatorial belt is immediately apparent. Low centers are deeper and more intense along the 60S latitude belt in the D-S results. The subtropical highs in the southern hemisphere are stronger in the D-S than in the M-A, but the reverse is true in the northern hemisphere. Also, in the northern hemisphere, the M-A version shows the larger pressure gradients of the two, whereas the reverse is true in the southern hemisphere. A comparison of the positions of the major pressure systems now indicates that the M-A has moved the features at a slightly faster east-west rate than the D-S.

Gradients at 500 mb are generally weaker for D-S. Contours on the D-S charts are displaced equatorward as compared with M-A, indicating a lower 500 mb surface for the former, and thus a colder atmosphere.

The accompanying plots of the global average of specific humidity (Figures 3 and 4) and of precipitation (Figures 5 and 6) vs. time show that, even at the end of the ten days of integration, the D-S version of the hydrological cycle was still in transition between the initial state it had inherited from the M-A history tape and a new equilibrium state. A longer history of the D-S will be generated.

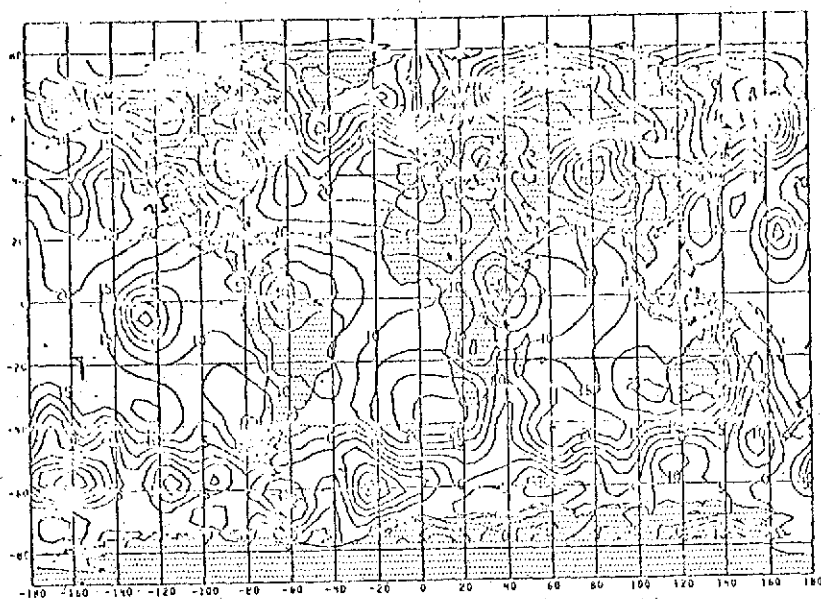


Figure 1. Smoothed
sea level pressure
values for the tenth
day (D-S).

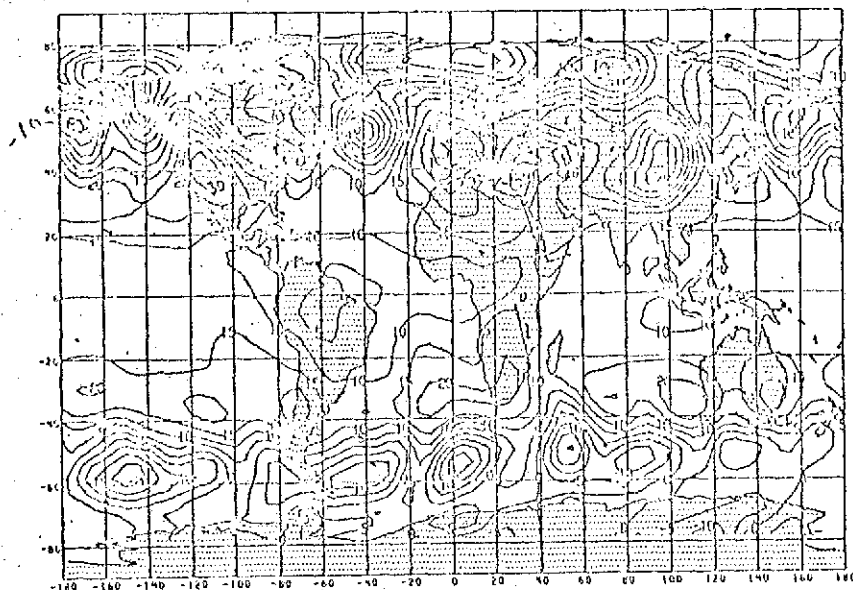


Figure 2. Smoothed
sea level pressure
values for the tenth
day (M-A).

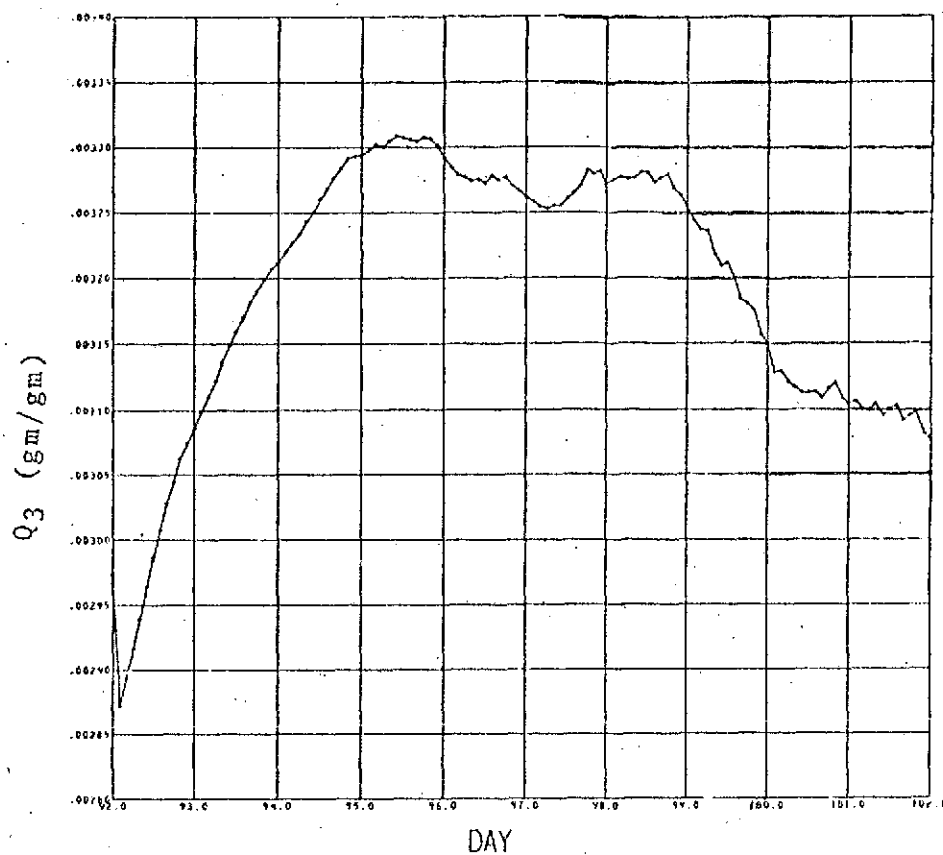


Figure 3. D-S
Model plot of global
average of specific
humidity.

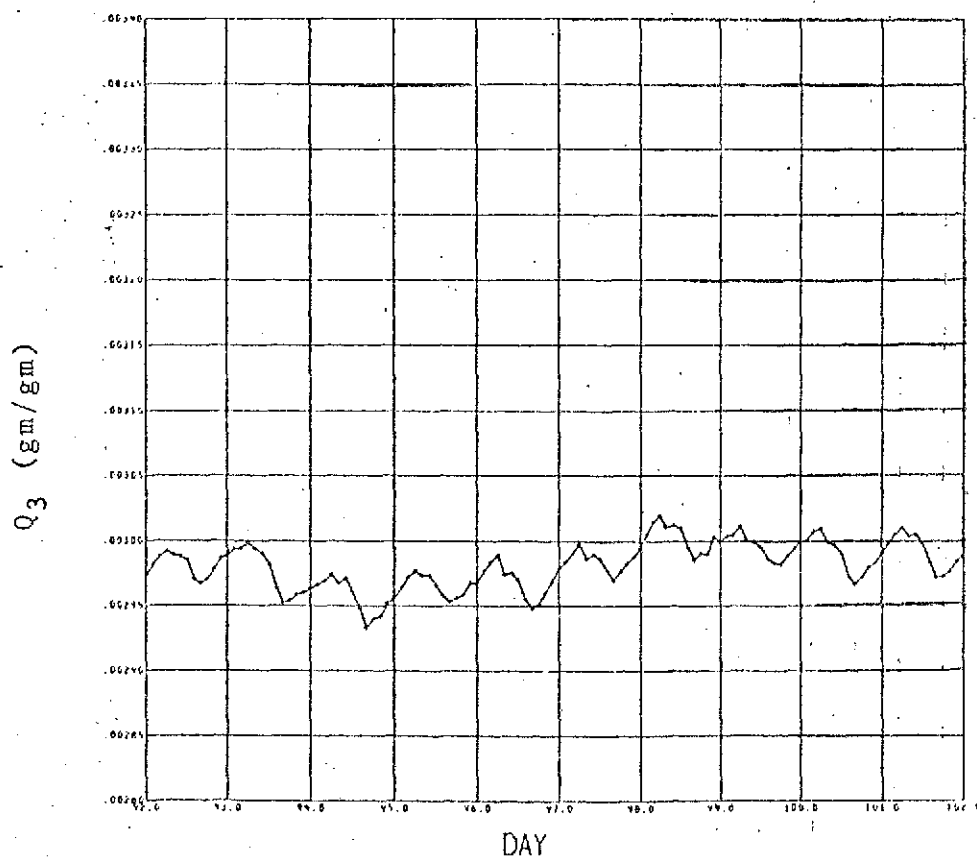


Figure 4. M-A Model
plot of global average
of specific humidity.

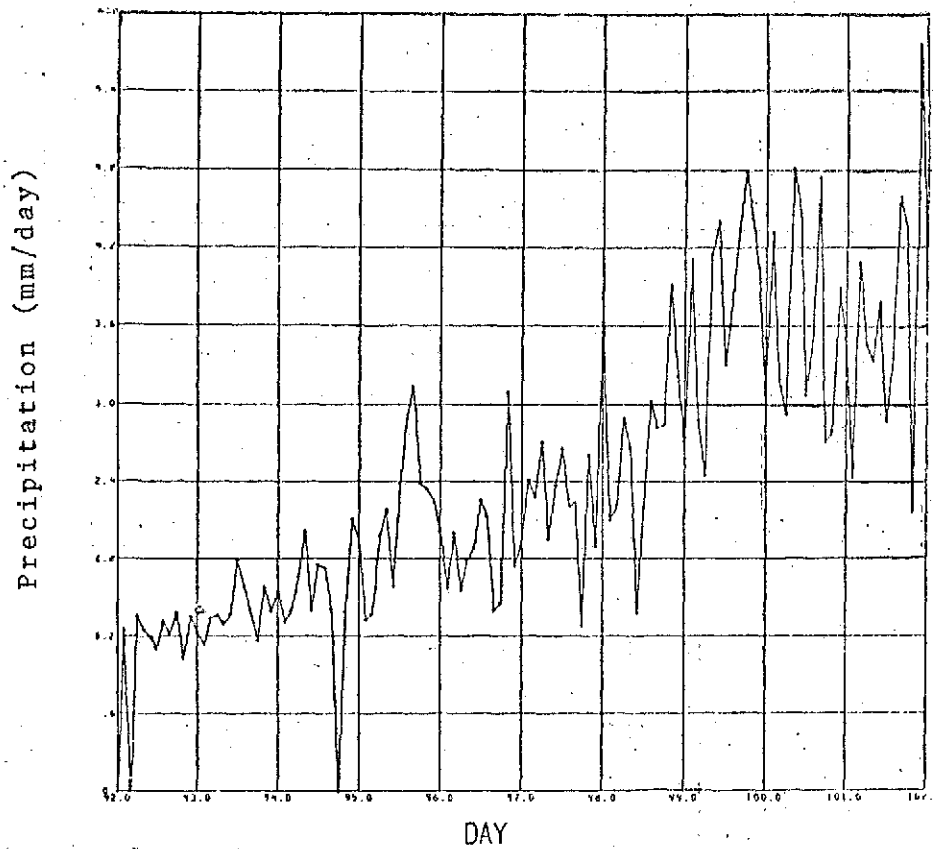


Figure 5. D-S Model
plot of global average
of precipitation.

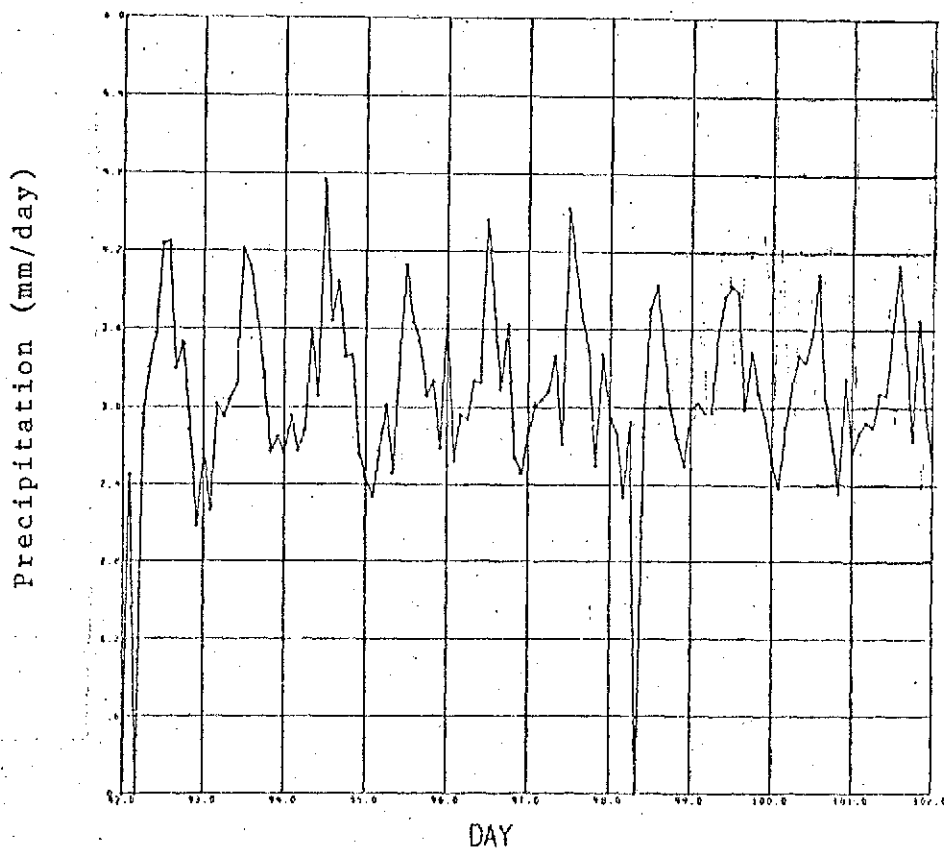


Figure 6. M-A Model
plot of global average
of precipitation.

PRELIMINARY STUDIES ON LONG-RANGE FORECASTS. (L. Druyan, M. Halem, R. Jastrow)

Investigations have been started on the application of satellite temperature measurements for long-range forecasts extending over periods of 15 days and longer. Such forecasts have been one of the principal objectives of GARP from the start of the GARP planning. The program for studying the use of satellite data in long-range and seasonal forecasts will be a major activity in the GISS program in the next two years, and may become the largest single program starting in 1975. Plans are in progress to develop a coupled ocean-atmosphere model for use in this program.

Theoretical studies by numerous investigators, as well as semi-empirical studies by Lorenz, have shown that with any currently realistic observing system, the useful range of forecasts is less than a week and essentially no information remains in the forecast after two weeks or more. However, if the predictions are averaged over space and time, useful information should come back into the predictions; that is, predictions of local weather at a given moment 15 days in advance will not be possible with present or planned observing systems; but a prediction of the mean temperature or precipitation for, say, the southern New England states averaged over a 3-day or 5-day period two weeks in advance, may be possible. This question relates to the statistical behavior of the atmosphere over extended periods of time.

As an initial experiment, 15-day and 30-day simulated forecasts were carried out for an ensemble of starting conditions, all representing the same initial data but with 1 degree random errors in the temperature field. The results for temperature and precipitation were averaged over an area representing the northeastern United States and also averaged over various periods of time at the end of the forecast run. The time averages were centered about 15 days and 30 days, respectively, in the two sets of experiments, and extended over intervals of 1, 2, 3, 4 and 5 days for the 15-day run, and 2, 4, 6, 8 and 10 days for the 30-day run.

In these preliminary experiments, 8 cases were run for the 15-day and the 30-day cases, respectively. Forecasts were generated from starting conditions which were the same in each case except for initial random errors in the temperature field lying within the same 1 degree error limits, and similarly for the 30-day runs.

The graphs below show the spread in the predicted mean surface temperature and rainfall among the 8 cases, plotted as a function of the time span over which the average was taken.

As expected, the spread is greatest when the time span is a day or less, and diminishes considerably for the maximum time span considered. These spreads represent the uncertainty in the forecasts corresponding to the errors in the initial conditions yielded by the observing system. For the longest time spans considered, the spread in temperature, for example, would represent a useful degree of accuracy.

The spread of surface temperature about the mean for the eight case in Figure 1 is less than 2° . In addition, 70% of the cases fall within 1° i.e., the standard deviation $\sigma \sim 1$. Analysis of the surface temperatures for the past seven years over a comparable region in the Northeast for the same month show a standard deviation of $\sigma \sim 3$.

Figure 2 shows the effect of 30 day forecasts with averages over longer time spans. For example, all cases lie within 1 degree for eight day averages and all lie within .5 degrees for a 10 day averaged centered about day 30.

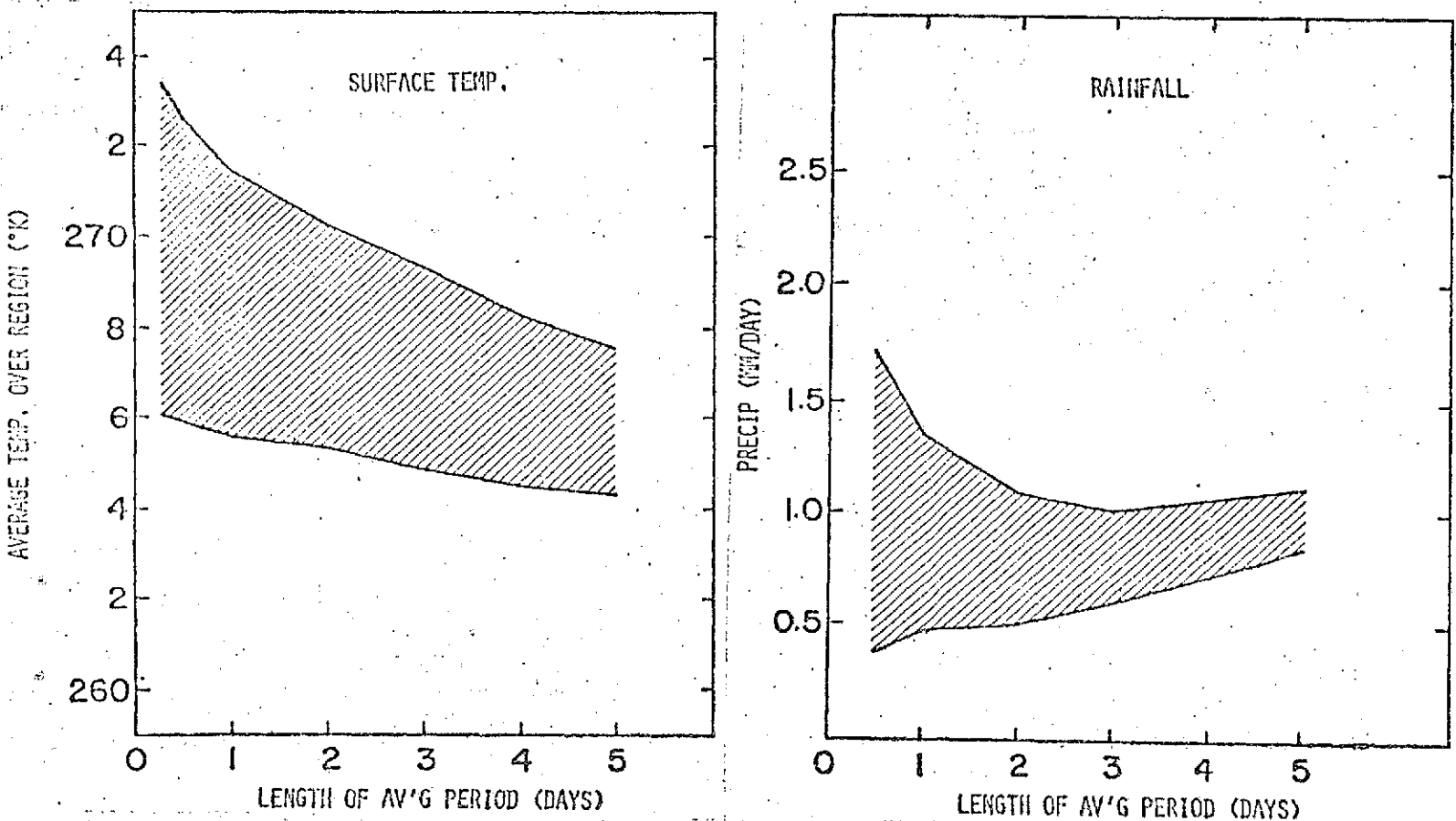


Figure 1. Surface temperature and rainfall 15 day forecasts for Northeast U.S.

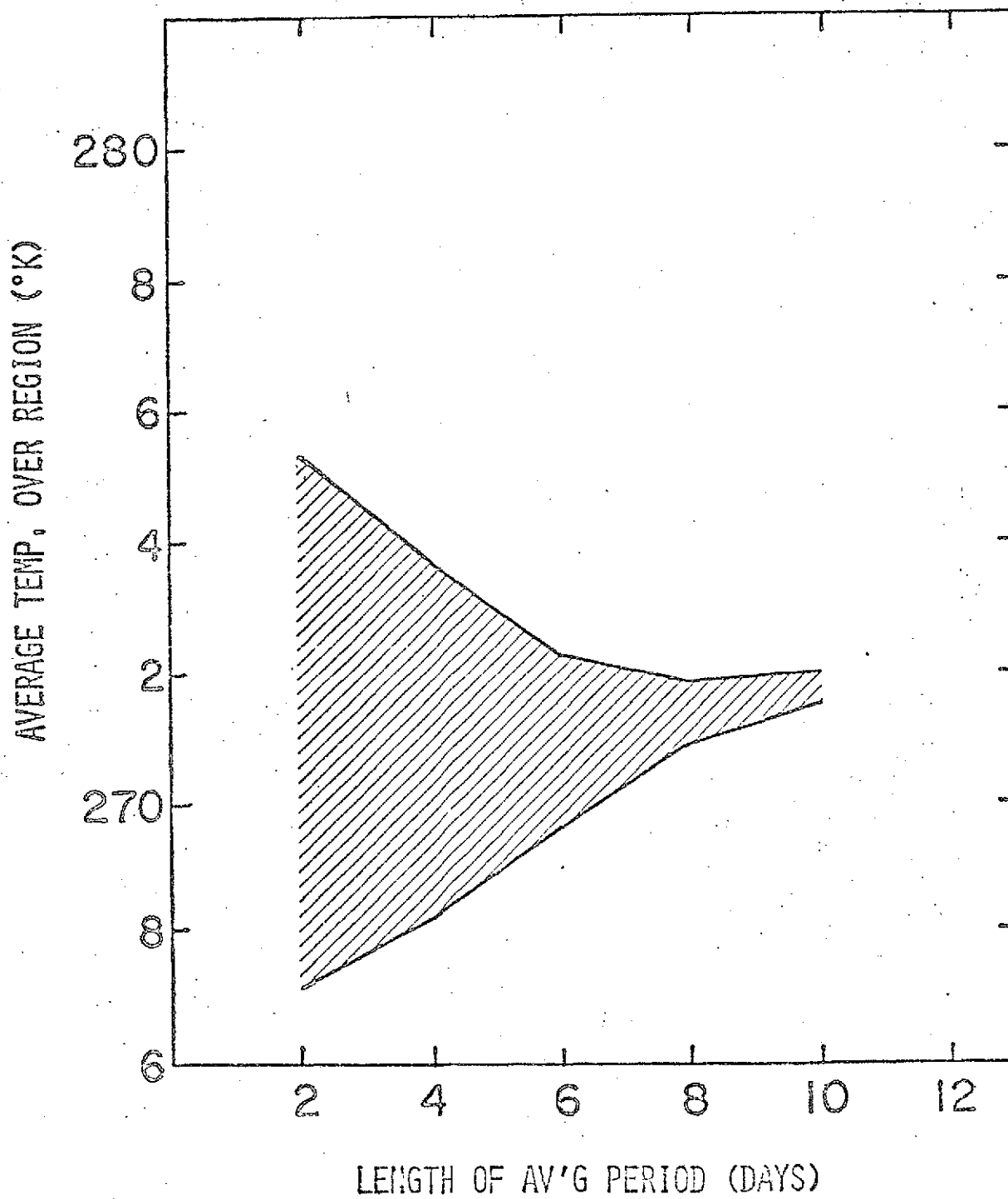


Figure 2. Surface temperature 30 day forecast for Northeast U.S.

NUMERICAL SIMULATION OF SMALL-SCALE CONVECTION. (R. Somerville)

A fully three-dimensional, time-dependent model for the numerical solution of the Boussinesq equations for non-hydrostatic thermal convection has been developed and used to simulate laboratory convection experiments. Figures 1 and 2 show initial and final states, respectively, of the vertical velocity field in a horizontal plane at the center of the domain from a computation simulating convection in a thin layer of air heated uniformly from below. The convection cells take the form of rolls on which large-amplitude traveling sinusoidal waves are superimposed. This structure is also observed at these parameter values in laboratory experiments. Other features of this strongly non-linear flow, such as the vertical heat transport, the temperature field, and the transient details of the evolution to an equilibrium unsteady state, are also reproduced by the numerical simulations.

The ready availability of high-quality laboratory data, for detailed quantitative verification of these simulations, makes such problems excellent test vehicles for numerical methods. The efficient implicit computational scheme, having been tested on laboratory convection, has now been modified by the addition of terms representing the effects of sub-grid-scale turbulence and of phase changes of water, and is now being used to simulate cumulus clouds and cloud populations. Such simulations, if successful, will permit more realistic parameterizations of the energetically crucial role of cumulus convection for the GISS models of the global atmosphere. The details of the flow in and near clouds and cloud clusters are required to determine the cloud-induced transports of heat, momentum, mass, and moisture. Thus a realistic small-scale convection model can be used to design a parameterization scheme which specifies these transports as functions of the large-scale fields explicitly calculated by the global model.

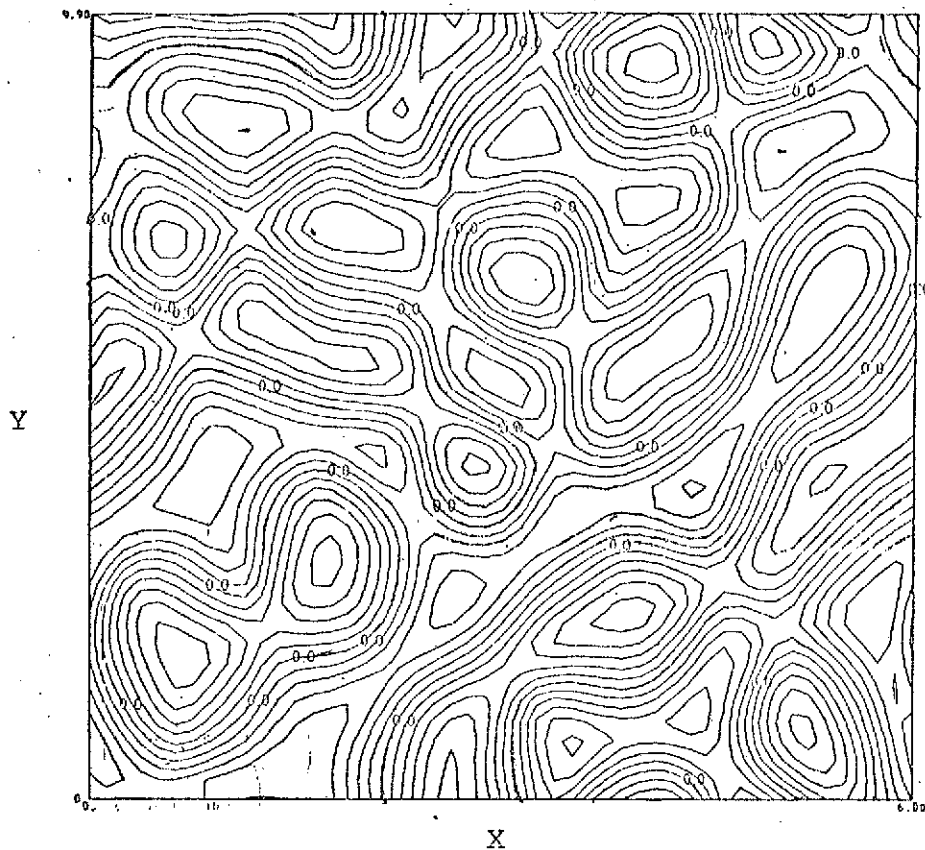


Figure 1. *Initial state of the vertical velocity field.*

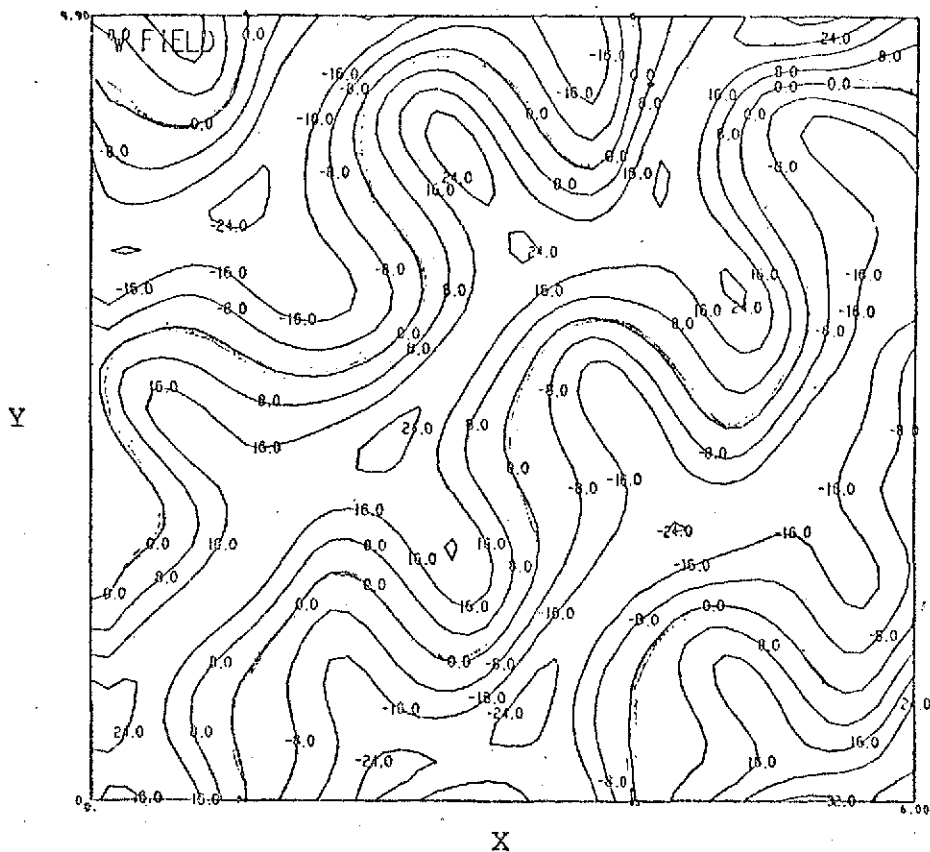


Figure 2. *Final state of the vertical velocity field.*

FLIGHT MEASUREMENTS OF CLOUD POLARIZATION, (J. Hansen, D. Coffeen)

Clouds play a major role in establishing the radiation budget of the lower atmosphere, both for shortwave solar radiation and longwave thermal radiation. Clouds also serve as a signal for atmospheric processes, such as storms and rainfall. Thus a knowledge of cloud types and their optical properties is important to climatology and meteorology. It has been recommended by several study groups that methods be sought for improved global monitoring systems of cloud types and cloud optical properties.

The goal of the work under this project is to define the role which polarization measurements can play in satellite observations of clouds. Theoretical calculations indicate that the polarization of reflected sunlight is sensitive to the particle phase in clouds and the mean particle size in water clouds. However, it is essential that actual observations be analysed to determine the practical value of measurements on real cloud systems. For this purpose Coffeen and Hansen made observations with a simple polarimeter during a series of cloud physics flights on the NASA Convair 990 in January, 1972.

The preliminary results of these measurements are encouraging. The polarizations for sunlight reflected by water and ice clouds differ dramatically (Figs. 1 and 2). The features in the polarization predicted theoretically for water clouds are easily measurable. The most satisfying result is that the polarization at $\lambda = 2.25\mu$ provides a sensitive measurement of particle size. Prior to these measurements, it was anticipated that it may be necessary to go to longer wavelengths to get a good measure of particle size; that would have involved the necessity of correcting for thermal emission and it would have required a rather complicated analysis in fitting each set of observations. The polarization at $\lambda = 2.25\mu$, however, has a simple dependence on particle size, the major effect being the movement of the zero point of polarization for scattering angles $\sim 70^\circ - 100^\circ$ toward larger phase angles as the mean particle size increases. A detailed analysis of the observations has yet to be made, but the particular cases shown in Fig. 1 are indicative of mean particle sizes ranging from $\sim 8\mu$ for the case on the left to $\sim 25\mu$ for the case on the right.

A limited number of observations were obtained on the first flights and it is probable that at least one additional series of flights will be required in order to fully assess the information content in the infrared observations. However, it is clear that observations at wavelengths larger than 2.25μ are not essential for the task of obtaining cloud particle phase and size. This means

that it will be practical to include measurements at several shorter wavelengths. If measurements are made in the range $0.4\mu \leq \lambda \leq 2.25$, it should be possible to also obtain the cloud height from the polarization, the basis for this being the amount of Rayleigh scattering observed above the clouds. Furthermore, polarization measurements in this wavelength range have been recommended as the best means of remote sensing of the aerosol distribution in the lower atmosphere (for cloud-free areas). It thus appears that it will be possible to develop a single instrument for measuring cloud type, cloud height and aerosol properties. A considerable amount of theoretical and practical work must be done before it will be possible to optimally design such an instrument and interpret the observations; however, the prospects for significant applications are very exciting.

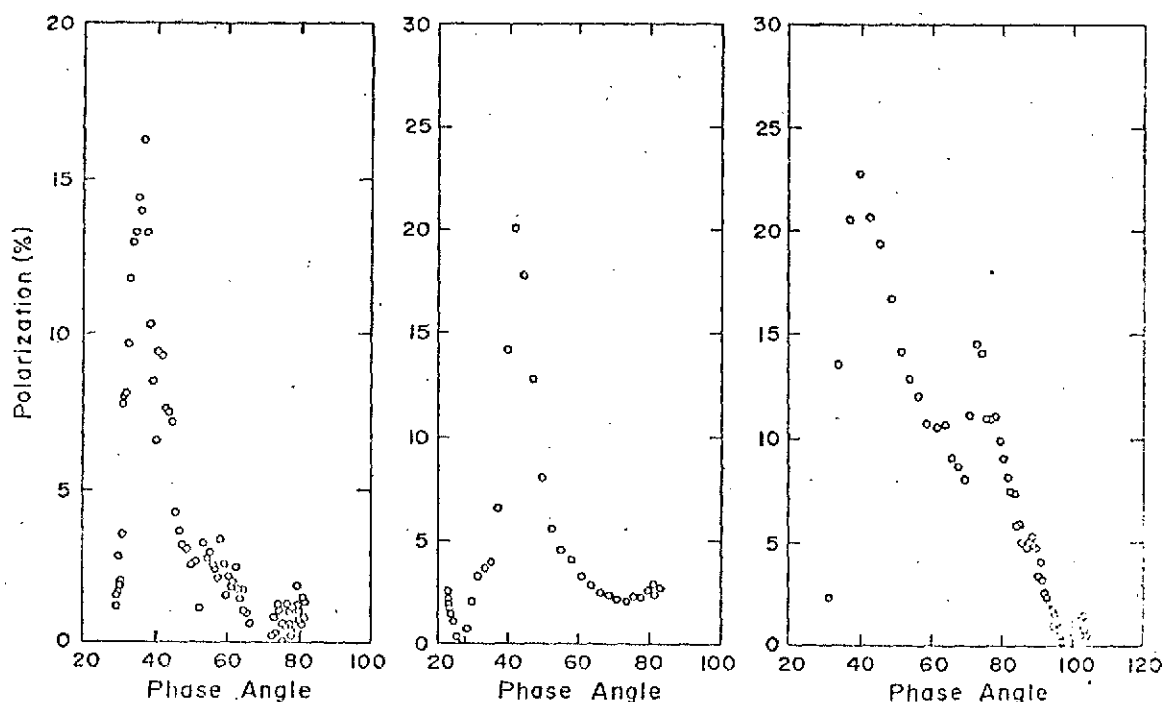


Figure 1. Polarization as a function of phase angle observed over three different water clouds.

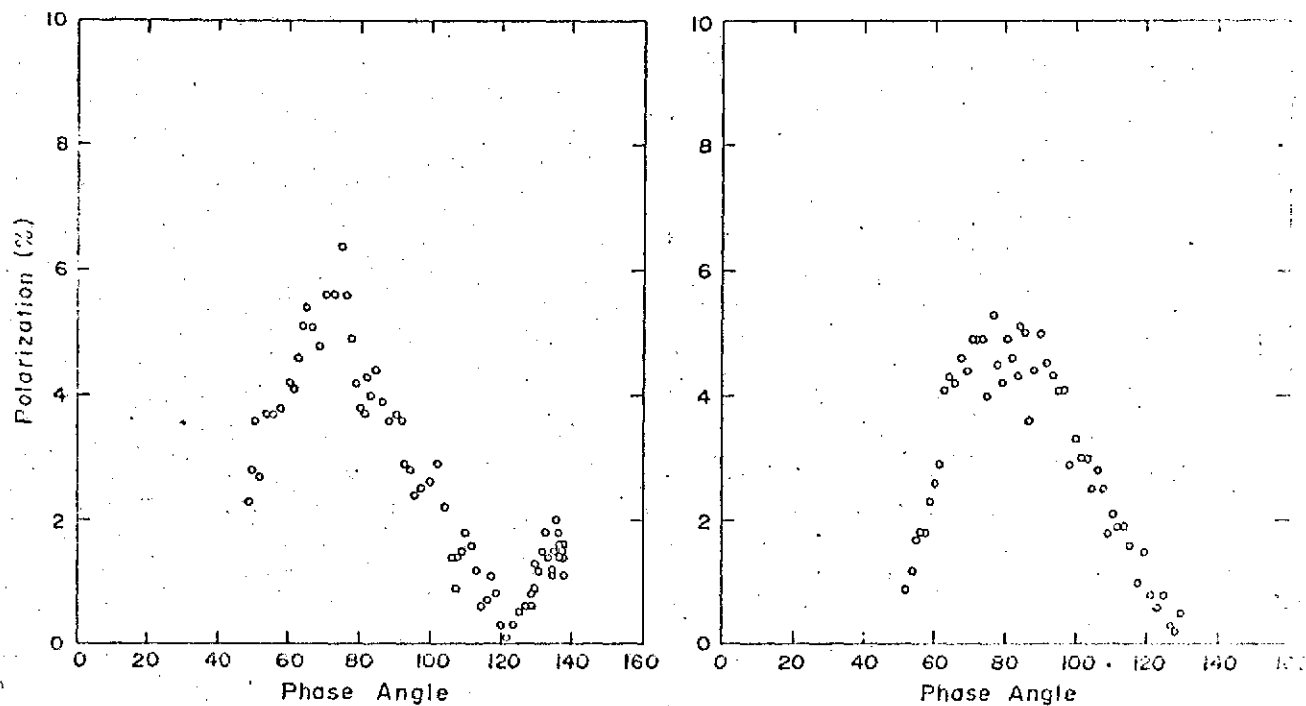


Figure 2. Polarization as a function of phase angle observed over two different cirrus cloud systems.

EARTH RESOURCES STUDY. (V. Gornitz)

An earth-resource research study has been initiated, with applications to economic geology and mineral exploration. The research effort consists of two parts: 1.) examination and interpretation of Gemini and Apollo earth photographs to evaluate the usefulness of such data for small-scale geological mapping and reconnaissance; 2.) obtaining reflectance spectra of a number of common rock types and taking multispectral photographs of the specimens in the lab, in order to determine the feasibility of discriminating among lithologic types. Ultimately, the multispectral photograph technique will be applied to enhance the differences between rock units, and therefore facilitate geological mapping from satellites.

Satellite Photogeology

The areas that are being examined for this study include south and central Arizona, southwest New Mexico, northern Arizona and the Colorado Plateau. These areas have been chosen for several reasons. The region has been extensively explored and good geological maps are available to provide ground truth. Furthermore the southwest boasts many economically important mining districts, notably the porphyry copper deposits in the southern half of Arizona. Therefore, this is a suitable area for seeking out the relationship between the occurrence and distribution of known mineral deposits, and the structure and lithology as inferred from space photographs.

Selected examples of the geological information observed from space photographs have been examined in detail. The first example spans the region over S.E. Arizona - S.W. New Mexico, as photographed on the Gemini IV and Apollo 6 missions (Figure 1). Exposed bedrock (darker, rougher terrain) in the mountains can be readily distinguished from unconsolidated alluvium or gravels (marked Qs, various shades of red or brown). However, a major disadvantage of space photography is that little detail of bedrock composition can be determined beyond the basaltic lava field (right, center) with associated cinder cones (marked Qb, * = cinder cone). The mountains consist primarily of a complex assemblage of non-distinguishable silicious volcanic rock. Some resistant sandstone or limestone layers in the Don Cabezas Mountains (upper, center), and the Dragoon Mountains (center, left) stand out as elongated, narrow ridges, oriented in a N.W. direction (Figure 1) reflecting the regional pattern of the Basin and Range Province in southern Arizona.

An Apollo 9 photograph illustrates the terrain of northern Arizona (Figure 2). A vast lava field covers the center of the view. Because of snow-cover, the exact boundaries of the lava

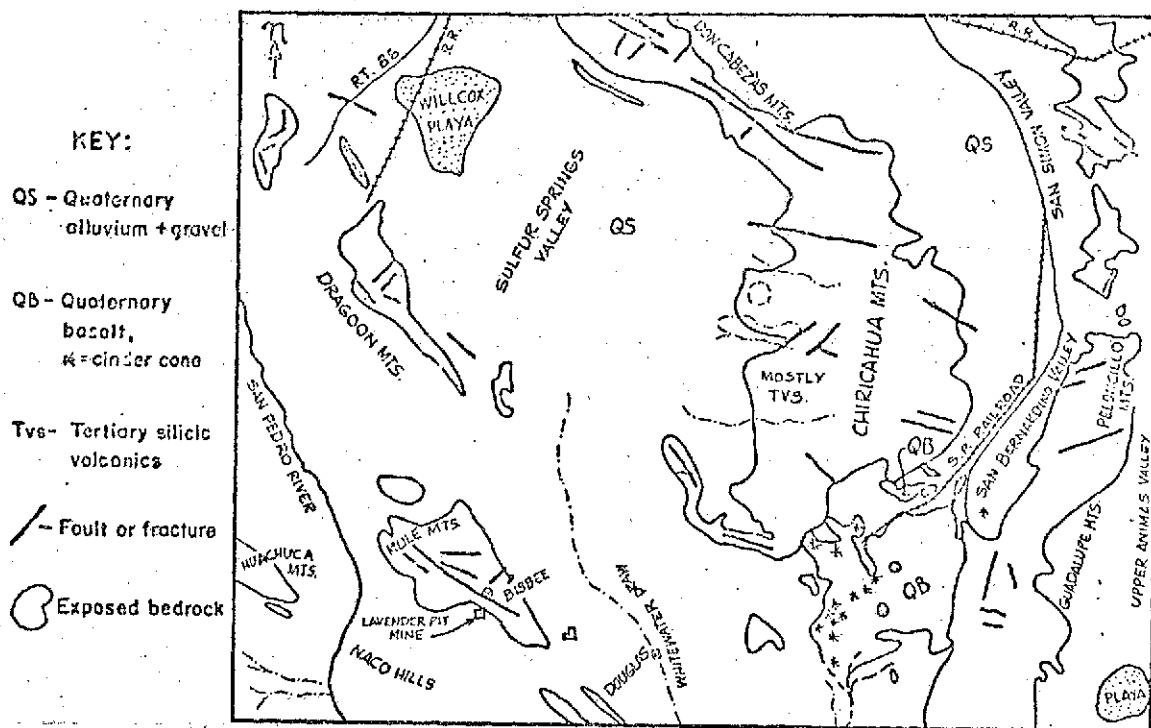


Figure 1. Geological sketch map of southeastern Arizona.

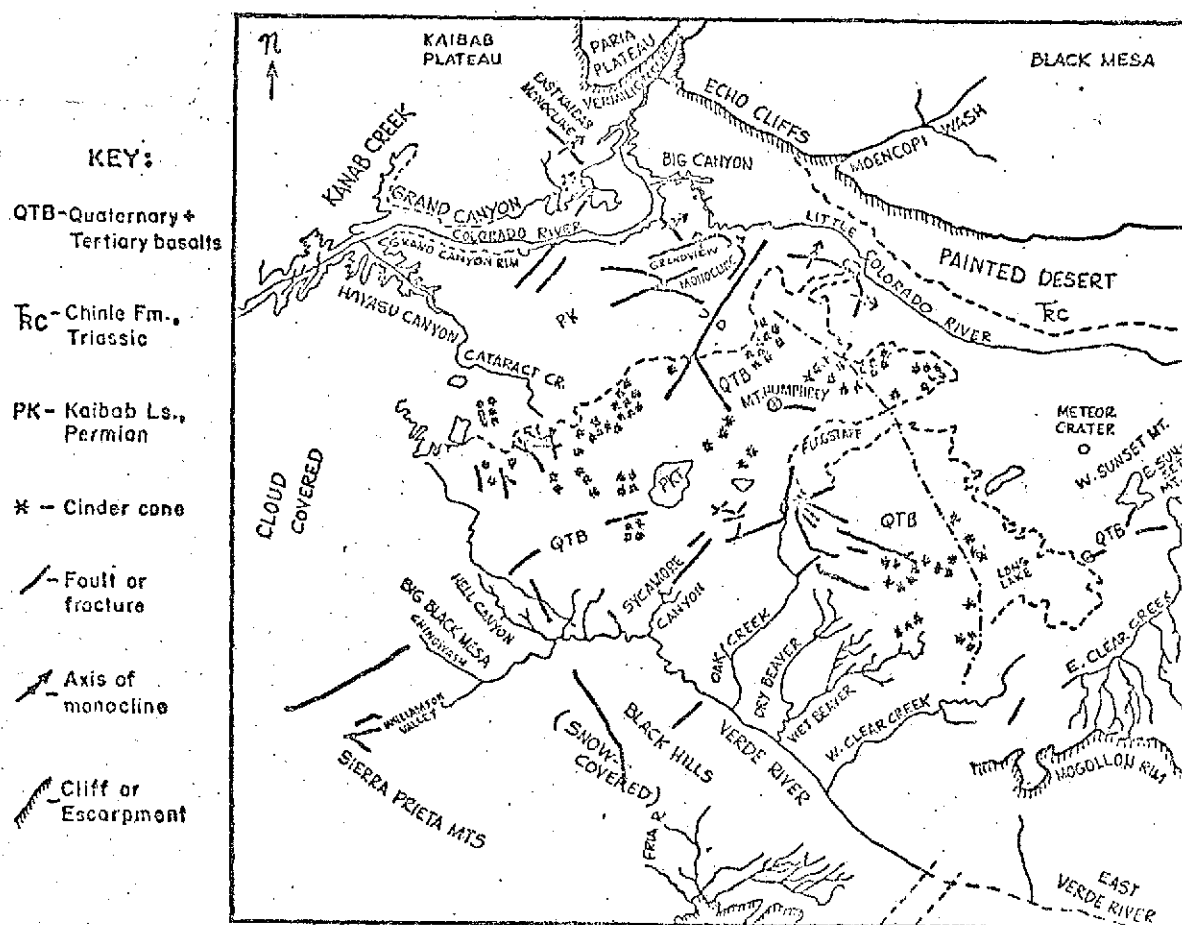


Figure 2. Geological sketch map of northern Arizona.

field are not clear -- however, numerous cinder cones are quite apparent. While the snow obscures boundaries of rock units, it also accentuates linear features such as faults or fractures, which are zones of weakness, more easily eroded away. Several of these are not marked on the state geological map. The East Kaibab monocline and Grandview Monocline are visible as is the Bright Angel Fault, which extends to the south of the canyon.

Measurement of Rock Reflectance Spectra

Space photography provides only limited ability to differentiate among rock types. However, this ability is necessary, because ore deposits typically occur in conjunction with specific lithologies, such as porphyry copper and molybdenum in quartz monzonites or lead and zinc in limestones (Figure 3). In order to use multispectral cameras on satellites for geological mapping, the spectral signatures of the rocks must be determined.

Therefore, the reflectance spectra of different rock types were measured at C.W. Post College, (in collaboration with E. Yost) with a field spectroradiometer in the wavelength range 400 to 1100 m μ , at 12 m μ intervals.

It was found that the reflectance spectra are strongly influenced by surface texture and surficial coatings. Considerable overlap in reflectances exists among the different lithologies, which preclude precise identification by remote sensing in the visible and near-IR. Yet individual rocks display enough spectral variety, so that they could still be classified as distinct units, even though they could not be specifically identified as basalt or granite, for instance. The results suggest that multispectral photography will be able to distinguish between dissimilar rock types, although the exact lithology cannot be identified from the spectra alone.

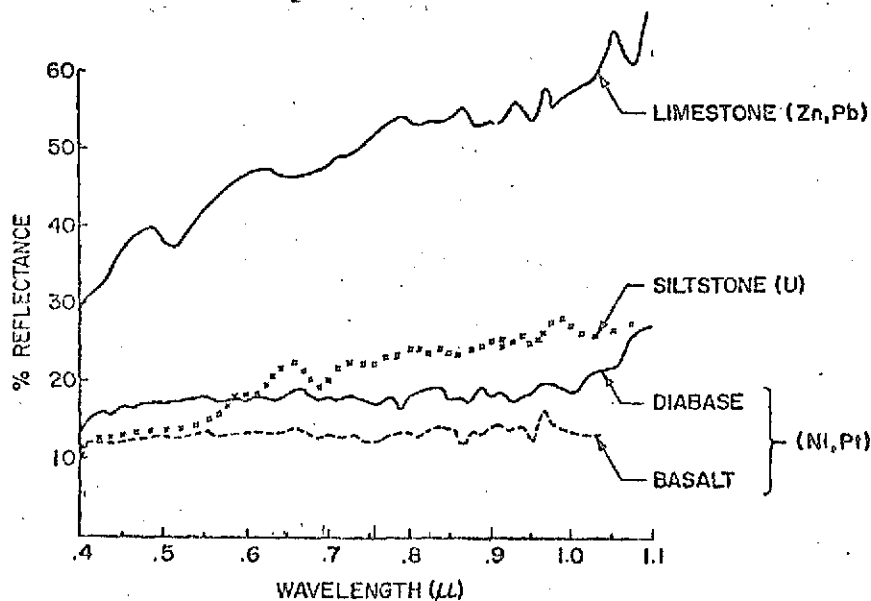


Figure 3. Spectra of host rocks.

Page intentionally left blank

July 1, 1972 to December 31, 1972

PARAMETERIZATIONS OF MOIST CONVECTION IN THE GISS MODEL OF THE GLOBAL ATMOSPHERE. (R. Somerville, J. Hansen, P. Stone, G. Russell)

The GISS model of the global atmosphere is used primarily for data assimilation studies, simulation of observing systems, and experimental weather forecasting. The value of all such research performed with the model depends on the realism of the model itself. Thus a continuing effort is required to identify and correct unrealistic features of the model treatment of important physical processes in the atmosphere.

Moist convection comprises one such group of processes, well-known to be crucial to the atmosphere budgets of heat, water, and kinetic energy. Such processes typically occur on the space scale of cumulus clouds, 2 to 3 orders of magnitude smaller than the horizontal finite-difference mesh size. Thus they cannot be resolved explicitly and must be treated parametrically. Such a parameterization may be regarded as an algorithm for uniquely determining the effect on the large-scale atmosphere of the small-scale convection, given the large-scale fields themselves, as calculated by the model. The assumption that such an algorithm exists is bold but necessary, since the cloud-scale fields cannot presently be neglected or calculated accurately.

The moist convection parameterization scheme in the GISS model originated in Arakawa's scheme for the UCLA 3-level model. At each horizontal grid point, the column of nine layers is examined every half hour of simulated time as follows: pairs of layers are compared in terms of static stability, and "convection" occurs when a layer is buoyant with respect to a higher layer. Such convection, in addition to stabilizing the column, condenses water vapor and releases latent heat to warm the air. It also creates clouds, which are used as input to the radiation portion of the model.

For purposes of the pairwise comparison of layers, the 9 model layers may be treated individually or combined into fewer than 9 by "strapping" together two or more contiguous layers into thicker ones, whose properties are averages of the smaller layers which comprise them, and performing the comparison between the thicker "strapped" layers. Additionally, the clouds formed when the convection criteria are satisfied may be assigned to one or more of the layers involved. Also, the radiative properties of the clouds (albedo, optical thickness, etc.) must be specified, which introduces further degrees of freedom into the parameterization scheme.

Recently the strapping, cloud assignment, and radiative property specifications were changed in a successful effort to bring the model cloud distributions into better agreement with observations. Typical maps of cumulus clouds at the same instant in two runs are shown in Figures 1 and 2. In the maps, the

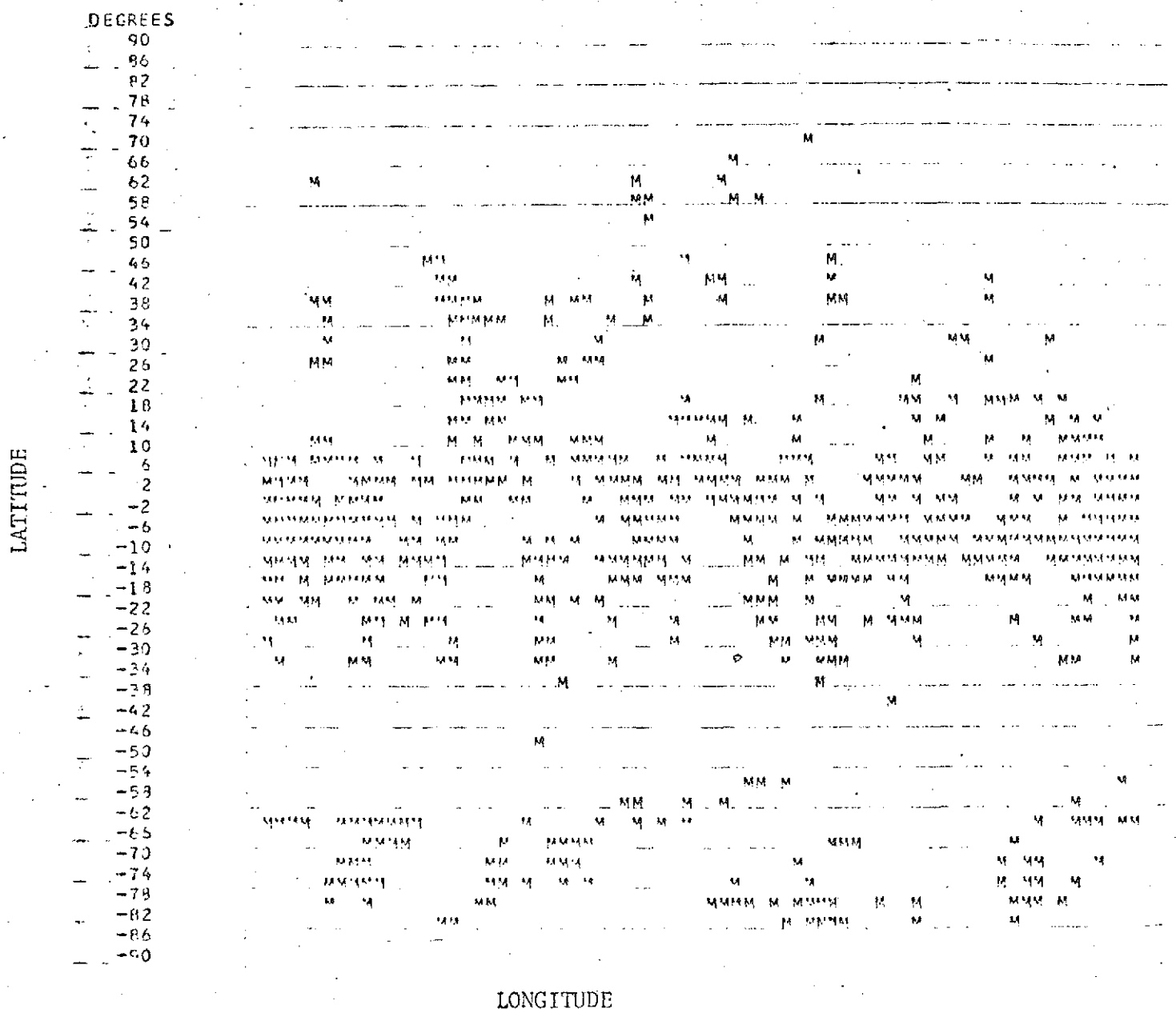


Figure 1. Convective clouds in the older model.

ordinate is latitude from 90 S at bottom to 90 N at top, and the abscissa is longitude with 0 degrees at the center. In the older model, only middle clouds occur, an obviously unrealistic result, although the predominantly tropical latitudinal distribution is realistic. In the newer model, the tropics are still most heavily

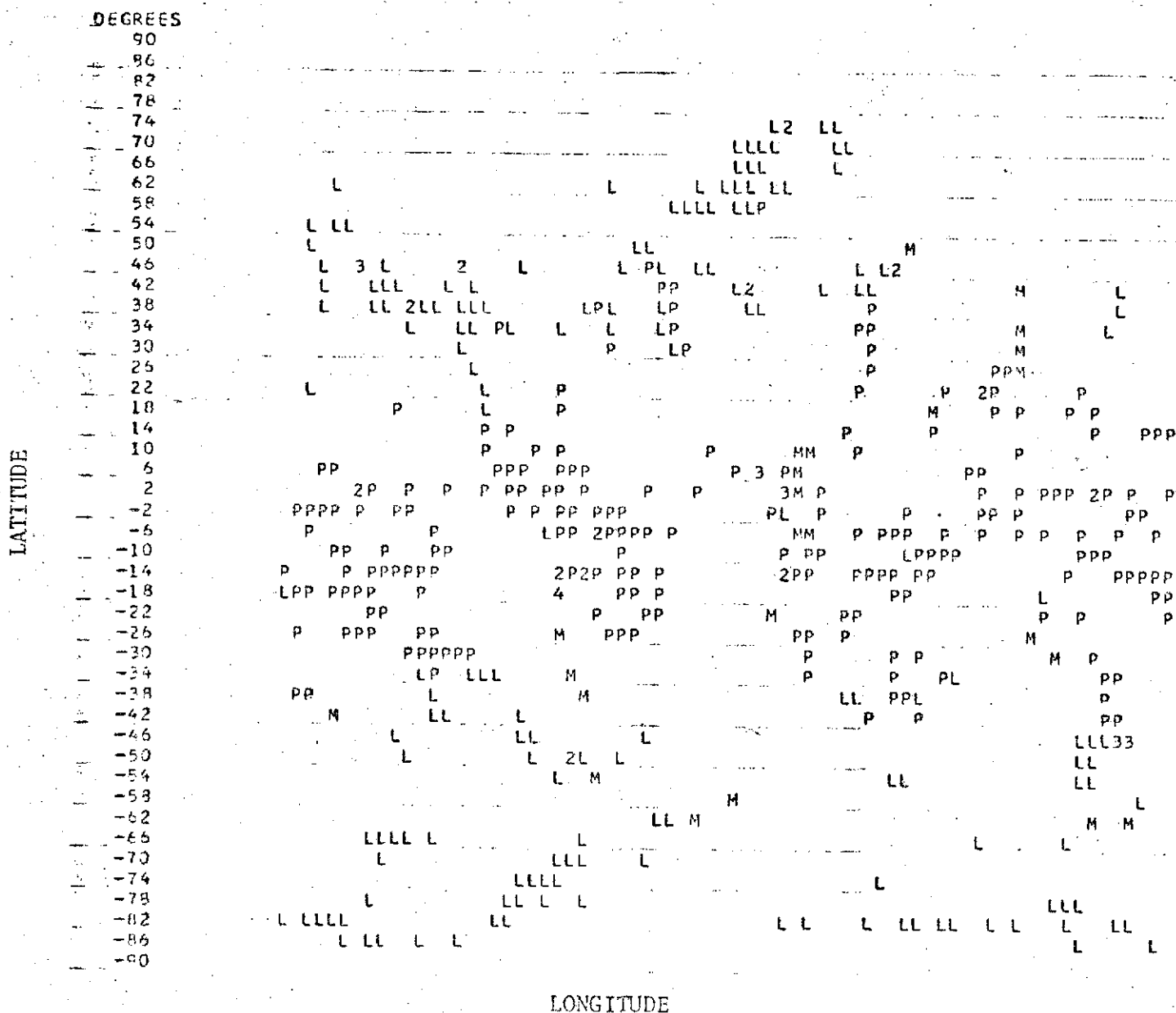


Figure 2. Convective clouds in the newer model.

populated with cumulus clouds, but the population is much more heterogeneous. This change has resulted in much more realistic vertical profiles of long-wave cooling rates, which formerly were

KEY TO CUMULUS CLOUD MAPS

L = low clouds

M = middle clouds

P = penetrating clouds

1 = L and M

2 = L and P

3 = M and P

4 = L and M and P

blank = no clouds

unrealistically large at the top of the bank of middle clouds. Only cumulus clouds are shown in these maps; at middle and high latitudes, the model cloud distributions are dominated by non-convective clouds formed by large-scale supersaturation.

Two other free parameters of the cumulus scheme were explored in a related series of experiments. One run tested the effect of the entrainment factor, which measures the extent to which deep penetrating convective columns mix with the environment during ascent. This factor is normally set to its maximum value. When it was set to zero, the only significant change was an increase in the latent heat supplied from condensation in the deep clouds.

Another run explores the arbitrarily chosen constant relaxation time for the elimination of an unstable temperature gradient. This constant is normally set to 30 minutes. When it was doubled, the amount of convective clouds increased substantially, although the convective heating rate and precipitation rate were not significantly affected.

On the basis of this work, the current version of the model, which was used for the ITOS-D VTPR experiment, contains the newer moist convection parameterization with maximum entrainment and the 30 minute time scale. Many further tests and trial modifications of model physics are in progress.

A PARAMETERIZATION FOR THE ABSORPTION OF SOLAR RADIATION IN THE GISS MODEL OF THE GLOBAL ATMOSPHERE. (A. Lacis, J. Hansen)

Solar radiation absorbed at the earth's surface and in the atmosphere represents the initial driving force for atmospheric motions. An accurate treatment of solar radiation is required for long-range numerical forecasts and for climatological studies.

Thus in the numerical circulation model it is required to compute the amount of solar radiation absorbed at the earth's surface and in each layer of the atmosphere. The method of computation must correctly incorporate the dependence of the absorption on the specific humidity, the cloud amount and type, the ozone distribution, the ground albedo and the zenith angle of the sun.

Exact solutions of the radiative transfer equation are not practical within the circulation model, because the integration over frequency would require more time than the computations of the dynamics. Moreover, the atmospheric data supplied by the circulation model allows a knowledge of only approximate optical properties for the atmosphere and ground. Thus what is needed is an approximate method for computing the amount of absorbed radiation within the accuracy to which the optical properties can be defined.

Lacis and Hansen have developed a parameterization for the solar absorption as a function of the physical variables listed in the second paragraph above. This parameterization is based on detailed and accurate computations made outside of the numerical circulation model. The calculations are made separately for several different spectral regions to make it practical to parameterize the results in terms of absorption by different constituents. The computations are based partly on the 'doubling' method, developed by van de Hulst and others, which is extended by Lacis and Hansen to yield results for an inhomogeneous atmosphere.

Numerical results. Figure 1 illustrates heating rates in the stratosphere due to ozone absorption of solar radiation. The total ozone amount for the computations was 0.34 cm-atm and the vertical distribution was that specified by Dutsch (1959). The solid curve illustrates the heating which would occur in the absence of multiple scattering and reflection from the Earth's surface. The other results illustrate the importance of including multiple scattering and surface reflection in the calculations. The additional absorption in the latter cases is due primarily to photons which were

passed down through the stratosphere without absorption, scattered in the troposphere and/or reflected by the Earth's surface, and then absorbed in the stratosphere on their upward path.

The effect of multiple scattering on the heating rate in the stratosphere is comparable to the effect of reflection from the ground. In the case of a low albedo surface, such as water and most land areas, multiple scattering in the atmosphere provides the major increase in the heating rate over that for a purely absorbing atmosphere. On the other hand, over water or ice the surface reflection is responsible for the major part of the increased heating rate.

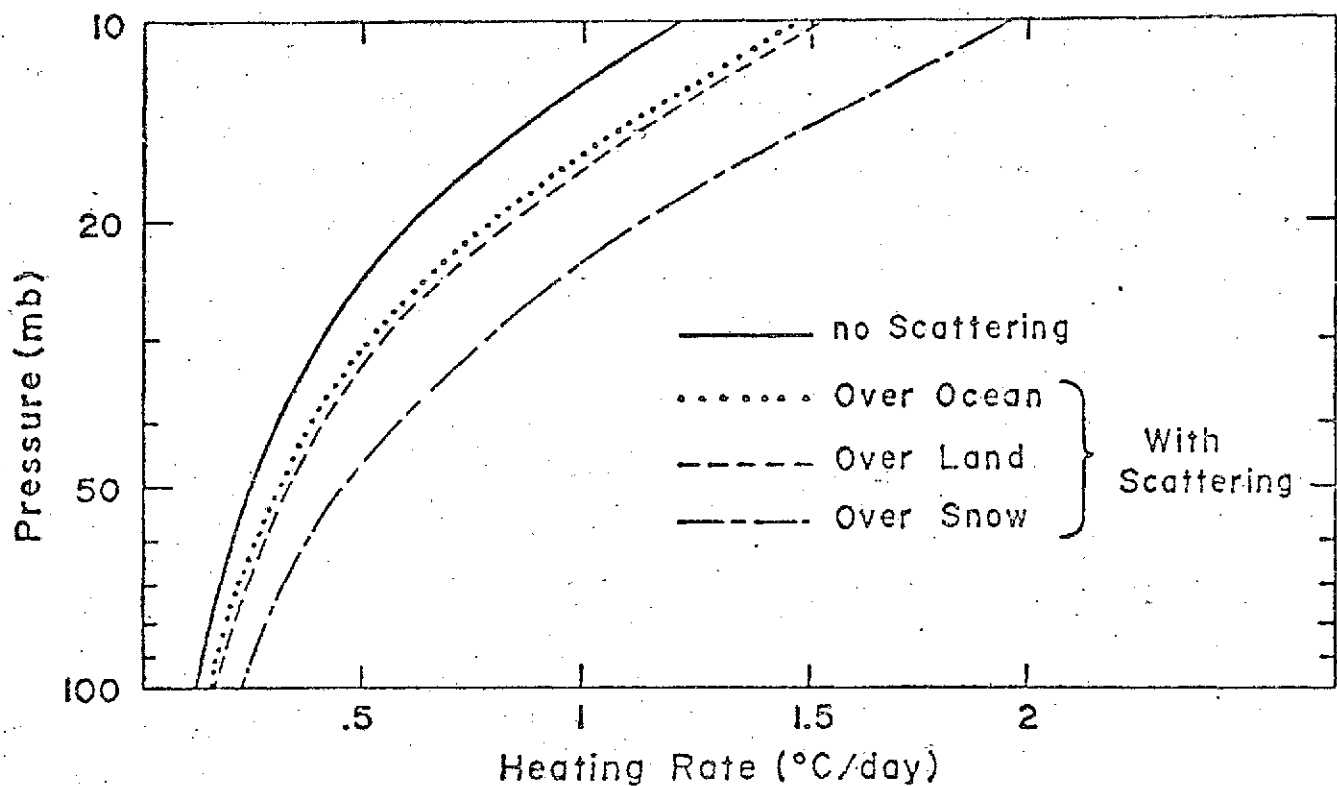


Figure 1. Heating rates in the stratosphere over three different types of surface, all with a clear sky. For the sake of comparison the result is shown which is obtained if multiple scattering and ground reflection are neglected.

Figure 2 shows an example of computed heating rates in the troposphere for clear sky conditions and for cases with clouds of different types present. The major effect of the clouds is to increase the heating rate within the clouds and decrease it beneath the clouds. The increased heating within the clouds is due to the increased photon path which results in additional absorption by both water vapor and cloud particles. The presence of clouds decreases the heating at lower levels as a consequence of the reduced solar flux beneath the clouds.

The impact of solar radiation on atmospheric motions has yet to be fully assessed, and that is one reason for developing methods to accurately compute this energy term in numerical circulation models. However, it is certain that solar radiation is important on climatological time scales, and parameterizations for the absorption of solar energy will be useful in investigations of the possible effects of man-made changes in the atmosphere.

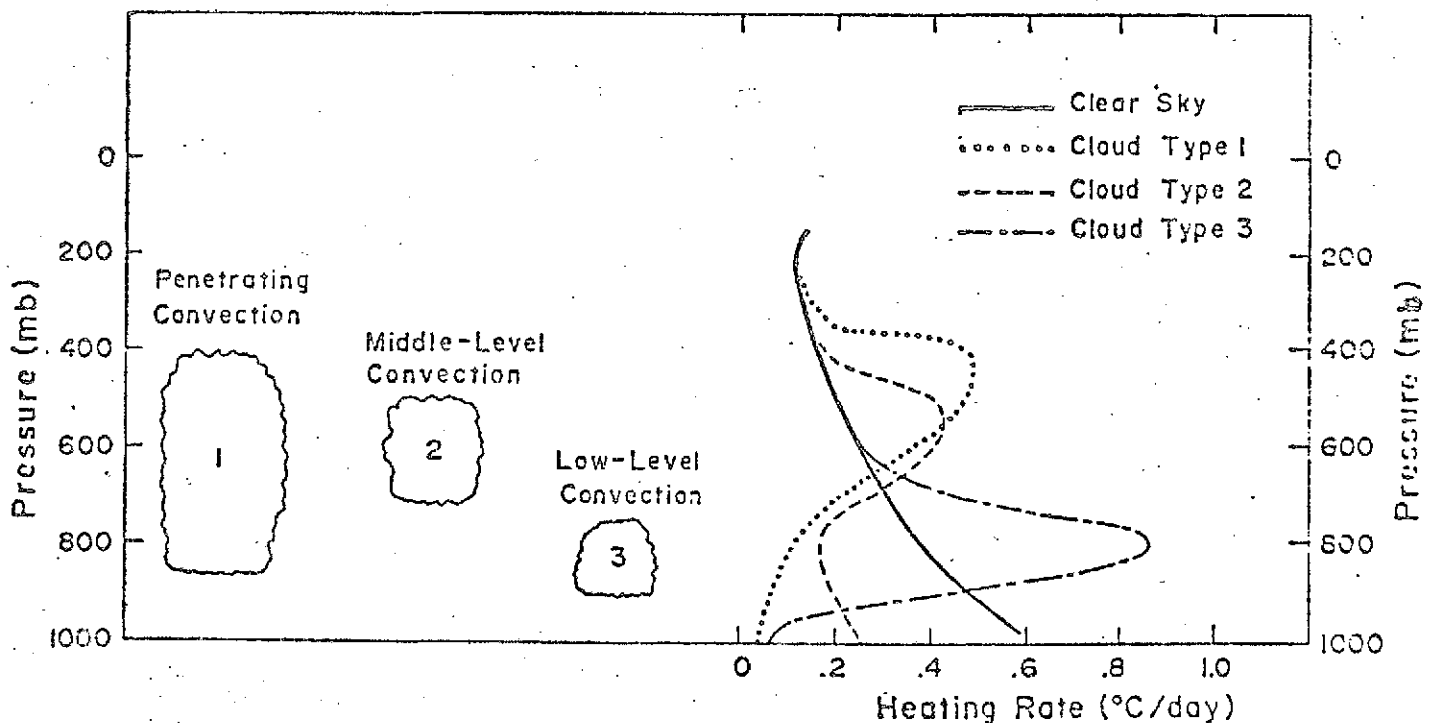


Figure 2. Heating rates in the troposphere due to solar radiation. Results are shown for clear sky conditions and for three different types of clouds which occur in the numerical circulation models.

TREATMENT OF LONG-WAVE RADIATIVE TRANSFER IN THE GISS MODEL OF THE OF THE GLOBAL ATMOSPHERE, (J. S. Hogan)

A method for treating long-wave radiative transfer in the GISS model has been developed. This method, a non-grey treatment of the radiative transfer (with an adjustable degree of greyiness) uses the surface temperature, atmospheric temperature and humidity profiles and clouds generated elsewhere in the dynamical model to calculate the long-wave radiative heating or cooling of the atmosphere. This appears to be the most sophisticated treatment of long-wave radiative transfer in use in any general circulation model.

The highest spectral resolution obtainable with Hogan's scheme is fifty-three spectral intervals between 4μ and ∞ . This mode consists of fifty absorbing intervals of uniform width (in wavenumbers) between 10.0μ and ∞ , one absorbing interval between 4.9μ and 8.7μ , and two regions 4.0μ to 4.9μ and 8.7μ to 10.0μ . The degree of greyiness between 10μ and ∞ can be varied by Planck mean averaging of the opacity in the fifty basic intervals into 25, 10, 5, 2, or 1 interval as desired.

The rotation band of H_2O contributes to the opacity between 10μ and ∞ . The opacity due to this band is calculated from absorption data of Benedict and Kaplan at three temperatures, by means of a "random exponential" band model, and interpolated to correspond to the atmospheric temperature profile. This band model assumes an ideal array of randomly spaced lines with an exponential distribution of line intensities, and should accurately simulate the actual absorption in the atmosphere due to the H_2O rotation band.

The CO_2 vibration-rotation band (15μ) contributes to the opacity between 11.6μ and 20μ . The opacity in this region is calculated from the line data of Drayson and Young for 2219 CO_2 lines at three standard temperatures with an interpolation to the atmospheric temperature profile. The procedure involves detailed line-by-line integration of line absorption coefficients, and is similar to that involved in calculating the CO_2 weighting functions used in GISS programs for retrieving temperature profiles from satellite radiance measurements.

The H_2O vibration-rotation band (6.3μ) is responsible for the opacity between 4.9μ and 8.7μ . This opacity is calculated from empirical formulae derived from low-resolution measurements of Howard, Burch, and Williams.

To properly simulate the long-wave net flux at the upper boundary of the dynamical model, an additional layer is added in the radiative transfer calculation, with a temperature derived from climatology, by interpolation in space and time, and with humidity extrapolated

upward assuming constant relative humidity at the value given for the top layer of the dynamical model. This permits an accurate estimate of the back radiation from the stratosphere.

The tops and bottoms of clouds as well as the ground serve as boundaries in the flux calculations. Clouds and ground are treated as perfect absorbers and emitters of long-wave radiation (black bodies). The net flux at a level in the middle of a cloud is calculated by differencing the downward black body flux (integrated over all wavelengths) from the upper layer and the upward black body flux from the lower layer. The net flux at the ground when there is a cloud adjacent to the ground is calculated by a similar procedure.

At each level in the atmosphere, four fluxes are computed from the standard equations of radiative transfer:

1. Direct flux from bottom of a cloud above a particular level, if any is present
2. Direct flux from ground or from a cloud top below a particular level, if any is present
3. Flux originating in clear atmosphere above a particular level
4. Flux originating in clear atmosphere below a particular level

The net flux is then obtained by subtracting the downward directed fluxes from the upward directed fluxes.

DIAGNOSTIC STUDIES OF THE GISS MODEL OF THE GLOBAL ATMOSPHERE

(R. Somerville, J. Tenenbaum, Z. Jao)

The raw output from a numerical model of the atmosphere can be as useless as unprocessed meteorological observations of the atmosphere itself, and for the same reason. To gain understanding of either the atmosphere or the model, a small number of meaningful statistics must be extracted from an immense data collection. By diagnostic studies we mean the generation and analysis of such statistics for the purpose of comparing the atmosphere with our model and targeting specific areas of the model for improvement.

Table 1 is a display of the gross energetics of a recent version of the GISS model in comparison with those of the atmosphere, as estimated from observational data by Oort (Monthly Weather Review, 92: 483, 1964), and with those of a well-known numerical model at the Geophysical Fluid Dynamics Laboratory (GFDL) of NOAA (Manabe, Smagorinsky, Holloway, and Stone, Monthly Weather Review, 98: 175, 1970). These energy integrals, taken over a hemisphere or the entire globe, are measures of the total kinetic energy and of the fraction of total potential energy, which is available, subject to various dynamical constraints, for conversion to kinetic energy. They serve to trace the flow of energy from its source in solar radiation, which is converted to potential energy (the density field), which in turn sustains the kinetic energy of the winds, to its ultimate dissipation in heat by friction. Thus these quantities are sensitive indicators of model realism. The numbers shown are equilibrium statistics and are divided into two parts: zonal (averaged with respect to longitude) and eddy (departures from this average). The numbers shown are in units of billions of ergs per square centimeter.

Table 1

ATMOSPHERIC ENERGETICS

	observed	GISS model	GFDL model
Zonal available potential energy	4.0 \pm 1.0	5.4	5.0
Eddy available potential energy	1.5 \pm 0.5	0.6	0.4
Zonal kinetic energy	0.8 \pm 0.3	1.0	1.3
Eddy kinetic energy	0.7 \pm 0.3	0.4	0.5

It is clear that the model amounts of total available potential energy and total kinetic energy are realistic, but the model carries too large a fraction in the zonal category and too small a fraction in the eddy form. This feature is common to the GFDL model and other models and is thought to be a consequence of inadequate resolution as well as of an imperfect representation of the physical processes (primarily baroclinic instability of the zonal flow) by which atmospheric eddies are maintained. The comparisons are quite approximate due to differences in domains and methods of computation, but give a preliminary overall indication of the realism of the model.

Figures 1-3 illustrate another useful type of diagnostic information. They depict the typical variation with latitude of zonally averaged precipitation, evaporation, and cloud cover, both from a recent version of the GISS model and from atmospheric observations. In general, the discrepancies between model and observation are smaller than the probable observational error. Major features, such as the subtropical relative minimum of precipitation in the latitude of the descending branch of the Hadley circulation, are quite realistic. The figures are for northern hemisphere winter.

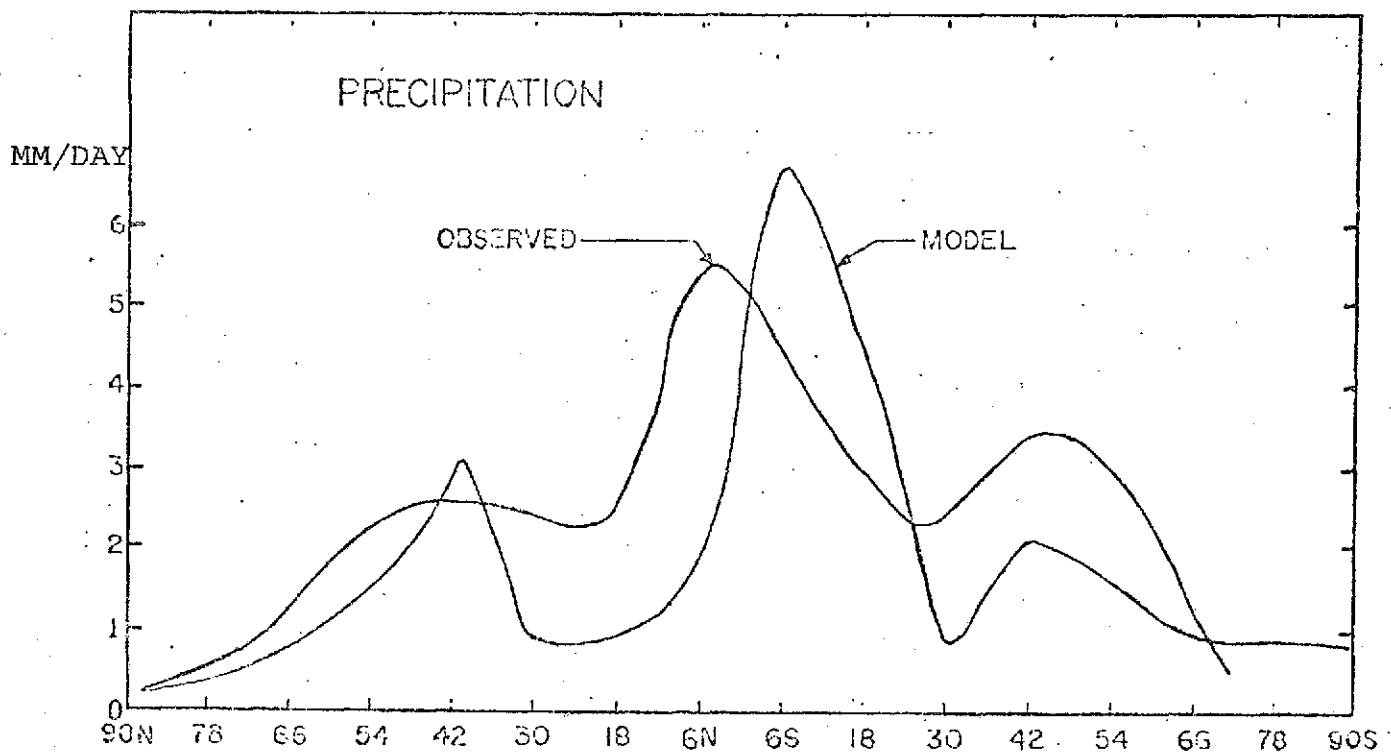


Figure 1. Model and observed precipitation.

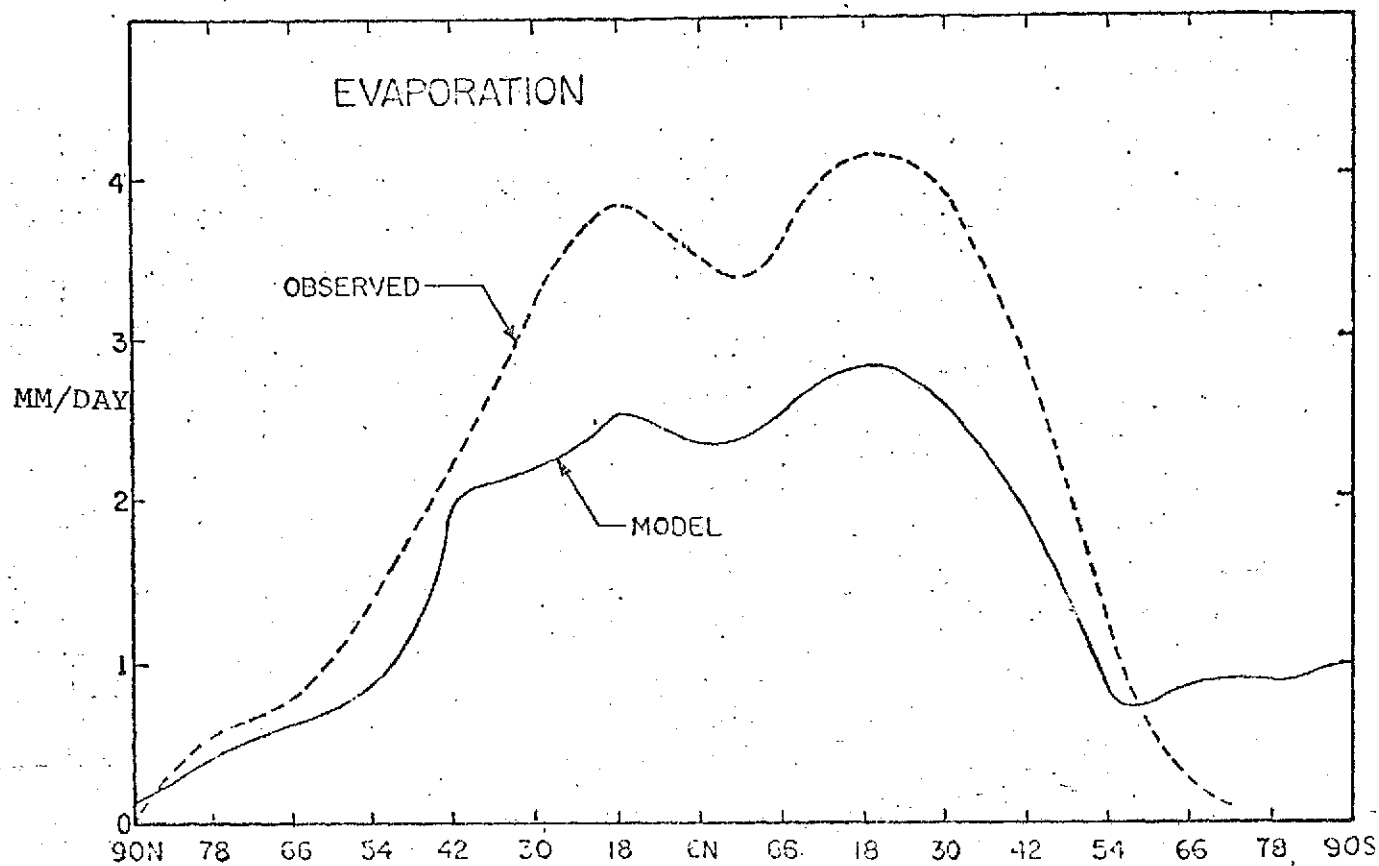


Figure 2. Model and observed evaporation.

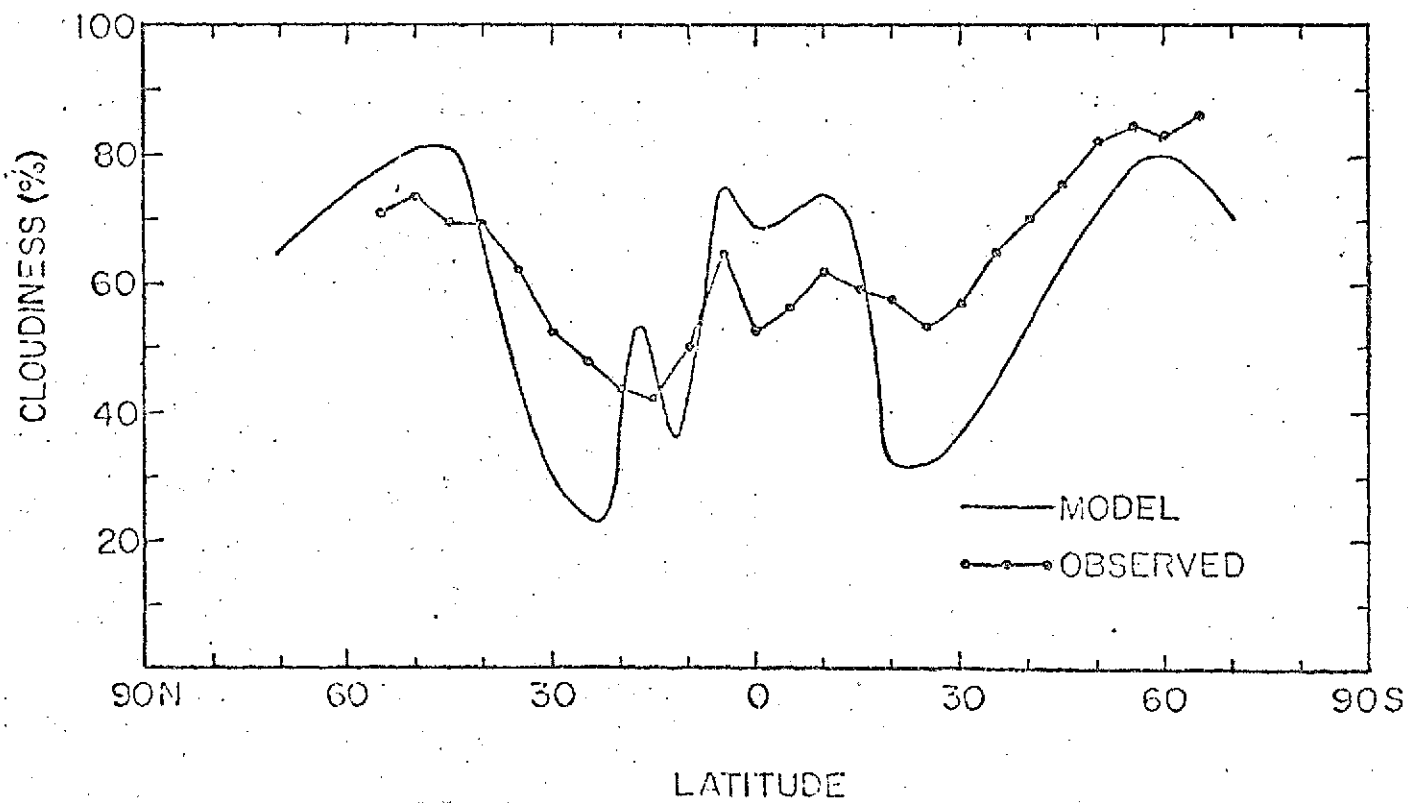


Figure 3. Model and observed cloudiness.

At present, diagnostic plots of this type, including zonal mean (latitude vs. height) cross sections of about 30 important fields, are routinely produced from all GISS model computations. They are invaluable aids to the appraisal of the effects of modifications of the model physics. They are also the basis for evaluating the overall realism of the GISS model as competitive in comparison to other current major models of the global atmosphere.

SPECTRAL STUDIES OF GISS MODEL OF THE GLOBAL ATMOSPHERE, (J. Tenenbaum)

The generalized energetics diagram of Saltzman will be calculated for the GISS model during this study. Other model groups have presented this data (Manabe et. al., Monthly Weather Review, 98, 175, 1970) but have not made explicit comparisons to observational data. Our purpose is to examine the effects of the major characteristics of the GISS model (latitude-longitude grid, global extent, cumulus convection, Arakawa difference scheme) in terms of the spectral energetics. During the current period the spectral equations have been specified and programming of the integral forms has started.

OBJECTIVE SEA-LEVEL PRESSURE ANALYSIS FOR SPARSE DATA AREAS.

(Leonard M. Druyan)

A computer based procedure has been developed that interpolates the sea-level pressure field to each point on a cartesian grid network whose grid points are separated by about 60 nautical miles. The procedure is intended for the analysis of data sparse areas; it uses a small number of observations of the sea-level pressure and wind velocity in combination with some specification of the wind speed field. The research was undertaken in anticipation of remote observation of wind speed above the ocean surface by a satellite-mounted microwave radar-radiometer instrument. (Limited testing of prototype equipment and observations from a space platform are scheduled for sometime during the Skylab program). Nevertheless, experimentation shows that the procedure may have applicability to sparse data pressure analysis in general.

Recent research has determined the procedure's sensitivity to the wind speed specification and to the number, distribution and quality of the pressure and wind velocity observations. All test analyses were made for a set of eleven synoptic times in February, 1967, for a region covering most of the North Pacific Ocean. For each synoptic time a verification analysis was generated based on a large number (about 250) of pressure and wind velocity observations. Each test analysis was then compared to the verification map by computing the root mean square (rms) pressure difference.

Table 1 shows the average rms pressure error for the eleven synoptic times verified in the high gradient northern half of the region. For each analysis, the pressures were specified along the northern boundary which roughly corresponds to the Pacific coasts of Asia and North America on the particular map projection that was employed. The values of the pressure at each low center were also given but no additional pressure or wind information was supplied.

The heading PPG (Perfect Pressure Gradient) in the first column of Table 1 indicates that the analyses were not based on wind speeds but rather on the "perfect" specification of the pressure gradient magnitudes at each grid point from the corresponding verification map. The heading over the second column, WSPD (wind speed), indicates that an objective analysis of the wind speed field derived from the available data used in the verification analysis was used. The third column with the heading CSPD (contaminated speeds) lists the errors that result when the wind speed analysis is contaminated by random-errors varying between -4 knots and +4 knots. The heading over the fourth column, 15K (15 knots), indicates that a wind speed of 15 knots

was specified at every grid point for that group of analyses.

Table 1

	PPG	WSPD	CSPD	15K
Avg Rms Pressure Error	3.5 mb	4.3 mb	4.7 mb	6.8 mb

The results clearly demonstrate that the acquisition of voluminous wind speed data such as from a satellite platform would clearly contribute to the quality of maritime sea-level pressure analysis through the procedure under discussion.

In Figure 1 the average rms error for the eleven synoptic

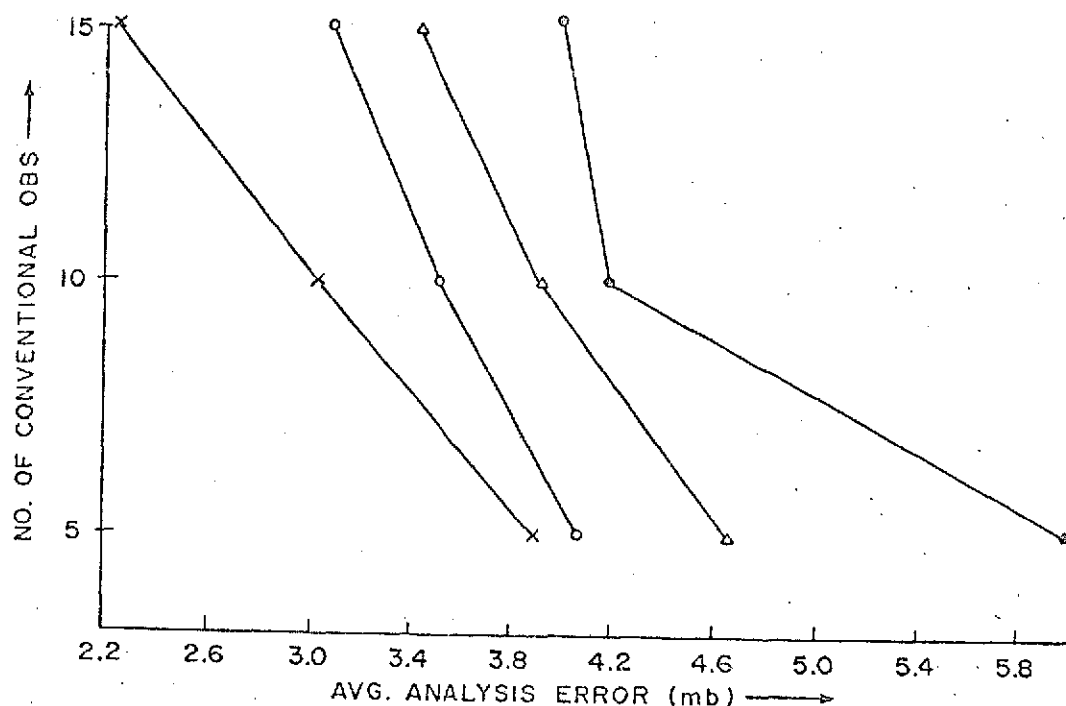


Figure 1. Average analysis errors for the eleven maps plotted as a functions of the number of observations. All analyses computed the pressure minima internally and the pressure gradients from well-specified wind speed fields. The observations simulate a uniform network of buoy stations (X), a northern shift network of buoy stations (O) and a random distribution of high quality ship observations (Δ); the remaining curve (•) shows the average analysis errors resulting from the random distribution of actual ship observations.

times has been plotted as a function of the number of observations of pressure and wind velocity that the analysis was based on. In each case the objective analysis of the wind speeds from the verification data was given.

Results show that:

1. The average rms pressure errors decrease as the number of pressure and wind velocity observations are increased.
2. A uniform distribution of the observations is more desirable than their concentration in the higher gradient northern portion of the area.
3. A consistent spacing between adjacent observations is superior to a random distribution.
4. Using a network of randomly distributed observations simulated from the verification analysis gives consistently better results than using the same number of randomly selected actual ships' observations.

FLIGHT MEASUREMENTS OF CLOUD POLARIZATION.

(J. Hansen, D. Coffeen,

L. Whitehill)

The purpose of the work under this project is to develop methods for obtaining specific global cloud characteristics from satellite observations. Theoretical work by Hansen has shown that measurements of the polarization of reflected sunlight at near-infrared wavelengths can be used to distinguish between ice and water clouds. As the next step toward obtaining the potential information in the polarization, an infrared polarimeter was designed by D. Coffeen and flown aboard the NASA Convair 990 by Hansen and Coffeen in the January, 1972, series of cloud physics flights.

The polarimeter was mounted in a side window of the aircraft and could scan in a single vertical plane parallel to the main axis of the plane. Observations were made at $\lambda = 1.25, 1.6$ and 2.25μ . The results are presently being analyzed, but some of the measurements which have been reduced are illustrated here.

Figure 1 shows polarizations measured over two different cloud systems on different days. These two clouds were special in the sense that they were the only ones for which a rainbow could be seen from the airplane with the naked eye. In the polarization, the rainbow is the sharp positive feature at phase angles $\sim 40^\circ$. These cloud systems were relatively uniform and thus the polarization curves are quite smooth. A comparison of these curves with theoretical computations indicates that the mean effective particle radius in the tops of these clouds was $20 - 25 \mu$. Rainbows were detected in the polarization for all clouds which were observed at the appropriate scattering angles and known (from their altitude and visual appearance) to be of the water type.

The most convenient indicator of particle size is the crossover point (neutral point) from positive to negative polarization at $\lambda = 2.25 \mu$. The phase angle of this neutral point increases monotonically as the average particle size increases, and at $\lambda = 2.25 \mu$ it has a wide potential range. This movement of the neutral point is caused by the increasing predominance of Fresnel reflection for large particles. The dependence of the neutral point on particle size is sufficiently simple that even a rather dull computer can be trained to use it automatically, and hence it should be useful for satellite observations.

Figure 2 shows observations of a thick cirrus cloud system. These two sets of observations were taken on the same day and they

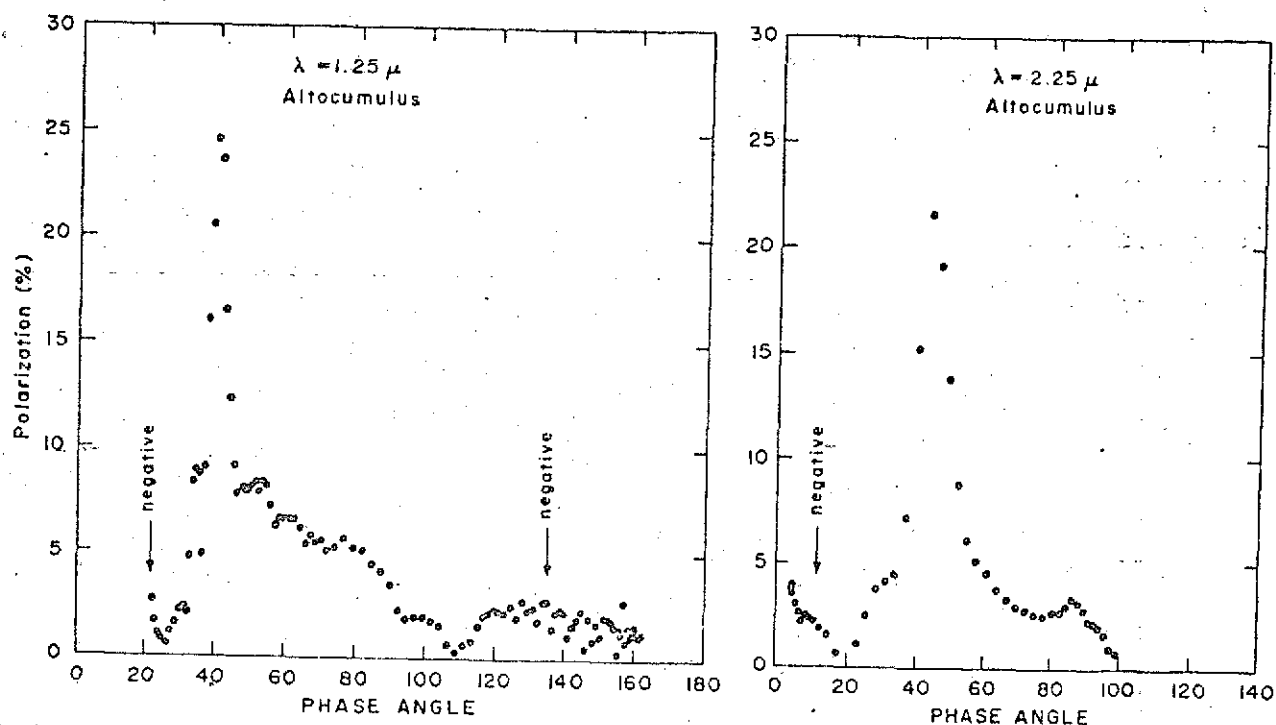


Figure 1. Percent polarization of reflected sunlight observed at $\lambda = 1.25 \mu$ (left) and $\lambda = 2.25 \mu$ (right) over two different clouds. "Negative" is used to indicate branches of the curves where the direction of polarization is predominately parallel to the plane of scattering.

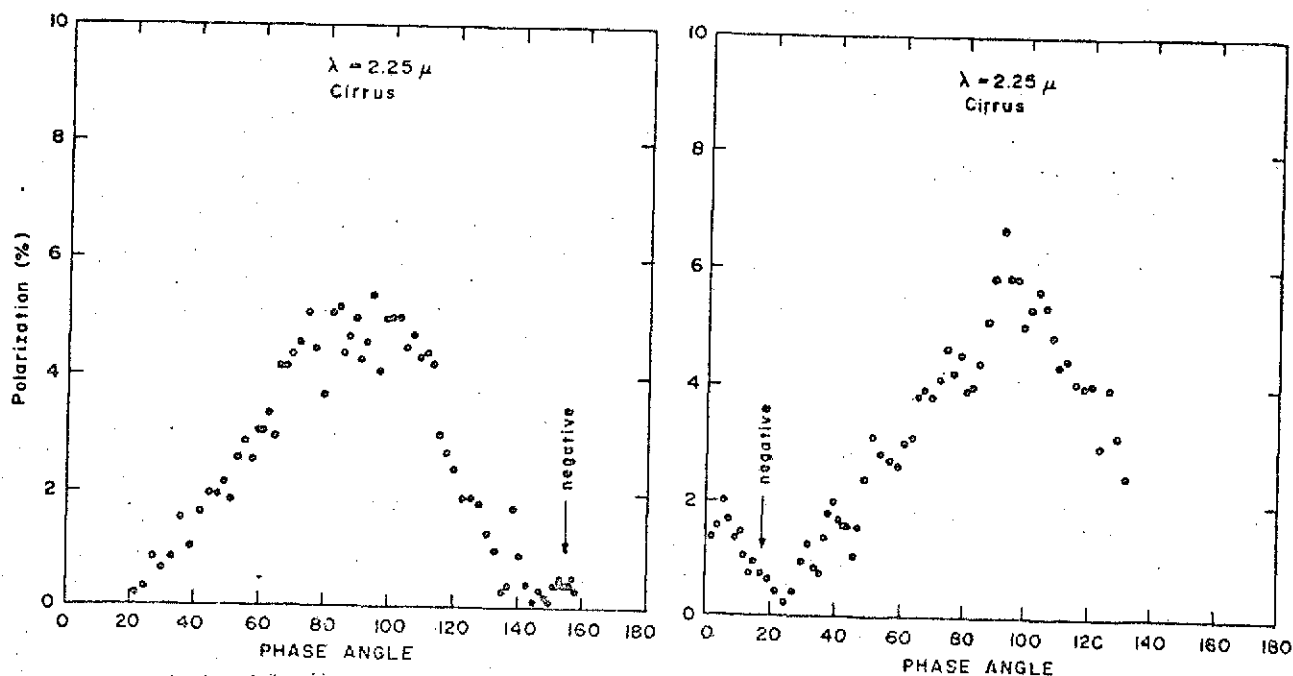


Figure 2. Percent polarization of reflected sunlight observed at $\lambda = 2.25 \mu$ over cirrus clouds. The two sets of observations were taken on the same day over clouds separated by several miles.

were the only cirrus observations in the data which have been reduced so far. Therefore conclusions should be reserved, but it is clear that the polarization for ice clouds is greatly different from that for water clouds, and in ways which can be understood. There is no rainbow for cirrus clouds. The broad positive polarization feature must be due to Fresnel reflection from the outside of the particles; this is expected since cirrus crystal are known to be large.

Figure 3 shows a series of observations over water clouds which were taken consecutively on one flight. The first observations, on the left, were over a front of raining cumulus clouds at least several kilometers long and a fraction of a kilometer wide. The clouds were very turbulent and nonuniform in brightness, thus accounting for the appearance of the polarization curve. The apparent neutral point for the polarization indicates an effective particle radius of at least $30\ \mu$. The clouds immediately behind the front (center part of Figure 3) had much smaller particles, about $10\ \mu$ in radius. Still further away (right part of Figure 3) were clouds with a mean size of about $5\ \mu$.

Although the observational program for terrestrial clouds is at an early stage, the results are sufficient to confirm that the polarization can be used to measure particle phase and particle size. Theoretical work indicates that it may also be possible to obtain the cloud height and the liquid water content from the polarization. This will require measurements at shorter wavelengths, which will therefore be included in future measurements.

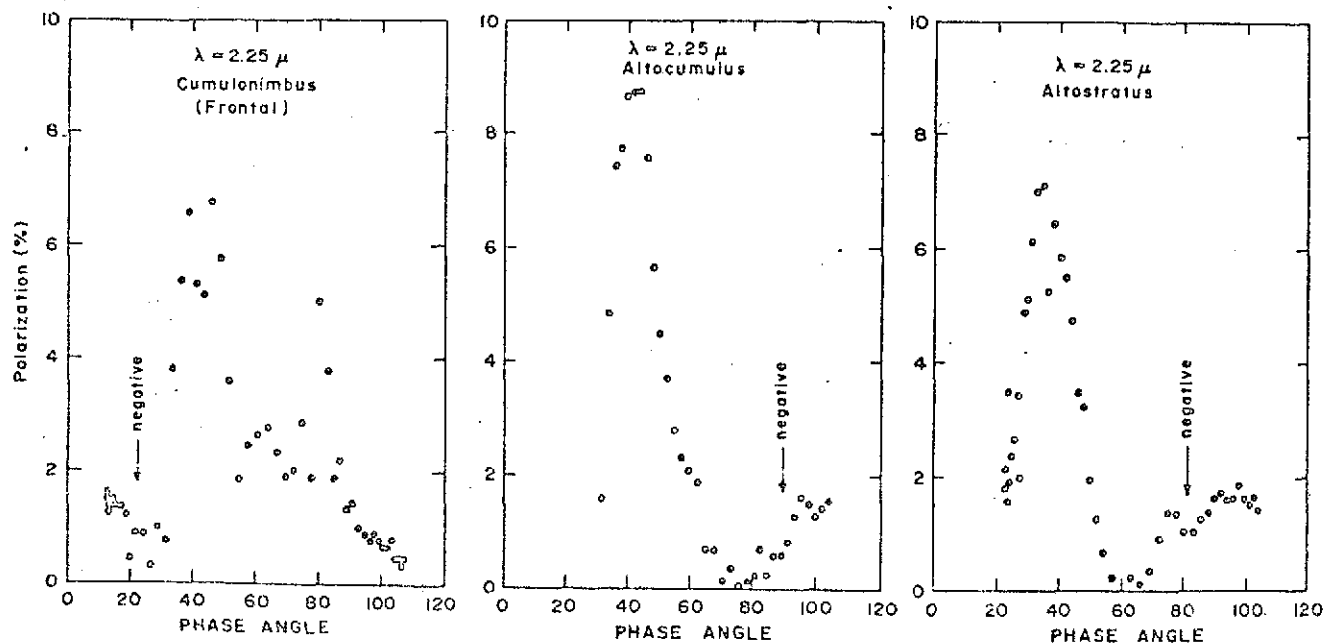


Figure 3. Percent polarization of reflected sunlight observed at $\lambda = 2.25\ \mu$ over three different clouds which were encountered consecutively in time from left to right. The observations on the left were over a narrow front of raining clouds. The other two sets of observations were taken behind the front and for the latter cases the cloud types indicated above are uncertain, except for the fact that they were fair weather clouds.

THEORETICAL STUDIES OF BAROCLINIC WAVES. (P. H. Stone)

The crucial role of baroclinic waves in determining the structure and general circulation of the atmosphere makes the theory of these waves of special importance for understanding many atmospheric phenomena. One such phenomenon is the "vacillation" of the mid-latitude jet stream--that is, its tendency to exhibit quasi-periodic variations, with a period of several weeks. In order to obtain a realistic theory for vacillation it is necessary to extend the theory of baroclinic waves to include both finite amplitude effects and the effect of latitudinal variations in the mean zonal flow. Fang Chen, a graduate student at Harvard, has succeeded in showing that both these effects may be included by combining Stone's theory for the effect of variations in the zonal flow with Pedlosky's theory for finite amplitude effects. In particular, he has proven that Rayleigh's necessary condition for instability and the semi-circle theorem for baroclinic waves hold for Stone's approximate equations, and therefore that Pedlosky's singular perturbation technique still works for finding finite amplitude effects when there are variations in the zonal flow. He is now recalculating the coefficients in Pedlosky's equation for amplitude vacillation, to see how the solution is changed by variations in the zonal flow.

One important application of the theory of baroclinic waves is the development of parameterizations of the large-scale eddy fluxes of heat and momentum for use in studies of climatic changes. With this goal in mind calculations have been carried out to determine the effect of latitudinal variations in the zonal wind on the eddy heat fluxes by baroclinic waves. The calculations show that the eddy heat fluxes in low latitudes are in the opposite direction from those in mid-latitudes. For example, Figure 1 illustrates the horizontal eddy flux as a function of latitude for a symmetric jet located at 45° latitude. This calculation provides an explanation for the actually observed reversal in the direction of the eddy flux in low latitudes. The numerical results have also been used to calculate the mean meridional motions driven by the eddy heat fluxes. The results show that these fluxes are at least as important as the eddy momentum fluxes in producing the mid-latitude Ferrel cell when variations in the zonal wind are included. Figures 2 and 3 illustrate the mean vertical velocity produced by the eddy heat fluxes and eddy momentum fluxes, respectively, that arise from a single baroclinic wave in the presence of a symmetric zonal jet located at 45° latitude.

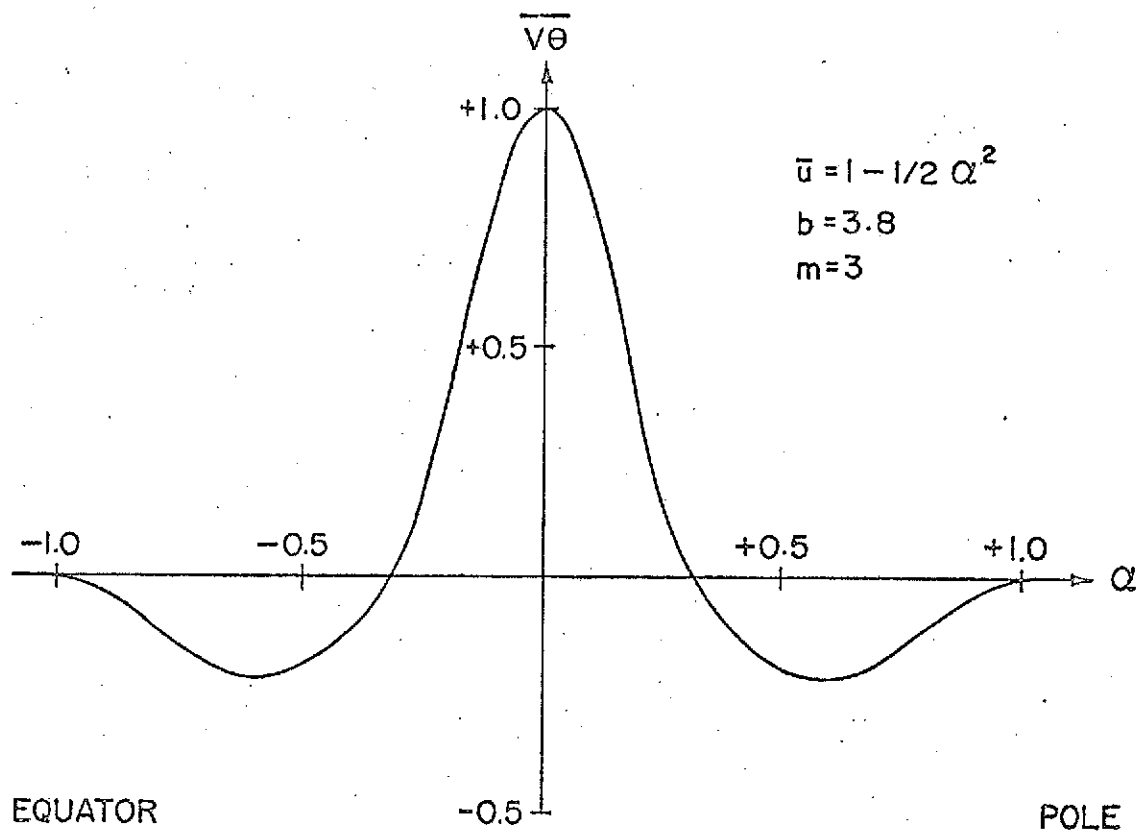


Figure 1. *Horizontal eddy flux.*

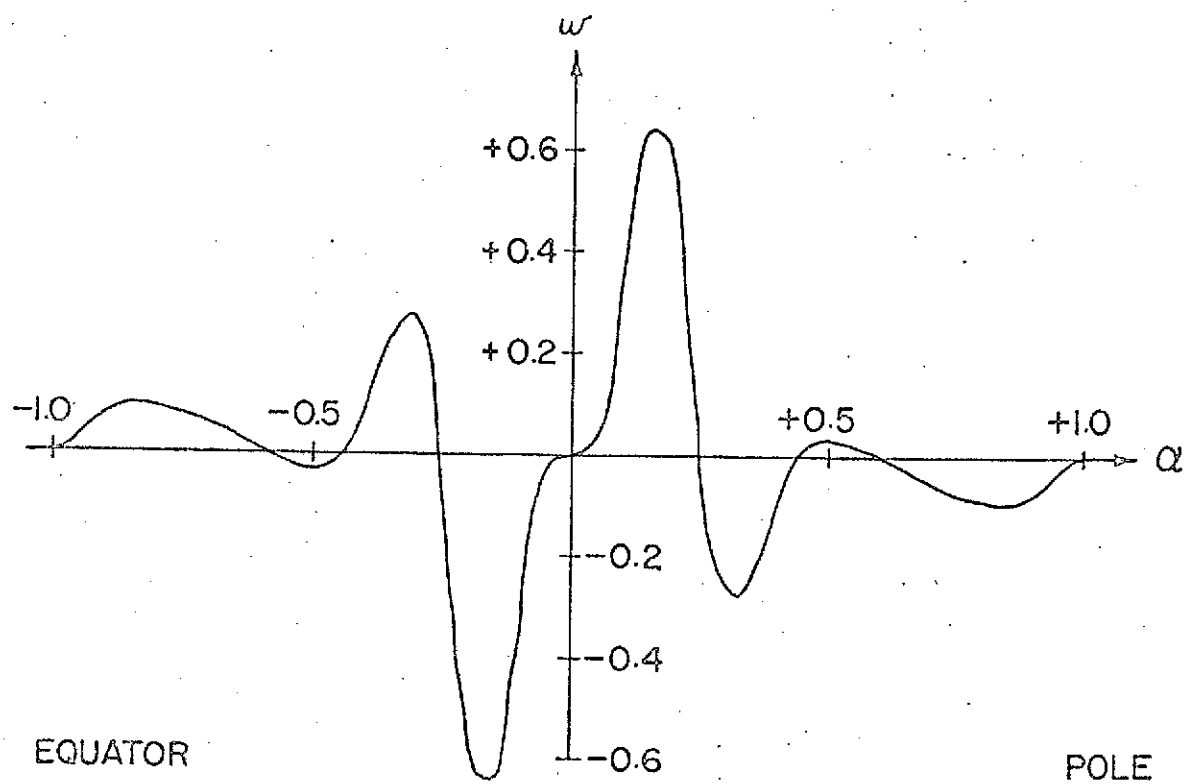


Figure 2. *Mean vertical velocity produced by the eddy heat flux.*

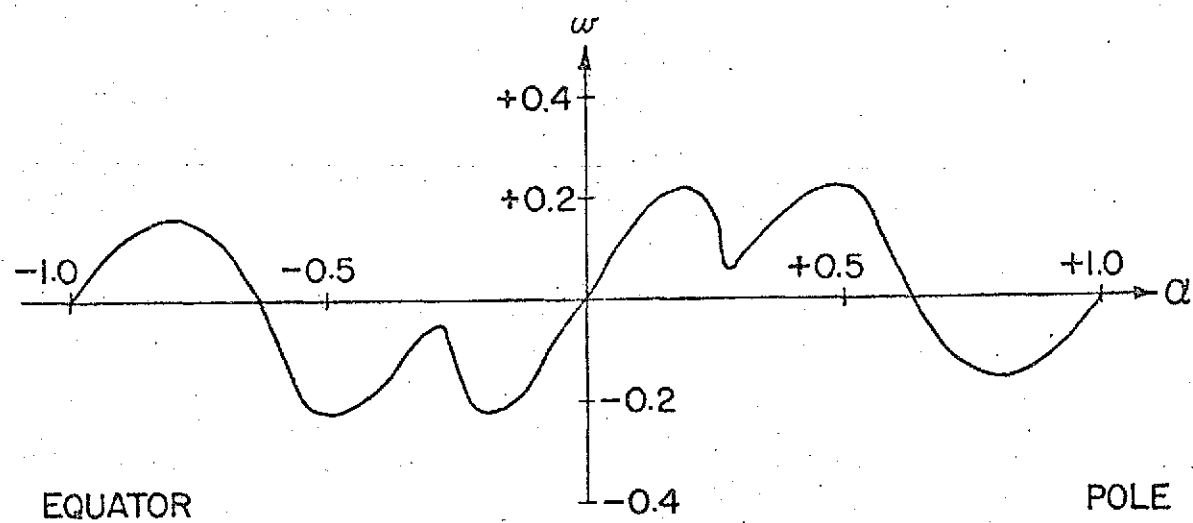


Figure 3. Mean vertical velocity produced by the eddy momentum flux.

NUMERICAL SIMULATION OF SMALL-SCALE CONVECTION. (R. Somerville, M. Broman)

One approach to the parameterization of small-scale processes, which are energetically crucial to the atmosphere but cannot be resolved by the GISS global atmospheric model grid, is to develop small-scale models of the processes themselves. A convection model has been constructed in a domain the horizontal extent of which is somewhat smaller than the grid size of the global model. The global model may be regarded hypothetically as providing boundary conditions and mean vertical structure to the convection model, which then calculates the details of the evolution of clouds and cloud clusters, from which the net effect of small-scale convection on the large-scale fields can be evaluated. In this way, although the process is too time consuming to be incorporated straightforwardly into the large-scale model, a parameterization scheme based on the small-scale detailed results may be devised. The concept is analogous to that of the present treatment of solar radiation in the global model, which is a parameterization based on detailed solutions of the radiative transfer equation performed outside the model.

The core of such a parameterization procedure is a realistic small-scale model. One difficulty in developing such a model is the lack of detailed and accurate observational cloud data for verification. For this reason, an effort has been made to compare a simplified version of the model with detailed observations of laboratory convection experiments. Quite realistic simulations of laboratory convection have been achieved, justifying confidence in the dynamical foundation of the model.

Programs have been constructed for the following types of time-dependent convection:

1. Both shallow (Boussinesq incompressible) and deep (anelastic compressible) flows. This is necessary because laboratory convection and clouds in the lower troposphere are shallow phenomena in which the decrease of density with altitude is of secondary importance, while penetrating cumulus clouds are deep phenomena in which these effects cannot be neglected.
2. Both two- and three-dimensional flows. The simplest example of convection are two-dimensional, and test calculations can be done economically in two-dimensions. The third dimension, however, is essential to realistic simulation.
3. Both dry and moist flows. Latent heat, released when

water vapor condenses, is thermodynamically important in atmospheric convection. The major differences between the laboratory and atmospheric programs are changes in boundary conditions and the inclusion in the atmospheric code of a water budget and its interaction with the dynamics.

The figures are plots of vertical velocity in a horizontal plane from a simulation of dry convection in air at Rayleigh number $R = 4000$. This case of three-dimensional incompressible laboratory convection is particularly interesting in that the details of the transient evolution correspond quite closely with a description of an experimental phenomenon observed by Willis and Deardorff (Journal of Fluid Mechanics, 44:661, 1970), who report as follows:

"In regions where the rolls are strongly curved (which occur even within a rectangular convection chamber), it seems that the roll or cell diameter often becomes too large for equilibrium to be maintained. Then a new cell appears as an expanding blob at the region of maximum curvature of a roll edge or in the centre of the larger cell. Invariably the new cell fails to remain symmetrically within the adjacent rolls or larger cell, and migrates to one side where it disturbs neighboring rolls until a new quasi-steady pattern is obtained."

Figures 1-4 apparently reproduce this complicated process quite faithfully. In Figure 1, the right-hand side of the flow is tending to rolls, but on the left a large cell of descending air has become "too large for equilibrium to be maintained." In Figure 2, 150 time steps later, "a new cell appears as an expanding blob ... in the center of the larger cell." This rising plume then "migrates to one side where it disturbs neighboring rolls." Because of the periodic side boundary conditions, the plume may be seen breaking out of the descending cell at the left side of Figure 3 and affecting the neighboring rolls on the right side of the figure. The plume then also breaks through the other side of the cell, and the resulting "new quasi-steady pattern" appears in Figure 4. The line of cells on the left side then coalesces to create the final steady state of rolls shown in Figure 5. Thus the numerical simulation seems to have captured in considerable detail the transient three-dimensional evolution by which the flow "solves" the preferred mode question en route to a two-dimensional steady state.

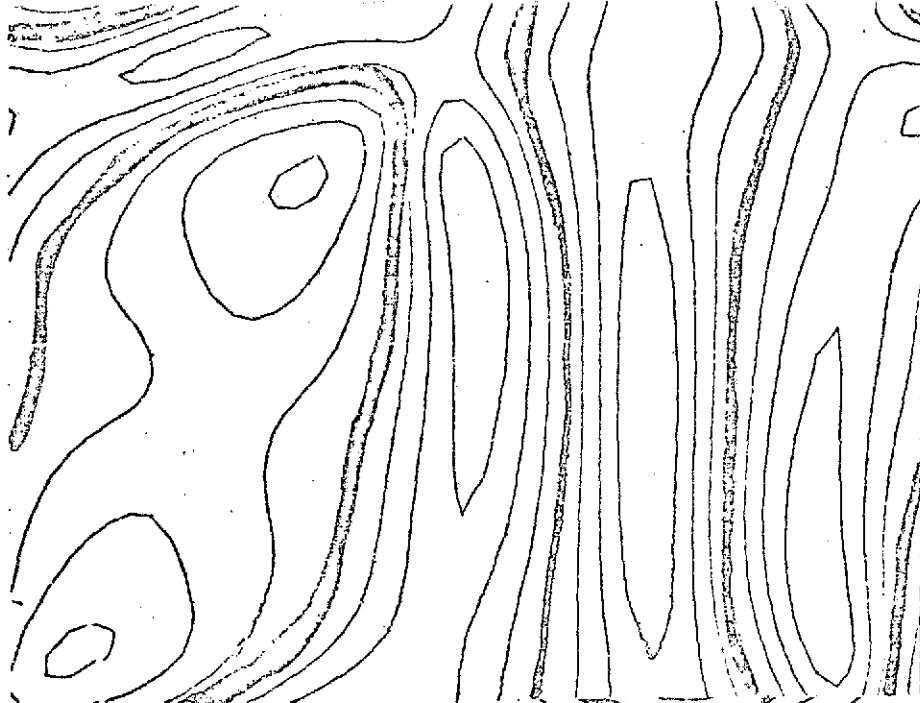


Figure 1. Vertical velocity at $R = 4000$ after 350 time steps.

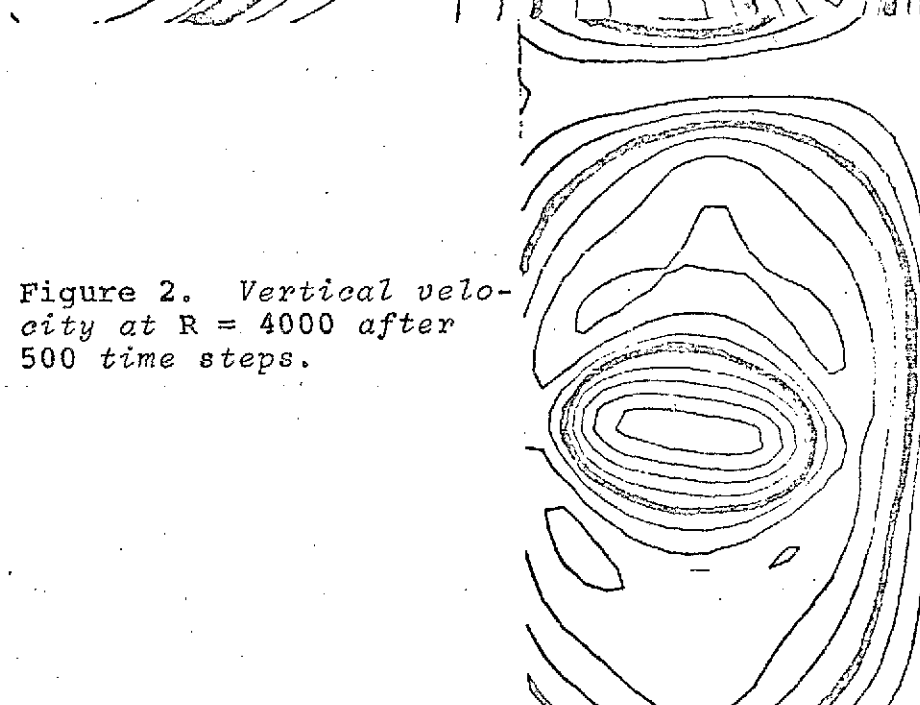


Figure 2. Vertical velocity at $R = 4000$ after 500 time steps.

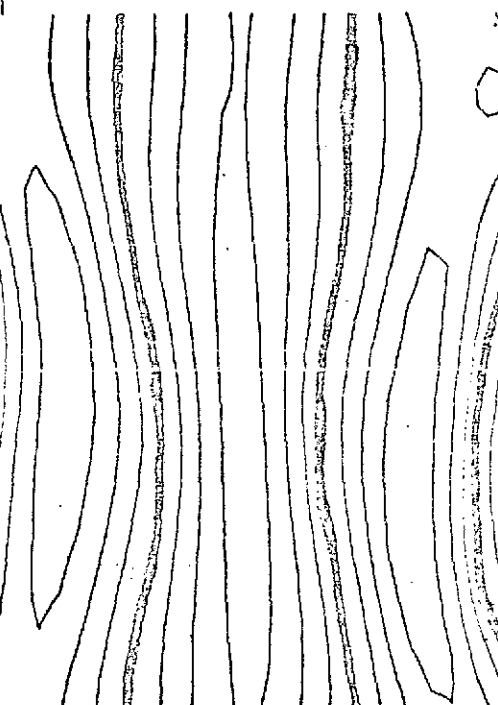
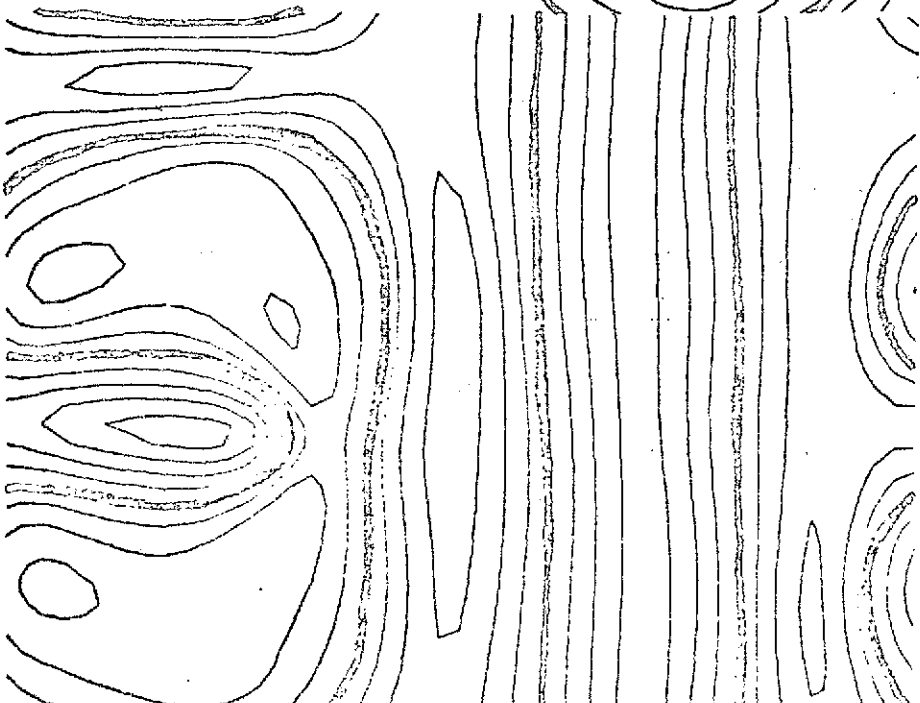


Figure 3. Vertical velocity at $R = 4000$ after 650 time steps.



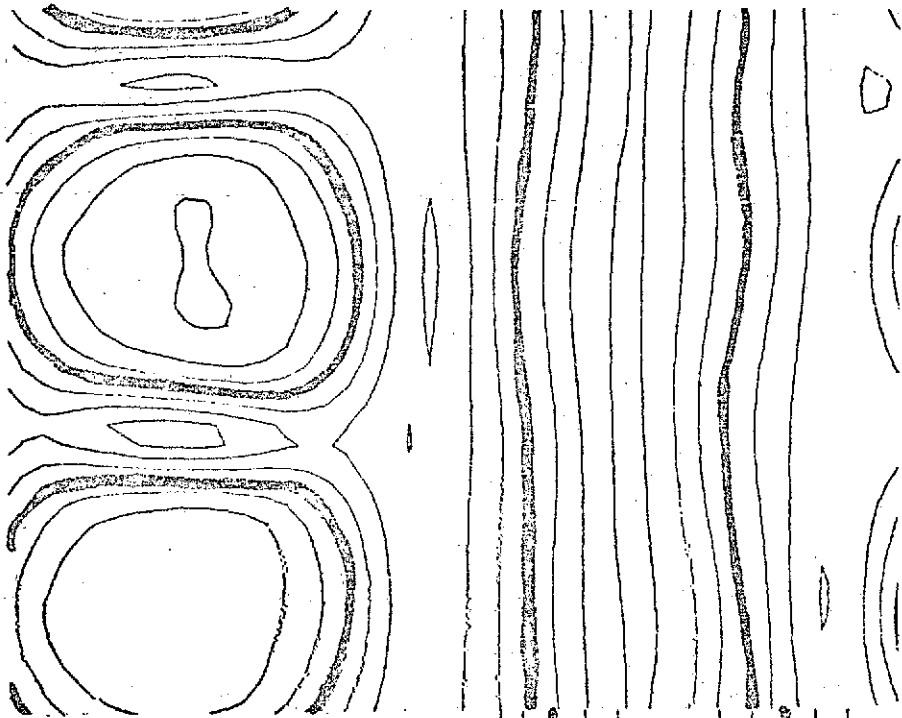
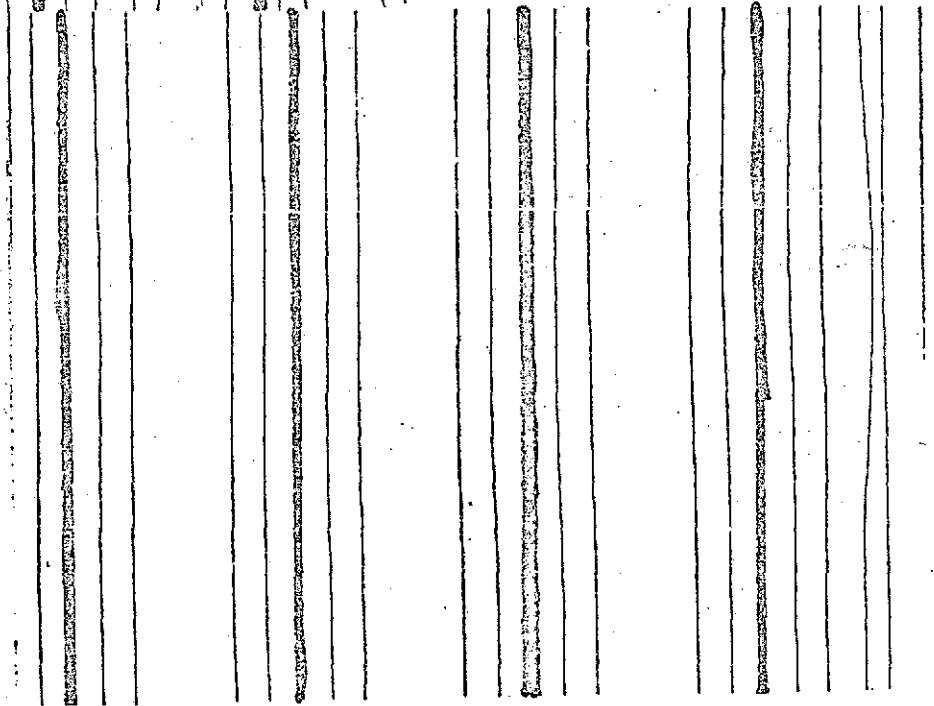


Figure 4. Vertical velocity at $R = 4000$ after 800 time steps.

Figure 5. Vertical velocity at $R = 4000$ after 1100 time steps. The solution is steady.



ATMOSPHERIC CHEMISTRY AND GLOBAL POLLUTION STUDIES, (R. W. Stewart)

The objective of this investigation is to determine the global distribution of minor constituents in the troposphere and stratosphere and the effects which changes in this distribution would have on the physical state of the atmosphere. The minor constituent concentration changes being studied are those which arise subsequent to variations in the natural factors controlling the atmosphere, such as the solar flux, and those which arise subsequent to man-made perturbations of the atmosphere, such as the injection of pollutants into the troposphere and stratosphere. Among the effects being investigated are possible changes in surface ultraviolet radiation levels and in meteorological conditions which might result from alterations in minor constituent distributions.

These studies are motivated by increasing general interest in the chemistry and transport of minor constituents in the atmosphere. This interest includes the effects of contaminant injection into the stratosphere, the emission and dispersal of pollutants and natural trace gases on urban, regional, and global scales in the troposphere, and possible climatic changes resulting from variations in minor constituent concentrations.

The GISS approach to this problem is to conduct concurrent investigations in several areas of atmospheric chemistry and physics each of which forms an independent contribution to an understanding of these areas in addition to being a component of a comprehensive global atmospheric model. A basic element in the program is the determination of the sensitivity of the results to variations in the key parameters on which the calculations are based. These sensitivity analyses are used to estimate confidence limits for the principal results of each computation.

The elements of the program are: atmospheric modeling, chemical kinetics, and remote sensing. Table 1 shows the milestones for the overall program. Table 2 shows the projected computer modeling studies for the 1/73 to 6/73 period. The elements of the program are described more fully in the following sections.

Atmospheric Modeling. (R. Stewart, M. Hoffert, S. Hameed, C. Weng, J. Pinto)

This element of the program is designed to study the spatial and temporal variations of various chemical species in the atmos-

phere. An accurate description of such variations requires the simultaneous solution of the atmospheric energy balance and motion equations and of the continuity equation for each chemical constituent. These calculations must ultimately be done with a time-dependent, multi-dimensional model to allow for both vertical and lateral transport. The extensive operational use of such models will require a significant increase in both computing speed and storage size over present day machines. Nonetheless, the environmental significance of investigations in this area requires that attempts be made to establish the magnitudes of the major effects involved. Accordingly, the present atmospheric modeling effort at GISS is on the development of multi-dimensional models and the operational use of a time-dependent, one-dimensional model. The models presently in use or under development are the following:

- A. GISS time-dependent, one-dimensional model
- B. Mintz-Arakawa two-level general circulation model
- C. GISS nine-level general circulation model
- D. Regional dispersion model

Table 1
Program Milestones

1. Complete development of one-dimensional model	4/72
2. Natural atmosphere and injection simulation experiments completed with one-dimensional model	6/73
3. Initial tracer and validation studies completed with partially coupled two- and nine-level models	6/73
4. Initial chemical/dynamic studies of natural atmosphere completed with global circulation models	1/74
5. Develop three-dimensional dynamic interaction model	6/74
6. Stratospheric injection simulation basic experiments completed with partially coupled global circulation model	7/74
7. Conduct natural and polluted stratosphere/troposphere studies with dynamic interaction model	7/74 - 1/77

Table 2

Computer Modeling Studies: 1/73 to 6/73

<u>Model Description</u>	<u>Objective</u>	<u>Status</u>	<u>S/C Ratio*</u>	<u>Projected Percent of Total Hours</u>	<u>Total Hours</u>
One-dimensional model	Study the response of the stratosphere to specified contaminant injection rates and the sensitivity of the results to variations in key parameters	Production	600	50%	1000
Mintz-Arakawa two-level model	Determine feasibility of employment in studies of global distribution of minor constituents, both natural and contaminant	Test and Development	70	12%	230
GISS nine-level model	Develop for use in studies of natural and contaminant minor constituent distributions in the troposphere and stratosphere	Test and Development	15	38%	770
Urban dispersion	Study dispersion of pollutants on urban and regional scales	Development	150 (est.)	0.3%	6
Chemical kinetics	Study chemistry of polluted atmospheres and methods of performing photochemical calculations in large scale models	Production	400	0.4%	8
Remote sensing	Compute radiance observable from polluted atmospheres. Study feasibility of various observing techniques	Test and Development	not applicable	0.3%	6

156

*The S/C ratio is the ratio of simulation time to computation time.

The projected computer simulation studies for the 1/73 to 6/73 period using the one-dimensional model are shown in Table 3, those for the general circulation models are shown in Table 4. The regional dispersion model is under development and is not expected to require substantial computing resources in the coming six months.

A. GISS time-dependent, one-dimensional model

This model is designed to study the response of the stratosphere to assumed rates of contaminant injection. The program milestones are shown in Table 5. The model is characterized by its ability to handle large numbers of chemical reactions among many constituents over the altitude range from 0 to 200 km. A significant obstacle to the development of such models is the large range of chemical and transport time constants (from micro-seconds to years) implicit in the coupled, non-linear continuity equations. A solution to this problem has been obtained, but at the cost of heavy computational requirements.

Table 3

Program of Computer Simulation Experiments: 1/73 - 6/73

Time-dependent, one-dimensional model

<u>Experiment</u>	<u>Runs Required</u>	<u>Simulation Period (yrs)</u>	<u>Estimated Computer Time (hrs.)</u>
1. Variation of contaminant injection rate	15	2	450
2. Variation of five key reaction rates for two injection rates	10	2	300
3. Variation of stratospheric diffusion coefficient for two injection rates	2	2	60
4. Variation of injection grid	3	2	90
5. Test and development	-	-	100
		Total	1000

Table 4

Program of Computer Simulation Experiments: 1/73 - 6/73

Global circulation models

<u>Experiment</u>	<u>Runs Required</u>	<u>Simulation Period (yrs)</u>	<u>Estimated Computer Time (hrs)</u>
A. Mintz-Arakawa two-level model			
1. Test and development	-	-	100
2. CO ₂ tracer study	1	1	120
B. GISS nine-level model			
1. Test and development	-	-	490
2. CO ₂ , O ₃ tracer study	1	0.5	270
		Total	980

Table 5

Program Milestones

One-dimensional model

1. Complete development, initiate production running	4/72
2. Complete natural atmosphere simulations	10/72
3. Complete injection simulation experiments and sensitivity analyses	6/73

(1) *Study of the Natural Atmosphere.* Initial simulation studies have been made of the natural background of minor atmospheric constituents. Complete validation of the present model is not possible due to the lack of observational data for many minor constituents over large altitude intervals. However, the overall quantitative and qualitative agreement of the preliminary results with observations and with other theoretical models establishes the general validity of the photochemical model and the theoretical methods used in this study.

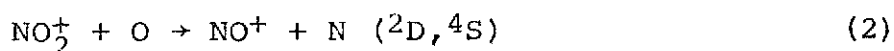
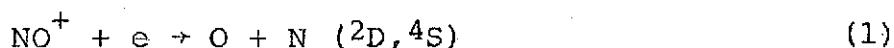
Figures 1 and 2 illustrate some of the results obtained from a four-month simulation of the natural atmosphere. These results are based on numerical solution of the continuity equations for 45 constituents. Ninety chemical reactions are included in the chemical source terms. The upper portion of Figure 1 shows the O and O₃ profiles computed with the present model (solid lines) and compares these profiles with various observations and standard models. The O profile agrees well with the CIRA 1965 model above 150 km. The oxygen profiles deduced from the EUV absorption observations of Hall et al., (1967), (curve 4); and the mass spectrometer measurements of Krankowsky et al., (1968), (curve 5); bracket the upper portion of the theoretical curve. The range of measured O densities at 150 km. compiled by U. von Zahn (1970) is shown by the vertical bar. Below 150 km. the calculated O values are lower than those of the CIRA model which are based on photochemical equilibrium calculations between 80 and 120 km. The inclusion of transport in this altitude region has the effect of lowering the O densities from the photochemical equilibrium values. This is also seen in the theoretical models of Keneshea and Zimmerman (1970) and Bowman et al. (1970). The low-altitude measurements of O densities by Henderson (1971) are shown by curve 2 in Figure 1.

The magnitude of the maximum O₃ densities shown in Figure 1 agrees with that of the ozone profile from the U. S. Standard Atmosphere Supplements 1966 (curve 1) but is about 6 km. higher in altitude. The upper portion of the computed O₃ profile is compared with the night time observations of Hays, Roble, and Shah (1972), (curve 3). The lower portion of Figure 1 shows the growth of O and O₃ with time in the theoretical model.

Figure 2 shows the calculated NO and NO₂ profiles (solid curves). The stratospheric NO profile computed by Crutzen (1971) (curve 1), the observed stratospheric values of Hale (1972) (curve 2), the observed mesospheric values of Barth (1966) (curve 4), and Meira (1971) (curve 3), the inferred thermospheric NO densities of Smith (1966) (curve 6), and Monro and Bowhill (1969) (curve 5, day; curve 7, night) are shown for comparison.

The NO values of Crutzen in the lower stratosphere are larger than those computed in the present model but are comparable to the total NO_x. Crutzen's theoretical profile also lacks the stratospheric NO minimum which is produced by ozone oxidation, $\text{NO} + \text{O}_3 \rightarrow \text{NO}_2 + \text{O}_2$ in this calculation. Such a minimum is present in the models presented by McElroy (1972) whose preferred NO values are somewhat lower in the 15 - 50 km. region than those of the current model. The observations of Hale (1972), as reported by McElroy (1972) agree well with the theoretical NO profile in the upper stratosphere.

The calculated mesospheric NO values are much lower than the observed values of Barth (1966) and Meira (1971). The mesospheric photochemistry of nitric oxide has been discussed in detail by Strobel et al. (1970) and Strobel (1971a, 1971b, 1972). These authors point out that the NO concentration in the mesosphere is extremely sensitive to the fraction of atomic nitrogen produced in the metastable N(2D) state. Since this fraction is unknown it is an adjustable parameter in theoretical models. The important reactions are



In the present model 67 percent of the N was assumed to be produced in the 2D state by (1) and 0 percent was produced in this state by (2). Model studies in progress assume 50 percent N(2D) production by reaction (2) and give much better agreement between observed and calculated NO densities in the mesosphere.

Above 120 km. the daily average NO profile falls between the day and night values inferred from the data of Monro and Bowhill (1969). The value of 6.3×10^{-10} cm³/sec for the $\text{O}_2^+ + \text{NO} \rightarrow \text{NO}^+ + \text{O}_2$ charge exchange reaction was used in computing the points on curves 5 and 7. The post-sunrise NO values of Smith (1966) are also shown for comparison (curve 6).

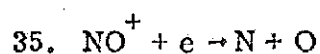
(2) *Injection Simulation Experiments.* Initial results from two injection simulation experiments are shown in Figures 3-7. The photochemistry included in these calculations was a reduced set of 47 reactions among the nitrogen and oxygen components of the atmosphere (Table 6). In this model sinks for odd nitrogen in the stratosphere and troposphere are implicit in the fixed number densities maintained at the lower boundary. The data used for the injection source are shown in Table 7. The first 6 months

Table 6

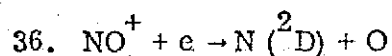
Reactions and Reaction Rates used in the Injection Simulation Experiments*

Reaction	Rate
1. $O(^1D) \rightarrow O(^3P) + h\nu$	9.1×10^{-3}
2. $N(^2D) \rightarrow N(^4S) + h\nu$	1.1×10^{-5}
3. $O_2(^1\Delta_g) \rightarrow O_2(^3\Sigma_u) + h\nu$	2.8×10^{-4}
4. $O(^1D) + N_2 \rightarrow O(^3P) + N_2$	8.0×10^{-4}
5. $O(^1D) + O_2 \rightarrow O(^3P) + O_2$	5.0×10^{-11}
6. $O_2(^1\Delta_g) + N_2 \rightarrow O_2(^3\Sigma_u^-) + N_2$	3.0×10^{-21}
7. $O_2(^1\Delta_g) + N_2O \rightarrow O_2(^3\Sigma_u^-) + N_2O$	7.5×10^{-20}
8. $O_2(^1\Delta_g) + O_2 \rightarrow O_2(^3\Sigma_u^-) + O_2$	$2.2 \times 10^{-18} \left(\frac{T}{300}\right)^{0.78}$
9. $O_2(^1\Delta_g) + O \rightarrow O_2(^3\Sigma_u^-) + O$	2.0×10^{-14}
10. $N(^2D) + O \rightarrow N(^4S) + O$	2.0×10^{-13}
11. $O + O_3 \rightarrow O_2 + O_2$	$1.0 \times 10^{-11} e^{-2169/T}$
12. $O + O + M \rightarrow O_2 + M$	$3.6 \times 10^{-31} T^{-1} e^{-170/T}$
13. $O + O_2 + M \rightarrow O_3 + M$	$6.2 \times 10^{-35} e^{1050/T}$
14. $O(^1D) + O_3 \rightarrow O_2 + O_2$	3.0×10^{-10}
15. $O_2(^1\Delta_g) + O_3 \rightarrow O_2 + O_2 + O$	2.8×10^{-15}

16. $\text{N}_2\text{O} + \text{O} (^1\text{D}) \rightarrow \text{NO} + \text{NO}$	1.0×10^{-10}
17. $\text{N}_2\text{O} + \text{O} (^1\text{D}) \rightarrow \text{N}_2 + \text{O}_2$	1.0×10^{-10}
18. $\text{NO} + \text{O}_3 \rightarrow \text{NO}_2 + \text{O}_2$	$9.0 \times 10^{-13} e^{-1200/T}$
19. $\text{NO}_2 + \text{O} \rightarrow \text{NO} + \text{O}_2$	$9.1 \times 10^{-12} e^{-530/T}$
20. $\text{NO}_2 + \text{O}_3 \rightarrow \text{NO}_3 + \text{O}_2$	6.1×10^{-17}
21. $\text{NO}_3 + \text{NO} \rightarrow \text{NO}_2 + \text{NO}_2$	1.0×10^{-11}
22. $\text{N} + \text{O}_2 \rightarrow \text{NO} + \text{O}$	$2.4 \times 10^{-11} e^{-3975/T}$
23. $\text{N}(^2\text{D}) + \text{O}_2 \rightarrow \text{NO} + \text{O}$	6.0×10^{-12}
24. $\text{N} + \text{O}_3 \rightarrow \text{NO} + \text{O}_2$	$3.0 \times 10^{-11} e^{-1200/T}$
25. $\text{N} + \text{NO} \rightarrow \text{N}_2 + \text{O}$	2.2×10^{-11}
26. $\text{O}^+ + \text{O}_2 \rightarrow \text{O} + \text{O}_2^+$	$2.0 \times 10^{-11} \left(\frac{300}{T}\right)^{0.5}$
27. $\text{O}^+ + \text{N}_2 \rightarrow \text{N} + \text{NO}^+$	$1.2 \times 10^{-12} \left(\frac{300}{T}\right)^{0.35}$
28. $\text{N}_2^+ + \text{O}_2 \rightarrow \text{N}_2 + \text{O}_2^+$	$4.7 \times 10^{-11} \left(\frac{300}{T}\right)^{1.66}$
29. $\text{N}_2^+ + \text{O} \rightarrow \text{N} + \text{NO}^+$	1.4×10^{-10}
30. $\text{N}_2^+ + \text{NO} \rightarrow \text{N}_2 + \text{NO}^+$	3.3×10^{-10}
31. $\text{O}_2^+ + \text{NO} \rightarrow \text{O}_2 + \text{NO}^+$	6.3×10^{-10}
32. $\text{O}_2^+ + \text{N} \rightarrow \text{O} + \text{NO}^+$	1.8×10^{-10}
33. $\text{N}_2^+ + e \rightarrow \text{N} + \text{N}$	2.8×10^{-7}
34. $\text{O}_2^+ + e \rightarrow \text{O} + \text{O}$	$2.1 \times 10^{-7} \left(\frac{300}{T}\right)$



$$1.0 \times 10^{-7} \left(\frac{300}{T} \right)$$



$$3.0 \times 10^{-7} \left(\frac{300}{T} \right)$$

* The reaction scheme also includes photodissociation and photoionization reactions involving O, O₂, O₃, N₂, N₂O, NO, NO₂, and NO₃. Units are sec⁻¹ for unimolecular reactions, cm³/sec for bimolecular reactions and cm⁶/sec for termolecular reactions.

Table 7

EMISSION DATA					
SMIC ESTIMATES (15,000 kg. fuel/hr.)*					
Constituent	Emission Index (g/kg. fuel)	Hourly Emission (kg.)	Natural Concentration in Stratosphere (ppm)	Pollution Injection Rate † (cm ⁻³ sec ⁻¹)	
				Max.	Min.
CO ₂	3000	45000	485	6.4 × 10 ⁶	1.8 × 10 ⁵
H ₂ O	1300	19500	2 - 40	6.7 × 10 ⁶	1.9 × 10 ⁵
CO	40	600	.04**	1.3 × 10 ⁵	3.8 × 10 ³
NO	40	600	.001 - .04	1.3 × 10 ⁵	3.5 × 10 ³
SO ₂	1	15	10 ⁻³ - 10 ⁻⁴	-	-
Soot	0.1	1.5	0 - 10 ⁻⁴	-	-

*Except as Indicated

**Seiler and Warneck (1972)

†Max. rates based on injection into a 2 km. height interval, 10° latitude belt
Min. rates based on injection into a 2 km. high spherical shell (360°)

of the simulation permits the natural background of minor constituents to attain near-equilibrium values. Pollutant injection is initiated at 6 months at an altitude of 26 km. and maintained at a constant rate thereafter. The injection altitude is chosen as 26 km. to compensate for the approximately 6 km. altitude error in the ozone profile.

The one-dimensional model, by assuming either negligible lateral re-distribution (maximum injection) or complete lateral re-distribution (minimum injection) of pollutants, can be used to delineate the maximum and minimum effects of pollution near the region of contaminant injection. An accurate treatment of lateral transport is required to assess the effects of stratospheric contamination at locations remote from the injection site.

Figures 3 and 4 show the NO, NO₂ and O₃, O profiles for the minimum rate after 18 months of injection. Figures 5 and 6 show the corresponding profiles for the maximum rate. Figure 7 shows the decrease of total ozone with time subsequent to injection. The triangles on the maximum injection curve show the result of doubling the rate assumed for the reaction $\text{NO} + \text{O}_3 \rightarrow \text{NO}_2 + \text{O}_2$ (which is believed known to $\pm 30\%$). Although the peak ozone densities were decreased by about 10 percent in this calculation, the decrease in total ozone amount, expressed as a percentage of initial ozone, was completely insensitive to this rate constant variation. Studies in progress indicate similar results for the sensitivity to some other important rate constants. The ozone decrease subsequent to NO_x injection appears to be far less sensitive to the values used for many chemical rate constants than are the computed densities of the various chemical species in the model. A precise determination of the values for the many rate constants of importance in stratospheric photochemistry, though certainly necessary for calculating accurate values of the natural background of stratospheric constituents, may not be essential for a determination of the response of the stratosphere to specified contaminant injection rates.

The large spread in effect between the maximum and minimum rates clearly indicates the need for a full three-dimensional calculation with the effect of dynamics on the pollutant distribution taken into account. Such a model is presently being developed at GISS and should become operational during calendar year 1973.

B. Mintz-Arakawa two-level model

This program is being tested to determine the feasibility of employing it in studies of the global distribution of natural and

contaminant minor constituents in the troposphere. The model is presently being employed in CO₂ tracer studies. Photochemical interaction will be added at a later date. The program milestones are shown in Table 8.

Carbon dioxide exists in the atmosphere as a trace gas with a global average concentration of 325 ppm. It is the main source of organic carbon for the world's plant mass, plays a major role in determining the earth's heat balance, and exhibits a long term increase due to industrial emissions. Carbon dioxide tracer studies with global circulation models will thus be useful not only in validating the model dynamics prior to the introduction of photochemical interactions, but in obtaining a fundamental understanding of the role of CO₂ in the earth's carbon cycle and in assessing the meteorological effects of anthropogenic sources.

The initial step in this study is the compilation of a global carbon dioxide emissions inventory. Such an inventory requires knowledge of the amounts of CO₂ in the various global reservoirs and the rates of CO₂ exchange between these reservoirs. Table 9 gives the masses and exchange rates presently being used. Emission rates have been computed from these data for the grid used in the Mintz-Arakawa model. These are shown in Figure 8. In this figure land areas have been divided into forests (F), grasslands (G), deserts (D), and agricultural (hatched) regions. The emissions calculated for each are:

forests	.087	g/cm ²
grasslands	.0249	g/cm ²
deserts	.000938	g/cm ²
agricultural	.142	g/cm ²

Emission rates over ice are zero. Efforts are presently underway to include the marine reservoir in the global emissions inventory.

In the current model runs, the CO₂ amounts assimilated and respired by each vegetation type are assumed to be proportional to the amount of carbon they contain. Assimilation is assumed to

Table 8
Program Milestones
Two-level model

1.	Develop tracer-study capability	2/73
2.	Complete 1 year simulation CO ₂ tracer study	6/73
3.	Begin study of atmospheric carbon cycle with simplified CH ₄ /H ₂ O photochemistry	7/73
4.	Complete 2 year simulation of natural atmosphere with CH ₄ /H ₂ O chemical scheme	1/74
5.	Couple to regional dispersion model; begin global pollution injection simulations	2/74
6.	Complete sensitivity analyses for natural atmosphere with CH ₄ /H ₂ O scheme	7/74
7.	Conduct natural and polluted atmosphere studies and sensitivity analyses	post 7/74

Table 9

Reservoir	mass	Exchange Rates (years ⁻¹)		
		atmosphere	biosphere	marine
atmosphere	2.5	- -	.333	.20
biosphere	4.5	.017	- -	- -
marine	3.05	.17	- -	- -

occur only during a specified growing season (March 21 to September 21, in the northern hemisphere). This should result in seasonal variations of ± 4.5 ppm CO_2 about the mean atmospheric value. Industrial emissions will not be included in the initial tracer studies so that their effects may be assessed in subsequent model runs.

C. The GISS nine-level model

This program is being developed for use in study of the natural and contaminant distribution in both stratosphere and troposphere. The model is presently being employed in CO_2 tracer studies for comparison with the results of the two-level model. Ozone tracer studies and photochemical interactions will be added at a later date. The program milestones are shown in Table 10.

D. Regional dispersion model

Work has just been initiated on a regional dispersion model at GISS. The objective of this effort is to predict the concentration of pollutant species over urban and regional areas given an emissions inventory and meteorological data for the region of interest. The program milestones for this study are shown in Table 11.

The approach to this problem is to divide the urban or regional area under study into a number of cells in each of which the various chemical species are assumed to be well mixed. The mass balance equation is then solved for each species in each cell with advection between cells being taken into account. In the future this model will be coupled to the GISS global circulation models to study the feasibility of using these models to provide the meteorological boundary conditions for regional dispersion calculations.

Chemical Kinetics. (M. Hoffert, R. Stewart, S. Lebedeff)

Objectives and approach: The objectives of this element of the program are as follows:

Table 10
Program Milestones
Nine-level model

1. Develop tracer-study capability	2/73
2. Complete 1/2 year natural atmosphere simulation with CO ₂ and O ₃ tracers	6/73
3. Complete 1 year natural atmosphere simulation with simplified O ₃ photochemistry	1/74
4. Complete 1 year natural atmosphere simulation with basic oxygen-nitrogen-hydrogen chemistry	7/74
5. Develop dynamic interaction model	6/74
6. Conduct natural and polluted stratosphere/troposphere studies with dynamic interaction model	post 7/74

Table 11
Program Milestones
Regional Dispersion Model

1. Develop production model	4/73
2. Validate on major urban and regional airsheds	7/73
3. Couple to chemical kinetics model	8/73
4. Complete study of major urban and regional airsheds	1/74
5. Couple to G.C.M. models	2/74

1. To carry out studies of the chemistry of minor constituents of special interest in polluted and natural atmospheres with a view to obtaining a basic understanding of the important chemical processes involved in production and loss of these constituents (such as SO_2 , NO_2 , O_3 and hydrocarbons).

2. To develop efficient programming and mathematical techniques for solving the equations of chemical kinetics, to utilize these techniques in studying the chemical processes occurring in the natural atmosphere and in polluted urban atmospheres, and to adapt these techniques to the more general problem of pollutant dispersion on urban, regional and global scales. Program milestones are shown in Table 12.

Chemical processes occurring in polluted atmospheres and in the natural atmosphere are complex and as yet little understood. A large number of organic and inorganic reactions are involved, many rates have yet to be measured, and it seems likely that important reactions remain to be discovered. These circumstances require that both objectives stated above be pursued. Basic studies of the chemistry of individual constituents are needed to determine the reactions (often in "lumped" parameter form) which must be included in the mathematical modeling.

Table 12

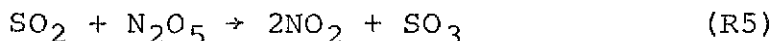
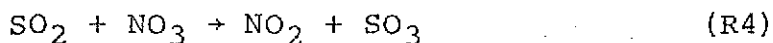
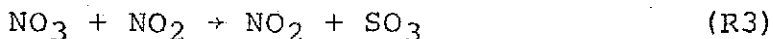
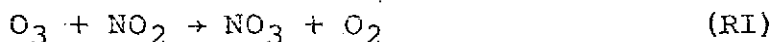
Program Milestones

Chemical Kinetics Model

1. Develop and validate production version	12/72
2. Complete study of NO_x - O_2 -CO- H_2O system	3/73
3. Complete study of SO_2 effect on photochemical smog	6/73
4. Complete study of natural background of minor constituents	7/73
5. Couple to urban/regional dispersion model	8/73
6. Complete study of polluted urban atmosphere using dynamic smog chamber model	1/74

Basic studies. In line with the first objective, M. Hoffert and R. Stewart have completed a study of the chemistry of sulfur dioxide (SO₂) in urban atmospheres. Although SO₂ is a major atmospheric pollutant, the chemical kinetic mechanisms by which it is removed from the atmosphere are not well understood. The problem is that proposed removal mechanisms predict a chemical lifetime of several days for SO₂ whereas observations of polluted atmospheres indicate lifetimes as short as several hours. Smog chamber experiments have shown that sulfur dioxide strongly influences the time-histories of other major pollutants such as nitrogen dioxide (NO₂) and ozone (O₃). Identification of the mechanism responsible for the removal of sulfur dioxide is thus a key link in understanding the chemistry of polluted urban atmospheres.

Hoffert and Stewart have proposed that inorganic oxidation reactions by NO₃ and N₂O₅ provide a major (though not necessarily unique) mechanism for the rapid removal of sulfur dioxide from polluted atmospheres. The basic set of reactions considered were



This hypothesis was shown to be consistent with smog chamber experiments on the evolution of RH, NO, NO₂, SO₂, and O₃ and with observed SO₂ lifetimes in polluted atmospheres.

Table 13 shows the ambient annual average concentrations of NO₂, O₃, and SO₂ measured in eight U. S. cities in the Continuous Air Monitoring Project (CAMP) of the U. S. Environmental Protection Agency and the corresponding lifetimes of sulfur dioxide computed on the basis of reactions R1-R5. Considerable variation exists between cities (and, we may presume, within cities, since concentrations fluctuate appreciably about the mean), but the lifetimes are generally of the correct magnitude. The significant fact about these results is that they were computed from measured average concentrations and chemical rate constants so that the major assumptions involve only the validity of the proposed kinetic scheme. An

additional conclusion drawn from this work is that it is not appropriate to treat sulfur dioxide removal as a linear process characterized by a "universal" time constant as has been done in several kinetic models.

Photochemical smog modeling has thus far focused on understanding the atmospheric chemistry in areas such as the Los Angeles basin. This study has shown that other major cities contain sufficient ambient ozone and nitrogen dioxide to seriously influence, and possibly dominate, sulfur dioxide removal rates. This suggests a much broader applicability of nonlinear chemical kinetics modeling to air pollution simulation problems than has hitherto been believed.

Mathematical modeling. A chemical kinetics computer program has been developed which is designed to investigate a wide range of air pollution problems with minimal re-programming for each particular case. Several

Table 13

Chemical lifetime of sulfur dioxide computed with proposed model from CAMP data for average conditions in urban atmospheres

City	NO ₂	O ₃	SO ₂	T _r
	(ppm)	(ppm)	(ppm)	(hr)
Chicago	0.044	0.026	0.142	41.3
Cincinnati	0.035	0.026	0.029	10.6
Denver	0.035	0.035	0.018	4.9
Los Angeles	0.054	0.037	0.018	3.0
Philadelphia	0.035	0.027	0.081	28.6
St. Louis	0.026	0.035	0.047	17.2
San Francisco	0.053	0.018	0.010	3.5
Washington, D.C.	0.035	0.026	0.053	19.4

mathematical techniques are being studied to determine which are best suited to dealing with the problem of "stiffness" (time constant domination) which characterizes the differential equations of chemical kinetics.

Problems to be investigated with this model include static and dynamic smog chamber simulation experiments, urban air pollution studies, and chemical modeling of the ambient natural atmosphere. Results thus far include simulation of the Hecht-Seinfeld photochemical smog model. The reactions included in the study are shown in Table 14. A comparison of computed and observed (smog-chamber experiment) time histories of NO_2 , NO , C_3H_6 , and O_3 are shown in Figure 9. These theoretical results are very close to those obtained by other investigators using the same chemical reaction scheme and constitute validation of the mathematical model.

Remote Sensing. (J. Susskind)

Objectives and approach. The objectives of this element of the program are:

- 1) To compute the observable radiance which would result from a given distribution of atmospheric pollutants, and
- 2) To invert given radiance values to obtain atmospheric pollutant distributions.

The program milestones are shown in Table 15.

The approach to this problem is to utilize molecular theory to compute the positions and intensities of the important lines in the vibration-rotation spectra of pollutant molecules such as NO_2 , SO_2 , CO , and CH_4 and to apply these results to the calculation of accurate transmissions for specified pollutant distributions. The first phase of this study (radiance calculation) will permit the utilization of experimental data for refinement and validation of the pollutant dispersion models being developed at GISS. Realization of the second phase (radiance inversion) may permit the utilization of experimental data for initialization and updating these dispersion models.

Table 14

Hecht-Seinfeld (1972) lumped parameter photochemical kinetic model for HC/NO₂/CO/H₂O mixture.

Hydrocarbon = HC = 1 Butene taken as kinetically equivalent to isobutene in Hecht-Seinfeld model

Ambient (smog chamber) background: [O₂] = 2.09 × 10⁵ ppm, [M] = 1.00 × 10⁶ ppm, [H₂O] = 3.1 × 10⁴ e;

e = relative humidity (e = 1.00 for RH 100%).

Reaction	Reaction rate, k _r	Comment
1. NO ₂ + hν → NO + O	k ₁ = 0.5 min ⁻¹	NO ₂ photolysis rate measured in Wilson-Levy (1968, 1969, 1970) experiments. Hecht and Seinfeld used 0.37 min ⁻¹ for evaluation of Westberg - Cohen (1971) experiment with isobutene. Hecht - Seinfeld pseudo-first-order rate recovered using ambient concentrations: k ₂ ' = [O ₂]. [M] · k ₂ = 2.76 × 10 ⁶ min ⁻¹ .
2. O + O ₂ + M → O ₃ + M	k ₂ = 1.32 · 10 ⁻⁵ ppm ⁻² min ⁻¹	
3. O ₃ + NO → NO ₂ + O ₂	k ₃ = 21.8 ppm ⁻¹ min ⁻¹	
4. O ₃ + NO ₂ → NO ₃ + O ₂	k ₄ = 6.0 · 10 ⁻³ ppm ⁻¹ min ⁻¹	
5. NO ₃ + NO ₂ + H ₂ O → 2HNO ₃	k ₅ = 4.62 · 10 ⁻⁶ ppm ⁻² min ⁻¹	Hecht-Seinfeld pseudo-second-order rate recovered for e = 0.7 ([H ₂ O] = 2.17 × 10 ⁴ ppm): k ₅ ' = [H ₂ O] k ₅ = 0.1 ppm ⁻² min ⁻¹
6. NO + NO ₂ + H ₂ O → 2HNO ₂	k ₆ = 1.15 · 10 ⁻⁷ ppm ⁻² min ⁻¹	
7. HNO ₂ + hν → OH + NO	k ₇ = 0.0068 min ⁻¹	Hecht-Seinfeld pseudo-second-order rate recovered for e = 0.7 ([H ₂ O] = 2.17 × 10 ⁴ ppm): k ₆ ' = [H ₂ O] k ₆ = 2.5 × 10 ⁻³ ppm ⁻¹ min ⁻¹
8. CO + OH + O ₂ → CO ₂ + HO ₂	k ₈ = 0.96 · 10 ⁻³ ppm ⁻² min ⁻¹	
9. HO ₂ + NO → NO ₂ + OH	k ₉ = 1800 ppm ⁻¹ min ⁻¹	scaled from Hecht-Seinfeld value of 0.005 min ⁻¹ by ratio of NO ₂ photolysis rates ~0.5/0.37 ~1.35
10. HO ₂ + NO ₂ → HNO ₂ + O ₂	k ₁₀ = 10 ppm ⁻¹ min ⁻¹	
11. HC + O → α ROO	k ₁₁ = 3.1 · 10 ⁴ ppm ⁻¹ min ⁻¹	Hecht-Seinfeld pseudo-second-order rate recovered using ambient O ₂ concentrations: k ₈ ' = [O ₂] · k ₈ = 200 ppm ⁻¹ min ⁻¹
12. HC + O ₃ → β ROO + γ RCHO	k ₁₂ = 0.017 ppm ⁻¹ min ⁻¹	
13. HC + OH → δ ROO + ε RCHO	k ₁₃ = 1. · 10 ⁴ ppm ⁻¹ min ⁻¹	effective stoichiometric coeff: α = (2.45; [NO]/[HC] ≤ 0.25) (9.8 × [NO]/[HC]; 0.25 < [NO]/[HC] ≤ 1), ROO is a lumped peroxy-alkyl or peroxyacyl specie
14. ROO + NO → NO ₂ + ROH	k ₁₄ = 1800 ppm ⁻¹ min ⁻¹	effective stoichiometric coeff: β = 1.9, γ not used
15. ROO + NO ₂ → PAN	k ₁₅ = 10 ppm ⁻¹ min ⁻¹	effective stoichiometric coeff: δ = 0.2, ε not used
		effective stoichiometric coeff: θ = 0.22

Utilization of experimental data. Reliance on molecular theory in the calculation of band intensities for important pollutant molecules is dictated by the dearth of experimental data available for such molecules. Experimental transmissions, when available at all, are ususally measured for a relatively small number of temperatures and path lengths. Such limited data can not be accurately extrapolated to the non-homogeneous paths which must be considered in atmospheric calculations. Laboratory spectra will be utilized in this study to determine the molecular parameters, such as rotational constants for different vibrational states, band strengths, and line widths, which are required for calculation of the absorptive properties of atmospheric pollutants.

The first molecule selected for study is nitrogen dioxide, a major atmospheric pollutant. The most intense absorption band of this molecule is the ν_3 band centered at 1617 cm^{-1} . This band is strongly overlapped by the ν_2 (6.3μ) band of water vapor which absorbs most of the terrestrial radiation at these wavelengths. There is, however, a window in the 6.3μ band between 1580 cm^{-1} and 1620 cm^{-1} which makes this region suitable for monitoring the NO_2 distribution.

Table 15

Program Milestones

Remote Sensing

- | | |
|--|-------|
| 1. Complete data acquisition and molecular structure calculation for NO_2 | 4/73 |
| 2. Complete development of atmospheric transmission model for $\text{CO}_2/\text{H}_2\text{O}/\text{NO}_2$ atmospheres | 7/73 |
| 3. Include SO_2 , SO_3 , CO , PAN, CH_4 , NO , NO_3 , HNO_2 , HNO_3 , H_2SO_4 , O_3 in transmission model | 6/74 |
| 4. Include particulates | 9/74 |
| 5. Couple to combined chemical/dynamic urban and regional pollution model | 11/74 |
| 6. Develop inversion model | 1/76 |

The ν_3 band of NO_2 has not been studied in the laboratory with sufficiently high resolution to determine accurate molecular constants. Present calculations are based on low resolution (5 cm^{-1}) measurements of the ν_3 band and extrapolation from higher resolution measurements on the $\nu_1 + \nu_3$ and $2\nu_1 + \nu_3$ bands and, although the agreement between these measurements and theoretical calculations is satisfactory (see below), improvement is anticipated as higher resolution data become available. In the near future the spectra of the ν_3 band of NO_2 will be measured using the Perkin-Elmer 621 infrared spectrometer in the Columbia University Chemistry Department. Resolution of up to 0.1 cm^{-1} may be obtained with this instrument which will permit an accurate determination of the band parameters used in the theoretical calculations as well as validation of these calculations.

Results of molecular structure calculations for NO_2 .
Some results obtained thus far in this program are shown in Figures 10-12. Figure 10 compares low resolution (5 cm^{-1}) ν_3 band absorption data with the theoretical calculation of the band absorption which would be observed at this resolution at 298K. The region of primary interest in the 6.3μ water vapor band window is indicated on the figure. Agreement is good except for the wings and band center. The deviations in the wings may be due to intensity perturbations in the higher rotational transitions which have not been included in the present calculations. The wings are of no concern since they are completely overlapped by the water vapor band. Agreement in the band center may improve once more accurate measurements are available.

Figure 11 shows the theoretical spectra at 298K that would be observed at 0.5 cm^{-1} and at 5.0 cm^{-1} resolution. The higher spectral resolution will clearly provide greater sensitivity to the presence of pollutants and will substantially reduce the relative H_2O background absorption in the region of interest.

Figure 12 shows the theoretical temperature dependence of the band absorption under 5 cm^{-1} resolution. At higher resolution the temperature dependence will be much greater. This result again illustrates the necessity of theoretical calculations of the molecular band structure since the temperature must be included in computing the absorption along atmospheric paths.

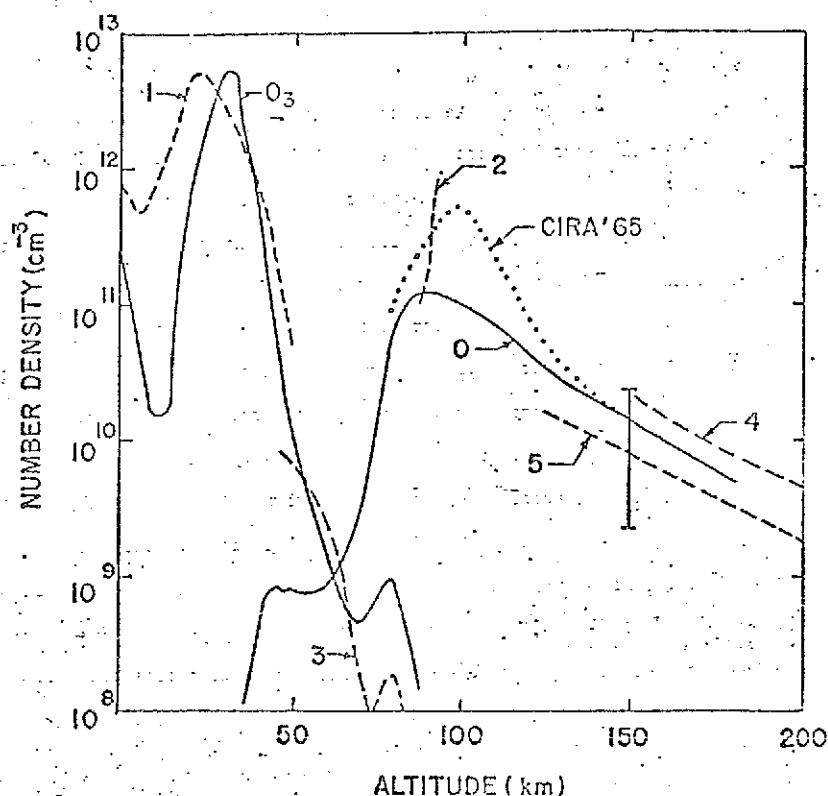
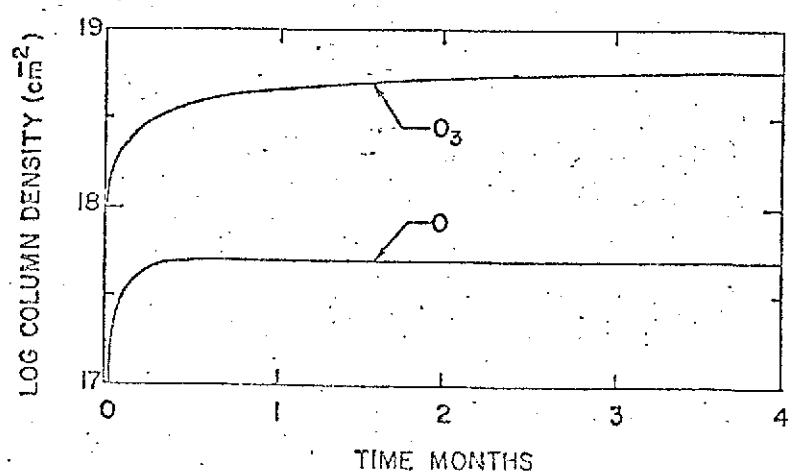


Figure 1. Upper figure: computed O_3 and O profiles (solid curves) compared with observations and standard models (dashed curves). Curve 1, U. S. standard atmosphere supplement O_3 profile. Curve 2, densities observed by O Henderson (1971). Curve 3, O_3 densities (night) observed by Hays, Roble, and Slah (1972). Curve 4, O densities observed by Hall et. al. (1967). Curve 5, O densities observed by Krankowsky et. al. (1968). The vertical bar is the range of O densities observed at 150 km. compiled by U. von Zahn (1970). The CIRA'65 mean O profile is also shown for comparison.



Lower figure: growth of total O_3 and O with time in the model calculations.

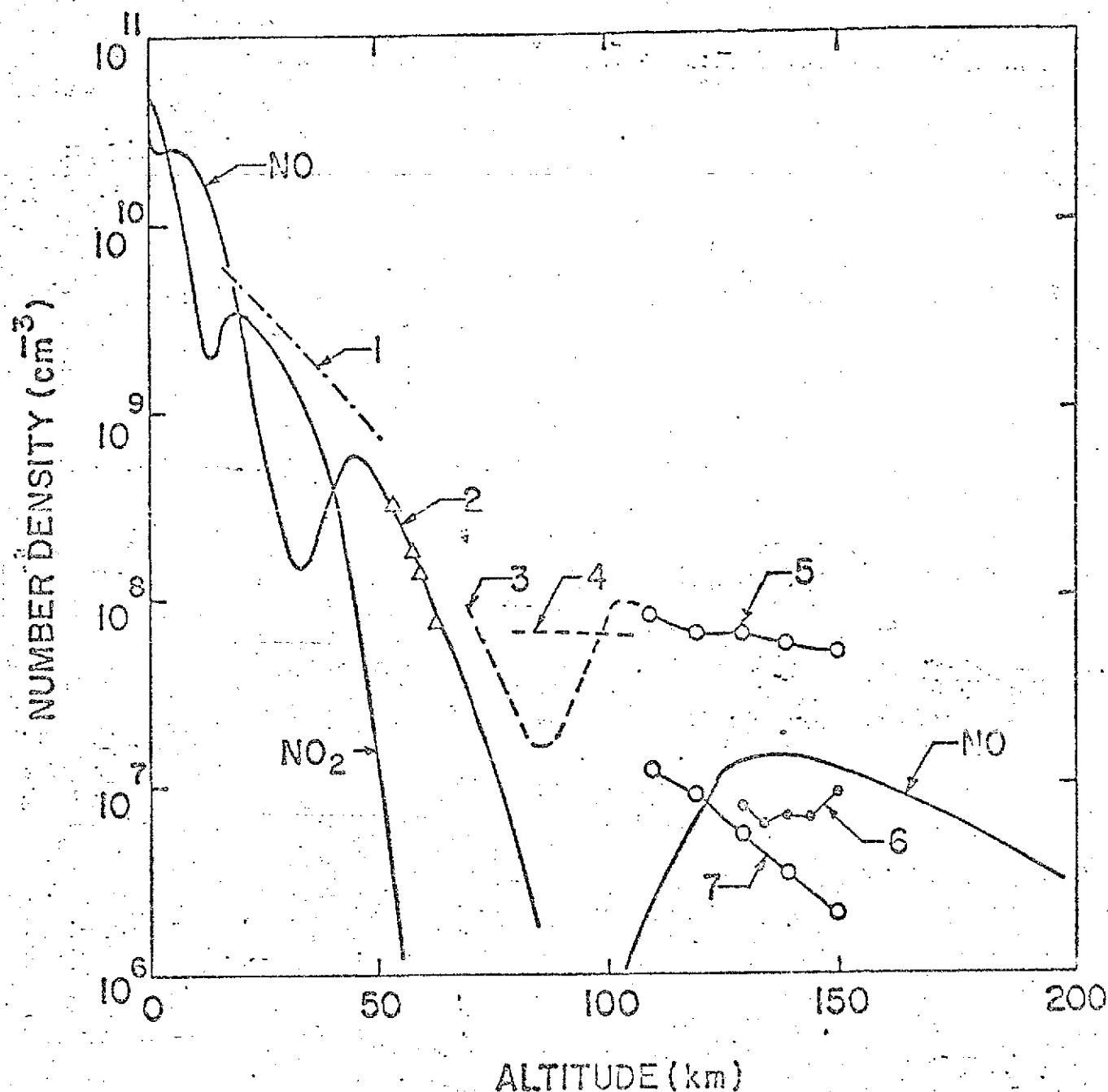


Figure 2. Computed NO₂ and NO profiles (solid curves) compared with observations (dashed curves or connected points) and with Crutzen's theoretical NO profile (dash-dot curve). Curve 2, NO-densities observed by Hale (1972). Curves 3 and 4, NO-densities observed by Meira (1971) and Barth (1966). Curve 5, daytime NO densities inferred from data of Monro and Bowhill (1966). Curve 6, post-sunrise NO densities of Smith. Curve 7, same as 5 for night time.

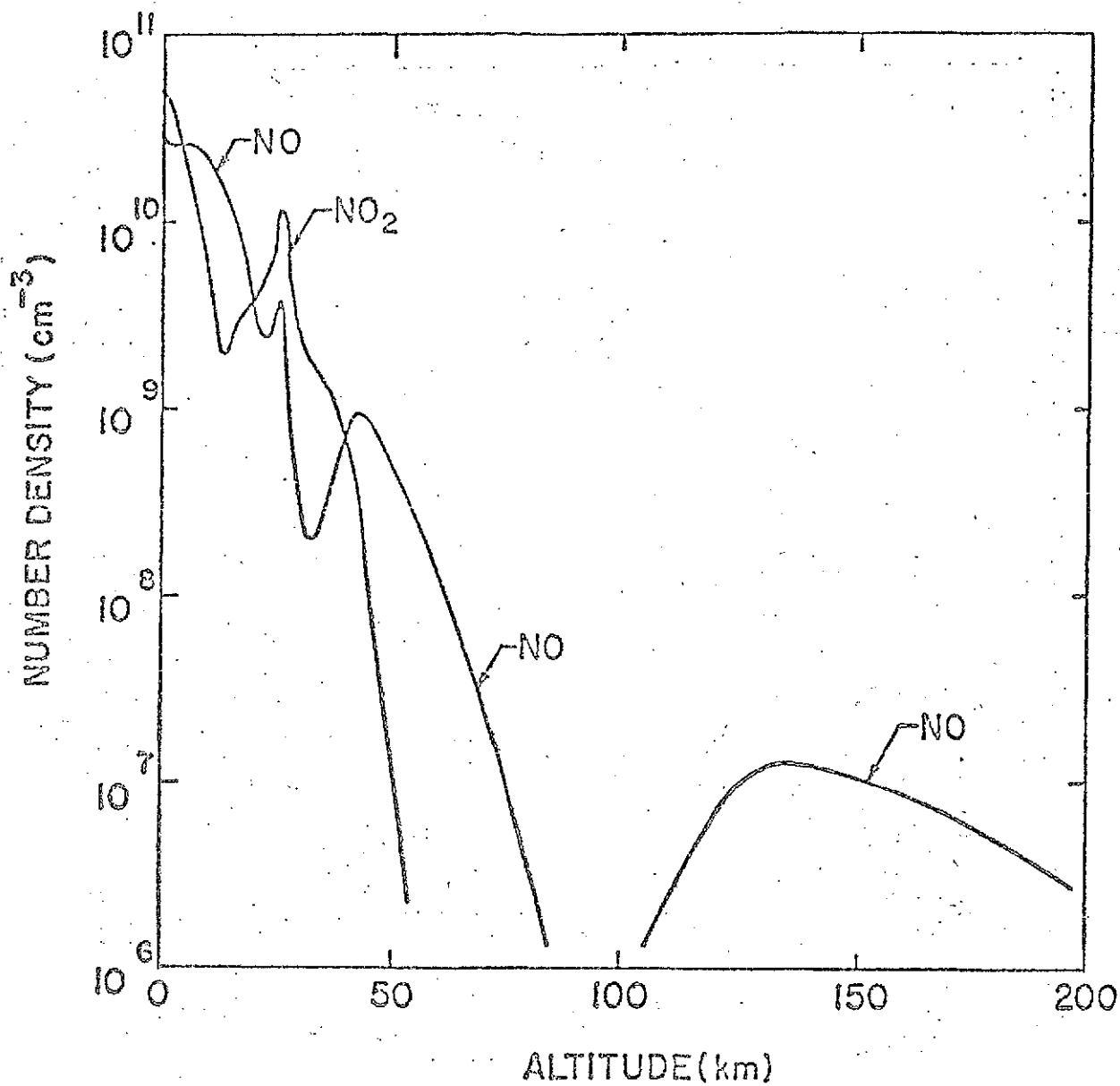


Figure 3. Computed NO₂ and NO profiles after 18 months of NO injection at 26 km. at the minimum rate.

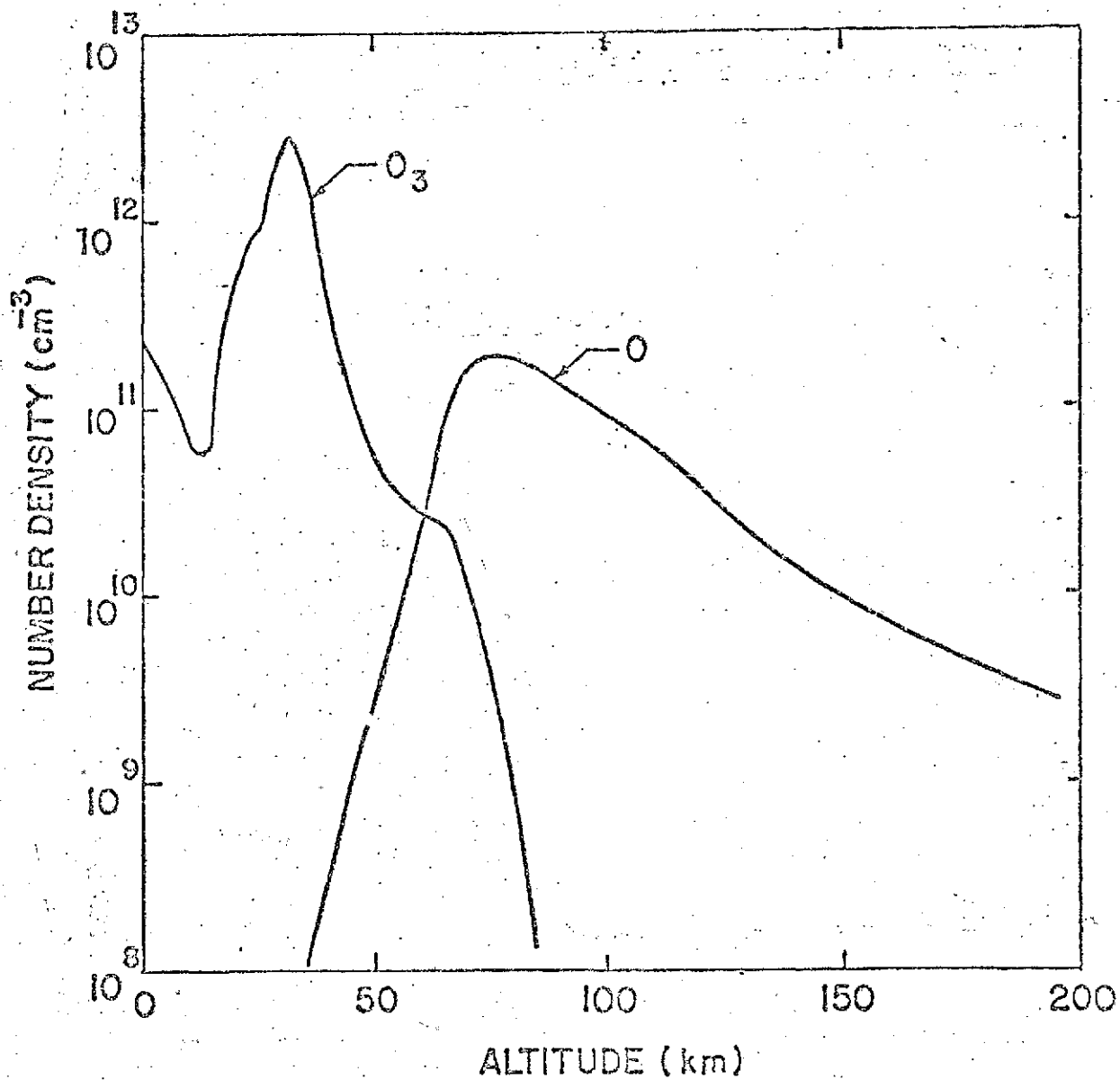


Figure 4. Same as Figure 3 for O_3 and O profiles.

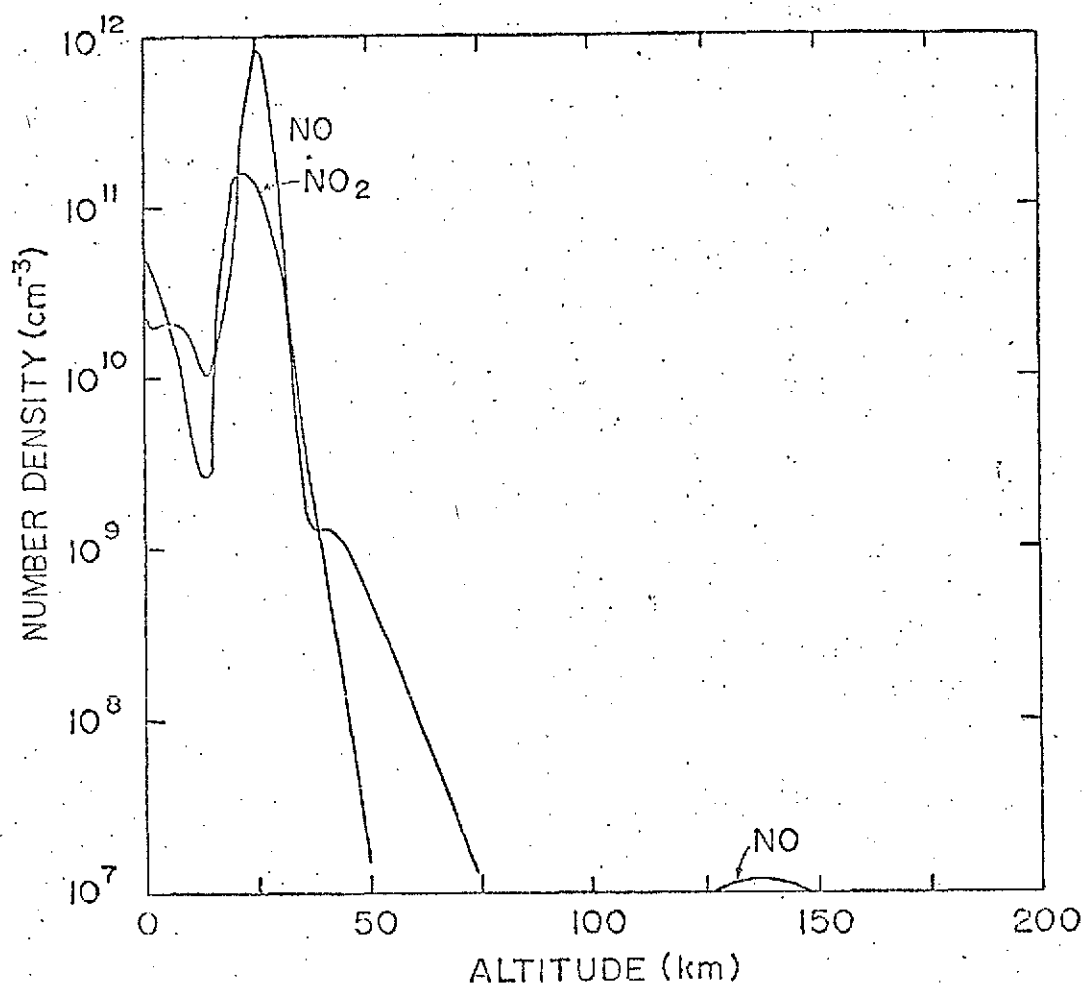


Figure 5. Computed NO₂ and NO profiles after 18 months of NO injection at 26 km. at the maximum rate.

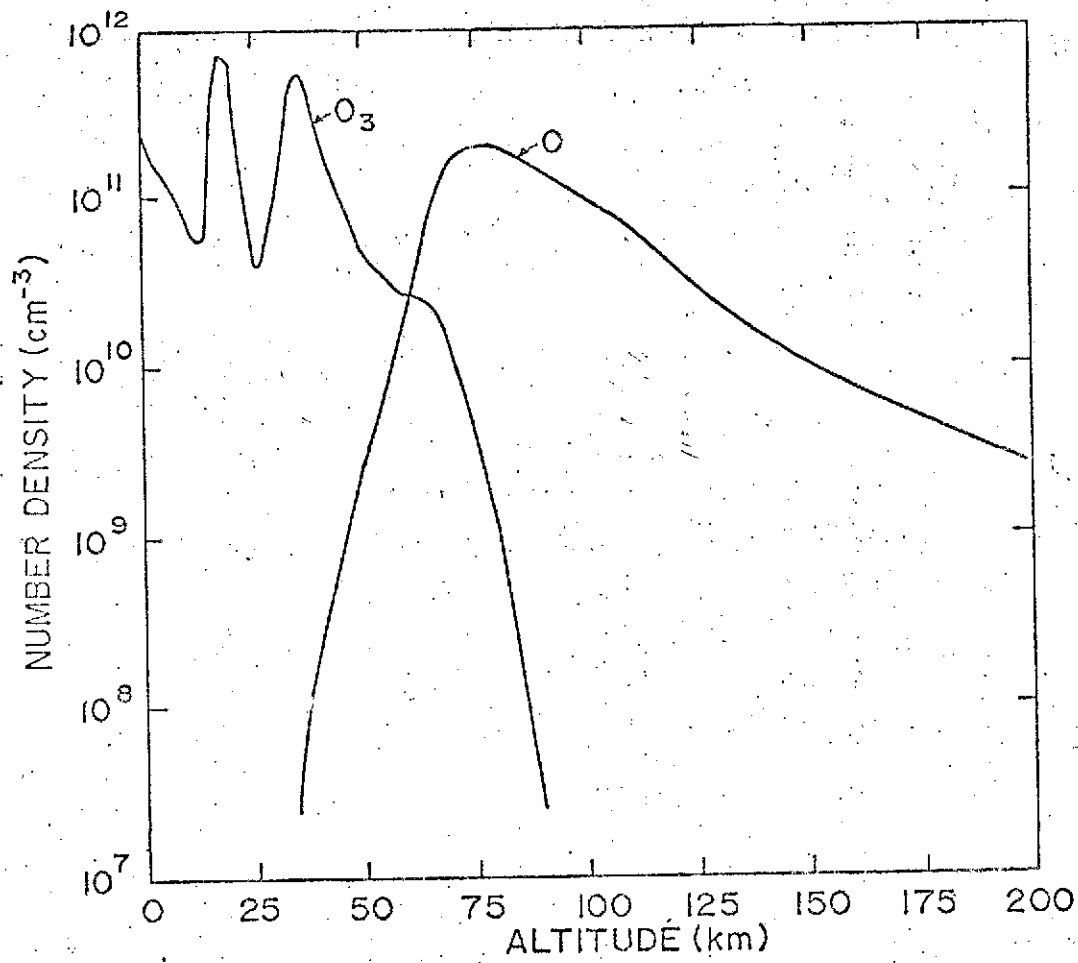


Figure 6. Same as Figure 5 for O₃ and O profiles.

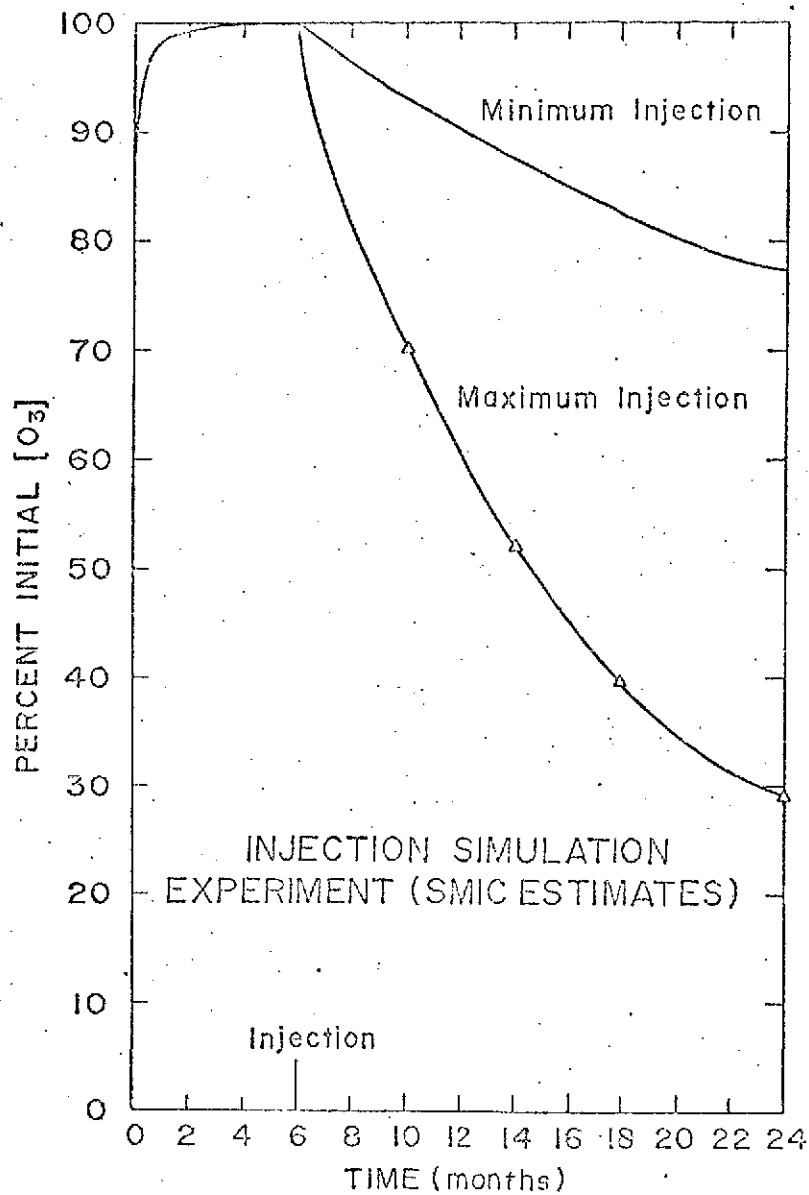


Figure 7. Change in total O_3 density as a function of time due to minimum and maximum NO injection rates.

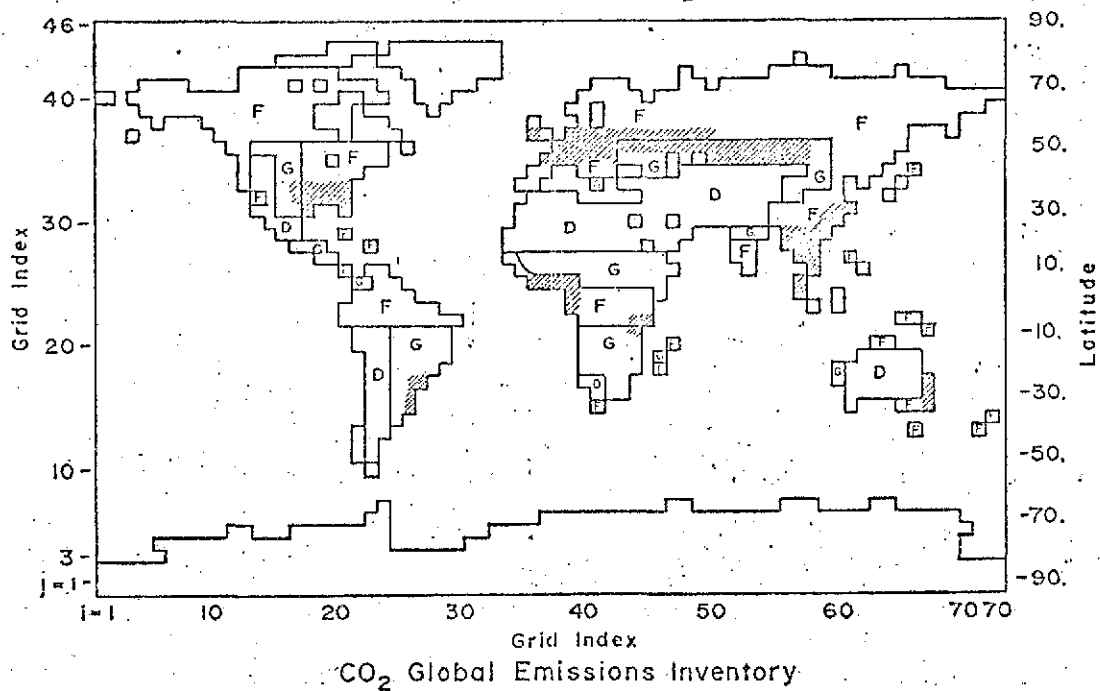


Figure 8. *Global emissions inventory for CO₂ used in global circulation models. The designated land areas are forests (F), grasslands (G), deserts (D), and agricultural (hatched).*

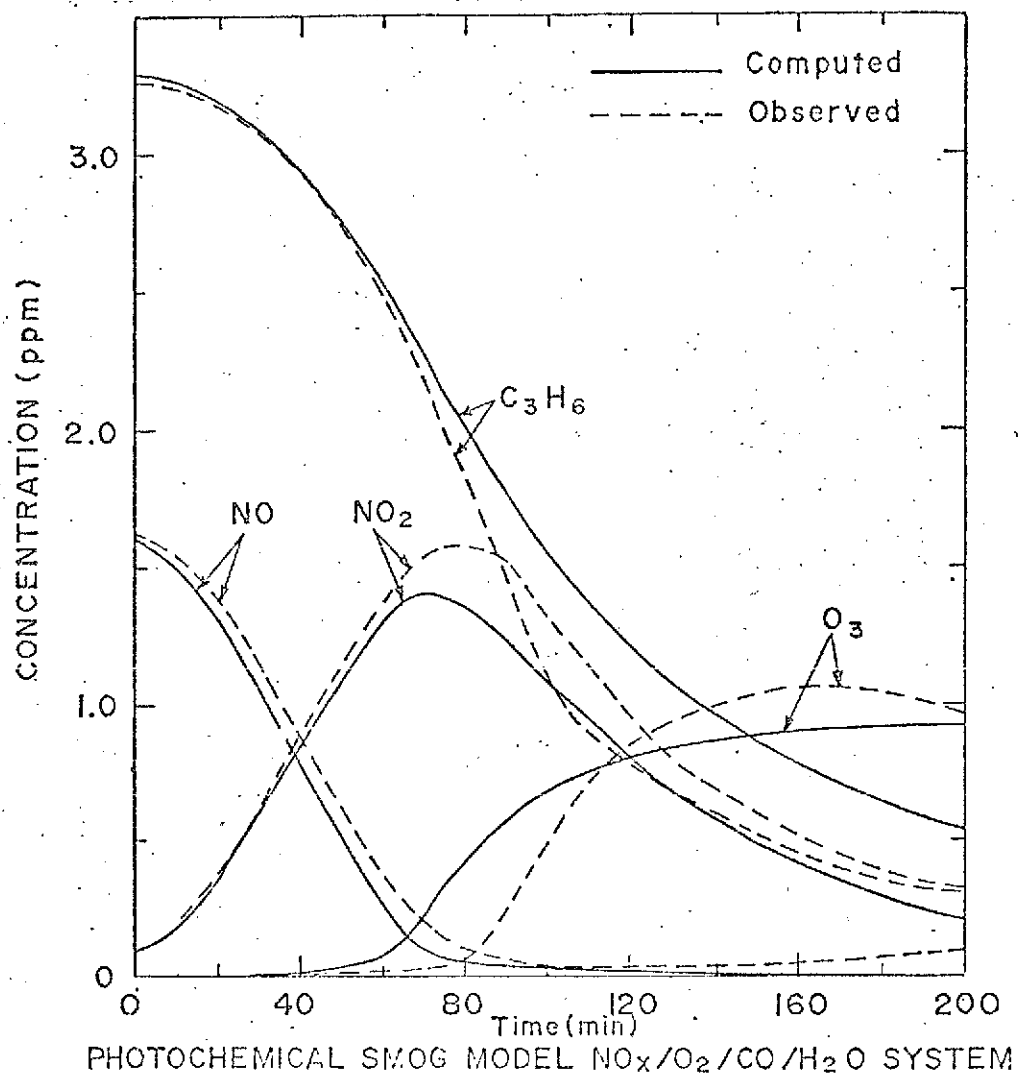


Figure 9. Computed and observed histories of C_3H_6 (propylene), NO_2 , NO, and O_3 for a static smog-chamber experiment. The Hecht-Seinfeld reaction scheme was used in the theoretical calculation.

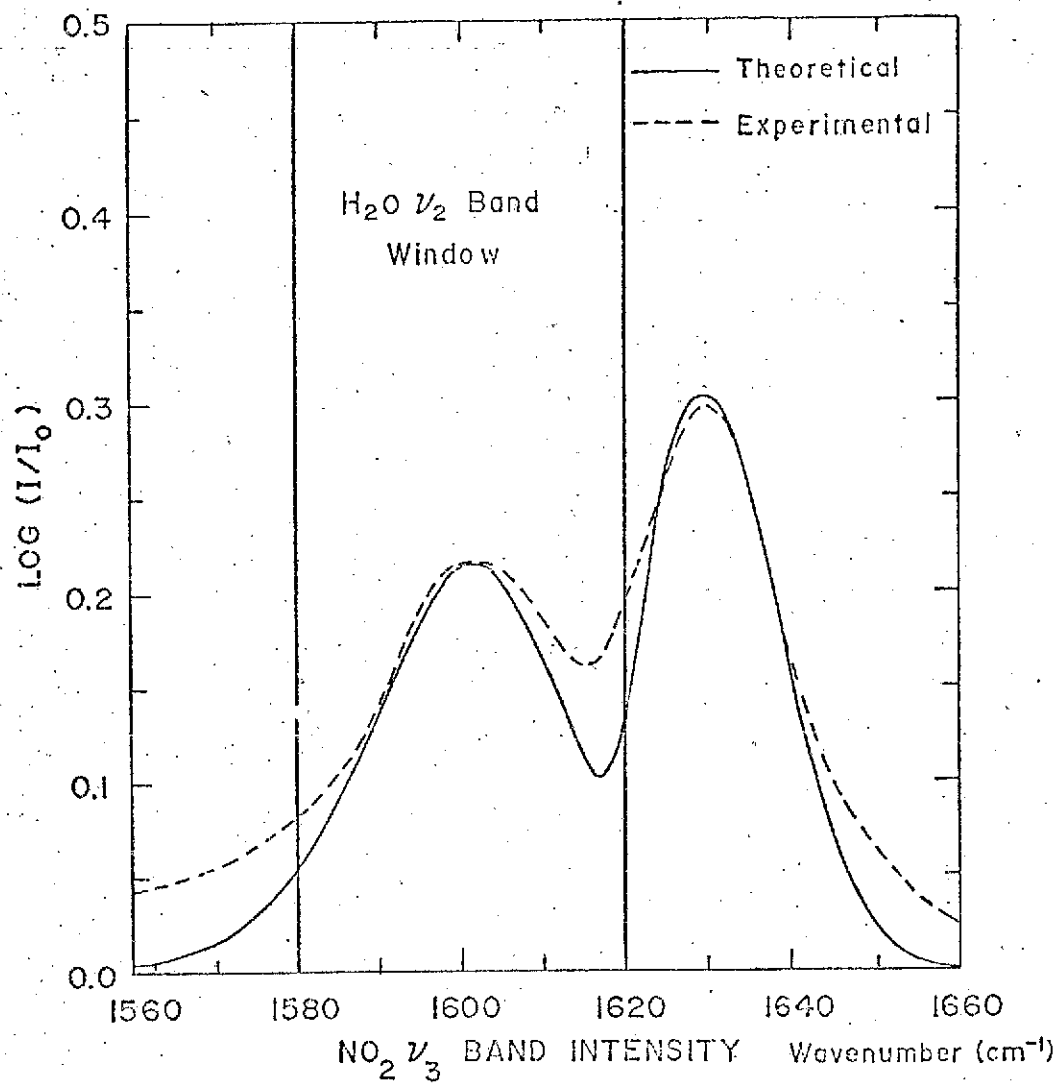


Figure 10. Theoretical and experimental band intensities at 5 cm^{-1} resolution for the ν_3 band of NO_2 .

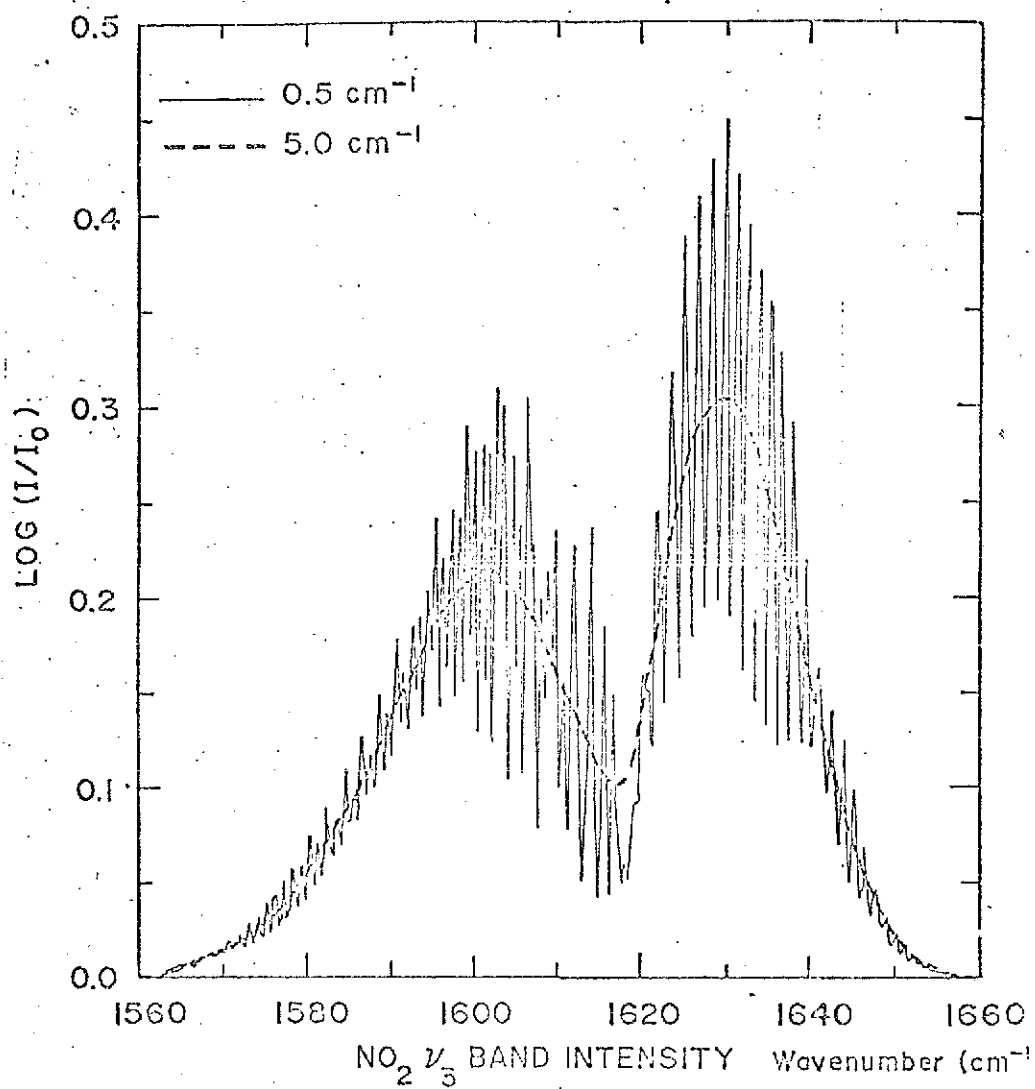


Figure 11. Theoretical band intensities computed at 0.5 cm⁻¹ and 5.0 cm⁻¹ resolution for the ν₃ band of NO₂.

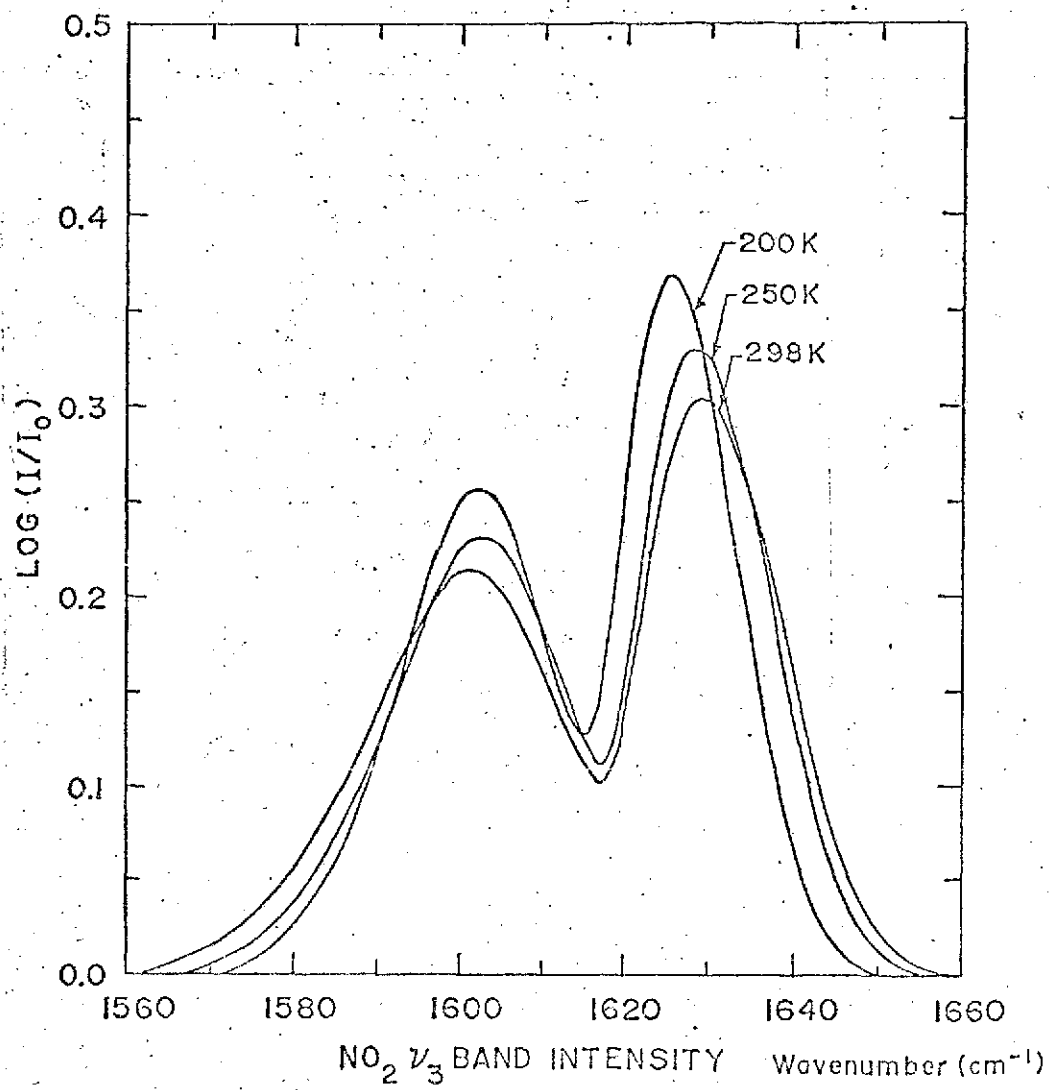


Figure 12. Theoretical band intensities at different temperatures at 5 cm^{-1} resolution for the ν_3 band of NO_2 .

REMOTE SENSING OF EARTH RESOURCES: MULTISPECTRAL PHOTOGRAPHIC DISCRIMINATION OF DIFFERENT LITHOLOGIES, BAGDAD, ARIZONA.

(V. Gornitz)

The experiment at Bagdad was designed to test the feasibility of multispectral photography in discriminating between two or more rock types. Specifically, the project was aimed at distinguishing the ore-bearing host rock (quartz monzonite, containing disseminated chalcopyrite, pyrite and molybdenite) from adjacent non-ore bearing rock, by measuring their reflectance spectra in the field and by aerial and satellite multispectral photography.

Field work at Bagdad was carried out during August, 1972, while a related earth resource project was in progress in Prescott, Arizona. Bagdad, 68 miles west of Prescott, is the site of an open-pit copper mine, owned by the Bagdad Copper Corp. The porphyry copper deposit occurs in quartz monzonite of Laramide age (71 million years old), which intrudes into Precambrian granites and schists. Extensive Tertiary and Quaternary basaltic lava flows surround the deposit.

Rock samples were collected in and around the mine for later laboratory analyses. Lithologies sampled include quartz monzonite (weathered, altered and fresh), granite, aplite, basalt and rhyolite. Because of various delays and exceptionally poor weather in the fall, ground measurements of spectral reflectances were drastically curtailed. However, multispectral photographs of the test site were obtained from low-flying aircraft in November.

Petrographic and chemical analyses of the rocks and photo-interpretation will be conducted. Both aerial and ERTS-A satellite photographs will be examined and compared.

In the near future, false-color composites will be developed to enhance spectral differences between adjacent rock units.

Preliminary indications from inspection of a single ERTS-A 18"x18" print (red band) centered on Bagdad are that various rock units can be distinguished. Multispectral treatment will probably further accentuate these differences. The results should make geological mapping by remote sensing a feasible undertaking.

MARINER 9: PRELIMINARY PHOTOGEOLOGIC EXAMINATION OF THE MARTIAN "CANYONLANDS" AND "CHAOTIC TERRAIN." (V. Gornitz)

Prior to the Mariner missions, nearly nothing was known about the geology of Mars. Mariner 4 in 1965 flew to within 10,000 km. of the surface and showed that Mars was a heavily cratered planet, like the moon, except that the degree of erosion seemed greater. The TV pictures from Mariners 6 and 7, by contrast, displayed a variety of land forms. The Mariner 9 TV pictures revealed even more unanticipated features: the vast "canyonlands", more detailed views of the "chaotic terrain", branched dendritic sinuous rilles and layered sediments at the polar caps. The processes responsible for the formation of many of these landforms are as yet unknown.

A photogeologic survey of Mariner 9 black and white prints, in progress, is concentrating on the origin of the martian "canyonlands" and "chaotic terrain". Geologic maps will be prepared from the Mariner 9 imagery. The scientific importance of these features is two-fold: 1. the canyons demonstrate large-scale tectonic activity on Mars; 2. the atmospheric pressure (as determined by the UV spectrometer) at the bottom of the canyons is above the triple pressure of water, so that moisture, if present, could condense there. Consequently the chances for life may be higher here than elsewhere on Mars.

A. Canyonlands

The martian canyon system extends from 110°W to 50°W and 0° to 15°S , covering the Tithonius Lacus, Ophir and Aurora Sinus regions. It spans a distance of 4,000 km. in length, 150 km. across and 5,000 km in depth.

A system of faults and fractures oriented N to S marks the western-most boundary of the canyonlands (110°W to 100°W). The canyon system terminates in Noctis Lacus--a severely fractured plateau, nicknamed "the Chandelier". The "Chandelier" consists of an intersecting network of N-S, NW-SE and NE-SW-trending rilles (grabens), that often merge into crater chains. High resolution photography reveals a top layer of erosion-resistant rock, overlying talus-covered slopes, much like lava-capped mesas in the southwestern U.S. The outcrops may consist of strata of successive lava flows, as suggested by the close proximity to a chain of giant volcanoes.

The main part of the canyon cuts into a regional slope, west to east. The main canyon has probably formed by normal faulting, because of the linear nature of its scarps and parallelism between the main valley, rilles and crater chains. A terrestrial analog would be a giant rift valley, such as the Red Sea. However, volcanism and erosion have also played important roles in shaping it (Figure 1). Crater-chains (generally interpreted as explosive volcanic vents aligned along fractures) lie parallel to the main canyon. In places, wind erosion has enlarged the craters into sausage-like segments, which widen into larger valleys that join the main canyon and contribute to its expansion.

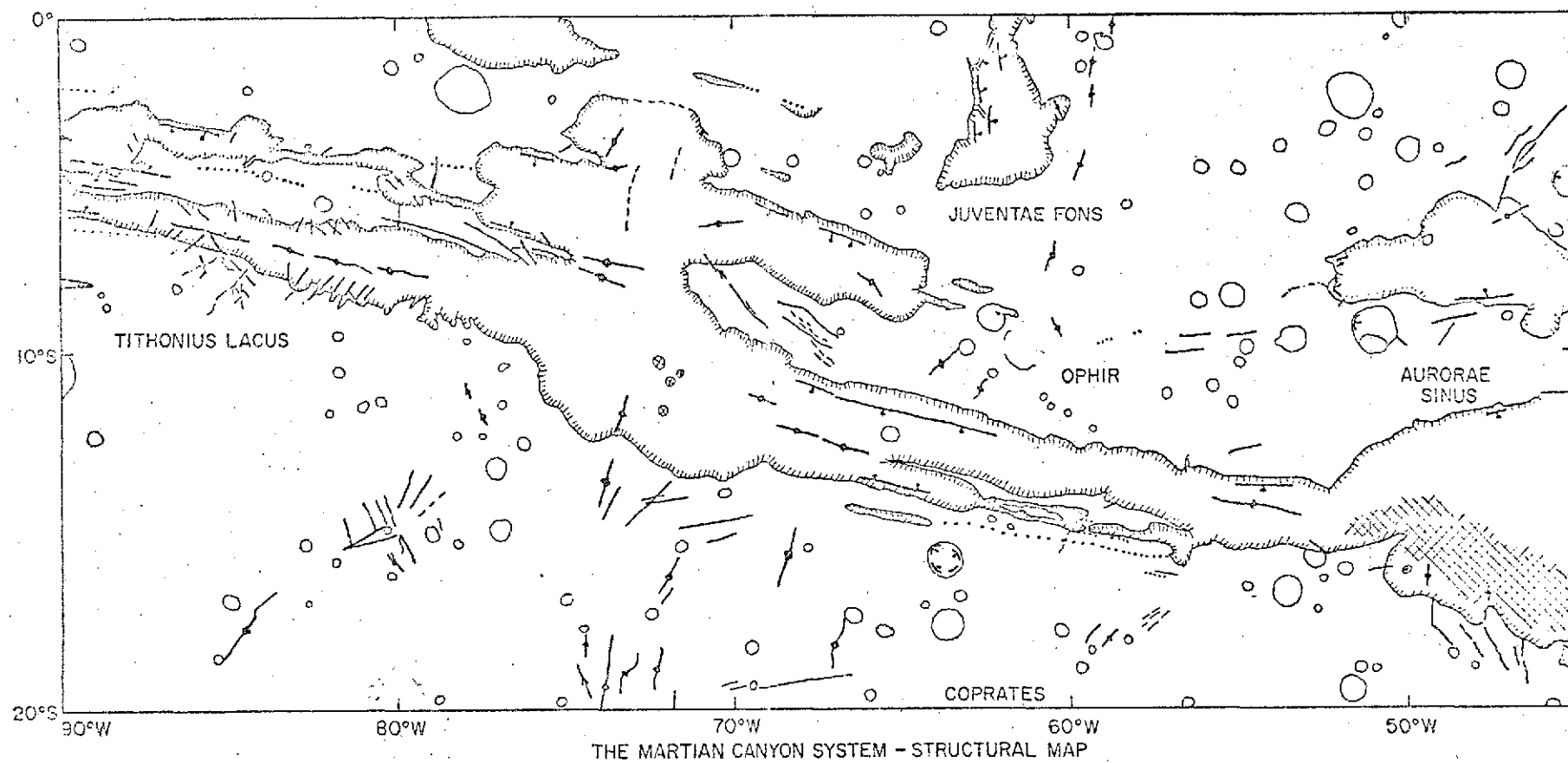
A ridge in the canyon floor has been compared to the mid-ocean ridge system which would imply that incipient sea-floor spreading has occurred on Mars. However, detailed examination of Mariner photographs shows that the ridge is a remnant of a block that has been detached from cratered terrain, by faulting but has been worn down by erosion --as illustrated by the gullies on its flanks.

Numerous, branched "tributary" canyons lead into the main valley. The largest tributary canyon (about 100 km. long and 25 km. wide) compares in dimensions and appearance with side valleys like Havasu Canyon and Bright Angel Canyon in Arizona's Grand Canyon. The martian side valleys therefore resemble a dendritic stream drainage system, produced by flowing water, on earth. The "branches however, lie parallel to three directions: N-S, NE-SW and NW-SE (as in the "Chandelier") indicating that erosion has proceeded along faults. In the absence of flowing water, the side channels could have developed by subsidence of unconsolidated regolith along subsurface faults or fractures, and by subsequent enlargement through wind erosion.

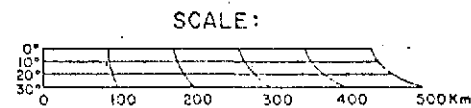
This preliminary survey suggests that the martian canyonlands have a complex origin. The canyonlands have been formed to a great extent by tectonic and volcanic activity, but erosion by wind and possibly water, has substantially contributed to the widening of the canyon system.

B. Chaotic terrain

The "Grand Canyon" of Mars grades into chaotic terrain at its eastern end, in the Margaritifer Sinus region. Stages in the development of chaotic terrain involve irregular fracturing, producing a "crackle" pattern in otherwise normal, cratered terrain. There is subsidence and slumping of blocks along a fault scarp. Erosion



- — CRATER, — CRATER CHAIN, — — — — — RILLE, - - - - - LINEATION, ~ ~ ~ ~ ~ SINUOUS RILLE
 / — RIDGE, \ — CANYON RIM, / — FAULT SCARP, DOWN THOWN TOWARD SIDE OF BARB.
 ○ — DEPRESSION, x x x x — CHAOTIC TERRAIN



BASE MAP--1:5,000,000 MARS CHART
 MC-18 (USGS)

Figure 1. Structural map of the canyon system on Mars.

enlarges the cracks, wears down slump blocks to be rounded mounds, until only isolated mounds remain in smoother, craterless terrain. The smooth terrain is topographically lower and younger than cratered terrain. Subsidence and collapse suggests that underlying material was removed. One suggestion has been that Mars is underlain by a thick permafrost layer, which thaws locally due to internal heat. The melting and subliming of the ice could cause thermokarst, or subsidence features; but the scale of the features would require a permafrost layer several km. thick.

Does Mars have vast underground deposits of ice? An estimate based on the daily escape rate of water yields a layer of ice only a half meter thick. If the ratio of H_2O to CO_2 from degassing of volcanoes is 6:1 as on the earth, then Mars would have an ice layer about 200 cm. thick. Clearly, more data are needed on the abundance of water vapor in the atmosphere and of water ice in the polar caps. The origin of chaotic terrain could involve other processes such as tectonic subsidence, suggesting a weak crust, perhaps underlain by nearly molten material. Both explanations - that of thermokarst, or crustal instability imply that the chaotic terrain should have a higher heat flow than average. Anomalous "hot spots" in this area should be sought by means of the IR radiometer. The exact relation of chaotic terrain to the canyon system remains to be determined, as well as a better understanding of erosional processes in general. The likelihood of wind erosion is demonstrated by the periodic dust storms that envelope the planet, but the evidence for flowing water, as strongly hinted by the Mariner pictures, needs to be confirmed.

EVALUATION OF THE GEOLOGICAL USEFULNESS OF GEMINI, APOLLO AND ERTS-A SATELLITE PHOTOGRAPHS OF THE SOUTHWEST. (v. Gornitz)

The objectives of this study have been to analyze and evaluate the usefulness of Gemini, Apollo and ERTS-A space photographs of the southwestern U. S. for small-scale (the small ratio between ground and map distances) geological mapping and reconnaissance. This region has been selected because the arid climate and low vegetation cover lead to widespread rock exposures and generally cloudfree conditions. Furthermore, the region has been extensively explored and good geological maps are available to provide ground truth.

The Southwest boasts many economically important mining districts, notably the porphyry copper deposits in southeastern Arizona, and New Mexico. Approximately 50% of the world's copper production comes from porphyry copper deposits, mostly in the southwestern U. S. (Skinner, 1969). (A belt of similar deposits occurs in the Western Andes of Peru and Chile). Therefore, this area is suitable for seeking out the relationship between the occurrence and distribution of known mineral deposits, and the structure and lithology as observed from space photographs.

The regional geology as seen from satellite photographs has been compared with the geology known from field work. New features, such as faults and domal structures, not marked on geological maps, have been located. The distribution of copper deposits has been related to the geology that can be deduced from the space photographs. Finally, the pattern of copper deposition has been examined in the larger geological context of the Basin and Range structure and its relation to sea-floor spreading.

The most useful aspect of satellite photography was found to be the clarity with which the regional structure was exposed, a conclusion consistent with earlier studies. The clearly visible north to northwesterly trends of the mountain ranges in southern Arizona and New Mexico has been related to the underlying Basin and Range structures. Three main sets of linear features (interpreted to be faults or fractures) have been observed, with NNW-SE, NE-SW, and to a lesser extent E-W orientations (Figure 1). Many of these fractures have not been marked on the state geological maps. This study has also discovered several circular features, believed to be domes, in south-central Arizona, and New Mexico (Figure 2).

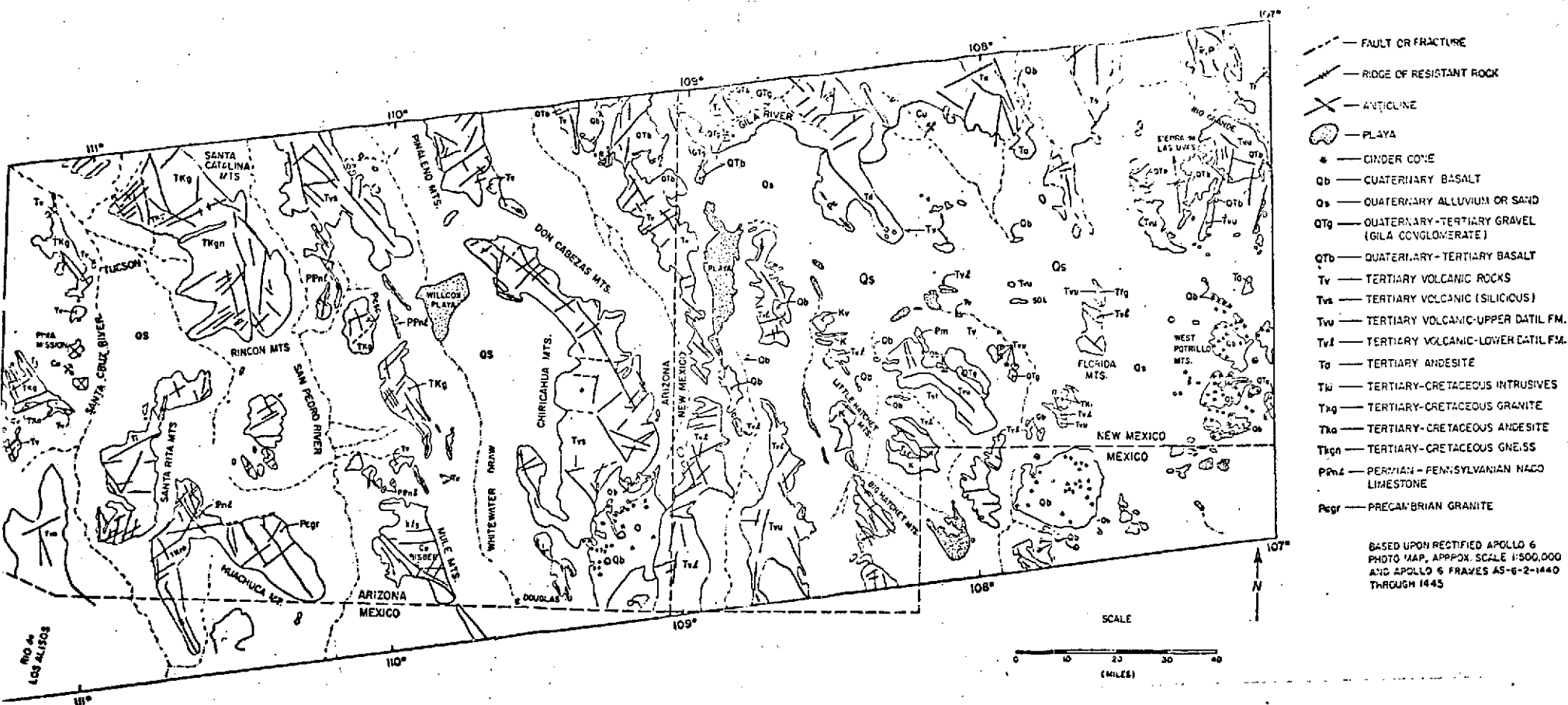
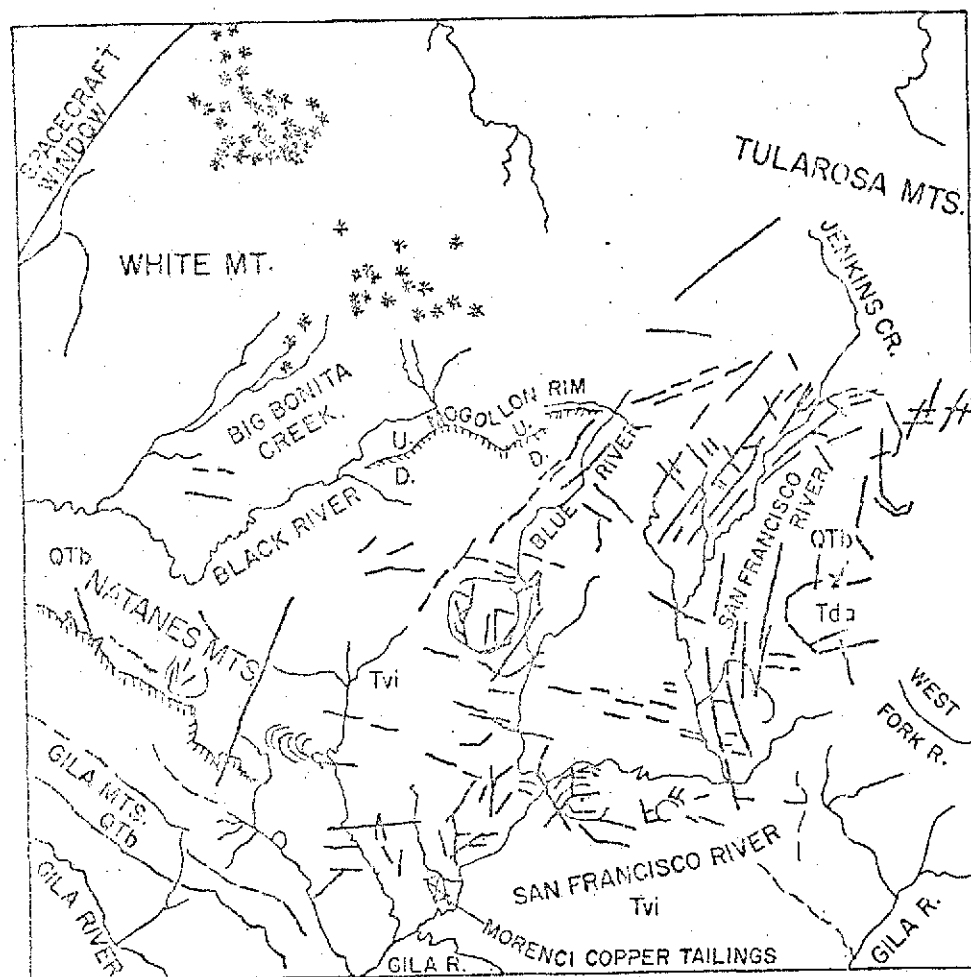


Figure 1. Space photogeological map of southeast Arizona-southwest New Mexico.

PHOTOGEOLOGICAL SKETCH MAP E. CENTRAL ARIZ.-NEW MEXICO



KEY

- FAULT OR FRACTURE
- ⊙ — CIRCULAR FEATURES (DOME)
- QTb — QUATERNARY-TERTIARY BASALT
- * — CINDER CONE
- Tvi — TERTIARY INTERMEDIATE VOLCANICS
- Tda — TERTIARY ANDESITE (DATIL FM)

Figure 2. Circular features, believed to be domes, detected on satellite photographs.

The distribution of copper orebodies is related to the regional geology. Copper deposits are frequently clustered along local or small-scale fractures and faults which lie parallel to the above-mentioned major fault directions. The N to NW trends of mountain ridges and faults can be traced into northern Sonora, Chihuahua Provinces in Mexico. This may be a useful guide in extending future mineral exploration to less well-mapped areas.

Space photographs prove valuable in outlining the boundaries between major geological provinces such as the Basin and Range, and the Colorado Plateau. The boundary between these two provinces, as outlined by faults along the Wasatch-Jerome and Walker lines, has acted as a structurally weak zone in the earth's crust affecting the concentration of many ore deposits.

The major disadvantages of space photography is the difficulty in identification of rock types, except in a few instances. In southern Arizona, for example, lighter-toned alluvium, filling the valleys, can be readily distinguished from darker bedrock in the mountains. Fresh basaltic lava fields, cinder cones, salt playas, and certain sedimentary rock units, as in the Grand Canyon, can be easily identified. However, in general, it is extremely difficult to determine the contacts between different rock formations.

IMPROVING THE EFFICIENCY OF COMPUTER PROGRAMS. (P. Schneck)

The high level programming languages in use today permit the scientist to express a problem in near-mathematical terms. Often, the original problem statement is not the most efficient form for a computer, though it is retained because of its familiarity value in debugging as well as ease of modification. Schneck has directed a research and development project aimed at using the computer to translate the scientist's problem formulation into a highly efficient program. The result of this effort is a compiler which achieves performance improvements of greater than 10% on almost all programs (to be published in The Computer Journal, 1973).

The Cocke-Allen interval analysis technique is used to order the blocks of a program. When this ordering is obtained, optimizations are applied within the blocks, and then on blocks within a loop. The following list summarizes the major optimizations employed:

- Common subexpression elimination

- Dead variable elimination

- Constant propagation

- Loop dependent subexpression elimination

- Movement of loop-invariant expressions

- Replacement of division by multiplication

The compiler unites the interval analysis technique with Schwartz's value numbering scheme and is able to effect extremely comprehensive common subexpression optimization. Of particular interest is the fact that the compiler is written in Fortran, reads a Fortran program for input, and writes an optimized Fortran program as output. This makes it possible for the compiler to be used on any Fortran program for almost any machine. Preliminary results indicate that the manufacturer-supplied optimizers (with the exception of the IBM Fortran H) do not improve upon the programs generated by the compiler described here. An example of the compiler's use is shown below (Figure 1).

```

SUBROUTINE SAMPLE
DIMENSION F(10)
DO 10 I=1,100
2 X=A+B
  IF (I-5)3,3,4
3 B=B+1.
  GO TO 9
4 X=X+C*D*(A+B)
  IF (I-8)5,6,5
5 A=A-1.
  GO TO 8
6 E=C
  C=C+1
  IF (A-B)7,7,8
7 X=X+E*D/(A+B)
  GO TO 10
8 X=X+C*D
9 X=X*(A+B)
10 WRITE (6,100)A,B,X
  DO 13 J=1,10
    F(1)=X
    Q=0.
    DO 12 I=1,10
      PI=3.14159265
      A=B+C*D/SIN(PI/4.)
      X=X+D*C/SIN(PI/4.)
      W=B*C
      Z=C
      Q=Q+1.
      D=D+Z*B/A+F(I)*C
      C=C/A+W
      Z=E
      X=X/(Z+1.)
12 X=X+(F(I+1)*C)
13 CONTINUE
14 RETURN
END

```

```

SUBROUTINE SAMPLE
DO 10 I=1,100
T00001=A+B
2 X=T00001
  IF (I-5)3,3,4
3 B=B+1.
  GO TO 9
4 T00003=C*D
  X=(X+(T00003*X))
  IF (I-8)5,6,5
5 A=(A-1.)
  GO TO 8
6 C=(C+1)
  IF (A-B)7,7,8
7 X=(X+(T00003/T00001))
  GO TO 10
8 X=(X+(C*D))
9 X=(X*(A+B))
WRITE (6,100)A,B,X
10 CONTINUE
  T00028=(1./(E+1.))
  DO 13 J=1,10
    F(1)=X
    T00030=F(1)*C
    DO 12 I=1,10
      T00016=(C*D)*1.4142136
      A=(B+T00016)
      X=(X+T00016)
      W=(B*C)
      T00020=1./A
      D=((D+(W*T00020))+T00030)
      C=((C*T00020)+W)
      X=(X*T00028)
    T00030=F(I+1)*C
12 X=(X+T00030)
13 CONTINUE
14 RETURN
END

```

Figure 1. Example program and resulting optimized code.

- a — Relative constant expression moved out of loop
- b — Common subexpression elimination
- c — Replacement of division by multiplication
- d — Loop dependent common subexpression elimination
- e — Dead variable elimination
- f — Use of named variable to replace a subexpression
- g — Constant propagation
- h — Initialization of loop dependent common subexpression

IMPLEMENTATION OF THE 370/165. (P. Schneck)

As described previously, an IBM 370/165 is in use and permits off-loading programs from the 360/95.

The operating system of the 370/165 contains only those functions essential to the operation of the processor, that is, only the ability to communicate. The 370/165 operating system calls upon the 360/95 to perform all other functions and make the results available. In particular, the 360/95 is responsible for scheduling and selecting jobs for the 370/165 and for storing and printing output generated by the 370/165.

The 360/95 also monitors the operation of the 370/165 and reports on any hardware or software malfunctions which it detects.

The programs running on the 370/165 include the GARP production model which has been modified to fit within the minimal memory available. The programs have been written to require a minimum number of services from the 360/95, so that they may continue running even when the 360/95 is not available. In this way, we are taking advantage of the newer technology employed in the 370 series which permits use of the machines without daily preventive maintenance.

RECEIPT OF VTPR SOUNDING DATA. (N. L. Durocher)

A dedicated 2400 bps data link was installed by NOAA on October 1 for the tape-to-tape transmission to GISS of VTPR data in order to receive, process and assimilate global satellite data from operational satellites on a daily, extended basis. The transmission includes hemispheric and global analyses and conventional meteorological data. Routine procedures were established for the once-daily transmission of 0000Z and 1200Z analyses and conventional data, and for the transmission of orbit-by-orbit VTPR data approximately 6 times per day.

Thus far GISS has processed calibrated raw data from the VTPR Sounder (launched October 12) in the following sequence: short segments of a few orbits each from the time data first became available to GISS on October 29; a continuous 3-day period from November 18 through 21; two continuous 15-day periods from November 9 through 23, and December 9 through 24. The December data were the basis for the temperature retrievals discussed below.

Transmission of data from NOAA was a source of serious problems during the December processing period and continues to be a source of difficulties. Comparison of tapes received both by courier and by data link revealed that one-third of the tapes sent by data link contained one or more uncorrected errors. Because of unreliable performance of the link all data in December were obtained by daily courier runs between New York and Suitland. VTPR data received by GISS comprised 90% of full coverage in the December 9 through 24 period. Of the data received at GISS, an additional 15% was not usable because of defective tapes, missing data or irrelevant data, or defective data (incorrect location on soundings, etc.). The net yield of usable VTPR data was 75%. Performance was poorer than the average at the beginning of the month and seemed to improve with time. Receipt of the Hemisphere and Global Analyses as well as conventional data was satisfactory with more than 90% of the information received in usable form.

PRE-PROCESSING OF VTPR DATA. (S. Ungar)

The pre-processing operation -- from receipt of raw calibrated data to construction of clear-column radiances, usually averaged for use in the atmospheric model -- required an average of two hours per day of dedicated 360/95 time, but can be reduced to 30 minutes per day if additional disk storage is available. Disk storage for this purpose has been requested.

The main steps in the pre-processing operation were as follows:

1. Raw sounding data from NOAA are (a) translated from their machine language (CDC 6600) to GISS machine language (IBM 360/95), and unpacked; (b) spooled to create one tape for a 15-day period out of ~ 150 separate tapes transmitted from NOAA and (c) earth-located according to the following procedure: Each set of VTPR radiances is tagged with the geographic and temporal coordinates of the center of the area being viewed by the instrument as well as information specifying the instrument's viewing angle. The input to this routine is a NESS 7 or 9 track 800 BPI magnetic tape. The input tape consists of a single "reader" record followed by a group of "documentation" records and generally represents information obtained from approximately one ITOS D orbit. The "reader" record specifies launch and general orbital parameters as well as the approximate time period spanned by the "documentation" records which follow it. The ITOS D radiometer (VTPR) is equipped to scan orthogonal to the satellite's trajectory. Each scan is composed of a total of 23 spots representing contiguous areas on the Earth's surface of approximately 60 km. diameter. A single "documentation" record represents a group of 8 adjacent scan lines. The following quantities are supplied on the NESS tape: the latitude and longitude of spots 5, 12 and 19 on scan line 4; the zenith angle (angle formed between satellite viewing line and local vertical) for spots 1 and 23 on scan lines 1 and 8, as well as for spots 5, 12 and 13 on line 4; the time of observation for spot 12 line 4; the set of 8 radiances and sea surface temperature

(if over ocean) for each of the 8 X 23 spots. From this information and the parameters of the reader record, an output tape is produced containing the following information for each scan spot: time of observation (day of year, hour, minute, second); line number; spot number; latitude; longitude; nadir angle (viewing angle of radiometer referenced to line from satellite to sub-satellite point); the 8 measured radiances sea surface temperatures flagged to 269.9° over land).

2. Quality-control checks (bad data and missing records) are applied to filter out the following: abnormally low radiances, judged by comparison with climatology; strings of zeros corresponding to calibration modes of the sounder; obviously incorrect coordinates, zenith angles, times, etc.
3. Extraction and storage of NESS temperature retrievals for future use in forecasting experiments.
4. Preparation of averaged data for insertion in model: all soundings obtained within a specified distance (usually 400 km) of each computing grid point, and within one time-step of the numerical integration in the model (usually 5 minutes) are averaged; also, for each set of soundings that is averaged, the minimum and maximum radiances are selected and stored, for use below in the cloud-filtering program.

The result of pre-processing is a set of averaged radiances (and minimum and maximum radiances) tagged with respect to time and co-located grid point. This set of radiances is ready for the operations of (a) cloud-filtering to obtain clear column radiances; (b) temperature retrieval and (c) insertion in the model. These steps are described in the next report.

RETRIEVAL PROGRAM. (J. Hogan)

The program for retrieving temperature profiles from the VTPR radiance measurements is a key element in the VTPR experiment. The nucleus of the method employed in the retrieval operation was developed previously by Hogan and Grossman. The basic technique has been expanded to allow for effects of H_2O vapor and clouds, and to take into account the variation of the atmospheric weighting functions with temperature. These refinements rendered the retrieval program suitable for use with the real radiance data obtained from the VTPR.

The retrieval program employs an initial guess for the temperature profile, and corrects this guess by comparing the radiances calculated from the guess with the radiances measured by the VTPR. An iterative technique is used to solve the integral equation of radiative transfer. The basic method for performing the temperature retrievals is similar in some respects to the technique developed by Chahine at JPL, incorporating a modification suggested by Smith at NESS, but is not identical with either of these methods.

In the method of Chahine, temperatures are retrieved at a number of pressure levels equal to the number of channels in which radiance measurements are made, with temperatures at other levels obtained by interpolation. Smith modified this approach to allow direct solution for the temperature at any desired pressure level. Smith took the differences between the observed radiances and the radiances corresponding to the guessed temperature profile as an indication of the correction to be applied to the temperature guess, while Chahine used the ratios of the observed to calculated radiances.

As in the case of Chahine's method, the GISS method uses the ratio of observed to calculated radiances in each channel to correct the temperature profile from the first guess via iteration. However, as in the case of Smith's method, the present method solves directly for the temperature at any desired pressure level by weighting the different temperature values indicated by the radiances in the separate VTPR channels by the values of the atmospheric weighting functions in these channels at the desired pressure level.

In the present experiment, an initial guess for the tropospheric temperature profile is taken from the GISS atmospheric model, while the stratospheric portion of the guessed profile is obtained from climatological data. Radiances corresponding to this guessed temperature profile are then computed for the VTPR channel centered near 747 cm^{-1} . From a

comparison between the measured and calculated radiances in this channel, an estimate of the fractional cloud cover present within the VTPR field of view is obtained (for a specific cloudtop pressure derived as described below). This fractional cloud cover estimate is then used with the guessed temperature profile to calculate "clear-column" radiances in the VTPR channels at 535 cm^{-1} , 668.5 cm^{-1} , 677 cm^{-1} , 695 cm^{-1} , 708 cm^{-1} , 725 , 747 , and 833 cm^{-1} . These clear-column radiances, which presumably the VTPR would measure if no clouds were present, are then inverted with the 747 cm^{-1} channel omitted, to obtain a new temperature profile, which is in turn used to obtain a new estimate of the cloud fraction from the 747 cm^{-1} channel, etc. This procedure is iterated until specified convergence criteria on the cloud fraction and temperature profile are met. An alternative procedure for obtaining clear-column radiances is described in the following report.

The present method is also capable of retrieving a consistent water vapor profile from the observed radiance in the 535 cm^{-1} channel. However, in the experiment, the water vapor distribution calculated by the dynamical model in the vicinity of the VTPR measurement was used to evaluate the water vapor transmission functions in the VTPR channels from available spectral line data. Detailed calculations were also performed to obtain the CO_2 transmission functions from available data on the CO_2 spectrum.

The pressure at the level of the cloudtops is derived by comparing retrievals made in several adjacent fields of view with the assumption of clear conditions. Such a neglect of cloud presence in making the retrieval produces a temperature profile which is too cold below the actual cloud level by an amount which is proportional to the amount of cloudiness present in the particular VTPR field of view. This effect can be noted in the figure below, where three retrievals are shown, resulting from separate VTPR observations made in the close proximity of a radiosonde launch at 00Z on 12/9/72 at Ostrov-Chetyrekhstovbovoy, USSR (70.63N , 197.60W). One notes the conspicuous divergence of the three retrievals below 450 mb , although all are in good agreement above this level. This graph implies that clouds are present in the field of view for these three observations, with tops close to the 450 mb level.

The last remark suggests that a procedure might be developed for calculating the average cloud-top pressure in a given area by inverting several soundings in the area and finding the pressure level at which they diverge. This suggestion has been implemented by Ungar and is discussed below in a separate report.

Note that the sounding does not reproduce the low-level temperature inversion measured by the radiosonde. Relatively fine-scale features of this kind cannot be retrieved, because of the width of the atmospheric weighting functions. The retrieval usually, as in the example shown here, tends to pass through the middle of the inversion feature, yielding temperatures that are too high at the surface and somewhat too low above the inversion.

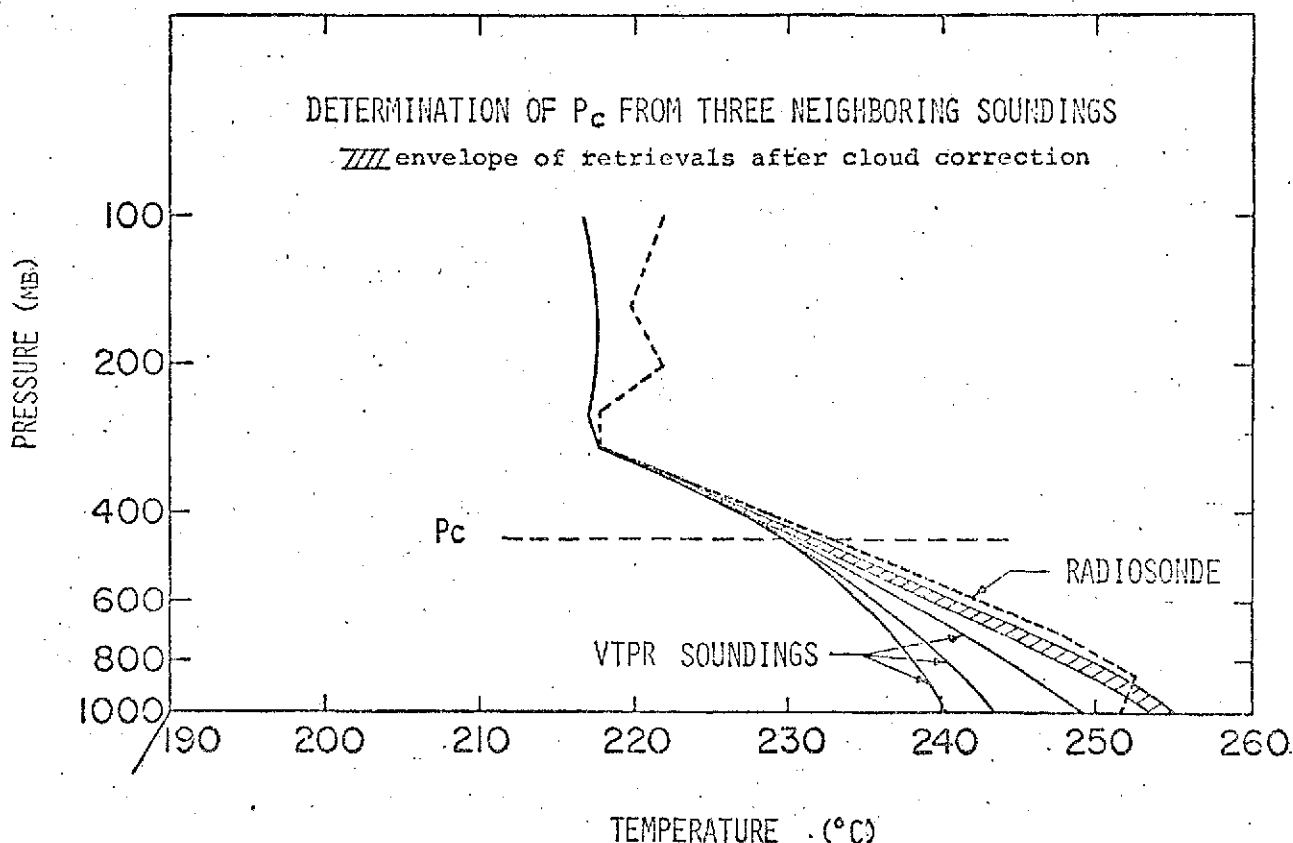


Figure 1. Comparison of VTPR retrievals with radiosonde at Ostrov-Chetyrekhtovbovoy, USSR (70.63° N, 197.60° W) 00Z, 12/9/72. The 3 curves labelled as VTPR soundings are the profiles retrieved from the VTPR radiance data without correction for cloud effects. The differences among them are presumably the result of differing amounts of cloud in the field of view of each sounding. Values of η , the cloud function, were computed for each sounding using the radiance in Channel 7, as described in the text. The results were: $\eta = 0.66$, 0.56 , and 0.26 . After elimination of cloud effects using these computed values of η , the three soundings yielded closely similar profiles lying within the shaded area. These are about 1.5° colder than the radiosonde profile, either because the elimination of cloud effects was incomplete, or because of overcompensation for the low-level inversion, as mentioned in the text.

ELIMINATION OF CLOUD EFFECTS IN VTPR DATA. (R. Jastrow and M. Halem)

Procedures have been developed for converting the pre-processed VTPR radiance data into (1) clear-column radiances and then (2) into vertical temperature profiles suitably averaged for insertion into the GISS 5-level and 9-level atmospheric models. The basic volume of data drawn on for the project consists of 160,000 soundings per day (2 per second). The aim of this part of the project is to produce accurate temperature profiles twice daily for every grid point in the atmospheric model. The model currently in use has a horizontal grid resolution of approximately 400 km and contains 3,312 grid points. Therefore roughly 6000 temperature profiles per day must be obtained from the VTPR soundings, each temperature profile being an average over approximately 25 soundings.

Because of the requirement for 6000 temperature profiles per day, it has not been possible to use the temperature data derived from the VTPR Sounder by NOAA for operational use. During the month of December, the NOAA operation yielded approximately 800 profiles per day, and the goal for the NOAA processing operation is an eventual 1400 profiles per day. GISS simulation studies and real data indicate that this degree of daily coverage is not adequate to produce a controlling effect on winds when inserted in atmospheric models. The original plan for the project called for use of NOAA temperatures, GISS-derived temperatures as a backup. Because of the limited number of NOAA temperature profiles being produced at this time, all available resources in the GISS project were shifted into the temperature retrieval program in December.

The vast majority of the VTPR soundings are contaminated by the presence of an unknown amount of cloud cover in the field of view of the sounder. Since clouds are opaque to infrared radiation, the contribution to the observed radiance in each channel is the sum of a radiation emitted from the entire atmosphere down to the ground plus radiation emitted only from the cloud-top level and above. The effect of the clouds on a given sounding depends on (a) the fraction of cloud cover in the field of view of the sounder and (b) the altitude of the clouds. The sounder does not see the ground whenever clouds are in the way. Instead, it sees the cloud top. Because the cloud top is always at a considerably lower temperature than the ground, the radiance values in all channels are reduced below the values that they would have if no clouds were present. The amount of the reduction depends on the altitude or pressure level of the cloud top, P_c , and on the fractional amount of cloud, η , present in the field^c of view.

Determination of Cloud Pressure. The method developed for determination of P_c was described by Hogan in the previous report. It can be summarized as follows: invert the radiances for several soundings in the neighborhood of the same point, that is, within a few hundred kilometers of each other; presumably the atmospheric temperature profile is the same for each sounding and the cloud height is also the same; the fraction of cloud (η) in each field of view will, however, differ greatly from one sounding to another; therefore, the temperature profiles derived from the group of soundings will resemble the family of curves sketched below. In particular, all profiles will meet at a pressure which is the approximate pressure of the cloud top, P_c .

This procedure for determining P_c was translated into a simple automatic computational algorithm by Ungar of CSC. The method selects the "hottest" and the "coldest" soundings in a group, i.e., the pair of soundings with the highest and lowest readings, respectively, in the window channel. These give the maximum spread in temperature below the clouds, and, therefore, the highest accuracy in the location of P_c . The Ungar algorithm first computes the mean difference between the two profiles, proceeding downward from the top of the atmosphere. Then, proceeding upward, a ratio is computed of the difference at a given level to the mean difference for all levels above that point. At the bottom of the atmosphere, this ratio is considerably larger than 1, because the divergence between the two curves is greater near the surface than at higher altitudes. Moving upward, the ratio remains greater than 1 until the level is reached at which the two curves come close together. At this level and above, the ratio is ≈ 1 . The program chooses P_c as the pressure level at which the ratio is 1.1. Tests show that the test is not sensitive to the value of the critical ratio. This algorithm for determining P_c has been incorporated into the GISS production program for VTPR temperature retrievals.

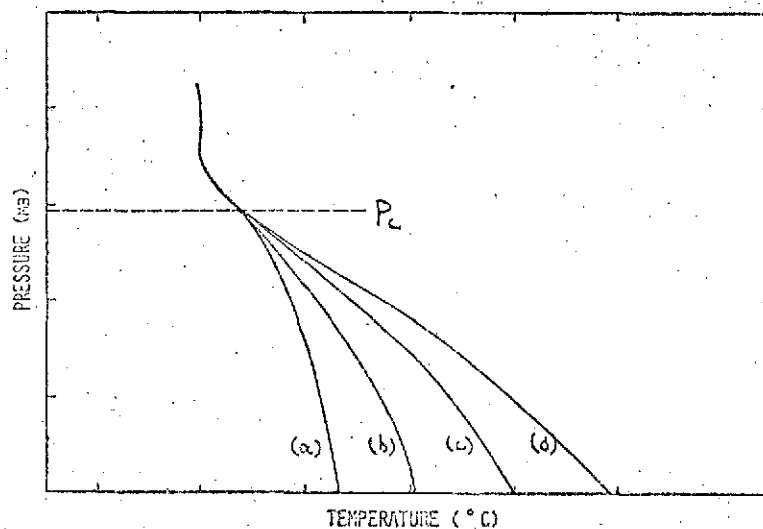


Figure 1. Schematic showing several soundings (a)-(d) over neighboring points, with varying amounts of cloud. The cloud level is the same for all soundings. Curves (a) and (d) represent the soundings with the greatest and least amounts of cloud, respectively. All curves meet at one level which gives the cloud-top pressure, P_c .

Determination of Cloud Fraction. With P_C determined, the next essential step is the determination of η . This is, however, not possible with the information provided thus far, because for any value of η , (and a given value of P_C), the observed radiances can be inverted to obtain an acceptable temperature profile. This is done by starting with the expression (where R^V is the radiance in the channel)

$$R_{\text{observed}}^V = (1-\eta) R_{\text{clear}}^V + \eta R_{\text{cloudy}}^V$$

and, with the assumed value of η , solving for the clear-column radiances, R_{clear}^V . This process can be carried out for any value of η between 0 and 1. The result is a family of curves, $T(P, \eta)$, which are sketched below for four cases, $\eta_1 < \eta_2 < \eta_3 < \eta_4$.

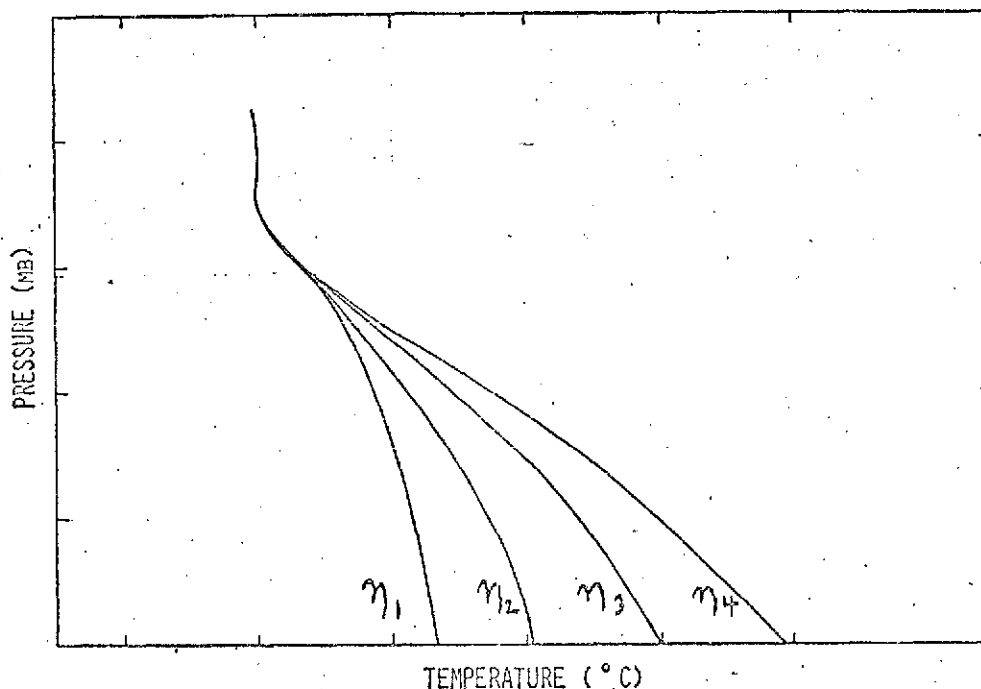


Figure 2. The curves represent four distinct retrievals, all from the same set of observed radiances, but with four different values assumed for η , the cloud fraction. The graph illustrates the indeterminacy introduced into the temperature inversion problem by the presence of clouds in the field of view of the sounder.

All these profiles were retrieved from the same set of observed radiances. It is clear that because of the presence of clouds, an essential indeterminacy exists in the problem of inverting a set of observed radiances to find a temperature profile. The indeterminacy can only be removed if additional information is provided, which in effect fixes the value of η .

What additional information would be most effective in determining η ? The sketch above suggests that a measurement of the surface temperature would be the most desirable form of input, because the spread in the profiles, calculated for various values of η , is greatest at the surface. Therefore a knowledge of T_s should determine the value of η with high accuracy.

In order to implement this idea, it is only necessary to perform the inversion for several values of η and find, by interpolation, the value that produces a profile agreeing with the observed T_s . This procedure is only useful, however, if accurate observed values of T_s are globally available. In practice, there are several sources of information regarding T_s . In the northern hemisphere, surface stations and ship reports provide data twice daily. In the southern hemisphere, sea-surface temperature measurements are sparser but climatology provides values with a dispersion of a few degrees that may be good enough to be useful. Sea-surface temperature measurements from the SR imaging radiometer are expected to become operational shortly, and should provide global coverage with a precision of 1°C . Microwave radiometers, such as NEMS on Nimbus 5, will provide other independent information. Experience must be acquired in the interpretation of the microwave data, but they hold promise for the future.

This η -interpolation method effectively anchors the entire profile to a value of T_s . It has been tested by comparison with radiosonde observations, using values of T_s from the NMC surface analysis, and has been found to yield good results. The method has been incorporated into the production code for VTPR retrievals.

In its production form it uses surface temperatures supplied by the GISS model, corrected twice daily by insertion of the NMC surface analyses.

An alternative procedure developed by Hogan solves for η in channel 7, using the expression,

$$R_{\text{obs}}^v = (1-\eta) R_{\text{clear}}^v + R_{\text{cloudy}}^v$$

The Hogan method also depends on T_s , which makes the main contribution to R_{clear} in channel 7 (747 cm^{-1}). It yields comparable results in the radiosonde comparisons. Further testing is necessary to determine which method will yield higher accuracy for the purposes of the insertion in the model and the forecasting studies.

The accuracy of the η -interpolation procedure has been investigated in an extended series of radiosonde comparisons involving ~ 125 stations over a 15-day period in December. The results are given in the concluding report.

TUNING THE RETRIEVALS. (R. Jastrow and M. Halem)

After cloud effects are eliminated or substantially reduced, systematic discrepancies appear clearly in the comparisons between the VTPR soundings and radiosonde observations. These systematic effects are obscured by cloud contamination and are not apparent in the results prior to the filtering out of the clouds. An example of such systematic effects is a uniformly negative error, i.e., (soundings systematically colder than radiosonde observations), at low latitudes in the mid-troposphere, between 200 and 800 mb.

Presumably the major source of such systematic effects is in the transmission functions used for the retrieval, whose theoretical values are uncertain by at least a few percent in each channel. However, the same types of systematic errors could also result from improper calibration of the sounder, or incorrectly specified filter functions for some channels, or residual errors in the determination of η and P_c described above.

These systematic errors can be minimized conveniently by small adjustments in the transmission functions employed in the calculation. Figure 1 on the next page shows the change in the retrieved temperature as a function of pressure, for changes of the order of 1 percent in channels 4 through 8. Similar curves exist for channels 2 and 3, with maxima at higher altitude and lower pressure. Inspection of these curves indicates that a superposition of channel corrections with properly chosen signs and magnitudes can approximate any desired change in the temperature profile in the region roughly between 100 and 900 mb, provided the desired change is smooth.

For example, if the VTPR temperature is too low in the 200 to 800 mb region, as noted above, an upward adjustment of the absorption coefficients in the channels that contribute to the radiation in this region will elevate the corresponding

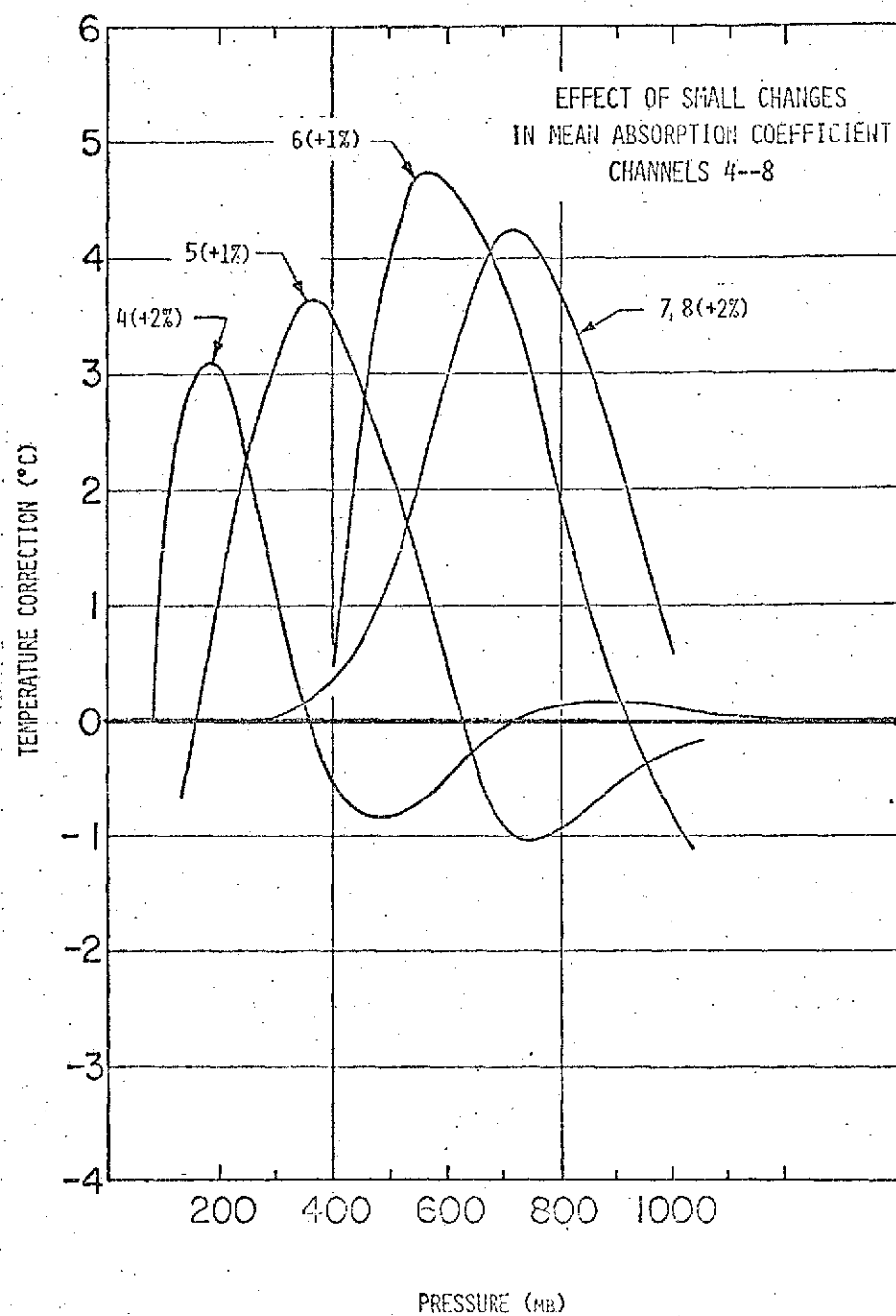


Figure 1. Curves of temperature variations produced by the indicated percentage changes in the mean absorption coefficient or optical thickness in each channel. These curves were used to tune the retrievals.

temperatures in the retrieved profile. Curve A of Figure 2 shows the systematic error between 200 and 800 mb which was referred to above, and curve B shows the result of tuning the retrieval by adjusting the mean absorption coefficient in each channel by the following amounts:

Channel 3: + 2%

Channel 5: + 0.75%

Channel 6: + 0.75%

Channel 7: + 1%

Channel 8: + 1%

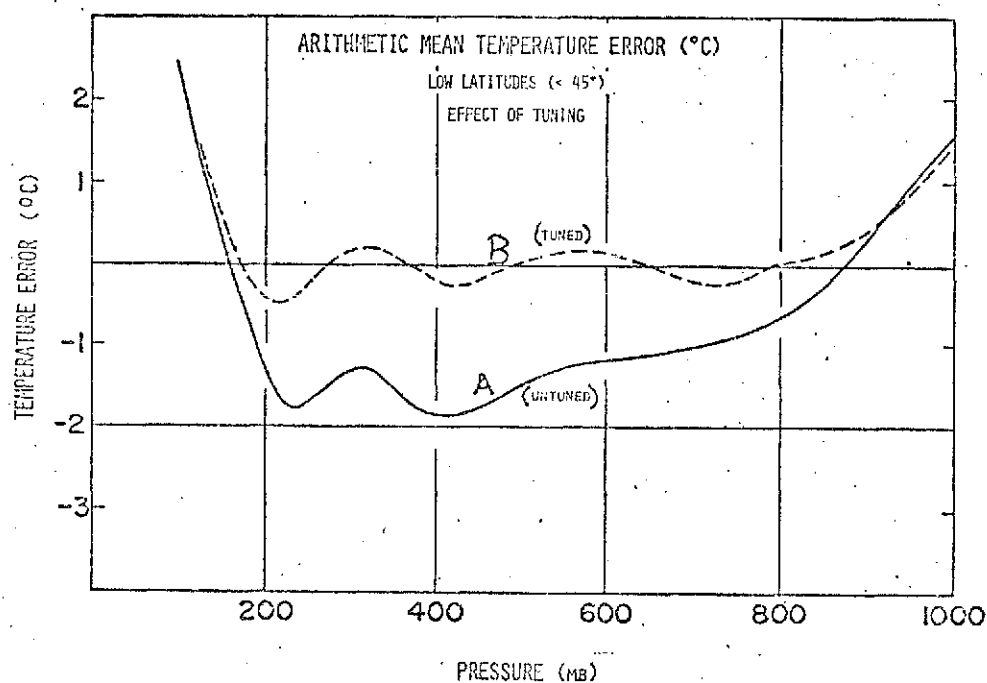


Figure 2. Curve A shows systematically cold retrievals (compared to radiosonde observations) obtained from VTPR soundings averaged over a 2 day period in December.

Curve B shows the average error in the same soundings after tuning, i.e., adjustment of the absorption coefficients in Channels 3 - 8 of the sounder.

ACCURACY OF VTPR TEMPERATURE RETRIEVALS. (M. Halem and R. Jastrow)

The VTPR temperature data were tested by comparison with the global network of radiosonde stations included in the daily list of station reports collected by NOAA. The list includes approximately 600 station reports for 00Z and 12Z each day. The test period began December 9 and ended December 24. The complete file of approximately 2.5 million VTPR soundings for this 15-day period was searched and soundings were selected lying within ± 1 hour of synoptic time. The radiosonde observations and the selected soundings were stored on disk and a second search was made for all soundings lying within a specified distance from all radiosonde stations (100, 200 or 400 km in various tests). Retrievals were then made for all VTPR soundings in the vicinity of a given radiosonde station, and RMS differences between the VTPR soundings and the radiosonde observations at standard pressure levels were computed and averaged. In some experiments, the individual soundings were converted to temperature profiles and the temperatures were averaged, while in other experiments, the radiances were first averaged and temperatures were then computed from the averaged radiances. The results differed by no more than a few tenths of a degree in most cases. The RMS error between the radiosonde observations and the soundings, averaged over all observations, during the period of the test, was taken as the criterion for judging the accuracy of the VTPR-derived temperatures.

In addition to computing the averaged RMS error, the *arithmetic* mean of the error at each standard pressure level was also computed. The arithmetic mean error was used as the basis for judging the presence of systematic effects, and for introducing compensating corrections into transmission functions, in the tuning procedure discussed above. Systematic effects were exhibited most clearly when the table of arithmetic mean errors was printed out separately for low-latitude ($< 45^\circ$) and high-latitude stations.

For the purpose of the test, the 15-day period was divided into five 3-day periods. Adjustments were made in the transmission functions to minimize the systematic errors for the first 3-day period of December 9-12. These adjustments were rough and represented coarse tuning aimed at eliminating the largest errors. The coarse tuning produced an average RMS of 1.99° C for the 3-day period of December 9-12.

The accuracy of this result was encouraging. However, it was important to know whether the tuning developed for the first 3 days would remain valid for the entire 15-day period of the

test. To test the stability of the tuning, the averaged RMS error was computed for the remaining 12 days of the test period without further adjustments in the transmission function. The results are shown in Table 1 below.

Table 1

December 9-12	1.99
December 12-15	missing data
December 15-18	2.04
December 18-21	2.31
December 21-24	1.87

The table does not suggest any significant trend away from the initial RMS error of approximately 2.0° C. Further tests are needed to determine whether this stability is maintained over still longer intervals than 15 days. However, the degree of stability already indicated by these results would be sufficient for operational purposes, since re-tuning could easily be carried out at 2 or 3-day intervals.

The mean value of the temperature error was 2.05° C for the 15-day period. The graph below shows the distribution of temperature errors around the mean value. This graph represents radiosonde comparisons for approximately 2500 separate soundings.

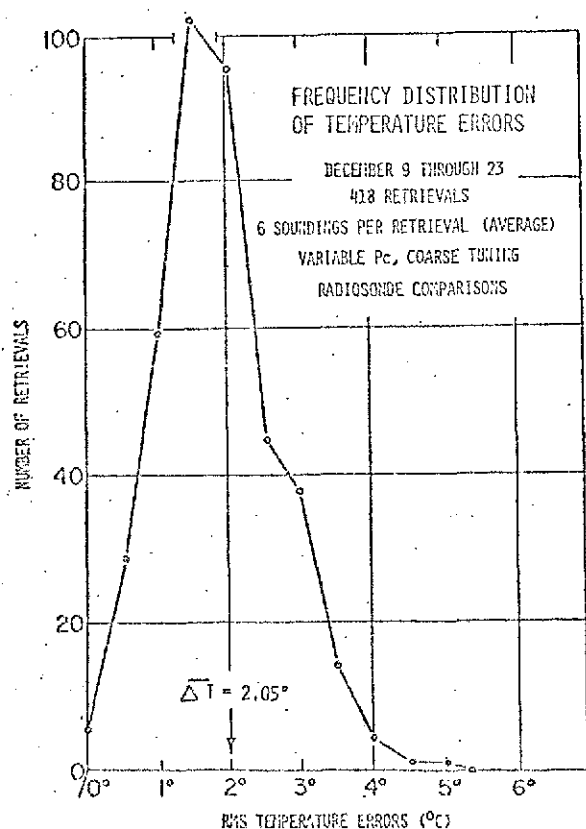


Figure 2. Distribution of RMS temperature errors.

A value for the cloud fraction η was computed for each temperature retrieval, using the η -interpolation method described in the previous report. The mean value of η was 0.52. The distribution of η values around the mean is shown in Figure 3.

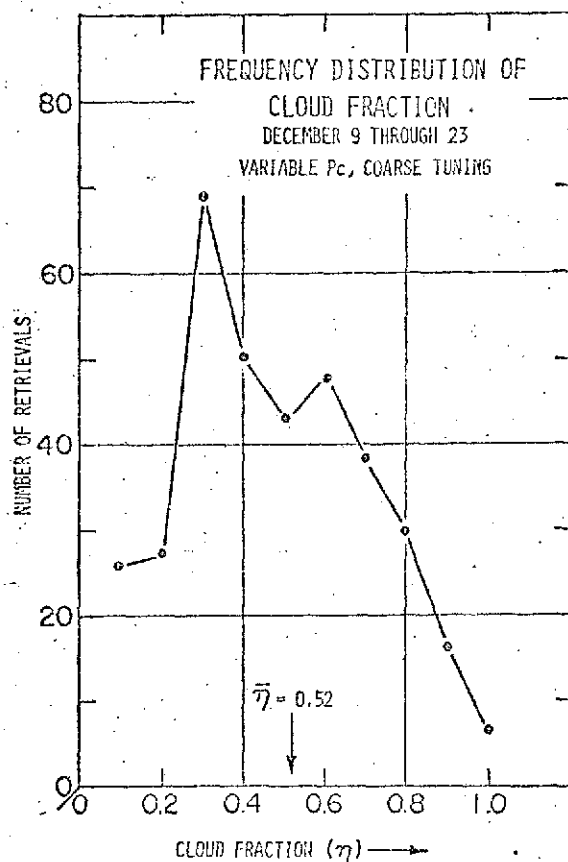


Figure 3. Distribution of fractional cloud amounts computed by anchoring the profile to a given surface temperature and interpolating η , as described in the text.

Effectiveness of the Cloud-Filtering Technique. As indicated earlier, cloud effects are the most serious source of error in the temperature retrievals. In view of the magnitude of the cloud effects, it is important to evaluate the effectiveness of the techniques employed here to correct the soundings for cloud-contamination. A graph of RMS temperature error $\bar{\Delta T}$ vs η should reveal the effectiveness of these techniques. If the techniques are ineffective the graph will show no correlation between $\bar{\Delta T}$ and η . If the techniques are reasonably effective, the graph will show a definite relation with ΔT smallest for $\eta = 0$ and becoming larger as $\eta \rightarrow 1$. Figure 4 shows such a graph based on the radiosonde comparisons for the complete test period of December 9 through 24.

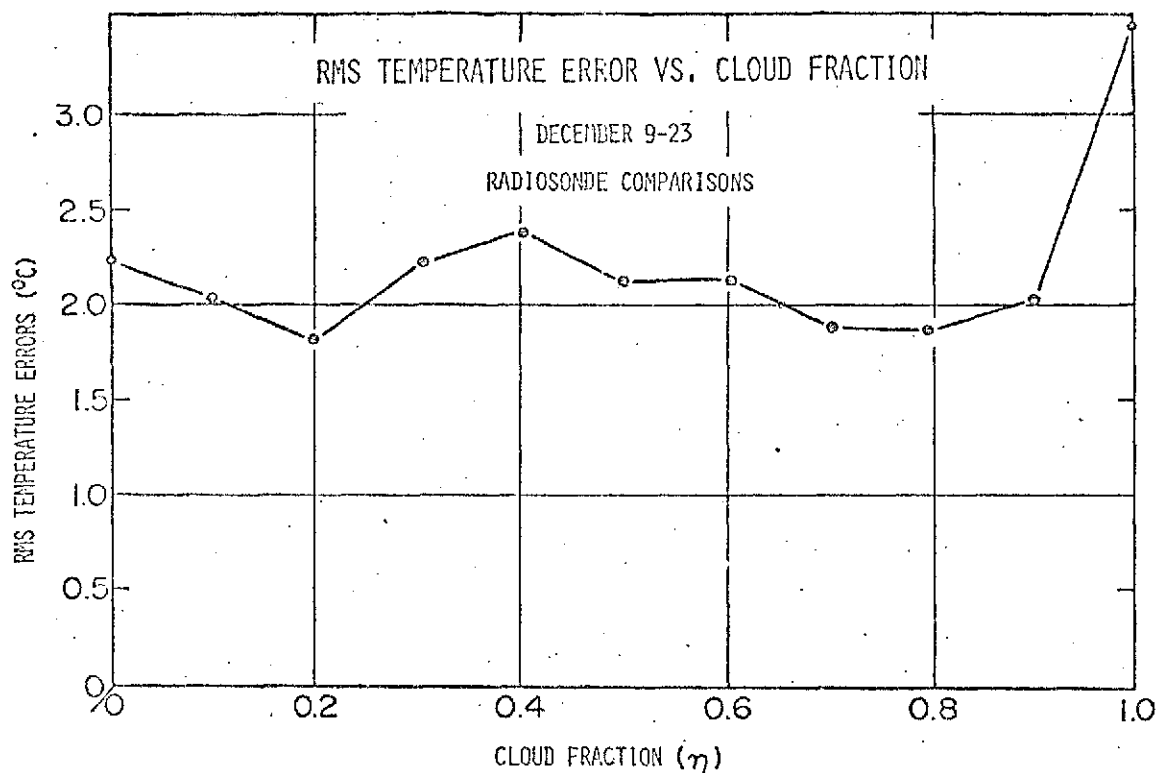


Figure 4. Graph of RMS temperature error vs η indicating that the cloud-filtering techniques are effective for cloud cover up to 80% of the field of view of the sounder.

The temperature error is seen to be approximately independent of η between 0 and 0.8, but increases substantially between 0.9 and 1. This graph suggests that the cloud-filtering technique is effective for soundings in which the cloud cover is as much as 80 per cent.

Possibility of Further Error Reductions. As indicated, an average RMS error of 2°C is the accuracy achieved for a 15-day test with coarse tuning based on eyeball inspection of the tables of mean errors. In tests performed with more accurately co-located radiosonde stations and soundings, but still with coarse tuning by eyeball, the average RMS error for a 2-day period is as low as 1.75°C . With improvements provided by computerized tuning, based on automatic least-squares adjustment of the transmission functions, it may be possible to reduce the RMS error over intervals of several days to as little as 1.5°C . This value probably represents the limit of accuracy obtainable with the VTPR sounder.

Page intentionally left blank

III. PUBLICATIONS

PUBLICATIONS

(January 1, 1972 to December 31, 1972)

- Cameron, A. G. W. EVOLUTION OF ELEMENTS IN THE GALAXIES. Galactic Astronomy, H. Y. Chiu and A. Muriel, eds., New York, Gordon & Breach, 2:171-200, 1972.
- Cameron, A. G. W. NEUTRON STARS. Stellar Evolution, H. Y. Chiu and A. Muriel, eds., Cambridge, MIT Press, 329-350, 1972.
- Cameron, A. G. W. STELLAR COALESCENCE. Stellar Evolution, H. Y. Chiu and A. Muriel, eds., Cambridge, MIT Press, 1972
- Cameron, A. G. W. SURFACE COMPOSITION AND COOLING HISTORIES OF NEUTRON STARS. Highlights of Astronomy, Volume 2. International Astronomical Union, General Assembly, 14th, Brighton, England, August 18-27, 1970, Proceedings. Dordrecht, D. Reidel, 731-736, 1971.
- Cameron, A. G. W. NUCLEOSYNTHESIS AND THE FORMATION OF SUPERHEAVY ELEMENTS. Proceedings of the Mont Tremblant International Summer School, 1971. Dynamic Structure of Nuclear States. D. Rowe, et al., eds., 1972.
- Canuto, V. and Chiu, H. Y. INTENSE MAGNETIC FIELDS IN ASTROPHYSICS. Stellar Evolution, H. Y. Chiu and A. Muriel, eds., Cambridge, MIT Press, 735-806, 1972.
- Canuto, V., Kumar, S., and Lee, H. J. ORIGIN OF STRONG MAGNETIC FIELDS. Nature, 235(53):9-10, January 3, 1972.
- Canuto, V., Chitre, S. M. QUANTUM CRYSTALS IN NEUTRON STARS: I.A.U. Symposium on Physics of Dense Matter, 1972.
- Canuto, V., Ventura, J. QUANTUM THEORY OF THE DIELECTRIC CONSTANT OF A MAGNETIZED PLASMA AND ASTROPHYSICAL APPLICATIONS: I. THEORY. Astrophysics and Space Science, 18:104-120, 1972.
- Carson, T. R. STELLAR OPACITY. Stellar Evolution, H. Y. Chiu and A. Muriel, eds., MIT Press, 1972.
- Chitre, S. M., Hartle, J. B., Thorne, K. S. SLOWLY ROTATING RELATIVISTIC STARS. VI. STABILITY OF THE QUASIRADIAL MODES. The Astrophysical Journal, 176:177-194, August 15, 1972.
- Chiu, H. Y. NEUTRON STARS. The Physics of Pulsars, A. M. Lenchek, ed., New York, Gordon & Breach, 111-118, 1972.

- Chiu, H. Y. PULSARS - ROTATING MAGNETIC NEUTRON STARS. The Physics of Pulsars, A. M. Lenchek, ed., New York, Gordon & Breach, 135-150, 1972.
- Chiu, H. Y. A REVIEW OF THEORIES OF PULSARS. Stellar Evolution, H. Y. Chiu and A. Muriel, eds., Cambridge, MIT Press, 351-396, 1972.
- Chiu, H. Y. STELLAR EVOLUTION AND PULSARS. Annals of the New York Academy of Sciences, 187:177-185, January 25, 1972.
- Chiu, H. Y., Canuto, V. MASER MECHANISM FOR PULSAR RADIATION. Accademia Nazionale dei Lincei, Quaderno N. 162:225-250, 1972.
- Coffeen, D. L., Hansen, J. E. AIRBORNE INFRARED POLARIMETRY. Eighth International Symposium on Remote Sensing of Environment Proceedings, 1972.
- Coffeen, D. L., Hansen, J. E. POLARIZATION STUDIES IN PLANETARY ATMOSPHERES. Planets, Stars and Nebulae Studied with Photopolarimetry, Gehrels, T., ed., University of Arizona press, 1972.
- DeZafra, R. L., Thaddeus, P., Kutner, M., Scoville, N., Solomon, P. M., Weaver, H., and Williams, D. R. W. SEARCH FOR INTERSTELLAR FURAN AND IMIDAZOLE. Astrophysical Letters, 10:1-3, January 1972.
- Druyan, L. M. OBJECTIVE ANALYSIS OF SEA-LEVEL WINDS AND PRESSURES DERIVED FROM SIMULATED OBSERVATIONS OF A SATELLITE RADAR-RADIOMETER AND ACTUAL CONVENTIONAL DATA. Journal of Applied Meteorology, 11(3):413-428, April 1972.
- Emery, R. ATMOSPHERIC ABSORPTION MEASUREMENTS IN THE REGION OF 1 mm WAVELENGTH. Infrared Physics, 12:65-79, March 1972.
- Ezer, D. and Cameron, A. G. W. THE EVOLUTION OF HYDROGEN-HELIUM STARS. Astrophysics and Space Studies, 14:399-421, December 1971.
- Gordon, Charlotte (Pecker-Wimel). SPECTRA OF TYPE I SUPERNOVAE. Astronomy and Astrophysics, 20:79-85, 87-98, 1972.
- Green, S. CALCULATED PROPERTIES FOR NO $X^2 \Pi$ and $A^2 \Sigma^+$. Chemical Physics Letters, 13(6):552-556, April 15, 1972.
- Green, S. ELECTRIC DIPOLE MOMENT OF DIATOMIC MOLECULES BY CONFIGURATION INTERACTION. V. TWO STATES OF $^2 \Sigma^+$ SYMMETRY IN CN. Journal of Chemical Physics, 57:4694, 1972.

- Green, S. ELECTRIC DIPOLE MOMENT OF DIATOMIC MOLECULES BY CONFIGURATION INTERACTION. IV. BASIS SET DEPENDENCE IN CO A II. Journal of Chemical Physics, 57:2830, 1972.
- Hansen, J. E. INFORMATION CONTAINED IN THE INTENSITY AND POLARIZATION OF SCATTERED SUNLIGHT. (Reprint) Goddard Institute for Space Studies, NASA, New York, 32pp., 1972.
- Hansen, J. E., Coffeen, D. L. POLARIZATION OF NEAR-INFRARED SUNLIGHT REFLECTED BY TERRESTRIAL CLOUDS. Preprint Volume of the Conference on Atmospheric Radiation, American Meteorological Society, 55-60, 1972.
- Hoffmann, W. F. REVIEW OF RESULTS IN INFRARED SPACE ASTRONOMY, Infrared Detection Techniques for Space Research -- Proceedings of the 5th ESLAB/ESRIN Symposium, Dordrecht; D. Reidel Co., 1972.
- Hoffmann, W. F. FAR-INFRARED OBSERVATIONS OF CELESTIAL OBJECTS BY BALLOON BORNE TELESCOPE, Infrared Detection Techniques for Space Research -- Proceedings of the 5th ESLAB/ESRIN Symposium, Dordrecht; D. Reidel Co., 1972.
- Hoffmann, W. F. BALLOON OBSERVATIONS OF GALACTIC AND EXTRAGALACTIC OBJECTS AT 100 MICRONS. 17^e Colloque International d'Astrophysique, Liège, 1971. Communications. In Société Royale des Sciences de Liège. Mémoires 355-361.
- Hoffmann, W. F. FUTURE INFRARED SPACE ASTRONOMICAL INSTRUMENTS Astronomy from a Space Platform, American Astronautical Society Proceedings 28, AAS-S&T, 1972.
- Hogan, J. S. and Grossman, K. TESTS OF A PROCEDURE FOR INSERTING SATELLITE RADIANCE MEASUREMENTS INTO A NUMERICAL CIRCULATION MODEL. Journal of the Atmospheric Sciences, 29(4): 797-800, May 1972.
- Hogan, J. S., Stewart, R. W., and Rasool, S. I. RADIO OCCULTATION MEASUREMENTS OF THE MARS ATMOSPHERE WITH MARINERS 6 AND 7. Radio Science, 7(5):525-537, May 1972.
- Hogan, J. S., Stewart, R. W., Rasool, S. I., and Russell, L. H. RESULTS OF THE MARINER 6 AND 7 MARS OCCULTATION EXPERIMENTS. NASA TN D-6683, March 1972.
- Jaffe, J. ANOMALOUS MOTION OF RADIATING PARTICLES IN STRONG FIELDS. Physical Review D, 5(12):2909-2911, June 15, 1972.
- Liou, K. N. LIGHT SCATTERING BY ICE CLOUDS IN THE VISIBLE AND INFRARED: A THEORETICAL STUDY. Journal of the Atmospheric Sciences, 29(3):524-536, April 1972.

- Liou, Kuo-Nan. ON DEPOLARIZATION OF VISIBLE LIGHT FROM WATER CLOUDS FOR MONOSTATIC LIDAR. Journal of the Atmospheric Sciences, 29(5):1000-1003, July 1972.
- Liou, Kuo-Nan. LIGHT SCATTERING BY CIRRUS CLOUD LAYERS. Conference on Atmospheric Radiation, Fort Collins, Colo., 1972 Preprints. Boston, American Meteorological Society, 121-127, 1972.
- Moore, J. F. INFRARED ABSORPTION OF CARBON DIOXIDE AT HIGH DENSITIES WITH APPLICATION TO THE ATMOSPHERE OF VENUS. Goddard Space Flight Center, X-630-72-48, December 1971.
- Quirk, W. J. ON THE GAS CONTENT OF GALAXIES, Astrophysical Journal, 176:L9-L14, August 15, 1972.
- Rasool, S. I., ed. PHYSICS OF THE SOLAR SYSTEM. NASA SP-300, Washington, D. C., 1972.
- Rasool, S. I. PLANETARY ATMOSPHERES. Exobiology, C. Ponamperuma, ed., North-Holland Publishing Co., 369-399, 1971.
- Rosen, L. C., Cameron, A. G. W. SURFACE COMPOSITION OF MAGNETIC NEUTRON STARS. Astrophysics and Space Science, 15:137-152, 1972.
- Seidl, F. G. P. and Cameron, A. G. W. A NUMERICAL HYDRODYNAMIC STUDY OF COALESCENCE IN HEAD-ON COLLISIONS OF IDENTICAL STARS. Astrophysics and Space Science, 15:44-128, 1972.
- Schneck, P. B. AUTOMATIC RECOGNITION OF PARALLEL AND VECTOR OPERATIONS IN A HIGHER LEVEL LANGUAGE. Association for Computing Machinery 1972 Proceedings, pp. 772-779, 1972.
- Schneck, P. B. AUTOMATIC RECOGNITION OF PARALLEL AND VECTOR OPERATIONS IN A HIGHER LEVEL LANGUAGE, SIGPLAN Notices, 7(11), December 1972.
- Schneider, S. H. NUMERICAL STUDY OF STRONG PLASMA SHOCK WAVES PRODUCED IN AN ELECTROMAGNETIC SHOCK TUBE. The Physics of Fluids, 15:805-814, May 1972.
- Schneider, S. H. CLOUDINESS AS A GLOBAL CLIMATIC FEEDBACK MECHANISM: THE EFFECTS ON THE RADIATION BALANCE AND SURFACE TEMPERATURE OF VARIATIONS IN CLOUDINESS. Journal of the Atmospheric Sciences, 29(8):1413-1422, November 1972.
- Scoville, N. Z., Solomon, P. M., Thaddeus, P. SURVEY OF MOLECULAR LINES NEAR THE GALACTIC CENTER. I. 6-CENTIMETER FORMALDEHYDE ABSORPTION IN SAGITTARIUS A, SAGITTARIUS B2, AND THE GALACTIC PLANE FROM $\ell_{\text{II}} = 359.4$ TO $\ell_{\text{II}} = 2.2$. The Astrophysical Journal, 172:335-353, March 1, 1972.

- Somerville, R. C. J. NUMERICAL SIMULATION OF SMALL-SCALE THERMAL CONVECTION IN THE ATMOSPHERE. Proceedings of the Third International Conference on Numerical Methods in Fluid Dynamics, Paris, July 3-7, 1972. Lecture Notes in Physics, Springer-Verlag, 19, 238-245 (1973).
- Stewart, R. W., Hogan, J. S. ERROR ANALYSIS FOR THE MARINER 6 AND 7 OCCULTATION EXPERIMENTS. Mathematics of Profile Inversion, NASA: TM X-62, 150, 1972.
- Stone, P. H. Comments on AGEOSTROPHIC EFFECTS ON BAROCLINIC INSTABILITY. Journal of Atmospheric Sciences, 29:986-997, 1972.
- Stone, P. H., Gierasch, P. Reply to Comments on A MECHANISM FOR JUPITER'S EQUATORIAL ACCELERATION. Journal of Atmospheric Sciences, 29:1008, 1972.
- Stone, P. H., Hadlock, R., Na, Y. DIRECT THERMAL VERIFICATION OF SYMMETRIC BAROCLINIC INSTABILITY. Journal of Atmospheric Sciences, 29:1391-1393, 1972.
- Stothers, R. STRUCTURE OF MASSIVE MAIN-SEQUENCE STARS. Stellar Evolution, H. Y. Chiu and A. Muriel, eds., Cambridge, MIT Press, 1972.
- Stothers, R. and Lucy, L. B. NATURE OF THE SECONDARY COMPONENT OF BETA LYRAE. Nature, 236(5344):218-219, March 31, 1972.
- Stothers, R. CONVECTIVE ENVELOPES AND RADIAL PULSATION OF MASSIVE RED SUPERGIANTS. Astronomy and Astrophysics, 18:325-328, May 1972.
- Stothers, R. A RECALIBRATION OF THE ABSOLUTE MAGNITUDES OF SUPERGIANTS. Astronomical Society of the Pacific, Publications, 84(499):373-378, June 1972.
- Stothers, R. UNDERLUMINOSITY AND MAGNETIC FIELDS IN BETA LYRAE. Nature, 238(79) (Physical Science):5-6, July 3, 1972.
- Stothers, R. FUNDAMENTAL DATA FOR MASSIVE STARS COMPARED WITH THEORETICAL MODELS. Astrophysical Journal, 175(2): 431-452, July 15, 1972.
- Stothers, R. RED SUPERGIANTS AND NEUTRINO EMISSION. II Astrophysical Journal, 175:717-730, August 1972.
- Stothers, R., Chin, C. W. THERMAL INSTABILITY OF THE HYDROGEN-BURNING SHELL IN NONDEGENERATE STARS. Astrophysical Journal, 177: October 1, 1972.

- Stothers, R., Ezer, D. SOLAR NEUTRINOS AND THE INFLUENCES OF OPACITY, THERMAL INSTABILITY, ADDITIONAL NEUTRINO SOURCES, AND A CENTRAL BLACK HOLE ON SOLAR MODELS. Astrophysical Letters, 12, November, 1972.
- Susskind, J. VAN-VLECK PERTURBATION THEORY APPLIED TO VIBRATION-ROTATION INTERACTION IN TETRAHEDRAL MOLECULES. Journal of Chemical Physics. 56:5152, 1972.
- Susskind, J. MEASUREMENT AND ANALYSIS OF THE ν_3 BAND OF METHANE. Journal of Chemical Physics. 56:5156³, 1972.
- Thaddeus, P. INTERSTELLAR FORMALDEHYDE. I. THE COLLISIONAL PUMPING MECHANISM FOR ANOMALOUS 6-CENTIMETER ABSORPTION. The Astrophysical Journal, 173:317-342, April, 15, 1972.
- Thaddeus, P. THE SHORT-WAVELENGTH SPECTRUM OF THE MICROWAVE BACKGROUND. Annual Review of Astronomy and Astrophysics. 10:305-334, 1972.
- Thaddeus, P., Kutner, M. L., and Penzias, A. A., Wilson, R. W., Jefferts K. B. INTERSTELLAR HYDROGEN SULFIDE. The Astrophysical Journal, 176:L73-L76, Sept. 1, 1972.
- Truran, J. W. and Cameron, A. G. W. EVOLUTIONARY MODELS OF NUCLEOSYNTHESIS IN THE GALAXY. Astrophysics and Space Science, 14:179-222, 1971.
- Truran, J. W. and Cameron, A. G. W. THE P-PROCESS IN EXPLOSIVE NUCLEOSYNTHESIS. The Astrophysical Journal, 171:89-92, January 1, 1972.
- Tsuruta, S., Canuto, V., Lodenquai, J., Ruderman, M. COOLING OF PULSARS. The Astrophysical Journal, 176:739-744, Sept. 15, 1972.
- Tucker, K. D., Tomasevich, G. R., and Thaddeus, P. LABORATORY MEASUREMENT OF THE 2-CENTIMETER, $2_{11}-2_{12}$, TRANSITION OF NORMAL FORMALDEHYDE AND ITS CARBON-13 AND OXYGEN-18 SPECIES. The Astrophysical Journal, 174(2):463-466, June 1, 1972.
- Ungar, Steven G., Lusignan, Bruce B. AN OCCULTATION SATELLITE SYSTEM FOR DETERMINING PRESSURE LEVELS IN THE ATMOSPHERE, Mathematics of Profile Inversion, Colin, L., ed., NASA TM X-62, 150, August, 1972.
- White, Richard, E. PHOTOELECTRIC OBSERVATION OF INTERSTELLAR CA I. Bulletin, American Astronomical Society, 4:327, 1972.

Willis, G. E., Deardorff, J. W., Somerville, R. C. J. ROLL-DIAMETER DEPENDENCE IN RAYLEIGH CONVECTION AND ITS EFFECT UPON THE HEAT FLUX. Journal of Fluid Mechanics, 54(2): 351-367, 1972.

Wilson, R. W., Penzias, A. A., Jefferts, K. B., and Thaddeus, P., Kutner, M. L. INTERSTELLAR NITROGEN-15 AND U 169, 3-- POSSIBLY A NEW METHANOL LINE. The Astrophysical Journal, 175:L77-L79, Sept. 1, 1972.

Wilson, R. E., Deluccia, M. R., Johnston, K., Mango, S. PHOTOMETRY & DIFFERENTIAL CORRECTIONS ANALYSIS OF ALGOL. The Astrophysical Journal, 177:191-208, 1972.

Page intentionally left blank

IV. GISS COLLOQUIA

Page intentionally left blank

GISS COLLOQUIA

(January 1, 1972 to December 31, 1972)

WHAT IS AN ELEMENTARY PARTICLE?, V. F. Weisskopf, Massachusetts Institute of Technology, January 6.

NUCLEAR ASTROPHYSICS, W. A. Fowler, California Institute of Technology, January 19.

CIRCULATION OF PLANETARY ATMOSPHERES, E. N. Lorenz, Massachusetts Institute of Technology, February 10.

ENVIRONMENTAL PROBLEMS, G. J. F. MacDonald, President's Council on Environmental Quality, March 9.

COMPACT X-RAY SOURCES, E. E. Salpeter, Cornell University, March 23.

STRUCTURE AND DYNAMICS OF PLANETARY ATMOSPHERES, Peter J. Gierasch, Florida State University, April 13.

PROBLEMS IN CONTROLLED FUSION, R. F. Post, Lawrence Radiation Laboratories, April 28.

ORIGIN OF THE SOLAR SYSTEM, A. G. W. Cameron, Yeshiva University, May 11.

PROBLEMS IN LOW TEMPERATURE PHYSICS, R. A. Guyer, University of Massachusetts, May 25.

OXYGEN AND LIFE, James Walker, Yale University, June 22.

LASER INDUCED FUSION, K. A. Brueckner, University of California, October 5.

NATURE AND EVOLUTION OF IRREGULARITIES IN THE UNIVERSE, P. J. E. Peebles, Princeton University, October 12.

COLLAPSING CLOUDS AND STAR FORMATION, Richard B. Larson, Yale University, November 16.